DISSERTATION ZUR ERLANGUNG DES DOKTORGRADES

DER FAKULTÄT FÜR CHEMIE UND PHARMAZIE

DER LUDWIG-MAXIMILIANS-UNIVERSITÄT MÜNCHEN

Metal-Organic Frameworks for

Chemical Sensing Applications

FLORIAN MATTHIAS HINTERHOLZINGER

AUS

MÜNCHEN, DEUTSCHLAND

2013

Erklärung

Diese Dissertation wurde im Sinne von § 7 der Promotionsordnung vom 28. November 2011 von Herrn Prof. Dr. Thomas Bein betreut.

Eidesstattliche Versicherung

Diese Dissertation wurde eigenständig und ohne unerlaubte Hilfe bearbeitet.

München, 17.04.2013

_____

Florian Hinterholzinger

Dissertation eingereicht am 19.03.2013

1. Gutachter: Prof. Dr. Thomas Bein

2. Gutachter: Prof. Dr. Konstantin Karaghiosoff

Mündliche Prüfung am 16.04.2013

Danksagung

Ich möchte mich an allererster Stelle bei meinem Doktorvater Prof. Dr. Thomas Bein für die freundliche Aufnahme in seinen Arbeitskreis und für das entgegengebrachte Vertrauen während meiner Promotion bedanken. Ich danke ihm besonders für den Freiraum, den er mir bei der Planung und der selbstständigen Durchführung der Projekte überließ. Er bot mir bereits während meiner Masterarbeit die Möglichkeit das Gebiet der Metall-organischen Gerüstverbindungen und deren Verwendung als chemische Sensoren zu untersuchen und im Zuge meiner Promotion weiter zu vertiefen und auszubauen. Dies ist auch auf die vielen Ideen, die aus zahlreichen Gesprächen, Treffen und Konferenzteilnahmen entsprungen waren, zurückzuführen. Neben der Freiheit und der Selbstständigkeit wurde es einem nicht zuletzt durch die hervorragende Ausstattung seiner Arbeitsgruppe ermöglicht verschiedene Projekte erfolgreich abzuschließen. Durch die Teilnahme auf zahlreichen nationalen wie internationalen Konferenzen konnte ich wichtige soziale Kontakte knüpfen und Erfahrungen sammeln, von denen ich heute noch profitiere.

Ich möchte mich bei Herrn Prof. Dr. Konstantin Karaghiosoff sowohl für die spannende und äußerst erfolgreiche Kooperation als auch für seine Bereitschaft das Zweitgutachten über meine Arbeit zu erstellen, herzlich bedanken.

Dr. Camilla Scherb danke ich fürs Empfehlen, für die Betreuung während meiner Masterarbeit und damit für den perfekten Einstieg in das Thema dieser Doktorarbeit. Durch unsere Zusammenarbeit an unseren zwei gemeinsamen Projekten konnte ich sehr viel von ihr lernen.

Ich möchte mich außerdem bei meinen zahlreichen internen wie externen Kooperationspartnern bedanken. Durch die gute Zusammenarbeit konnten wir gemeinsam unsere Ziele erreichen und somit einige Projekte erfolgreich abschließen. Hierfür danke ich Herrn Prof. Dr. Norbert Stock, Frau Prof. Dr. Bettina Lotsch und Frau Prof. Dr. Adelheid Godt, Dr. Tim Ahnfeldt, Dr. Jennifer Williams, Hans Feckl, Annekathrin Ranft (AK Lotsch), Dr. Pascal Roy (AK Godt), Thomas Preuße (AK Godt), Dr. Stefan Wuttke und ganz besonders Bastian Rühle für seine Hilfsbereitschaft und Geduld beim Beantworten vieler wissenschaftlicher wie auch technischer Fragen, für seine Zeit und Hilfe beim Entwerfen der zahlreichen POV-Ray-Bilder und für unsere äußerst erfolgreichen Kooperationen.

Ganz entscheidend für die Freude an der Arbeit war die ausgesprochen angenehme und freundschaftliche Atmosphäre untereinander. Ich möchte mich hierfür beim gesamten AK Bein bedanken, allen voran bei meinen MOF-COF-Subgroupmitgliedern Mirjam, mit der ich lange die 2-Mann-Subgroup bildete und mit der ich viele lustige wie auch enttäuschende Erfahrungen teilen und sammeln durfte, bei Dana, Mona, Maria und Erika, denen ich für ihren weiteren Weg viel Erfolg und Spaß wünsche, bei meinem 3-Jahres-Bürodreamteamkollegen Basti, dem ich nochmal für die perfekte Zusammenarbeit danke und dem ich noch viele wissenschaftliche Erfolge wünsche (aber davon bin ich überzeugt), bei Hans (ich sag nur Sorrent! und Danke für deine soziale Ader ohne die wir nicht so viele lustige Auszeiten erlebt hätten), bei Stefan Wuttke, dem ich weiterhin viel Freude und Enthusiasmus am MOF-Forschen wünsche und natürlich bei Jörg, Norma, Flo, Stefan, Benni, Christian, Alex, Fabi, Halina, Alesja, Askhat, Cindy, Ksenia, Noggi, Andi, Lissi, Dina, Karin und Matze (ich erwähne dich mal hier, auch wenn du kein

ABSTRACT

Over the past decades a great deal of attention has been devoted to the discovery of new analytical methods and to the synthesis of novel sensor materials. In terms of the design of selective optical chemosensors the reliable detection and differentiation among target species is imperative. In addition to numerous other applications of metal-organic frameworks (MOFs), their implementation as chemical sensors has captured increasing interest. MOFs are promising candidates owing to their high surface area and open porosity as well as to the ability to synthetically tailor the chemical environment of their pore system; hence, allowing to endow these materials with a specific recognition-transduction scheme or selective host-guest properties. However, MOF based chemosensors are still quite rare and the development of alternative receptor-transducer systems is subject of current research.

This work aims at the synthesis of MOFs and thin films and at exploiting their potential as chemo-sensory materials. For analyte detection it is of particular interest to incorporate a readable recognition-transduction scheme within the MOF host material. For this purpose, different synthetic strategies were developed to implement certain read-out schemes within the MOF scaffold. Differences in sorption behavior upon exposure to various vapors as well as the selective recognition of different analyte species were achieved by using tailored MOFs as chemo-optical sensor material.

Tailored MOF structures can also be successfully presented as oriented thin films. This was demonstrated for the amino-functionalized and flexible framework structure NH_2-Fe-MIL-88B and the large-pore MOF NH_2-Fe-MIL-101. Direct growth on self-assembled monolayers (SAMs) was achieved by immersing functionalized gold substrates in solvothermally pretreated synthesis solutions. This control of crystal and channel orientation is anticipated to result in facilitated diffusion and analyte uptake. Within this context, oriented MOF thin films were employed for vapor sorption studies using a quartz-crystal microbalance (QCM). It was demonstrated that the introduction of amino groups into the framework strongly affects the host–guest interactions towards ethanol vapor. Upon exposure to the organic vapor, thin films of NH_2–Fe–MIL-88B show a significantly higher uptake of ethanol than its unfunctionalized counterpart. It is anticipated that the implementation of chemical functionalities into oriented MOF films will lead to selective molecular recognition events that are of key importance for chemical sensing applications.

In a joint project between our group and the group of Prof. Bettina Lotsch, a one-dimensional photonic composite material (Bragg stack) based on a microporous MOF and titanium dioxide was developed. The Bragg stack heterostructures were obtained using two complementary synthesis approaches utilizing the bottom-up assembly of heterogeneous, *i.e.,* two-component photonic crystal multilayer structures. Zeolitic imidazolate framework ZIF-8 and mesoporous titanium dioxide were chosen as functional components with different refractive indices. The label-free monitoring of molecular recognition events relies upon changes of the effective refractive index or on a change of the layer thickness. The embedded MOF material

additionally endows the optical transducer with a high degree of selectivity. By means of ellipsometric *in-situ* vapor sorption studies the discrimination among various alcoholic vapors could be demonstrated. The findings have shown that this novel signal transduction scheme inherent to 1-D photonic crystals could be successfully extended to metal-organic frameworks such that MOF-based Bragg stacks will provide a versatile platform for future selective, label-free optical sensors.

With the support of Prof. Adelheid Godt and her group (Bielefeld University), who contributed the amino-functionalized and elongated spacer molecules, large-pore and accessible porous structures having the UiO-68 topology were obtained. Mesoporous UiO-68-NH$_2$ thin films were grown in a highly oriented fashion on two different types of SAMs. MOF growth upon phosphonate-terminated self-assembled monolayers was achieved for the first time. The oriented MOF films were covalently modified with fluorescent reporter molecules inside the pore system, which was demonstrated with size-selective fluorescence quenching studies.

Moreover, luminescence as signal transduction mode was additionally studied on a prototype MOF with intrinsic luminescent properties. For this purpose organic linker molecules with an anthracene unit were incorporated into the scaffold of UiO-68(anthracene). Intense chemiluminescence was elicited by the reaction between oxalic acid esters and hydrogen peroxide in the presence of a base. This work was also pursued in a joint project between our group and the group of Prof. Godt providing the fluorescent linker molecules that were utilized for the optical read-out of the recognition event (such as H$_2$O$_2$ detection).

Finally, we were able to introduce a novel concept for highly sensitive and at the same time highly selective MOF-based sensors. The analyte-induced degradation of the MOF material that coincides with a triggered release of a bound fluorophore could be demonstrated. In order to perform fluorescence sensing experiments, the aluminum based MOF NH_2-MIL-101(Al) was post-synthetically modified with a fluorescein dye as reporter molecule. The dye-labeled MOF shows exceptional turn-on fluorescence in aqueous fluoride-containing solutions. In addition, an unprecedented selectivity for fluoride ions in competition with other halogenide ions and other anions was observed. A mechanistic understanding of the processes that result in the degradation of the crystalline framework was revealed by NMR titration experiments (Collaboration with Prof. Konstantin Karaghiosoff).

In summary, functionalized metal-organic frameworks and MOF thin films were used as a platform for chemical sensing concepts. Different signal transduction schemes were introduced into the porous MOF environment to monitor specific molecular recognition events. In addition, the new and innovative concept of implementing tailored MOF structures as host species for analyte-induced decomposition, followed by a simultaneous release and signaling process, is anticipated to greatly enhance the scope of MOF-based chemical sensing.

Table of Contents

1   Introduction

1.1   Porous materials in nanotechnology

Nanotechnology has been defined as being "concerned with materials and systems whose structures and components exhibit novel and significantly improved physical, chemical and biological properties, phenomena and processes due to their nanoscale size".[1]

Within this context, porous materials offer an enormous degree of structural and compositional diversity as well as a large range of chemical and physical properties. Zeolites, one of the most prominent representatives of nanoporous ordered materials, have been intensively studied and applied in various domestic and industrial fields. Their versatile applications such as catalysts[2] in the petrochemical industry, ion exchangers in detergents[3] and as molecular sieves[4] for separation purposes emphasize the ubiquity of this materials class. However, certain limitations such as their limited pore size or their structural rigidity motivated the development of alternative porous materials such as ordered mesoporous materials[5-7] or metal-organic frameworks. Since the mid-nineties this hybrid counterpart of zeolites has offered many novel perspectives and has been the subject of a large and rapidly increasing number of studies.

During the last decades extensive studies have been focused on the discovery of novel structures and on the tailored design of these materials for a target application. The ability to precisely control their structure and composition, hence their chemical and physical properties allows one to endow the resulting frameworks with the desired structural and functional elements for potential applications including gas storage[8-10] and separation[11] as well as heterogeneous catalysis.[12, 13] More recently, their implementation as host materials for drug delivery[14] or for chemical sensing applications has also attracted growing attention.[15]

The following work will particularly address the potential of metal-organic frameworks as chemical sensors. Along these lines, different structures and synthetic pathways towards the design of a chemo-sensitive platform will be highlighted and discussed. Several strategies for the implementation of a specific recognition-transduction mode were developed and studied, thus contributing to our understanding of molecular sensing and recognition and adding to the growing toolbox for future chemical sensor design.

1.2   Metal-Organic Frameworks: Design and Applications

Although the story of metal-organic frameworks (MOFs) or inorganic-organic hybrid materials already began in the middle of the 20$^{\text{th}}$ century,[16-20] – even though not named as such at the time – the intensive development of MOF chemistry was initiated in the mid nineties.[21-23] This new domain of research has captured the

attention of many academic and industrial researchers in such a way that an abundance of breakthroughs and discoveries can be traced in the literature over the past two decades.[24] Several aspects such as the extraordinary intrinsic properties, the chemical tailorability as well as the structural diversity of MOFs afford an almost infinite number of possible structures and constitute MOFs as subject of intense research. In particular, the modular assembly provides the possibility to adjust pores sizes, to design the shape of the material and to implement different functionalities within the pores.[25] Consequently, the synergistic impact of the inorganic and organic component within a MOF provides intriguing properties for this class of porous solids. Such hybrid materials are thus envisioned as promising candidates for many target applications.

Hybrid inorganic-organic solids are often constructed in a building-block fashion. MOFs are crystalline structures wherein inorganic bricks (*i.e.,* metal ions or clusters) are connected by organic linkers.[26] The coordinative bonding plays the key role for the formation of extended 3-dimensional hybrid structures being the subject of the present work.

The first hybrid open frameworks were labeled as 'coordination polymers' before the general term '*Metal-Organic Frameworks*' (MOFs) was introduced by Omar Yaghi in 1995.[21] Nowadays, this notation is widely used for three-dimensional open frameworks built up from inorganic ions or clusters that are linked by organic units.

In a typical approach, MOFs are synthesized at low temperatures (< 250°C) under solvothermal conditions. Conventional solvents include water, alcohols,

dimethylformamide (DMF), pyridine or acetonitrile. The self-assembly process illustrated in Figure 1-1 yields 1-D, 2-D or 3-D skeletons through the coordination of organic struts to inorganic metal centers.
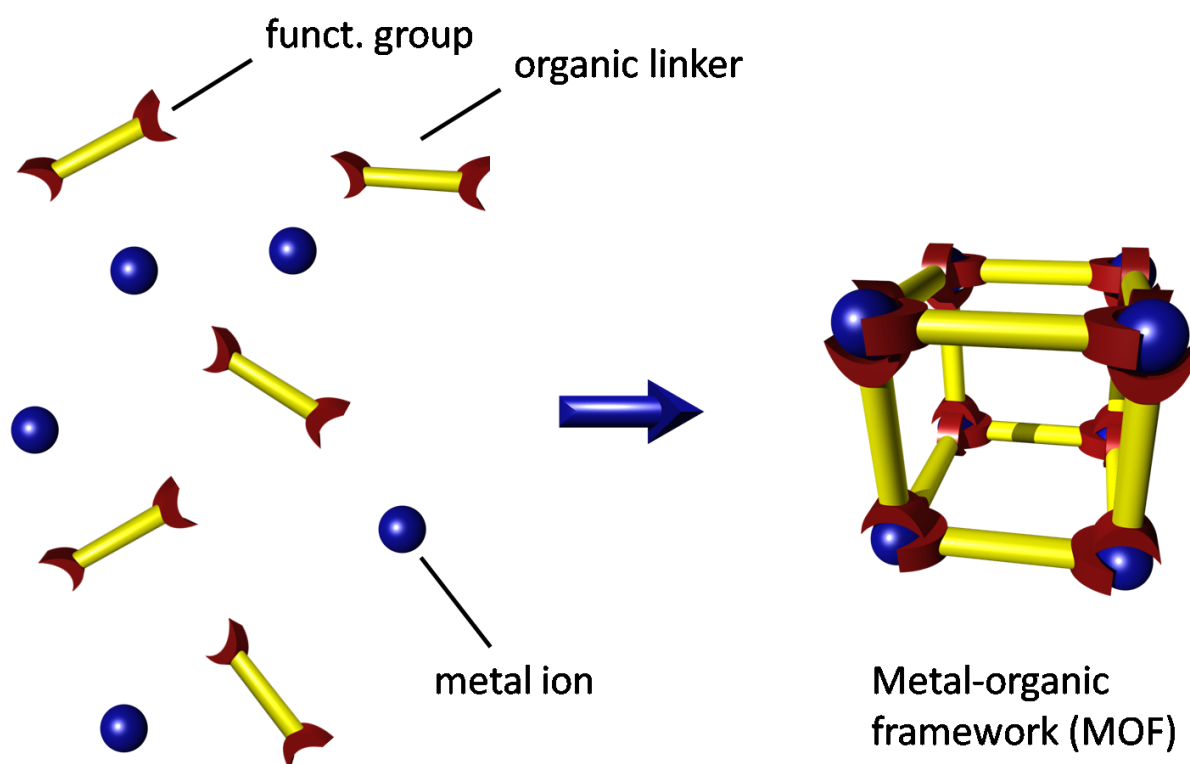
Figure 1-1   Schematic illustration of the modular synthesis concept resulting in a 3-dimensional open framework structure.

In terms of the large variety of a chemist's choice of building blocks an enormous number of possible combinations of metal ions and organic linkers can be envisioned. One can resort to a wide variety of di-, tri- or tetravalent cations, various clusters as well as to a tremendous number of functionalized organic linkers. The reactivity between the building blocks usually emerges from donor groups such as carboxylates, phosphonates, sulfonates or nitrogen derivatives (cyanides, pyridine and imidazoles). The backbone of the organic component is often chosen to be rigid

and aromatic systems are thus preferred. Moreover, the ligand itself can be modified with versatile functional groups (halogeno-, hydroxyl-, nitrile- or amino groups) depending on the targeted applications.

The underlying modular concept of combining inorganic metal-clusters and organic linker molecules allows for the targeted design of three-dimensional crystalline molecular skeletons with defined pore dimensions, uniform pore shapes and versatile functionalities.[23, 27-29] In 2002, O. Yaghi and co-workers presented their results of a series of isoreticular MOF-structures (IRMOFs), based on the network topology of MOF-5.[30] Cubic zinc-terephthalate framework structures linked by 16 different organic molecules varying in length and functionality are demonstrated in Figure 1-2.[31-33]
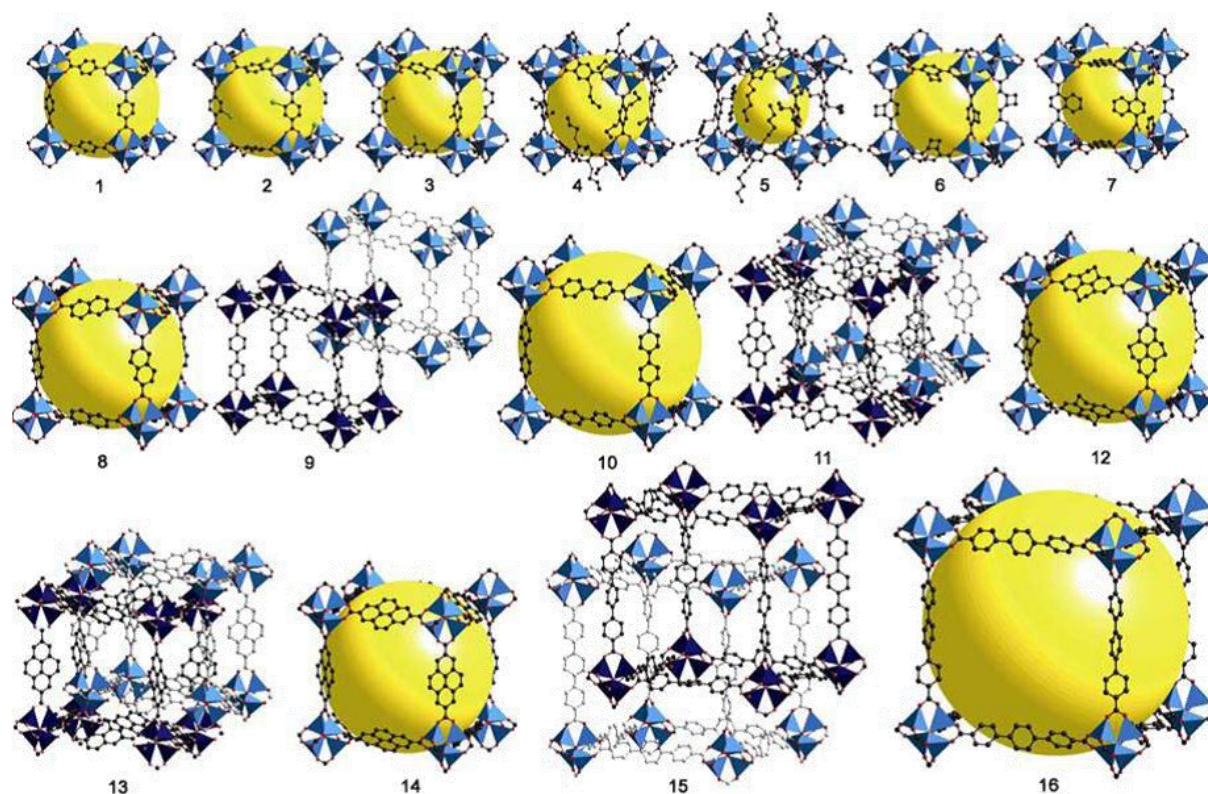
Figure 1-2   **Series of isoreticular MOF structures (IRMOFs) with the same cubic network topology; the particular linkers differ in functionality and length. While expansion of the linkers increases the internal void space represented by yellow spheres), it also allows the formation of catenated (interpenetrated) phases.**[34]

The incorporation of extended organic ligands can lead to the formation of interpenetrated networks, with smaller specific surface areas and smaller pore dimensions than the corresponding non-catenated structure.[35] The reduction of the free diameter of the pores, as consequence of catenation, represents a potential strategy for improving hydrogen uptake.[8, 36]

Novel synthetic methods, *e.g.,* the microwave approach or high-throughput (HT) techniques were established to accelerate the optimization of reaction conditions (*e.g.,* time, temperature and concentration) and to minimize the consumption of

chemicals. The microwave method, already applied for zeolites and related nanoporous inorganic compounds,[37-40] proved to be an appropriate tool for the synthesis of MOFs. To illustrate the several advantages of microwave irradiation, recently Chang *et al.* has shown a faster crystallization as well as a phase selective formation of their hybrid inorganic-organic materials.[41] For instance, chromium trimesate was formed efficiently within several hours, whereas an even shorter reaction time of 1 minute could be observed for chromium terephthalate (MIL-101). The influence of microwave irradiation was again illustrated by comparing the preparation of cubic nickel glutarate $[Ni_{20}[C_5H_6O_4)_{20}(H_2O)_8] \cdot 40\, H_2O$ under conventional hydrothermal conditions to the significantly accelerated formation of a tetragonal nickel glutarate $[Ni_{22}[C_5H_6O_4)_20(OH)_4(H_2O)_{10}] \cdot 38\, H_2O$ within a few minutes. According to Morris *et al.,* the microwave-assisted synthesis of anionic MOFs under ionothermal conditions results in a phase-pure and highly crystalline product. They synthesized two new isostructural coordination polymers either containing nickel or cobalt as metal ion under microwave conditions using an ionic liquid EMIm-Br (=1-ethyl-3-methyl imidazolium bromide) as solvent and template.[42] These studies demonstrate that the microwave approach provides a promising tool for a significant reduction of time. Thus, the hydrothermal formation of metal–organic hybrid materials in a matter of minutes becomes possible, indicating the potential of developing of commercially viable routes for producing MOFs.

High-throughput (HT) methods are applied for the systematic and accelerated study of the reaction parameters (concentration, pH, solvent, temperature) of MOF synthesis.[43-47] By means of HT methods a tremendous data flow is usually obtained and thus an adequate evaluation and characterization is required. For this purpose,

statistical methods and evaluation programs in addition to the so-called AASBU (automated assembly of secondary building units) have shown to be powerful tools.[48, 49] The HT technique proved to be a very useful tool for systematic investigations and optimizations of synthesis parameters while consuming less time and low amounts of chemicals.

Another important issue is the implementation of chemical functionality into a MOF structure. The ability to modify the pores and cavities within the hybrid framework serves as a possibility to tailor the chemical stability and reactivity of the MOF. There are numerous functional groups that can be employed within the hybrid open framework. Different strategies can be used in order to modify the porous material. For instance, the introduction of transition metals or the use of functionalized ligands can yield MOFs with adequate properties for a specific application. In particular, the large variety of functional groups, *e.g.*, unsaturated alkene-, halogeno- and hydroxyl-groups in addition to carboxylic acids, amines and heterocyclic compounds as well as their various derivatives demonstrate the potential of implementing functionalized ligands.

For instance, the group of Kitagawa puts a main focus on the synthesis of microporous coordination polymers that exhibit a modified pore surface. By introducing coordinatively unsaturated metal centers, possible implementations such as selective separation, chemisorption, catalysis and sensory devices became feasible.[50, 51] Further potential applications such as enantioselective catalysis realized by the utilization of chiral ligands[52-54], the incorporation of amino acids[55] or using MOFs as drug delivery systems[14, 56] are gaining in importance.

An alternative strategy to the *in-situ* or pre-synthetic (*e.g.,* as part of the ligand monomers) functionalization of MOFs is represented by the post-synthetic modification (PSM) approach of the pores. Although a relatively new area of research within the MOF field, the PSM has become a well-established and straightforward way to implement functionality into MOFs. The post-synthetic variation of MOFs possibly circumvents some limitations, such as interference of the functional group and the framework structure or the incompatibility of the functionalized moieties with the synthesis conditions for MOFs.
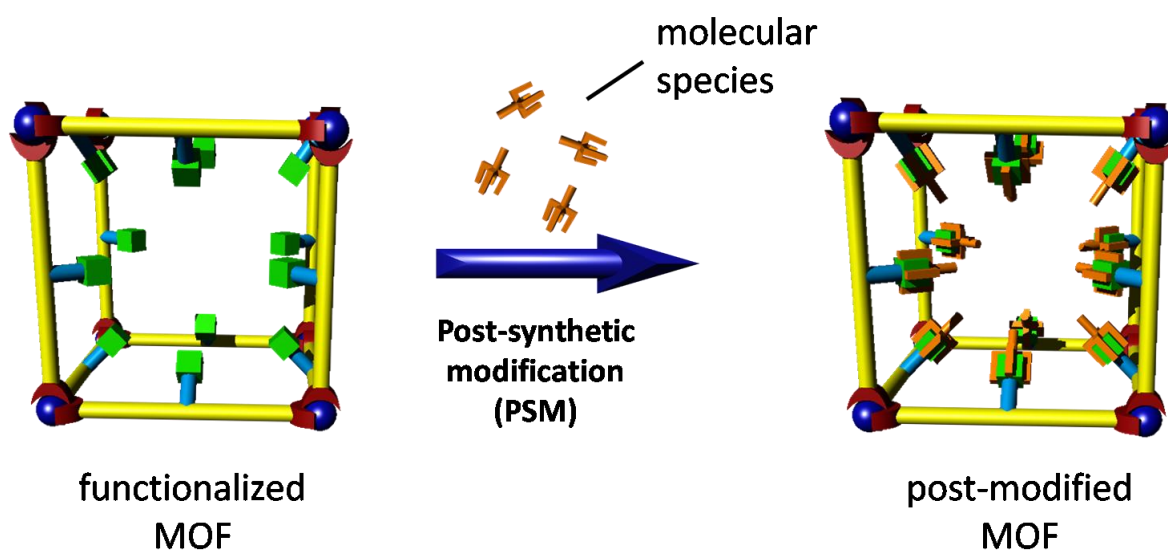
Figure 1-3   Generic scheme for a post-synthetic modification reaction with a functionalized MOF.

Pioneering work on 3-dimensional (3-D) coordination solids and first hypothetic formulations of the potential to post-synthetically modify these structures have been made in the early nineties. In fact, Robson *et. al.* described 3-D coordination solids based on metal cyanates and speculated on which properties these new, crystalline

materials might possess.[20] This concept will be the subject of the following discussion.

There are basically three different pathways by which a MOF can be modified in a post-synthetic manner. Depending on the type of bond that is formed or broken, post-synthetic modifications of MOFs are broadly divided into three areas, *i.e.,* covalent PSM, dative PSM and post-synthetic deprotection (PSD).[51] The very first examples of covalent post-synthetic modifications of a class of coordination solids constructed from Ag(I) and rigid nitrile-containing ligands were reported by Lee and co-workers.[57, 58] Their studies revealed that the installation of a pendant functional group is a hallmark feature of most ligands used for covalent PSM. The incorporation of an alcohol-derivatized ligand into the MOF structure was shown to be highly reactive upon exposure to vapors of trifluoroacetic anhydride. The overall reaction was proposed to occur in a heterogeneous fashion and with preservation of the crystalline structure.[58]

Another example of covalent PSM of MOFs appeared in 2000. Seo *et al.* reported a 2D homochiral MOF (POST-1) for enantioselective separation and catalysis.[59] POST-1 was built up from a Zn(II) trimer SBU and an enantiopure tartrate derivative containing a pyridyl moiety. Although all the carboxylate groups coordinate the Zn(II) trimers within the MOF, only half of the pyridyl units are engaged in coordinative bonding. The other half is exposed in the channels without any interaction with the metal ions. It was assumed that these free pyridyl groups were essential for the enantioselective catalysis of the transesterification of 2,4-dinitrophenyl acetate and ethanol yielding in 77 % of ethyl acetate as product.

Experiments with larger alcohols occur with a negligible rate in the transesterification reaction, suggesting that the catalysis mainly occurs within the channels. Treatment of the crystalline POST-1 in DMF with excess CH_3I at room temperature for 2 h results in the conversion of the pyridyl groups to *N*-methylpyridinium ions, as indicated by ^1H NMR analysis. X-ray diffraction data reveal the framework structure to be intact after the modification, whereas Raman spectroscopy confirms the presence of I_3^- counterions, which can be reversibly exchanged for other anions. POST-1 was also modulated by additional N-alkylations of the pyridyl groups. Interestingly, in contrast to the unmodified MOF, the alkylated MOF showed very little catalytic activity for the same transesterification reactions, suggesting the importance of free pyridyl groups for catalysis and confirming the successful post-modification on the MOF.

These first covalent PSM examples beautifully highlight the principles and methods that became central features in the numerous reports on PSM that have appeared since 2007.[60-62] A central focus was put on amine- or aldehyde tagged MOFs, *e.g.*, the amino-functionalized IRMOF-3. Wang and Cohen were able to show that the aromatic amines in IRMOF-3 do not engage in binding to the SBUs and thereby provide the chemical handle for performing PSM. After the reaction with acetic anhydride IRMOF-3 was isolated in >90% yield. The successful conversion into the amide-derivative was confirmed by ^1H NMR spectroscopy. The authors conclude that the high degree of conversion highlights the fact that the reagent can access both the exterior and interior of the MOF, resulting in modification of all of the organic linkers.[63]

It is particularly the aforementioned prototype linker, *i.e.*, 2-amino-1,4-benzenedicarboxylate (NH$_2$-BDC) that is subject of extensive and ongoing studies yielding a continuous growth of reports in literature. Several different MOF structures, including the IRMOF series, UMCMs, UiOs, MILs and ZIFs among many others were employed to demonstrate the feasibility and potential of PSM of MOFs. In addition to the covalent PSM, newer developments such as the dative PSM[51, 64-71] and the post-synthetic deprotection (PSD)[72-76] have become mainstream approaches for tailoring the pore functionality of MOFs.

1.3   Self-assembled monolayers (SAMs)

Self-assembled monolayers (SAMs) are well ordered arrays of amphiphilic molecules that are chemically bound to a substrate. Regarding their potential applications, *e.g.*, as biomembranes, selective and structure-directing composites, as pH-sensors or photoresists, self-assembled monolayers have gained more and more importance in several research fields.

In general, a self-assembled monolayer can be prepared using various amphiphilic organic molecules and different substrates. In a typical approach, self-assembled monolayers are formed when an organic compound, usually functionalized alkane chains, spontaneously adsorbs onto a solid surface. The adsorption can either occur from solution or the vapor phase and is associated with the formation of chemical bonds. The organic component is generally composed of a 'head group' varying in its functionality and affinity for different substrates and a 'tail group', which is often

composed of long alkane chains exhibiting 10-20 methylene units. While the head groups adsorb readily from solution or the vapor phase onto the substrate, the alkane chains point outwards from the surface. By exposing the substrate over an elongated period to the adsorbates, a spontaneous self-organization results ideally in well-ordered and low-defect crystalline or semi-crystalline structures.

There are widespread examples concerning the formation of self-assembled monolayers. One of the most extensively studied class of SAMs consists of alkanethiols on gold and other noble and coinage metals;[77-80] a schematic representation of an ideal SAM of alkanethiolates on gold is depicted in Figure 1-4.
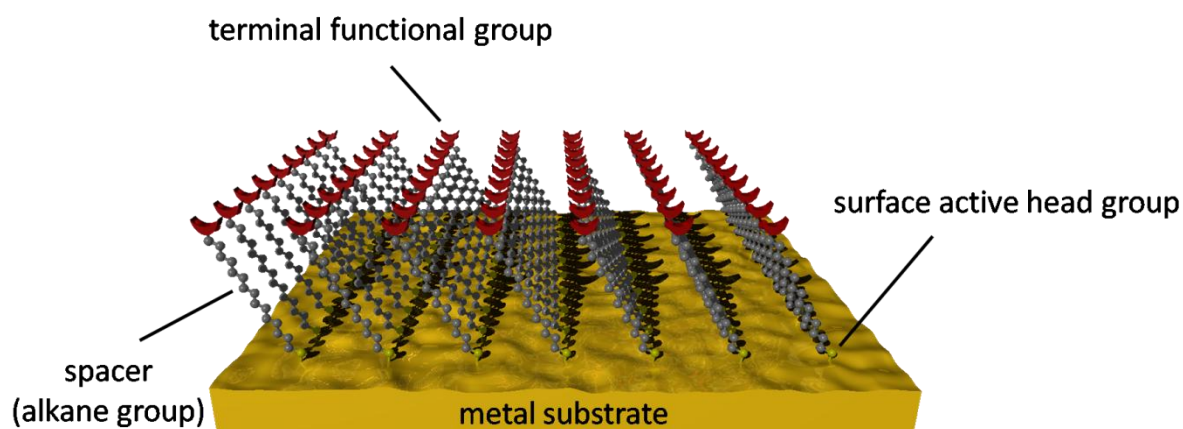
Figure 1-4   **Schematic representation of a self-assembled monolayer on gold (111) showing the functional terminal group, the alkane chain and the head group of the organic component.**

In addition to SAMs of thiol-functionalized organic compounds, different systems are known. For instance, alkoxysilane or fatty acid SAMs were prepared on oxidic materials like SiO_2. In this study, self-assembled monolayers of functionalized alkanethiols on gold (111) surfaces were employed and will be further discussed.

The (111) surface is a popular crystal face of gold substrates for the preparation of alkanethiolate SAMs, as it proved to be an accessible system due to its relatively low surface roughness.[80] Au(111) surfaces can be obtained either form single crystals or by evaporation of thin gold films on planar supports, typically mica, glass or silicon wafers.[81]

For the preparation of SAMs on gold substrates different parameters like the alkanethiol concentration, the immersion time, the choice of solvent and the temperature have to be considered.[82] In a typical approach a low concentration (1-2 mM) of the alkanethiol in ethanolic solution is used. Immersion times at room temperature ranging from 18-48 hours result in well-ordered assemblies of the monolayer.[83]

The self-organization of monolayers results from chemical interactions between the surfaces and the organic molecules. The adsorbate molecules lower the surface energy of the substrate and the amphiphilic alkane chains show dense packing due to van-der-Waals interactions, thus a stable and well defined monolayer is formed.[80, 84] The binding energy of about 100 kJ/mol of the thiol-gold bond, which is postulated to be analogous to the assembly of thiolates on gold from the gas phase,[85] is essential for the stability and self-assembly of the organic monolayer.

In order to characterize the structure of SAMs on planar substrates, a large number of surface analytical techniques have been applied. Among the most frequently used methods are reflection absorption infrared spectroscopy (RAIRS), optical

ellipsometry, contact angle goniometry and electrochemistry, as well as scanning tunnelling microscopy (STM).[86, 87]

The thiols are believed to attach to the 3-fold hollow sites of the gold surface. During this process they loose their proton and form a ($\sqrt{3}\times\sqrt{3}$)R30° overlayer.[88] There is agreement in the literature that the organization of the thiol molecules on the surface adopts a secondary ordering of the chains corresponding to a c(4 × 2) superlattice.[89, 90] A schematic model is shown in Figure 1-5. The light gray circles with dashed lines indicate the approximate projected surface area occupied by the alkane chains. The red dashed lines in Figure 1-5 mark the formal c(4 × 2) unit cell, the blue dashed lines mark the $2\sqrt{3} \times 3$ unit cell. The alkane chains are tilted in the direction of their next-nearest neighbours; the dark wedges indicate the projection of the CCC plane of the alkane chain onto the surface. The distance between pinning sites in this geometry is 5.0 Å, resulting in an available area for each molecule of 21.4 Å^2. Since the van-der-Waals diameter of the alkane chain is too small (4.6 Å) for the chain to completely occupy that area, the chains will tilt, forming an angle of approximately 30° with the surface normal.[80]
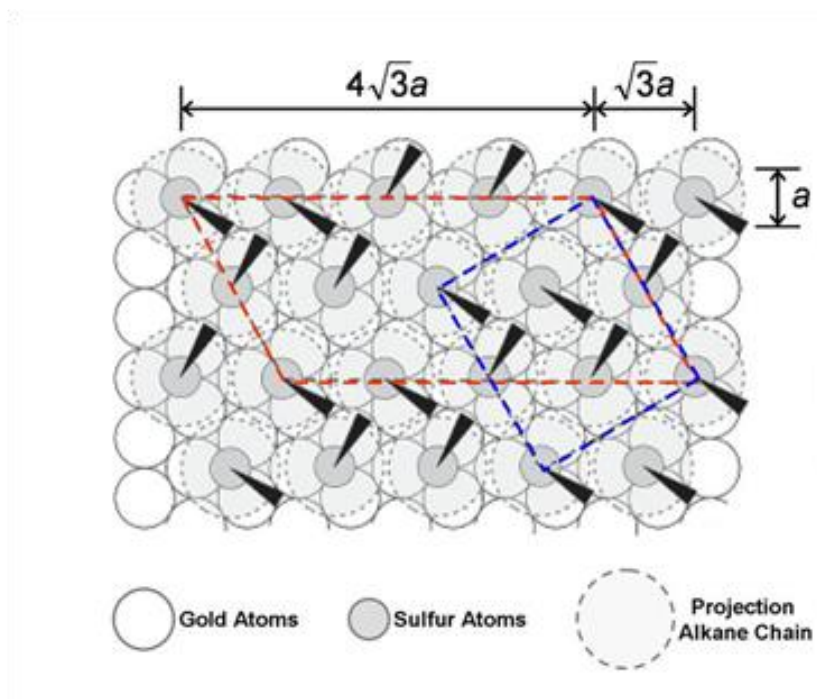
Figure 1-5 **A schematic model of the ($\sqrt{3} \times \sqrt{3}$)R30° overlayer structure formed by alkanethiolate SAMs on Au(111).**[91]

Well-ordered and dense self-assembled monolayers formed from thiols with an alkane chain length of twelve or more methylene units exhibiting a considerable stability towards various solvents, temperatures and potentials have been obtained. The van-der-Waals forces between the adjacent methylene groups add up increasingly depending on the alkane chain length (10-20 methylene groups) and play a key role in aligning the alkyl chains in the optimal all-trans configuration. A loss in stability, however, is observed for a decreasing chain length in combination with increasing temperature due to weaker interactions and higher concentrations of gauche defects.[86]

In summary, within the last decades SAMs have gained considerable attention in fields like biology, electrochemistry and electronics. Beside various fundamental

aspects[82] SAMs can serve as model for studying membrane properties,[80] as molecular recognition devices,[92] for corrosion protection,[93] and in organic-molecular electronics.[94] A main focus is put on the tail group of SAMs and its versatile functionality. There are different ways for the implementation of functionality. One can either directly deposit multifunctional molecules, or one can perform a post-modification of the terminal group. In the present work hydroxyl-carboxyl- and phosphonate-functionalized alkane thiols are employed and investigated with respect to their structure-directing properties.

1.4   Metal-Organic Framework Thin Films

This work describes the implementation of MOFs as chemo-sensory materials. For the design of a MOF based chemical sensor it is most often of significant importance to present a physical interface between the MOF and the device. Hence, a main part of the present work particularly focuses on the direct growth of functionalized MOFs on gold substrates modified with different self-assembled monolayers. Within this section, the principal concept of controlled surface growth of porous structures on solid supports as well as existing work on this subject will be introduced.

Zeolites, the prototype ordered porous solids have been extensively studied and numerous approaches to create zeolite thin films have been reported.[95-98] Several strategies have been developed to deposit or anchor zeolites onto a solid support. The studies cover simple deposition methods, *e.g.*, using spin-coating[99] or covalent

bonding of zeolite crystals to a substrate,[100, 101] while being extended towards the direct growth of zeolite-type materials on appropriately functionalized substrates. Based on the underlying principle of biomineralization[102-104] this method makes homogeneous film growth feasible and allows controlling the crystal orientation with regard to the substrate.[96, 105, 106]

The topic of this work addresses the oriented growth of MOFs rather than purely inorganic porous solids on surfaces modified with an organic monolayer. The underlying mechanism for the direct growth of hybrid inorganic-organic materials on functionalized surfaces is presumed to be analogous to the self-assembly process during the formation of MOFs (see Chapter 1.2). The concept of direct growth of MOF crystals on organic monolayers is depicted in Figure 1-6.
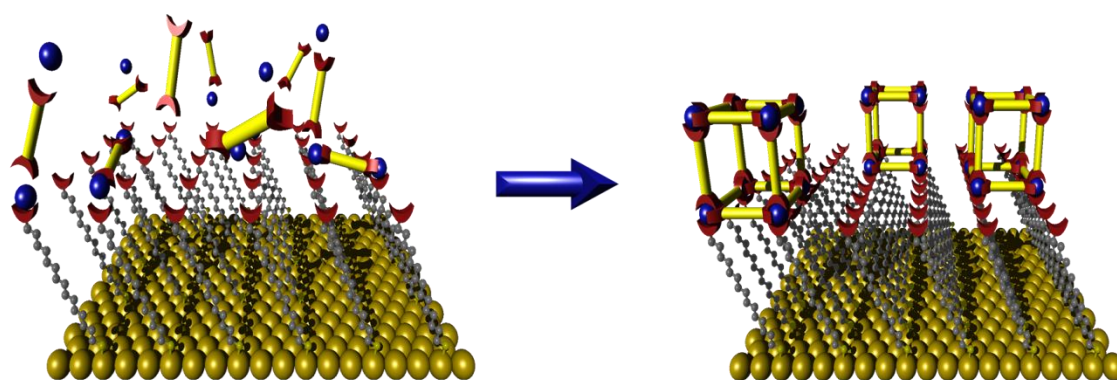
Figure 1-6   **Concept of direct growth of MOFs on SAM-functionalized gold substrates.**

The terminal functionality of the SAMs or substrates essentially serves as a nucleation interface for the coordination to the metal centre or secondary building units (SBUs) possibly leading to direct crystal growth. In this approach the functionality of the employed SAM is used in order to mimic the particular

functional groups of a certain MOF structure. Thus, a coordination of the molecular building units or SBUs from solution to the surface can be anticipated. Once the metal center or SBU is attached, further coordination by the organic ligands can occur. If the coordination sites of the different ligands have distinct orientations in the crystal structure, different functionalities on a surface can lead to the growth of MOF crystals along preferred orientations.

So far five different concepts have been employed for the growth of MOF thin films on solid substrates: (A) the direct growth/deposition from solvothermal synthesis solutions, (B) the assembly of preformed, size-selected nanocrystals, (C) the stepwise layer-by-layer growth onto the substrate, (D) the electrochemical deposition of thin MOF-films on metal substrates and (E) the deposition of MOF thin films using a gel-layer approach. In the following, the approaches based on the oriented growth of MOFs on SAM modified substrates will be discussed in more detail.

A first study on the attachment of a MOF structure on SAMs was published by Hermes *et al.* in 2005.[107] Fischer and co-workers showed for the first time that direct attachment of MOF-5 crystals on a functionalized gold substrate is possible. The authors were able to pattern a substrate by applying Micro Contact Printing (μCP) and to introduce two different functionalities, *i.e.*, −COOH- and −CF$_3$ terminated organothiols. The functionalized substrate was immersed into a pre-treated crystallization solution leading to crystal growth on the carboxylic acid terminated SAM, whereas no crystallization occurred on the CF$_3$-groups. This first example demonstrates that the concept of providing anchoring sites at the SAM

surface can be applied for the preparation of MOF thin films. However, the deposited MOF films are polycrystalline and consist of randomly oriented crystallites.

Two years later the same group reported the selective nucleation of MOF-5 crystals on carboxylic acid terminated SAMs. In contrast to the previous work, modified SiO_2 and ultrathin, amorphous Al_2O_3 adhesion layers (via atomic layer deposition (ALD)) were used.[108] More recently, Yoo et al.[109] reported on a microwave induced thermal deposition (MITD) of MOFs on porous aluminium substrates. The nanoporous anodized aluminium discs (Anodisc®) were coated with conductive thin films, *e.g.*, amorphous carbon, graphite or gold and placed vertically in vials containing the precursor solution. MOF-5 crystals were grown under irradiation using a domestic microwave oven with 500 W for 5-30 seconds. The rapid growth of smaller and densely packed MOF-5 crystals on the surface is surmised to be a result of the sharp temperature rise of the conductive layers. Thus, upon the absorption of microwave energy on the surfaces, a substantial increase in the rate of the heterogeneous nucleation and thus in the growth of MOF-5 crystals is assumed.

In subsequent work by the group of Prof. Wöll a newly designed layer-by-layer (lbl) or liquid-phase epitaxy (LPE) strategy for the synthesis of MOFs on functionalized surfaces was developed. In 2007, Shekkah *et al.*[110] showed homogeneous and highly crystalline growth of [$Cu_3(btc)_2$] (HKUST-1; btc = 1,3,5-benzenetricarboxylate) crystals on SAM-functionalized gold substrates. In contrast to the established synthesis protocol where the precursors are mixed and treated under solvothermal

conditions, a sequential exposure of the functionalized substrate to solutions of the two reactants was performed (Figure 1-7).
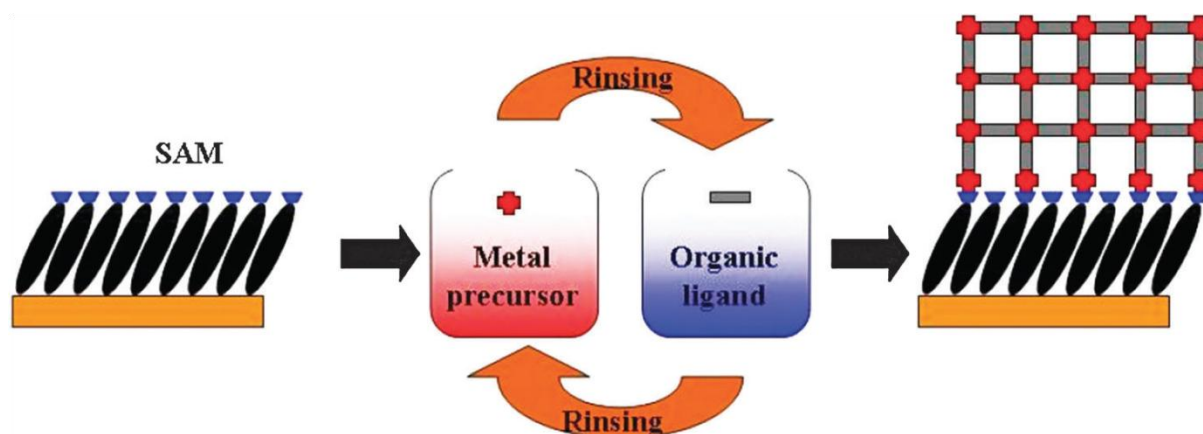
Figure 1-7   **Schematic illustration of the step-by-step approach. MOF surface growth on substrates functionalized with SAMs is achieved by repeated immersion cycles in solutions of the metal precursor and the organic ligand.**[111]

Shekkah *et al.* were able to study the evolution of crystal growth *in-situ* by applying surface plasmon resonance (SPR) and *ex-situ* by appropriate surface characterization methods, *e.g.*, atomic force microscopy (AFM), infrared spectroscopy or X-ray photoelectron spectroscopy (XPS). Moreover, the surface-grown MOF crystals (referred to as "SURMOFs") were shown to be oriented along the [100] direction, which is in agreement with the results previously observed by the group of T. Bein.[112] The authors state that the layer-by-layer approach provides the possibility to coat surfaces with MOF layers of a defined thickness and to synthesize structures possibly not accessible by bulk synthesis, while allowing for the simultaneous monitoring of the growth process.[111]

The findings mentioned above were most recently confirmed and strengthened by investigations on the growth mechanism and nucleation of MOFs.[113] The authors focus on the growth of a particular MOF along different crystallographic directions combined with a variation of the metal precursor in order to study and elucidate the importance of the reactants and formed intermediates (*e.g.*, SBUs). Again, the layer-by-layer method was applied to grow highly ordered and oriented SURMOFs on different templates such as SAM-functionalized gold substrates. After completion of the first deposited layer further growth proceeds as a MOF-on-MOF homoepitaxy. Mechanistic studies were feasible since the substrate was sequentially exposed to the different reactants. Additional information about the relevance of the "controlled SBU approach"[114] for the MOF synthesis were gained by varying the metal precursor such as copper(II) acetate ($Cu(OAc)_2$) and copper(II) nitrate ($Cu(NO_3)_2$). The deposition process of HKUST-1 crystals was determined using surface plasmon resonance (SPR). The authors were able to show that after several immersion cycles of copper nitrate no substantial gain in thickness was observed whereas an exposure to copper acetate at once leads to an increase in thickness. By using different terminally functionalized SAMs, preferred orientations of crystal growth along [100] and [111] direction were observed verifying the results obtained by Bein and co-workers.[112] In conclusion, by *in-situ* SPR monitoring of the stepwise formation of MOFs, the determination of the growth rate of MOFs as a function of crystallographic orientation is possible. Novel mechanistic insights into the nucleation and formation of the SBUs were gained by performing the deposition of the building blocks separately. It was shown that the formation of secondary building units is essential for further "epitaxial" crystal growth of the MOF. Thus,

the authors claim that the layer-by-layer approach offers a convenient method to study the effect of using chemically different metal-ion sources leading to a more systematic search for new components of MOFs.

A related deposition method has been developed by H. Kitagawa and co-workers.[115, 116] It relies on metallo-porphyrin MOF layers that have been obtained by a combination of the lbl-method and the Langmuir Blodgett (LB) technique. Homogeneous and preferentially oriented MOF thin films have been fabricated that are stacked together by π-π-interactions between the pendant pyridine groups. As a result, the individual sheets are remarkably ordered, with an average tilt angle of 0.3° parallel to the substrate, and the overall thickness of the film corresponds to deposition of one single layer at each cycle.

Both previously described methods demonstrate proof of principle that it is possible to fabricate ultrathin MOF films, or SURMOFs, in a controlled manner. Fundamental investigations on the oriented growth of MOF crystals on different SAM termini have been performed in the group of T. Bein. Biemmi *et al.*[112] were able to demonstrate the control of highly oriented grown HKUST-1 crystals on differently functionalized gold substrates (Figure 1-8).
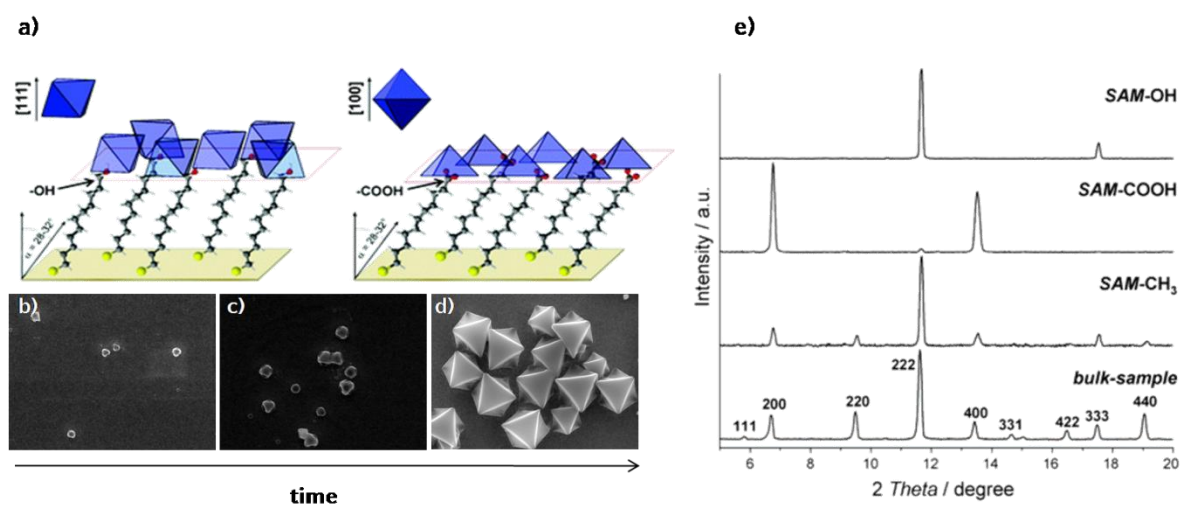
Figure 1-8 **a) Schematic representation of oriented HKUST-1 crystal growth on an 11-mercaptoundecanoic acid SAM, and on 11-mercaptoundecanol-modified gold surfaces as well as scanning electron micrographs of face-down samples after immersion in the crystallization solution for b) 16 h, c) 24 h, and d) 45 h. e) The X-ray diffraction patterns (background corrected) of thin films of Cu$_3$(BTC)$_2$ on functionalized gold surfaces are compared with a polycrystalline Cu$_3$(BTC)$_2$ powder sample.[112]**

The authors demonstrated for the first time that the potential of SAMs goes well beyond just providing nucleation centers for the growth of MOF thin films. By using SAMs with three different termini (−COOH, −OH and −CF$_3$) the authors proposed an oriented attachment of the growth species at the molecular interface for carboxyl and hydroxyl terminations, respectively, followed by crystal growth in distinct orientations. The X-ray data show that the film grown on the −COOH self-assembled monolayer is highly oriented along the [100] direction, while the −OH modified surface induces a completely different orientation along the [111] crystallographic direction. The selective nucleation on the gold substrate is explained by the paddle-wheel motif of HKUST-1. Here, either a chelating coordination with the carboxylic

acid terminus or an axial coordination with the alcohol group leads to the different orientations.

One year later, Bein and co-workers reported the oriented crystal growth of a different MOF type, that is, MIL-88B. Here, Scherb *et al.*[117] not only demonstrated the selective attachment of the growth species to the terminal SAM group, but also showed favored thin film growth of a particular MOF phase in a highly oriented fashion. Whereas MIL-53 was found to be the product of homogeneous nucleation, oriented MIL-88B was grown from the same crystallization solution. The effect of the selective heterogeneous nucleation of Fe-MIL-88B on the functionalized surfaces is tentatively attributed to favorable symmetry relationships between the hexagonally ordered SAMs and the hexagonal structure of MIL-88B. Consequently, the growth of the hexagonal MIL-88B phase is apparently favored over its monoclinic counterpart MIL-53.

The previously described methods have one drawback in common, *i.e.*, the fast nucleation rate in the crystallization solution. To overcome the homogeneous nucleation, Bein and co-workers introduced a method that has routinely been used in bulk MOF synthesis to obtain single crystals. Schödel *et al.*[118] developed an alternative way that allows one to store one reactant at high concentrations in a thin gel-layer deposited onto the surface of SAM-functionalized gold substrates. Crystal growth was achieved by slow diffusion of the other reaction partner into the polymer gel layer and to the nucleation interface provided by the terminal groups of the SAM (Figure 1-9).
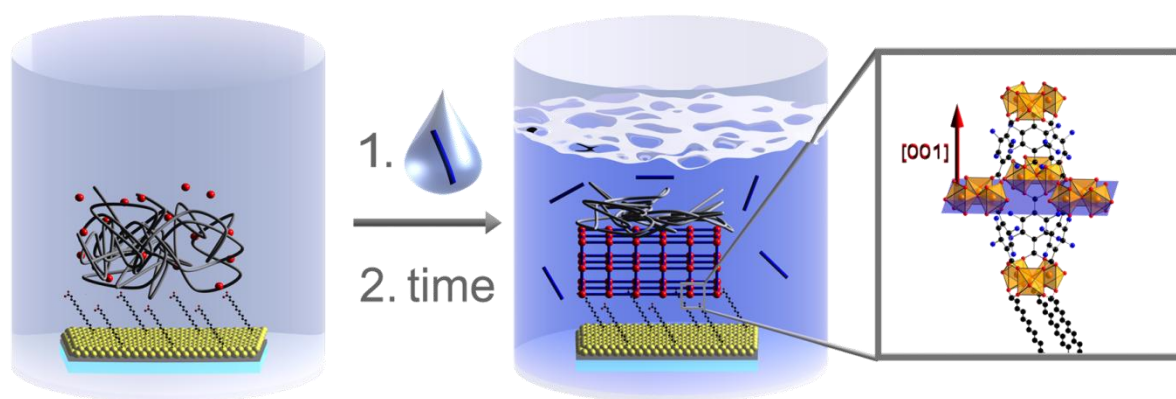
Figure 1-9   Representation of the gel-layer approach yielding uniquely oriented nanoscale films of metal–organic frameworks. A SAM-functionalized gold slide is loaded with the metal-salt-containing poly(ethylene glycol) gel layer (metal ions in red) and covered with a solution containing the linker molecules (blue).[118]

In contrast to the fast homogeneous nucleation in solution a high heterogeneous nucleation rate is achieved owing to the high local concentration of the metal precursor close to the nucleation interface. Structural analysis of the MOF films using XRD revealed an oriented growth of HKUST-1 and the amino-functionalized, flexible framework Fe-MIL-88B-NH$_2$ [Fe$_3$O(BDC)$_3$(OAc)] (BDC^{2-} = 1,4 benzenedicarboxylate). In contrast to the results obtained by Biemmi *et al.*[112] the gel-layer synthesis of HKUST-1 on –COOH- and –OH-terminated SAMs yielded the same orientation along the crystallographic [111] direction. The flexible Fe-MIL-88B-NH$_2$ was grown along the preferred [001] direction, while a higher degree of orientation was observed for the carboxylate termini than for the hydroxyl-functionalized SAM. Parameters such as the chain length of the polymer and the concentration of metal ions in the gel can easily be varied to control the morphology and thickness of the final film. Thus, the authors anticipated that the gel-layer

approach is a powerful tool to grow homogenous MOF thin films with a high level of control in oriented film synthesis.

In 2012, Hinterholzinger *et al.*[119] were able to grow a mesoporous and functionalized MOF structure on two different types of SAMs. The authors could show for the first time that mesoporous (*i.e.,* pore size regime ~ 2.7 nm) MOF thin films could be grown in a highly oriented fashion on phosphonate termini of an organic monolayer. The zirconium-based MOF (denoted as UiO-68-NH$_2$) features the essential prerequisites that are required for targeted post-modification reactions. Thus, a fluorescent dye could be successfully accommodated into the MOF structure, which was confirmed by quenching experiments with differently sized quenching agents. In summary, the concept of oriented crystal growth on SAM-modified gold substrates could successfully be extended to functionalized and mesoporous MOF structures, while the growth upon phosphonate-terminated self assembled monolayers is new and broadens the repertoire of chemistries that can be used for initiating MOF growth.

1.5 Metal-Organic Frameworks as Chemical Sensors

Based on our experience in MOF synthesis as well as in MOF thin film fabrication this work aims at developing chemical sensing concepts that allow us to transform a specific recognition event into a readable output signal. In fact, owing to their structural versatility and exceptional tunability MOFs are anticipated to offer some advantages over other candidate classes for chemical sensing applications.[15] In the

following section the prerequisites for the development of a MOF sensor, state-of-the-art techniques and prospective alternatives are reviewed.

For many domestic, industrial and environmental applications it is imperative to reliably detect a target species and to differentiate targets from one another.[120-122] There is a great demand for analytical methods that selectively and sensitively detect an analyte species and that allow one to distinguish whether or not the compound might be explosive, toxic or harmful.[123, 124]

According to IUPAC, a chemical sensor is a device that transforms chemical information into an analytically useful signal.[125] This highlights the critical difference between a receptor and a sensor, that is, the communication event. To be deemed a sensor the system must incorporate appropriate signal transduction capabilities that can report a specific recognition event. In case of a MOF-based chemosensor this can be achieved by endowing the MOF with two central functional units, *i.e.,* the receptor and transducer element. Upon exposure to an external stimulus a molecular recognition event is induced and converted into a readable output signal (Figure 1-10).
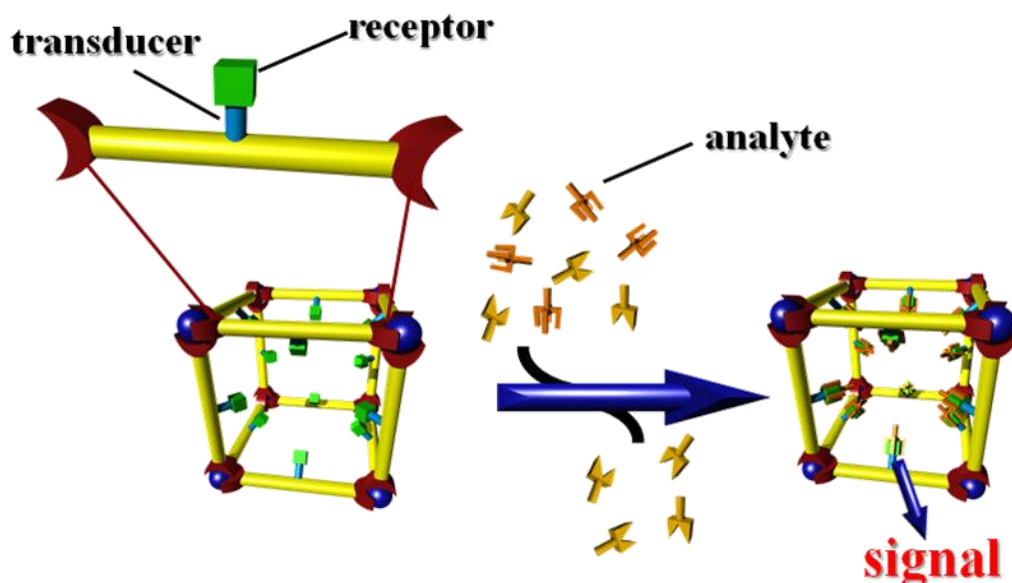
Figure 1-10   **Schematic illustration of a recognition-transduction scheme implemented into a metal-organic framework. The complementary interaction between a guest analyte and a host binding pocket is translated into an output signal.**

Among the numerous potential applications of MOFs, chemical sensing has captured increasing attention. So far, several different strategies to implement MOFs into chemical sensing devices have been reported. In the following, specific examples of MOF sensors, categorized by their method of signal transduction including optical, electrical and mechanical schemes are introduced and discussed in more detail.

When selecting MOFs for chemical sensing purposes a number of essential elements have to be considered, *e.g.,* sensitivity, selectivity, response time, materials stability, and reusability. Although many MOFs inherently meet several of these requirements this rather new material class is at an early stage in its

development to chemical sensing, and substantial problems will first have to be solved before MOFs can proceed from the realm of laboratory synthesis to practical implementation.

Along these lines, the most extensively studied signal transduction scheme in MOFs is luminescence quenching or enhancement. In contrast to traditional solvatochromic[126, 127] and vapochromic[128] effects that induce a visible color change of the MOF, different types of luminescence, *e.g.,* fluorescence or phosphorescence are by far the most common forms of signal transduction. A number of lanthanide and transition metal MOFs have been employed to detect vapor-, liquid- or solution-phase analytes.[129-132] Recently, Lan and co-workers[133] reported on the detection of nitro-containing derivatives using two fluorescent Zn-based MOFs. Their study was essentially relevant for the detection of explosives or rather of a byproduct, *i.e.,* 1,4 dinitrotoluene formed during the synthesis of 2,4,6-trinitrotoluene (TNT) and 2,3-dimethyl-2,3-dinitrobutane (DMNB). Upon exposure to the byproduct bathochromic shifts (red shifts) in the emission spectra were recorded. Most remarkably, this MOF sensor displays unparalleled sensitivity to DMNB and outperforms sensors based on conjugated polymer films in terms of response time. Two years later, the same group not only reported the quenching effect but also demonstrated analyte induced fluorescence enhancement.[134] Figure 1-11 illustrates the trend in the quenching and enhancement behavior when exposing the luminescent MOF to nitro-containing molecules or to analytes featuring electron-donating substituents, respectively.
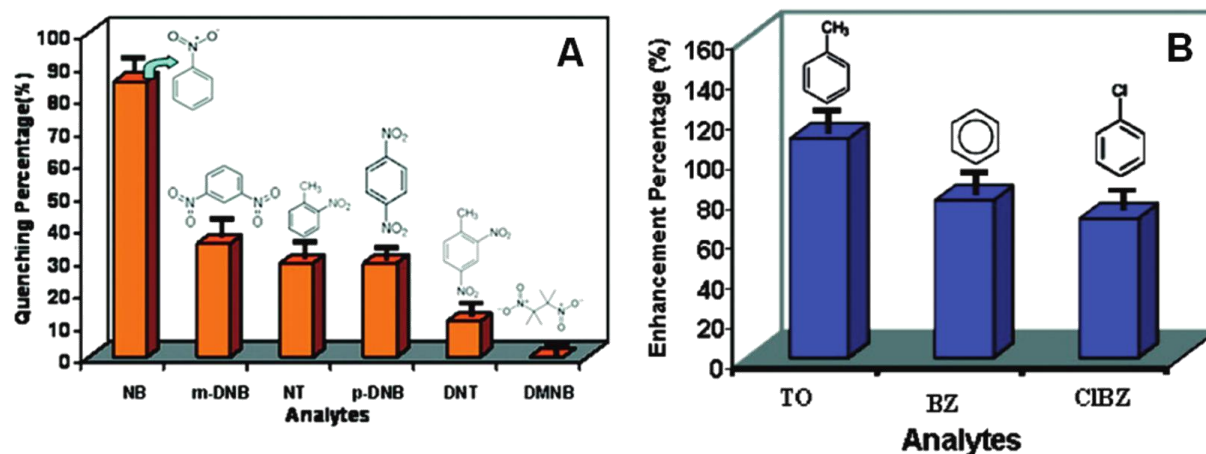
Figure 1-11   **(A) Fluorescence quenching percentage induced by electron-deficient analytes, and (B) fluorescence enhancement percentage by electron-rich analytes in the luminescent MOF [Zn$_2$(oba)$_2$(bpy)] · DMA (H$_2$oba = 4,4´-oxybis(benzoicacid); bpy = 4,4´-bipyridine; DMA = $N,N´$-dimethylacetamide).[134]**

Contrary to the authors' interpretation of the fluorescence enhancement through energy transitions similar to those occurring in semiconductors, Kreno *et al.*[15] proposed the following mechanism: The sorbed molecules are anticipated to inhibit linker motions (*e.g.*, vibrations, torsional displacements, etc.), thus, yielding an increased fraction of excited species that can decay radiatively resulting in enhanced fluorescence intensities.

However, the previously described methods do not allow for the discrimination of chemically similar analytes. In 2011, the group of Kitagawa introduced a strategy that overcomes this limitation for a specific set of analytes. Takashima *et al.*[122] developed a luminescent MOF for which the emission wavelength depends on the chemical identity of the guest molecule. Aromatic compounds with different substituents were shown to cause luminescence at different wavelengths, thus the

unknown species can be easily identified. The same group also developed a new methodology for visualizing and detecting gases. So far, there are only a few literature reports that describe the detection of O_2 as purely-gas phase analyte by a luminescent MOF.[131, 135] Kitagawa and co-workers[123] report a novel strategy in which gas molecules are detected by signals from a reporter guest that can read out a host structural transformation (Figure 1-12).
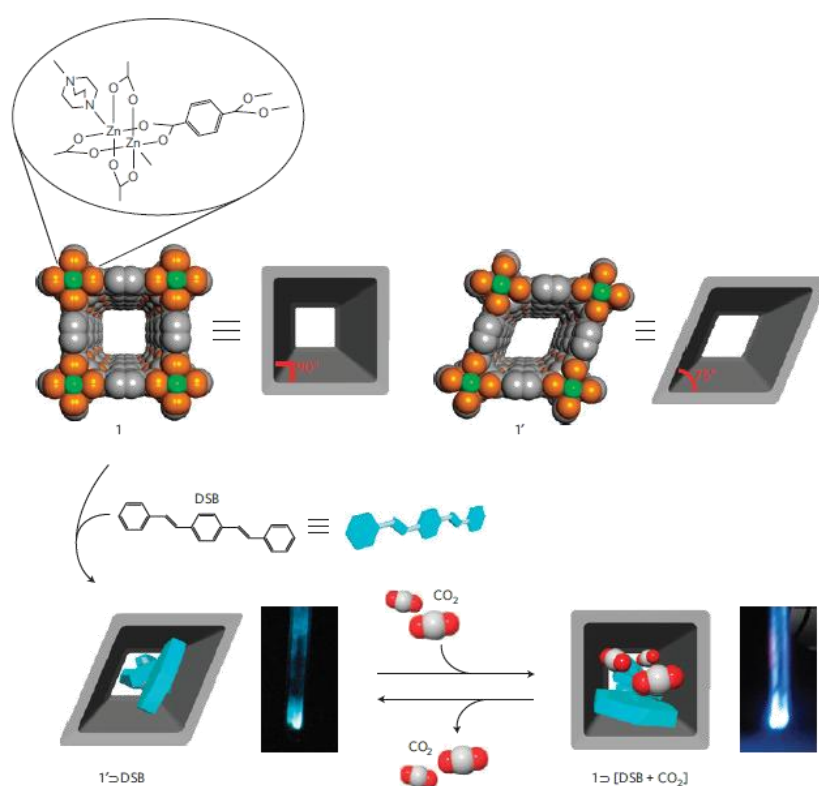
Figure 1-12 **Introduction of reporter molecule DSB (= distyrylbenzene) into flexible host 1. The original and deformed host structures are denoted as 1 and 1′, respectively. The adsorption of CO_2 on 1′+DSB induces the coupled changes of the MOF structure and DSB conformations, resulting in the critical fluorescence response towards CO_2. Photographs of the composite materials were taken at 195 K under ultraviolet irradiation (excitation at 366 nm).[123]**

For this purpose the fluorescent reporter molecule distyrylbenzene (DSB) was introduced into nanochannels of a flexible host compound $[Zn_2(\text{terephthalate})_2(\text{triethylenediamine})]_n$ in which two-dimensional (2D) square grids are bridged by triethylenediamine. The obtained MOF–DSB composite material selectively adsorbed CO_2 over other atmospheric gases, such as N_2, O_2, and Ar. In addition, the composite material was shown to distinguish two gases with similar physicochemical properties, e.g., CO_2 and acetylene (C_2H_2), by means of different luminescence outputs. The authors conclude that their unique detection methodology can be applied to monitor specific gases and their pressures by a fluorescence change in the guest reporter. The signal transduction scheme is based on a structural transformation rather than any chemical interaction or energy transfer, thus, extending the scope for the development of advanced detection systems.

Alternative optical methods including interferometry or localized surface plasmon resonance (LSPR)[136, 137] that have been applied for sensing rely upon analyte-induced changes of the MOF refractive index (RI). In contrast to a change of luminescence based on the absorption or emission of light this bulk property changes depending on the amount and RI of an adsorbed analyte. In 2010, the group of J. Hupp[138] reported a MOF based vapor sensor that circumvents the need for molecular-level reporters and instead relies upon a readout of changes in the MOF refractive index. In contrast to the fluorescence-based detection schemes described above, this measurement requires the MOF to be in thin-film form. Thus, Lu et al. have chosen the zeolitic imidazolate framework ZIF-8 as sensing material and have configured it as a transparent film on appropriate support materials (e.g.,

glass or silicon). By carefully adjusting the film thickness the authors were able to optically monitor the energies of the interference peaks as a function of analyte exposure (Figure 1-13).
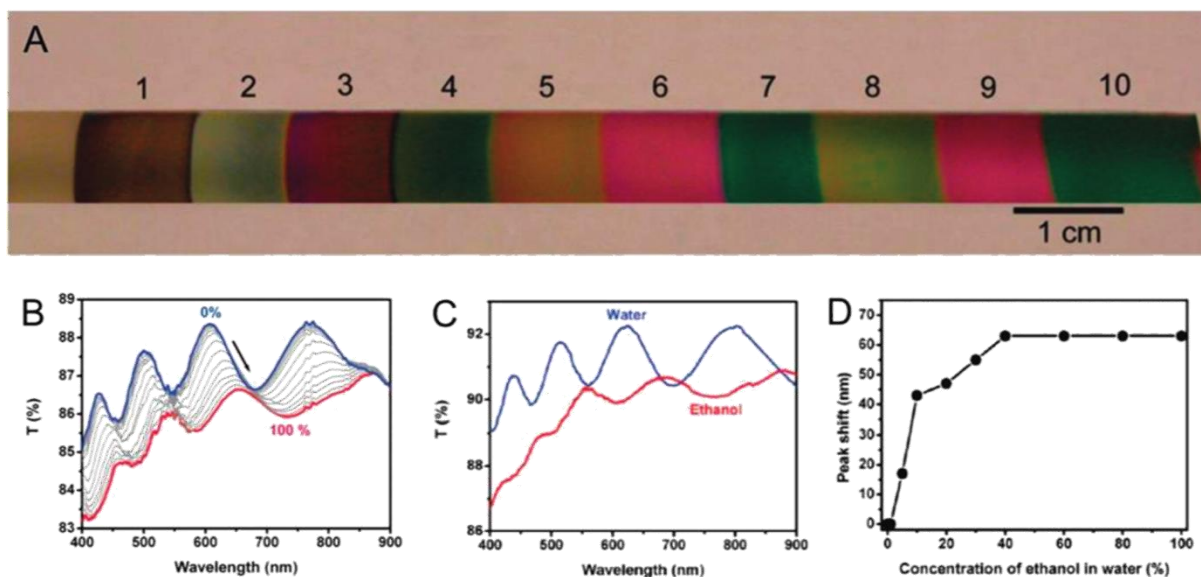
Figure 1-13 **(A) Photograph of a series of ZIF-8 films of various thicknesses on Si substrates. UV-Vis transmission spectra of a 1 µm ZIF-8 film on glass after exposure to (B) propane vapor of various concentrations from 0% (blue) to 100% (red) and (C) ethanol (red) or water (blue). (D) Interference peak (originally at 612 nm) shift versus ethanol concentration (v/v %) in ethanol/water solutions.**[138]

Films of approximately 1 µm thickness were prepared in a step-by-step fashion by repeated immersion cycles in two solutions containing the MOF precursors. UV-Vis spectroscopy was performed to record the changes of the interference peaks upon exposure to different vapors. Exposure to propane red-shifts the visible-region fringes by up to 49 nm (Figure 1-13B). Note that the ZIF-8 sensor is not only sensitive towards a series of vapors, but also displays some chemical selectivity. For example, the ZIF-8 sensor is unresponsive to water vapor, but ethanol vapor

produces a readily detectable shift, as shown in Figure 1-13C,D. These findings are consistent with the known hydrophobicity of ZIF-8. In addition, the small pores (~ 3.4 Å) allow for sieving small molecules as shown with *n*-hexane that is readily adsorbed, whereas the sterically more demanding cyclohexane is not.

Another opportunity for optical detection of analytes was recently reported by two different groups. The authors presented another refractive index-based sensor by fabricating MOF-containing colloidal crystals (CCs). These ordered 3D photonic crystals principally act as a diffraction grating for light at a specific wavelength (stop band). Upon filling the MOF pores and the interstitial voids of the 3D ordered array with analyte medium the effective refractive index changes, this can be monitored as a shift in the optical spectrum. Both groups addressed the selectivity by integrating different MOFs into three-dimensional inverse opal structures. While Wu *et al.*[139] employed a colloidal crystal templating approach using a polystyrene opaline "mold", the group of J. Hupp[140] deposited MOF crystals onto a silica template to obtain hybrid MOF–silica colloidal crystal (MOF–SCC) films. The authors could show that the introduction of an ordered porous structure imparts useful optical features to HKUST-1 and ZIF-8. For MOF–SCC an optical signal displayed by distinct stop band shifts upon analyte sorption was readily observed.

In contrast to 3D photonic architectures, we introduce herein a one-dimensional photonic composite material based on a microporous MOF and titanium dioxide.[141] A more detailed consideration of the synthetic pathway towards our optical transducer system and of the methodology to efficiently convert molecular adsorption into an optical response is given in Chapter 4.

In general, the different transduction schemes implemented within a MOF sensor can be categorized into optical, electrical and mechanical schemes. Despite one study by Achman *et al.*[142] electrical transduction modes have not been widely used to translate molecular recognition events into a readable output signal. This is due to the fact that MOFs are principally insulating materials that have rarely been utilized for conductivity-based sensing applications. In contrast, electromechanical devices including a quartz-crystal microbalance (QCM),[143-145] surface acoustic wave sensors (SAWS)[143, 146] and microcantilevers (MCL)[143, 147] are well-established methods in the field of MOF based chemical sensing. As an extension of the work from the Bein group[148, 149] using zeolite thin films for humidity and organic vapor sensing, Biemmi *et al.*[144] reported the selective growth of HKUST-1 on functionalized QCM gold electrodes to monitor the sorption performance in a controlled humidified atmosphere. Film growth was achieved by modifying the gold surface with a 11-mercaptoundecanol SAM. As a consequence of the mass loading, lower QCM frequencies were determined. As a result, a total water uptake of 41 wt% was revealed. The uptake of water was additionally illustrated as a function of the partial pressure in the form of ad- and desorption isotherms. This first study clearly showed that the QCM is a straightforward technique that allows for MOF based chemical sensing applications, while exhibiting extremely low detection limits (~ 1 ng) and providing a useful platform for recording adsorption isotherms.

Within the scope of this work, the QCM method was applied for different MOF thin films. In Chapter 3 a detailed discussion on the sorption performance of functionalized MOF thin films revealed by QCM measurements is given.

1.6   References

[1]   G. Cao, *NANOSTRUCTURES AND NANOMATERIALS, Synthesis, Properties, and Applications*, World Scientific Publishing Co. Pte. Ltd., London, **2011**.

[2]   P. B. Venuto and E. T. Habib, Jr., *Chemical Industries, Vol. 1: Fluid Catalytic Cracking with Zeolite Catalysts*, 1979.

[3]   C. J. Adams, A. Araya, S. W. Carr, A. P. Chapple, K. R. Franklin, P. Graham, A. R. Minihan, T. J. Osinga and J. A. Stuart, *Stud. Surf. Sci. Catal.* , 1997, **105B**, 1667-1674.

[4]   R. M. Barrer, *Zeolites and Clay Minerals as Sorbents and Molecular Sieves*, **1978**.

[5]   J. S. Beck, J. C. Vartuli, W. J. Roth, M. E. Leonowicz, C. T. Kresge, K. D. Schmitt, C. T. W. Chu, D. H. Olson, E. W. Sheppard and et al., *J. Am. Chem. Soc.*, 1992, **114**, 10834-10843.

[6]   C. T. Kresge, M. E. Leonowicz, W. J. Roth, J. C. Vartuli and J. S. Beck, *Nature (London, United Kingdom)*, 1992, **359**, 710-712.

[7]   M. G. Kanatzidis, *Adv. Mater.* , 2007, **19**, 1165-1181.

[8]   M. P. Suh, H. J. Park, T. K. Prasad and D.-W. Lim, *Chem. Rev.*, 2012, **112**, 782-835.

[9]   U. Mueller, M. Schubert, F. Teich, H. Puetter, K. Schierle-Arndt and J. Pastre, *J. Mater. Chem.*, 2006, **16**, 626-636.

[10]   Y.-S. Bae, C. Y. Lee, K. C. Kim, O. K. Farha, P. Nickias, J. T. Hupp, S. T. Nguyen and R. Q. Snurr, *Angew. Chem. Int. Ed.*, 2012, **51**, 1857-1860.

[11]   J.-R. Li, R. J. Kuppler and H.-C. Zhou, *Chem. Soc. Rev.*, 2009, **38**, 1477-1504.

[12]   J. Lee, O. K. Farha, J. Roberts, K. A. Scheidt, S. T. Nguyen and J. T. Hupp, *Chem. Soc. Rev.*, 2009, **38**, 1450.

[13]   M. Fujita, Y. J. Kwon, S. Washizu and K. Ogura, *J. Am. Chem.Soc.*, 1994, **116**, 1151-1152.

[14] P. Horcajada, R. Gref, T. Baati, P. K. Allan, G. Maurin, P. Couvreur, G. Férey, R. E. Morris and C. Serre, *Chem. Rev.*, 2012, **112**, 1232-1268.

[15] L. E. Kreno, K. Leong, O. K. Farha, M. Allendorf, R. P. Van Duyne and J. T. Hupp, *Chem. Rev.*, 2012, **112**, 1105-1125.

[16] E. Kokot and R. L. Martin, *J. Chem. Soc.*, 1965, 187.

[17] E. A. Tomic, *J. Appl. Polym. Sci.*, 1965, **9**, 3745-3752.

[18] K. A. Hirsch, D. Venkataraman, S. R. Wilson, J. S. Moore and S. Lee, *J. Chem. Soc., Chem. Commun.* , 1995, 2199-2200.

[19] D. Venkataraman, G. B. Gardner, S. Lee and J. S. Moore, *J. Am. Chem. Soc.*, 1995, **117**, 11600-11601.

[20] B. F. Hoskins and R. Robson, *J. Am. Chem. Soc.*, 1990, **112**, 1546-1554.

[21] O. M. Yaghi, G. Li and H. Li, *Nature*, 1995, **378**, 703-706.

[22] G. Ferey, *Chem. Soc. Rev.*, 2008, **37**, 191-214.

[23] S. Kitagawa, R. Kitaura and S.-i. Noro, *Angew. Chem., Int. Ed.*, 2004, **43**, 2334-2375.

[24] D. Farrusseng, *Metal-Organic Frameworks – Applications from Catalysis to Gas Storage*, Wiley-VCH, Weinheim, **2011**.

[25] G. Ferey, C. Mellot-Draznieks, C. Serre, F. Millange, J. Dutour, S. Surble and I. Margiolaki, *Science*, 2005, **309**, 2040-2042.

[26] L. R. MacGillivray, *Metal-Organic Frameworks – Design and Application*, Wiley, Hoboken, New Jersey, **2010**.

[27] A. K. Cheetham, G. Ferey and T. Loiseau, *Angew. Chem.*, 1999, **38**, 3268-3292.

[28] N. W. Ockwig, O. Delgado-Friedrichs, M. O'Keeffe and O. M. Yaghi, *Acc. Chem. Res.*, 2005, **38**, 176-182.

[29] J. L. C. Rowsell and O. M. Yaghi, *J. Am. Chem. Soc.*, 2006, **128**, 1304-1315.

[30] H. Li, M. Eddaoudi, M. O'Keeffe and M. Yaghi, *Nature*, 1999, **402**, 276-279.

[31]   M. Eddaoudi, J. Kim, N. Rosi, D. Vodak, J. Wachter, M. O'Keeffe and O. M. Yaghi, *Science*, 2002, **295**, 469-472.

[32]   H. Deng, C. J. Doonan, H. Furukawa, R. B. Ferreira, J. Towne, C. B. Knobler, B. Wang and O. M. Yaghi, *Science*, 2010, **327**, 846-850.

[33]   H. Deng, S. Grunder, K. E. Cordova, C. Valente, H. Furukawa, M. Hmadeh, F. Gándara, A. C. Whalley, Z. Liu, S. Asahina, H. Kazumori, M. O'Keeffe, O. Terasaki, J. F. Stoddart and O. M. Yaghi, *Science*, 2012, **336**, 1018-1023.

[34]   J. L. C. Rowsell and O. M. Yaghi, *Microporous Mesoporous Mater.*, 2004, **73**, 3-14.

[35]   S. R. Batten and R. Robson, *Angew. Chem.*, 1998, **37**, 1461-1494.

[36]   J. L. C. Rowsell and O. M. Yaghi, *Angew. Chem.*, 2005, **44**, 4670-4679.

[37]   D. M. P. Mingos and D. R. Baghurst, *Chem. Soc. Rev.*, 1991, **20**, 1-47.

[38]   S. S. Y. Chui, S. M. F. Lo, J. P. H. Charmant, A. G. Orpen and I. D. Williams, *Science*, 1999, **283**, 1148-1150.

[39]   S. H. Jhung, J. W. Yoon, J.-S. Hwang, A. K. Cheetham and J.-S. Chang, *Chem. Mater.*, 2005, **17**, 4455-4460.

[40]   Y. K. Hwang, J.-S. Chang, S.-E. Park, D. S. Kim, Y.-U. Kwon, S. H. Jhung, J.-S. Hwang and M. S. Park, *Angew. Chem.*, 2005, **44**, 556-560.

[41]   S. H. Jhung, J.-H. Lee, P. M. Forster, G. Férey, A. K. Cheetham and J.-S. Chang, *Chem.– Eur. J.*, 2006, **12**, 7899-7905.

[42]   Z. Lin, D. S. Wragg and R. E. Morris, *Chem. Commun.*, 2006, 2021-2023.

[43]   N. Stock and T. Bein, *Angew. Chem., Int. Ed.* , 2004, **43**, 749-752.

[44]   S. Bauer, T. Bein and N. Stock, *Inorg. Chem.* , 2005, **44**, 5882-5889.

[45]   S. Bauer, C. Serre, T. Devic, P. Horcajada, J. Marrot, G. Ferey and N. Stock, *Inorg. Chem.*, 2008, **47**, 7568-7576.

[46]   M. Plabst and T. Bein, *Inorg. Chem.*, 2009, **48**, 4331-4341.

[47]   N. Stock and S. Biswas, *Chem. Rev.*, 2012, **112**, 933-969.

[48]   A. Corma, M. Moliner, J. M. Serra, P. Serna, M. J. Diaz-Cabanas and L. A. Baumes, *Chem. Mater.*, 2006, **18**, 3287-3296.

[49]   C. Mellot-Draznieks, J. Dutour and G. Ferey, *Angew. Chem., Int. Ed.*, 2004, **43**, 6290-6296.

[50]   S. Kitagawa, S.-i. Noro and T. Nakamura, *Chem. Commun.*, 2006, 701-707.

[51]   S. M. Cohen, *Chem. Rev.*, 2012, **112**, 970-1000.

[52]   N. G. Pschirer, D. M. Ciurtin, M. D. Smith, U. H. F. Bunz and H.-C. zur Loye, *Angew. Chem., Int. Ed.*, 2002, **41**, 583-585.

[53]   Y. Cui, H. L. Ngo, P. S. White and W. Lin, *Chem. Commun.*, 2003, 994-995.

[54]   C.-D. Wu, A. Hu, L. Zhang and W. Lin, *J. Am. Chem. Soc.* , 2005, **127**, 8940-8941.

[55]   L. Chen and X. Bu, *Chem. Mater.*, 2006, **18**, 1857-1860.

[56]   C.-Y. Sun, C. Qin, C.-G. Wang, Z.-M. Su, S. Wang, X.-L. Wang, G.-S. Yang, K.-Z. Shao, Y.-Q. Lan and E.-B. Wang, *Advanced Materials*, 2011, **23**, 5629-5632.

[57]   G. B. Gardner, D. Venkataraman, J. S. Moore and S. Lee, *Nature*, 1995, **374**, 792-795.

[58]   Y. H. Kiang, G. B. Gardner, S. Lee, Z. Xu and E. B. Lobkovsky, *J. Am. Chem. Soc.*, 1999, **121**, 8204-8215.

[59]   J. S. Seo, D. Whang, H. Lee, S. I. Jun, J. Oh, Y. J. Jeon and K. Kim, *Nature*, 2000, **404**, 982-986.

[60]   Z. Wang and S. M. Cohen, *Chem. Soc. Rev.*, 2009, **38**, 1315-1329.

[61]   K. K. Tanabe and S. M. Cohen, *Chem. Soc. Rev.*, 2011, **40**, 498-519.

[62]   S. M. Cohen, *Chem. Sci.*, 2010, **1**, 32-36.

[63]   Z. Wang and S. M. Cohen, *J. Am. Chem. Soc.*, 2007, **129**, 12368-12369.

[64]   S. S. Y. Chui, S. M. F. Lo, J. P. H. Charmant, A. G. Orpen and I. D. Williams, *Science*, 1999, **283**, 1148.

[65]   O. K. Farha, K. L. Mulfort and J. T. Hupp, *Inorg. Chem.*, 2008, **47**, 10223.

[66]   Y. K. Hwang, D. Y. Hong, J. S. Chang, S. H. Jhung, Y. K. Seo, J. Kim, A. Vimont, M. Daturi, C. Serre and G. Férey, *Angew. Chem., Int. Ed.*, 2008, **47**, 4144.

[67]   A. Demessence, D. M. D'Alessandro, M. L. Foo and J. R. Long, *J. Am. Chem. Soc.*, 2009, **131**, 8784-8786.

[68]   M. Banerjee, S. Das, M. Yoon, H. J. Choi, M. H. Hyun, S. M. Park, G. Seo and K. Kim, *J. Am. Chem. Soc.*, 2009, **131**, 7524-7525.

[69]   D. Farrusseng, S. Aguado and C. Pinel, *Angew. Chem., Int. Ed.*, 2009, **48**, 7502-7513.

[70]   L. Ma, J. M. Falkowski, C. Abney and W. Lin, *Nat. Chem.*, 2010, **2**, 838-846.

[71]   M. Servalli, M. Ranocchiari and J. A. Van Bokhoven, *Chem.Commun.*, 2012, **48**, 1904-1906.

[72]   T. Yamada and H. Kitagawa, *J. Am. Chem. Soc. *, 2009, **131**, 6312-6313.

[73]   R. K. Deshpande, J. L. Minnaar and S. G. Telfer, *Angew. Chem., Int. Ed.*, 2010, **49**, 4598.

[74]   K. K. Tanabe, C. A. Allen and S. M. Cohen, *Angew. Chem., Int. Ed.*, 2010, **49**, 9730-9733.

[75]   H. Sato, R. Matsuda, K. Sugimoto, M. Takata and S. Kitagawa, *Nat. Mater.*, 2010, **9**, 661-666.

[76]   D. J. Lun, G. I. N. Waterhouse and S. G. Telfer, *J. Am. Chem. Soc.*, 2011, **133**, 5806.

[77]   D. L. Allara and R. G. Nuzzo, *Langmuir* 1985, **1**, 52-66.

[78]   C. D. Bain and G. M. Whitesides, *J. Am. Chem. Soc. *, 1989, **111**, 7164-7175.

[79]   G. E. Poirier and E. D. Pylant, *Science*, 1996, **272**, 1145-1148.

[80]   J. C. Love, L. A. Estroff, J. K. Kriebel, R. G. Nuzzo and G. M. Whitesides, *Chem. Rev. *, 2005, **105**, 1103-1169.

[81]   J. Kang and P. A. Rowntree, *Langmuir*, 2007, **23**, 509-516.

[82]   A. Ulman, *Chem. Rev.*, 1996, **96**, 1533-1554.

[83]   C. D. Bain, E. B. Troughton, Y. T. Tao, J. Evall, G. M. Whitesides and R. G. Nuzzo, *J. Am. Chem. Soc.*, 1989, **111**, 321-335.

[84]   A. Kaifer, ed., *Supramolecualr Electrochemistry*, Wiley VCH, **2001**.

[85]   F. Schreiber, *Prog. Surf. Sci.*, 2000, **65**, 151-256.

[86]   M. D. Porter, T. B. Bright, D. L. Allara and C. E. D. Chidsey, *J. Am. Chem. Soc.* , 1987, **109**, 3559-3568.

[87]   M. Kind and C. Woell, *Chemie in Unserer Zeit*, 2008, **42**, 128-141.

[88]   L. H. Dubois, B. R. Zegarski and R. G. Nuzzo, *J. Chem. Phys.*, 1993, **98**, 678-688.

[89]   G. E. Poirier, *Langmuir*, 1997, **13**, 2019-2026.

[90]   N. Camillone, III, C. E. D. Chidsey, G. Y. Liu and G. Scoles, *J. Chem. Phys.*, 1993, **98**, 3503-3511.

[91]   L. H. Dubois, B. R. Zegarski and R. G. Nuzzo, *J. Chem. Phys.*, 1993, **98**, 678-688.

[92]   A. Y. Lee, A. Ulman and A. S. Myerson, *Langmuir*, 2002, **18**, 5886-5898.

[93]   Y. Xia, X.-M. Zhao and G. M. Whitesides, *Microelectronic Engineering*, 1996, **32**, 255-268.

[94]   A. M. Rawlett, T. J. Hopson, I. Amlani, R. Zhang, J. Tresek, L. A. Nagahara, R. K. Tsui and H. Goronkin, *Nanotechnology*, 2003, **14**, 377-384.

[95]   T. Bein, *Chem. Mater.*, 1996, **8**, 1636-1653.

[96]   S. Feng and T. Bein, *Nature*, 1994, **368**, 834-836.

[97]   S. Feng and T. Bein, *Science*, 1994, **265**, 1839-1841.

[98]   V. Valtchev and S. Mintova, *Microporous Mesoporous Mater.*, 2001, **43**, 41-49.

[99]   S. Mintova and T. Bein, *Adv. Mater.*, 2001, **13**, 1880-1883.

[100]   S. Y. Choi, Y. J. Lee, Y. S. Park, K. Ha and K. B. Yoon, *J. Am. Chem. Soc.*, 2000, **122**, 5201–5209.

[101]   A. Kulak, Y.-J. Lee, Y. S. Park and K. B. Yoon, *Angew. Chem., Int. Ed.*, 2000, **39**, 950-953.

[102]   S. Mann, *Nature*, 1993, **365**, 499-505.

[103]   E. Dujardin and S. Mann, *Adv. Eng. Mater.*, 2002, **4**, 461-474.

[104]   S. Weiner and L. Addadi, *J. Mater. Chem.*, 1997, **7**, 689-702.

[105]   S. Feng and T. Bein, *Stud. Surf. Sci. Catal.*, 1997, **105**, 2147-2154.

[106]   J. S. Lee, Y.-J. Lee, E. L. Tae, Y. S. Park and K. B. Yoon, *Science*, 2003, **301**, 818-821.

[107]   S. Hermes, F. Schroeder, R. Chelmowski, C. Woell and R. A. Fischer, *J. Am. Chem. Soc.*, 2005, **127**, 13744-13745.

[108]   S. Hermes, D. Zacher, A. Baunemann, C. Woell and R. A. Fischer, *Chem. Mater.*, 2007, **19**, 2168-2173.

[109]   Y. Yoo and H.-K. Jeong, *Chem. Commun.*, 2008, 2441-2443.

[110]   O. Shekhah, H. Wang, S. Kowarik, F. Schreiber, M. Paulus, M. Tolan, C. Sternemann, F. Evers, D. Zacher, R. A. Fischer and C. Wöll, *J. Am. Chem. Soc.*, 2007, **129**, 15118-15119.

[111]   O. Shekhah, *Materials*, 2010, **3**, 1302-1315.

[112]   E. Biemmi, C. Scherb and T. Bein, *J. Am. Chem. Soc.*, 2007, **129**, 8054-8055.

[113]   O. Shekhah, H. Wang, D. Zacher, R. A. Fischer and C. Woell, *Angew. Chem., Int. Ed.*, 2009, **48**, 5038–5041.

[114]   S. Surble, F. Millange, C. Serre, G. Ferey and I. Walton Richard, *Chem. Commun.*, 2006, 1518-1520.

[115]   R. Makiura, S. Motoyama, Y. Umemura, H. Yamanaka, O. Sakata and H. Kitagawa, *Nat. Mater.*, 2010, **9**, 565-571.

[116] R. Makiura and H. Kitagawa, *Eur. J. Inorg. Chem.*, 2010, **2010**, 3715-3724.

[117] C. Scherb, A. Schoedel and T. Bein, *Angew. Chem., Int. Ed.*, 2008, **47**, 5777-5779.

[118] A. Schoedel, C. Scherb and T. Bein, *Angew. Chem., Int. Ed.*, 2010, **49**, 7225.

[119] F. M. Hinterholzinger, S. Wuttke, P. Roy, Preu, A. Schaate, P. Behrens, A. Godt and T. Bein, *Dalton Trans.*, 2012, **41**, 3899-3901.

[120] O. S. Wolfbeis, *Anal. Chem.*, 2004, **76**, 3269-3284.

[121] M. D. Allendorf, C. A. Bauer, R. K. Bhakta and R. J. T. Houk, *Chem. Soc. Rev.*, 2009, **38**, 1330-1352.

[122] Y. Takashima, V. M. Martínez, S. Furukawa, M. Kondo, S. Shimomura, H. Uehara, M. Nakahama, K. Sugimoto and S. Kitagawa, *Nat. Commun.*, 2011, **2**, 168.

[123] N. Yanai, K. Kitayama, Y. Hijikata, H. Sato, R. Matsuda, Y. Kubota, M. Takata, M. Mizuno, T. Uemura and S. Kitagawa, *Nat. Mater.*, 2011, **10**, 787-793.

[124] Y. Salinas, R. Martinez-Manez, M. D. Marcos, F. Sancenon, A. M. Costero, M. Parra and S. Gil, *Chem. Soc. Rev.*, 2012, **41**, 1261-1296.

[125] A. Hulanicki, S. Glab and F. Ingman, *Pure Appl. Chem.*, 1991, **63**, 1247-1250.

[126] Z.-Z. Lu, R. Zhang, Y.-Z. Li, Z.-J. Guo and H.-G. Zheng, *J. Am. Chem. Soc.*, 2011, **133**, 4172-4174.

[127] L. G. Beauvais, M. P. Shores and J. R. Long, *J. Am. Chem. Soc.*, 2000, **122**, 2763-2772.

[128] H. Lee, S. H. Jung, W. S. Han, J. H. Moon, S. Kang, J. Y. Lee, J. H. Jung and S. Shinkai, *Chem.-Eur. J.*, 2011, **17**, 2823-2827.

[129] Y. Qiu, H. Deng, J. Mou, S. Yang, M. Zeller, S. R. Batten, H. Wu and J. Li, *Chem. Commun.*, 2009, 5415.

[130] L. Basabe-Desmonts, D. N. Reinhoudt and M. Crego-Calama, *Chem. Soc. Rev.*, 2007, **36**, 993.

[131] Z. Xie, L. Ma, K. E. deKrafft, A. Jin and W. Lin, *J. Am. Chem. Soc.*, 2009, **132**, 922.

[132] Y. Li, S. Zhang and D. Song, *Angew. Chem., Int. Ed.*, 2013, **52**, 710-713.

[133] A. Lan, K. Li, H. Wu, D. H. Olson, T. J. Emge, W. Ki, M. Hong and J. Li, *Angew. Chem., Int. Ed.*, 2009, **48**, 2334.

[134] S. Pramanik, C. Zheng, X. Zhang, T. J. Emge and J. Li, *J. Am. Chem. Soc.*, 2011, **133**, 4153.

[135] J. An, C. M. Shade, D. A. Chengelis-Czegan, S. p. Petoud and N. L. Rosi, *J. Am. Chem. Soc.*, 2011, **133**, 1220-1223.

[136] K. A. Willets and R. P. Van Duyne, *Annu. Rev. Phys. Chem.*, 2007, **58**, 267.

[137] L. E. Kreno, J. T. Hupp and R. P. Van Duyne, *Anal. Chem.*, 2010, **82**, 8042.

[138] G. Lu and J. T. Hupp, *J. Am. Chem. Soc.*, 2010, **132**, 7832-7833.

[139] Y.-n. Wu, F. Li, W. Zhu, J. Cui, C.-a. Tao, C. Lin, P. M. Hannam and G. Li, *Angew. Chem., Int. Ed.*, 2011, **50**, 12518-12522.

[140] G. Lu, O. K. Farha, L. E. Kreno, P. M. Schoenecker, K. S. Walton, R. P. Van Duyne and J. T. Hupp, *Adv. Mater.*, 2011, **23**, 4449-4452.

[141] F. M. Hinterholzinger, A. Ranft, J. M. Feckl, B. Rühle, T. Bein and B. V. Lotsch, *J. Mater. Chem.*, 2012, **22**, 10356-10362.

[142] S. Achmann, G. Hagen, J. Kita, I. M. Malkowsky, C. Kiener and R. Moos, *Sensors* 2009, **9**, 1574-1589.

[143] K. M. Goeders, J. S. Colton and L. A. Bottomley, *Chem. Rev.*, 2008, **108**, 522-542.

[144] E. Biemmi, A. Darga, N. Stock and T. Bein, *Microporous Mesoporous Mater.*, 2008, **114**, 380-386.

[145] R. Ameloot, L. Stappers, J. Fransaer, L. Alaerts, B. F. Sels and D. E. De Vos, *Chem. Mater.*, 2009, **21**, 2580-2582.

[146] A. L. Robinson, M. D. Allendorf, V. Stavila and S. M. Thornberg, *Materials Research Society Proceedings*, San Francisco, CA, **2011**.

[147] J. H. Lee, R. T. J. Houk, A. Robinson, J. A. Greathouse, S. M. Thornberg, M. D. Allendorf and P. J. Hesketh, *Proc. SPIE*, 2010, 767927.

[148]   S. Mintova and T. Bein, *Microporous Mesoporous Mater.*, 2001, **50**, 159-166.

[149]   X. Xu, J. Wang and Y. Long, *Sens. Actuators, B*, 2006, **6**, 1751-1764.

2   Characterization

2.1   X-Ray Diffraction

X-ray diffraction (XRD) is a non-destructive analytical technique that can be applied for the identification of unknown specimens and for the determination of materials properties. Characteristic information about the crystallographic structure, the preferred crystal growth as well as the grain size or the periodic ordering of porosity can thus be provided.

The principle of generating X-ray radiation is based on the bombardment of a target with high-energy electrons. The acceleration and interaction of electrons with target materials partially results in a radiation showing a continuous background spectrum termed 'Bremsstrahlung'. Another characteristic property depends on the elemental composition of the target and is shown by narrow lines in the spectrum resulting from X-ray fluorescence. This is caused by the impact of primary electrons creating a hole in a lower shell of an atom. The vacancy is subsequently occupied by upper shell electrons and the surplus energy is released as X-ray photons. By applying blocking filters, a single energy spike can be isolated resulting in fairly monochromatic X-ray radiation.

The wavelengths of X-ray photons are typically in a range of 10^{-8} to 10^{-12} m, which is the same order of magnitude as the size of atoms and the spacing d between lattice

planes.[1, 2] Structural information about the specimen can be obtained by evaluating the diffraction patterns caused by constructive and destructive interference of X-rays scattered by the regular array of atoms in the lattice planes (Figure 2-1).
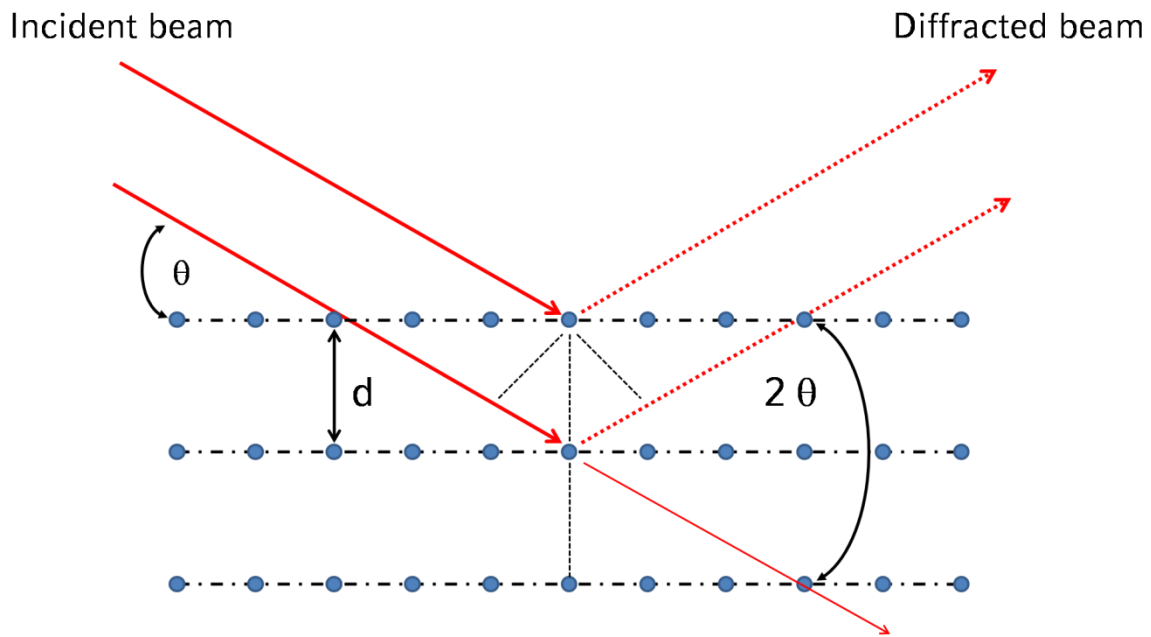
Figure 2-1   Schematic illustration of X-ray diffraction at a crystal lattice plane according to the Bragg relation. Constructive interference occurs when the path-length difference is an integer multiple of the incident wavelength.

Depending on the type of the applied technique one has to distinguish between absorption, reflection and scattering. Scattering results from X-rays that impinge on the atoms and produce secondary spherical waves emanating from the electron. The regular array of atoms within a crystal produces a regular array of scattered waves. In many directions these waves are cancelled out due to destructive interference, but they also add constructively in a few directions, determined by Bragg's law:

$$n \cdot \lambda = 2d \sin \theta$$

n: order of interference

λ: wavelength of X-rays

d: lattice spacing

θ: angle of incidence.

According to Bragg's law the elastically scattered waves combine constructively only in directions where their path-length difference is an integer multiple of the incident X-ray wavelength.

The most precise method for structural analysis is single-crystal X-ray diffraction in which a beam of monochromatic X-rays strikes a single crystal. A regular diffraction pattern is recorded as the crystal is gradually rotated in the beam such that Bragg's law is fulfilled for every orientation.

In powdered samples consisting of randomly oriented crystallites every possible crystallographic orientation is represented. The resulting diffraction patterns are formed by a set of cones from all planes that satisfy the Bragg conditions. Powder diffraction allows for quick and non-destructive analysis of crystalline phases by comparison with sample libraries.

In this thesis, X-ray diffraction was essentially applied for the structural analysis of powder samples and for the determination of crystal growth along a preferred crystallographic orientation. More specifically, powder diffraction was combined

with *in-situ* vapor pressure control experiments to investigate the dependence of materials properties upon an external stimulus.

2.2   Scanning electron microscopy

Scanning electron microscopy (SEM)[2, 3] reveals information about the topography or composition of a specimen with a spatial resolution down to the nanoscale.

In contrast to an optical microscope operating with visible light, SEM is performed using a narrow and coherent electron beam that is generated under vacuum. High-resolution images are recorded by scanning the focused electron beam across the surface of the specimen. Depending on the size of the electron spot, the interaction volume and the material properties images can be produced revealing details less than 1 nm in size.

In Figure 2-2 the Scanning Electron Microscope and its working principle is depicted. In a typical setup an electron gun fitted with either a tungsten filament or a field emission gun is used to generate the electron beam. During the process the electrons are accelerated and focused to a coherent and highly energetic beam by several electromagnetic condenser lenses. Scanning in a raster fashion is achieved when the electron beam passes pairs of scanning coils or deflector plates. Before impinging and scanning the specimen the beam is focused by a set of objective lenses onto the surface of the sample.
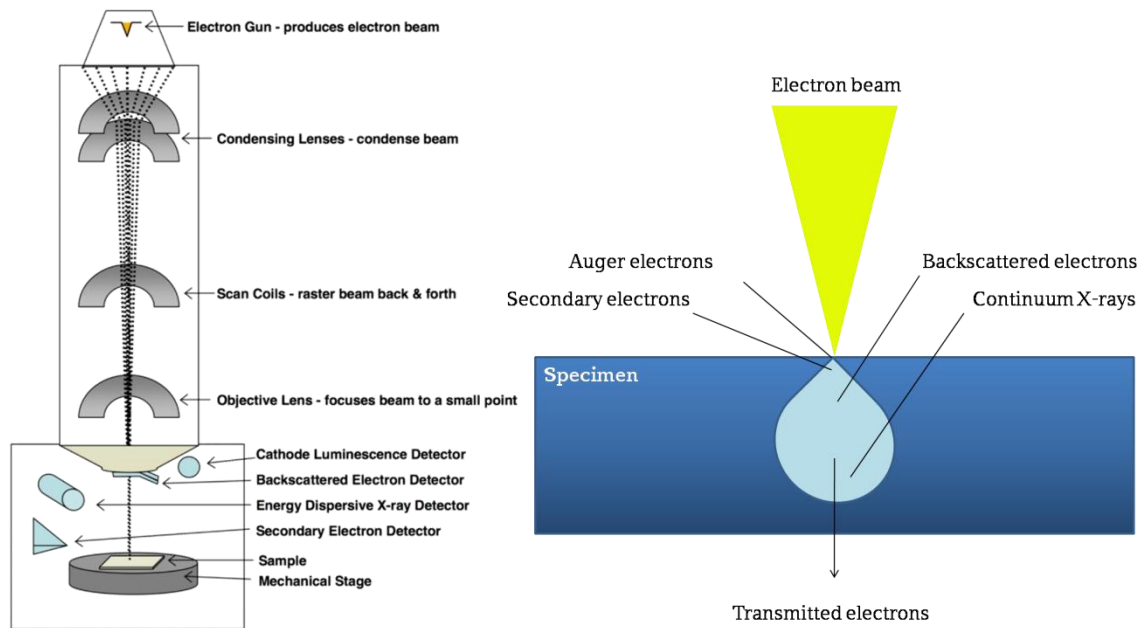
Figure 2-2   Schematic setup and working principle of a Scanning Electron Microscope showing the main components as well as the generation and pathway of the electron beam to the surface of a sample.[4]

The interactions of the accelerated electrons with the specimen result in the emission of electromagnetic radiation including secondary electrons (SE), backscattered electrons (BSE) or photons.

When transmitted electrons emerge from the specimen no change in their direction or energy loss is observed, whereas elastically scattered electrons like diffracted and backscattered electrons differ with respect to their energy and angle of diffraction. The emission of secondary and backscattered electrons induced by a highly energetic primary beam is dependent on the acceleration and on the morphology of the specimen. Since the former electrons exhibit a low energy, only a small amount of electrons close to the surface is detectable. Another generation of electrons

occurs when the atom is excited to a higher energetic state. The vacancy of the electron has to be filled by an electron from an outer shell. The surplus energy is either released by emission of characteristic X-rays or by Auger electrons.

In general, a SEM is operating at high voltage ranging from a few hundred Volts to 40 keV. The bundled and coherent electron beam scans the specimen and dislodges the secondary electrons by inelastic scattering. Secondary electron detectors are standard equipment in all SEMs and display an amplified electric signal as an intensity distribution proportional to the number of emitted electrons. This powerful technique allows one to gain information about the elemental composition and the topographical nature of a specimen, even yielding images with three-dimensional appearance.

2.3   Vibrational spectroscopy

Infrared spectroscopy

The physical background of infrared (IR)[5] and Raman spectroscopy[6] relies upon the interaction with electromagnetic radiation that induces the excitation of vibrational modes to higher energy levels. These techniques are applied in order to analyze the chemical bonding in a material and to gain information about the structural composition.

IR-spectroscopy is a direct absorption technique using light of the electromagnetic spectrum ranging from $200 - 4000 \ cm^{-1}$ for excitation. IR-spectroscopy is usually

employed for studying the fundamental vibrations of chemical bonds on the condition that the molecule is IR-active. The molecule needs to have either a permanent dipole moment and/or its dipole moment has to change during vibration. The absorption of radiation results in transitions to higher energy levels and thus a characteristic absorption spectrum providing information about the chemical composition and bonding of the sample can be detected.

Whereas FT-IR spectroscopy is typically employed to investigate powder samples or liquids, Reflection-Absorption IR spectroscopy (RAIRS) utilizes an alternative geometry for analysis of thin layers such as self-assembled monolayers on reflecting substrates. In Figure 2-3 a detailed set-up of a RAIR experiment is shown.
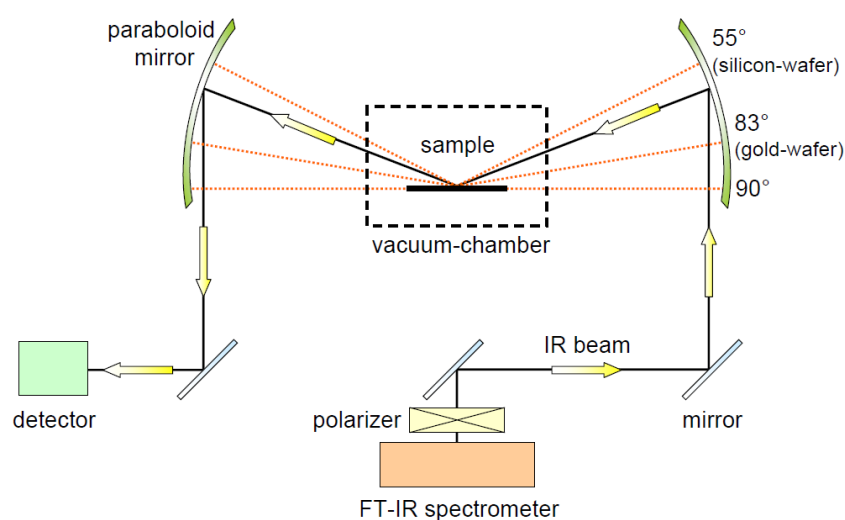
Figure 2-3   Schematic setup of the reflection absorption IR spectrometer.

The infrared radiation is directed onto the sample and reflected from the underlying surface. As the IR beam interacts with the organic components that are present on

the substrate, characteristic absorption bands can be observed. Due to the properties of surface reflection a special selection rule occurs: only vibrations with transition dipole moments that are aligned or have components perpendicular to the reflecting surface can be excited. Whereas the incident and reflected p-polarized components of the radiation superimpose constructively and enhance the signal, the s-polarized components cancel each other as they undergo a phase change on reflection from the reflecting surface.

Raman spectroscopy

For Raman-spectroscopy monochromatic light, usually generated by a laser, is used to illuminate the sample. In contrast to IR-spectroscopy the Raman absorption is a two-photon process and based on a change in the bond polarizability. Figure 2-4 illustrates the possible excitation and relaxation processes occurring during a Raman experiment. The incident light can be scattered in two different ways. Either the monochromatic light is scattered elastically (Rayleigh scattering) or inelastically (Raman scattering). The latter has to be distinguished depending on the vibrational state it is relaxing to. As a result of illuminating a substance with monochromatic light, excitation of an electron to a virtual energy state occurs. The following relaxation generates the emission of a photon exhibiting either a lower energy (Stokes scattering) or a higher energy (Anti-Stokes scattering) than the incident radiation.
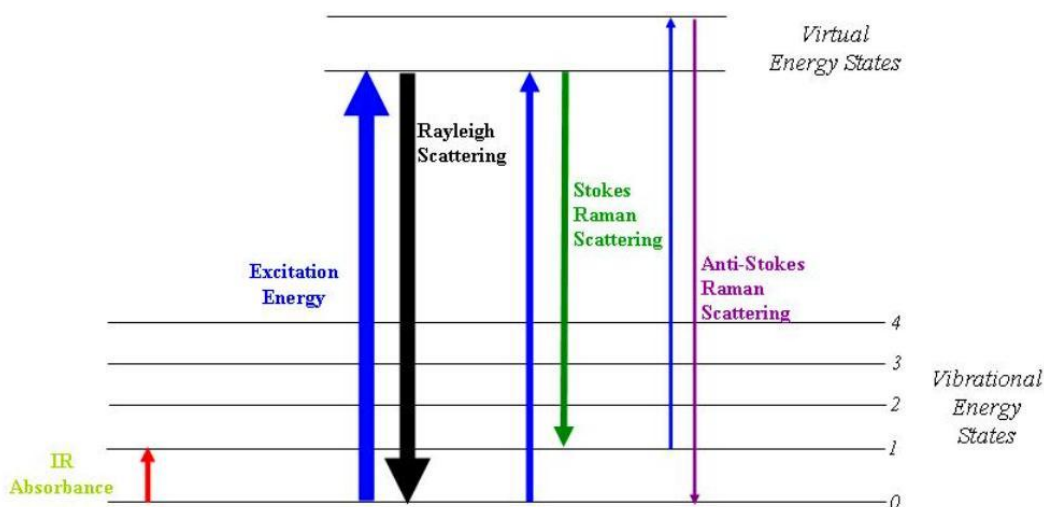
Figure 2-4   Absorption, relaxation and scattering processes in a Raman experiment.[7]

Vibrational spectra of solid samples present a large number of peaks, each corresponding to specific vibrational transitions. Thus, IR as well as Raman techniques are suitable to identify specific functional groups (*e.g.*, in organic molecules), as well as the molecular structure of the solid material.

2.4   Fluorescence

Fluorescence spectroscopy[8] is a type of electromagnetic spectroscopy that allows one to record the emission of fluorescence light induced by photon absorption. Fluorescence itself is the process of light-emitting deactivation of electronically excited states as visualized with a Jablonski diagram (Figure 2-5).
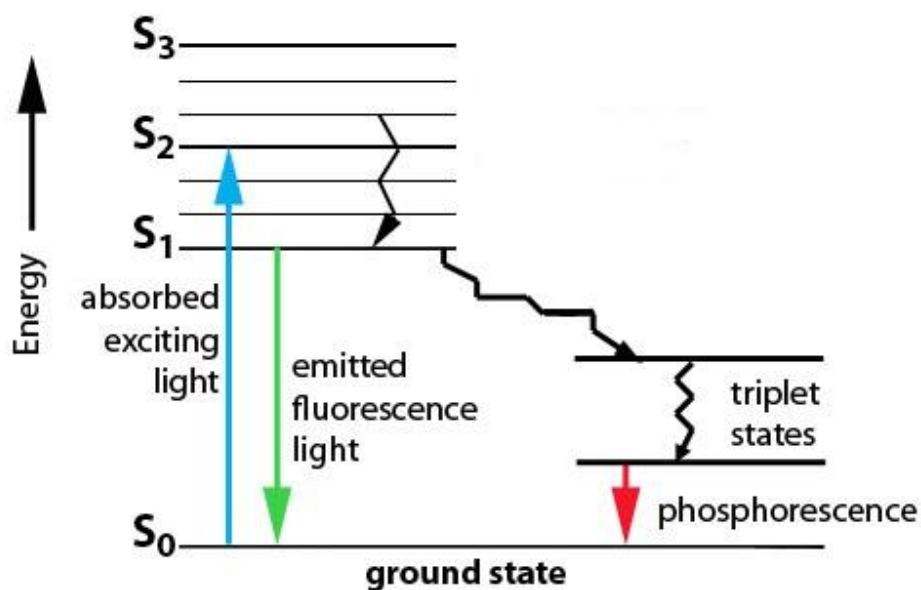
Figure 2-5   **Jablonski diagram illustrating the absorption of light, the non-radiative deactivation and the relaxation to the ground state causing the emission of fluorescence light.[9]**

According to Franck-Condon´s principle the absorption of photons causes an electronic transition that is essentially instantaneous compared with the time-scale of nuclear motions. This fact results in a so-called vertical electronic excitation. The excited molecule dissipates its energy upon collisions with its environment until it reaches the vibrational ground state of the excited electronic state. The energy released upon relaxation into the electronic ground state results in a photon emission. The energy difference in the excitation and emission wavelengths is called "Stokes-shift" and caused by the radiation-free deactivation of the molecule between the vibrational states of the excited electronic state.

Fluorescence spectroscopy is applied to qualitatively study the degree of sample labeling with a fluorescent dye and for fluorescence titration experiments, thus

allowing for a straightforward visualization of a specific recognition event *via* "turn-on/off-fluorescence" mechanisms.

2.5   Nuclear magnetic resonance (NMR)

Nuclear magnetic resonance (NMR)[10] spectroscopy is a very powerful technique that exploits the magnetic properties of a certain nuclear isotope. This method can be applied to provide detailed information on the topology, dynamics and three-dimensional structure of molecules in solution and the solid state. The physical phenomenon relies upon nuclear magnetic resonance that is achieved for nuclei possessing a permanent magnetic dipole moment. Nuclei such as ^{1}H, ^{13}C, ^{19}F exhibit a permanent magnetic dipole or non-zero spin that is always associated with a non-zero magnetic moment (μ) *via* the relation:

$$\mu = \gamma S$$

γ: gyromagnetic ratio (ratio of magnetic dipole moment to angular moment)

S: spin angular moment

It is this magnetic moment that allows the observation of NMR absorption spectra caused by transitions between nuclear spin levels.

The orientations of their magnetic moments are limited to discrete quantum states relative to an external magnetic field. By applying electromagnetic waves in the radiofrequency region, transitions between these states can be induced when the resonance condition is met:

$$\omega = \gamma B_{loc} = \gamma(B_0 + B_{int})$$

ω : frequency of the electromagnetic radiation at resonance condition

y: gyromagnetic ratio

B_{loc} : magnetic field strength at the nuclei

B_0 : externally applied magnetic field

B_{int} : internal field arising from electronic environments and surrounding magnetic

moments

In solid-phase media, such as crystals, microcrystalline powders or gels, it is in particular the dipole-dipole interactions between the magnetic moments of adjacent nuclei that cause broadening of the spectral lines. One common technique to achieve high spectral resolution in solids is to eliminate the anisotropic effect by fast rotation of the sample around an angle of 54.74° relative to the electric field, *i.e.,* magic angle spinning nuclear magnetic resonance (MAS-NMR). In conventional liquid-phase NMR experiments no elimination of anisotropy is required since the intrinsic mobility of the nuclei averages out the chemical shift anisotropy (CSA).

In this work, NMR titration experiments were performed to study the decomposition of a host framework that results in the triggered release of a guest reporter molecule.

2.6   Ellipsometry

Ellipsometry is a specular optical technique that measures the change of polarization of light upon reflection or transmission of a sample. In general, linearly or circularly polarized light is used which is usually elliptically polarized after reflection at an interface. Ellipsometry is commonly used to measure optical constants (*e.g.*, refractive index, absorption coefficient, complex permittivity) or film thicknesses for single layers or complex multilayer stacks ranging from a few angstroms to several micrometers with an excellent accuracy. The schematic setup is depicted in Figure 2-6.
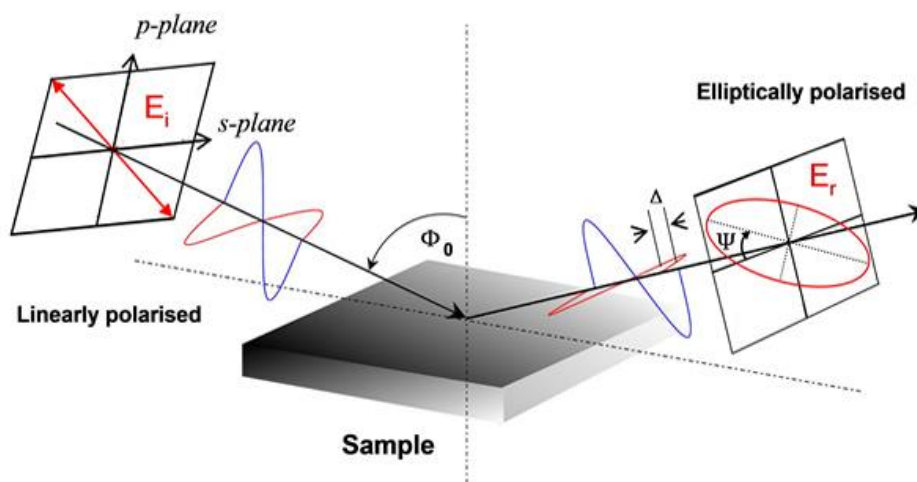

Figure 2-6   Schematic setup of an ellipsometric measurement.[11]

Electromagentic light is emitted by a light source and linearly polarized before it is reflected off a sample. After reflection the light is elliptically polarized due to different reflectivity for the components of the incident beam that are either perpendicular (s-plane) or parallel (p-plane) to the plane of incidence. The

amplitudes of the s and p components, after reflection and normalization to their initial values, are denoted by r_s and r_p, respectively (Figure 2-7).
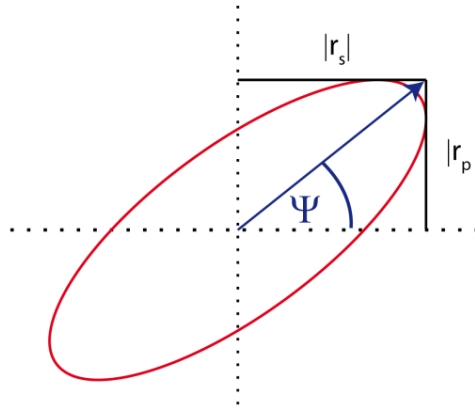
Figure 2-7   **Field vector of elliptically polarized light and the amplitudes of the different components r_s and r_p.**

Ellipsometry measures the complex reflectance ratio ρ that is described by the fundamental ellipsometric equation:

$$\rho = \frac{r_p}{r_s} = \tan\psi e^{i\Delta}$$

Thus, tan Ψ is the amplitude ratio upon reflection, and Δ is the phase shift (difference). Since ellipsometry is measuring the ratio of two values, it is very accurate and reproducible, relatively insensitive to scattering and fluctuations, and requires no standard sample or reference beam. Ellipsometry is an indirect method, *i.e.*, in general the measured Ψ and Δ cannot be converted directly into the optical constants of the sample. Normally, a layer model must be established, which considers the optical constants (refractive index or dielectric function tensor) and thickness parameters of all individual layers of the sample including the correct

layer sequence. Using an iterative procedure (least-squares minimization), the unknown optical constants and thickness parameters are varied, and Ψ and Δ values are calculated using the Fresnel equations. The calculated Ψ and Δ values that best match the experimental data provide the optical constants and thickness parameters of the sample. In spectroscopic ellipsometry (SE) a broad-band light source is employed, which covers a certain spectral range in the infrared, visible or ultraviolet region. Thus the complex refractive index or the dielectric function tensor in the corresponding spectral region can be obtained, which gives access to a number of fundamental physical properties.

Here spectroscopic ellipsometry was employed to determine both the optical properties as well as the layer thicknesses of two dielectric materials with different porosities. More advanced studies were performed by means of ellipsometric vapor sorption experiments to investigate the response of multistacked architectures towards external stimuli.

2.7   Physisorption

Sorption measurements are an effective technique for the determination of the porosity, the surface area or the pore size distribution of a porous solid.[12, 13] In general, the gas referred to as adsorptive, which is in equilibrium with the adsorbate (the adsorbed gas molecules), is kept at a constant temperature near to its boiling point and the increase in the adsorbed volume is measured as a function of the partial pressure. Thus, the adsorption, *i.e.*, the enrichment of an adsorptive

gas, usually N_2, Ar, Kr, on an adsorbent (solid) is examined. Most commonly, physisorption (physical sorption) is performed to investigate the capacity and pore-volume of a material. The weak interactions occurring during physisorption measurements are mainly van-der-Waals forces such as dipole-dipole interactions, London forces or hydrogen bonding. Chemisorption, however, involves the formation of covalent chemical bonds between the adsorbate and the surface and is thus less preferred for the determination of porosity.

During the measurement an equilibrium state is established between the adsorptive gas and the adsorbate depending on the relative pressure *p/p0*. Equilibrium isotherms are obtained by plotting the adsorbed volume as a function of *p/p0*. Adsorption isotherms can be classified as one of six types according to the IUPAC[14] classification (Figure 2-8, Table 2-1), each type being characteristic for certain material types.
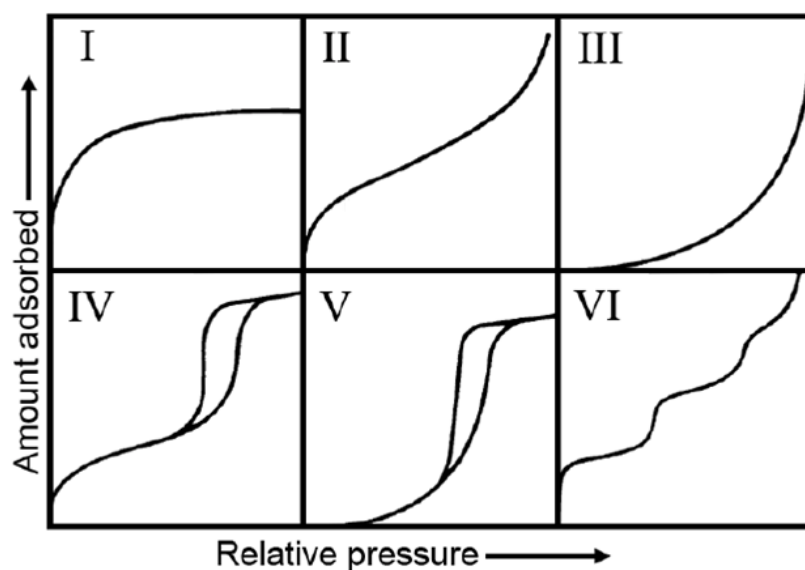
Figure 2-8   IUPAC classification of gas sorption isotherms showing the most prominent types I-VI.[14]

Table 2-1   Interpretation of IUPAC isotherms.

Type	Interpretation
I	Chemisorption isotherms or physisorption in microporous materials, where a plateau is reached after filling of the micropores
II	Nonporous and macroporous materials with high energies of adsorption
III	Nonporous and macroporous materials with low energies of adsorption
IV	Mesoporous materials with high energies of adsorption, often contain hysteresis loops attributed to mesoporosity
V	Mesoporous materials with low energies of adsorption, often contain hysteresis loops attributed to mesoporosity
VI	Several possibilities, including multiple pores sizes and multiple distinct energies of adsorption

Microporous materials generally exhibit the shape of type I isotherms. A characteristic property is the steep increase of adsorbed volume at very low relative pressures corresponding to the formation of an adsorbate "monolayer" within the micropores of the material. As the dimensions of the pores are approximately in the size-range of the adsorbate, the monolayer formation can be considered equivalent to a complete filling ("micropore filling") of the pores, and no significant further increase of adsorbed volume is observed until a high pressure close to $p/p_0 = 1$ is reached. If the adsorbent particles have nano-scale dimensions, the interparticle voids may fall into the mesoporous range, leading to textural porosity. Hence, a steady increase in adsorbed volume is observed after micropore filling.

For the interpretation of adsorption isotherms several different models can be adopted. The two principal methods currently applied in the study of porous materials are the Brunauer-Emmett-Teller (BET) theory and the density functional theory (DFT). The BET theory is widely used for porous materials and based on a number of simplifying assumptions in order to extend the Langmuir model to multilayer adsorption: First, particles in a layer do not interact and second the adsorption enthalpy for the first monolayer is different from those of the added layers, because of adsorptive-adsorbent interactions. For low partial pressures ($p/p_0 < 0.3$) the following BET equation can be expressed in a linear form:

$$\frac{p/p_0}{n \cdot (p - p_0)} = \frac{1}{n_m \cdot C} + \frac{C - 1}{n_m \cdot C} \frac{p}{p_0}$$

p/p_0 : relative pressure; p_0 is the saturation pressure of the adsorptive

n: amount of adsorbate

n_m: monolayer capacity

C : BET constant

Thus, the BET plot of $(p/p_0)/[n(1-p/p_0)]$ versus p/p_0 gives a linear correlation with a slope of $(C-1)/n_m C$ and intercept $1/n_m C$. Based on these data and the cross-sectional area of an adsorbate molecule, the specific surface area A_S of the adsorbent can be calculated according to

$$A_S(BET) = n_m \cdot N_A \cdot a_m$$

N_A: Avogadro constant

a_m: cross-sectional area of the probe molecule

In a strict sense, the BET method is not applicable for microporous solids, because the diameter of the micropores is too small to allow multilayer formation.[15] However, the BET theory was shown to be consistent for relative pressures below $p/p_0 = 0.1$ and is thus used for microporous materials to deliver comparative values.

Metal-Organic Frameworks (MOFs) usually exhibit a microporous (or sometimes mesoporous) character and can feature rough surfaces. Many of these materials have been shown to exhibit very large BET surface areas. It has been suggested that

adsorption occurs through a pore filling mechanism rather than by layer formation,[16] thus it is unclear whether the reported BET surface area numbers are really meaningful.[17] By comparison of the geometric surface area calculated from the particular crystal structures with the simulated adsorption isotherms, deduced from grand canonical Monte Carlo simulations, Walton *et al.* could demonstrate that the BET theory is applicable for the evaluation of sorption data of MOFs.[17]

In addition to the macroscopic theories used for describing adsorption, there are several microscopic models including molecular simulations (Monte Carlo simulations), molecular dynamics, statistical mechanics techniques, and density functional theory (DFT), which yield more realistic results. The validity of the DFT method has already been shown, using various reference materials. However, specific knowledge about the structure and surface atoms of the investigated materials is required in order to correctly calculate the forces and input parameters of these models. Therefore, such approaches cannot be applied to unknown surfaces, and the macroscopic theories are still frequently employed.

There are two principal experimental methods for the collection of adsorption isotherms, that is, volumetric and gravimetric techniques. In both cases, the adsorbent is held at a constant temperature, which is usually at or near the boiling point of the adsorptive, *i.e.*, by cooling with liquid nitrogen in the case of nitrogen sorption. By step-wise increase of the adsorptive pressure followed by equilibration of the system, the increase in the amount of adsorbed molecules can be measured. Volumetric measurements are carried out by dosing a certain gas volume into the sample chamber, and by measuring the pressure decrease due to adsorption in the

pores. In contrast, in gravimetric systems the mass gain of the sample is recorded after each addition step of the adsorptive.

2.8   Quartz-crystal microbalance

The Quartz Crystal Microbalance (QCM) is a gravimetric technique that allows for a highly accurate determination of the mass per unit area by measuring the change of frequency of a quartz crystal resonator. Even very small mass changes such as those occurring during the gas or vapor sorption in thin films can be recorded. The central part is a thin AT-cut quartz crystal with key-hole electrodes patterned on both sides (Figure 2-9).
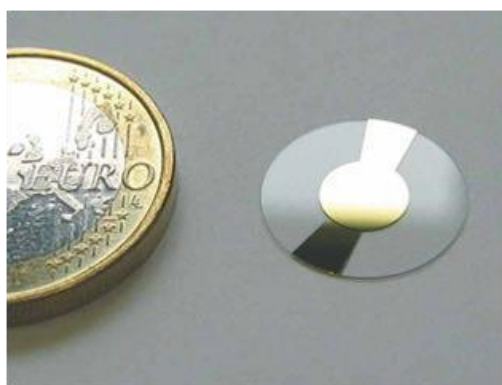
Figure 2-9   **Quartz crystal microbalance chip (XA 1600, KVG Quartz Crystal Technology) next to a 1 Euro coin.**[18]

The working principle of the QCM chip is the piezoelectric effect, which was first described in 1880 by Jacques and Pierre Curie. Piezoelectric materials are charging if a force such as traction, torsion or pressure is applied on them. The inverse piezoelectric effect is defined as the mechanical deformation of these materials

upon application of an electric field. For quartz crystals, *i.e.*, the QCM chips, application of an alternating electric field leads to an oscillation of the chip, in the present work with a resonance frequency of $f_0 \sim 10$ MHz. The change of this fundamental frequency upon mass changes on the QCM chip was analyzed in 1959 by G. Sauerbrey.[19] The relation between mass change and frequency change is given in the so-called Sauerbrey equation:

$$\Delta f = -\frac{2f_0^2 \Delta m}{A\sqrt{\rho_q \mu_q}}$$

Δf : frequency change

Δm : mass change

f_0 : resonance frequency of the basic mode of the crystal

A : piezo-active area of the electrode

ρ : density of quartz

μ : shear modulus of quartz

This gives a frequency change of 1 Hz corresponding to a mass loading of $4.42 \cdot 10^{-9}$g onto a surface area of 1 cm^2 on a quartz disc. As mentioned above, this very high gravimetric sensitivity can be employed to record the uptake of an adsorptive, *e.g.*, any gas or liquid by a porous material. The porous material is usually prepared as a thin film on the QCM chip. The experimental setup given in Figure 2-10 refers to using a liquid sorptive; the usual applied temperature is 25 °C. The control of the partial pressure of the adsorptive in the sample chamber is

achieved by diluting the evaporated compound with a carrier gas, for example nitrogen, using digital mass-flow controllers and a calibrated gas-flow system.
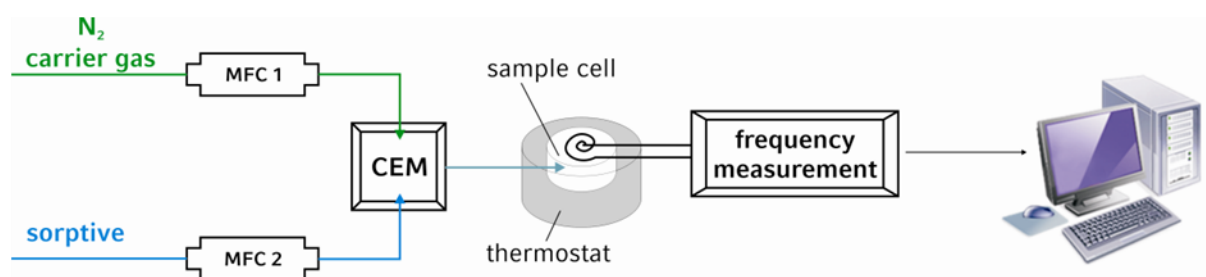

Figure 2-10 **Experimental set-up for the collection of sorption data with the help of a QCM device: the carrier gas (N_2) and the sorptive are dosed with the help of two digital mass flow controllers (MFC 1 and 2) and are mixed in the controlled evaporation mixer (CEM) to be transported into the sample chamber, the temperature of which is controlled by the thermostat. The data collected during the frequency scans are transferred to a computer.**[18]

2.9   Thermogravimetric Analysis and Differential Scanning Calorimetry

Thermogravimetric analysis (TGA) and differential scanning calorimetry (DSC) are two complementary techniques used to detect mass changes as a function of temperature or time. Depending on the desired information, the heating can be performed under gas flow of reactive or inert atmospheres, *i.e.,* to control or prevent combustion *via* oxidative processes.

In a typical experiment the sample is placed into an adjustable oven and the weight changes at different temperatures are measured by a coupled thermobalance. The mass loss resulting either from desorption of adsorbed molecules, the evaporation

of volatile compounds or the decomposition of the material is recorded simultaneously. The thermogravimetric analysis of porous compounds also enables the quantification of adsorbed water or template molecules and provides information about their release.

A complementary thermoanalytical technique for determining the enthalpy changes during endo- or exothermic reactions is Differential Scanning Calorimetry (DSC). The difference of heat needed to hold a sample and a reference at the same temperature is measured. For this purpose, the amount of energy required for heating the sample is measured as a function of temperature. Thus a signal directly proportional to the changes in energy or heat capacity can be detected. DSC yields information about exothermic and endothermic processes occurring in the sample during heating, *e.g.,* combustion steps, phase transitions, and evaporation of adsorbed molecules.

2.10   References

[1]   M. F. Toney, *Encyclopedia of Materials Characterization - Surfaces, Interfaces, Thin Films; XRD - X-Ray Diffraction*, Manning Publications, Greenwich, **1992**.

[2]   D. Brandon and W. D. Kaplan, *Microstructural characterization of materials*, John Wiley & Sons Ltd., Chichester, **2008**.

[3]   J. B. Bindell, *Encyclopedia of Materials Characterization - Surfaces, Interfaces, Thin Films; SEM - Scanning Electron Microscopy*, Manning Publications, Greenwich, **1992**.

[4]   R. M. Barrer, *Zeolites and Clay Minerals as Sorbents and Molecular Sieves*, **1978**.

[5]   J. N. Cox, *Encyclopedia of Materials Characterization - Surfaces, Interfaces, Thin Films; FTIR - Fourier Transform Infrared Spectroscopy*, Manning Publications, Greenwich, **1992**.

[6]   W. B. White, *Encyclopedia of Materials Characterization - Surfaces, Interfaces, Thin Films; Raman Spectroscopy*, Manning Publications, Greenwhich, **1992**.

[7]   M. P. Suh, H. J. Park, T. K. Prasad and D.-W. Lim, *Chem. Rev.*, 2012, **112**, 782-835.

[8]   P. W. Atkins, *Physikalische Chemie*, Wiley-VCH, Weinheim, **2001**.

[9]   M. G. Kanatzidis, *Adv. Mater.* , 2007, **19**, 1165-1181.

[10]   H. Eckert, *Encyclopedia of Materials Characterization - Surfaces, Interfaces, Thin Films; - Solid State Nuclear Magnetic Resonance*, Manning Publications, Greenwich, **1992**.

[11]   J. Lee, O. K. Farha, J. Roberts, K. A. Scheidt, S. T. Nguyen and J. T. Hupp, *Chem. Soc. Rev.*, 2009, **38**, 1450.

[12]   F. Rouquerol, J. Rouquerol and K. Sing, *Adsorption by Powders & Porous Solids - Principles, Methodology and Application*, Academic Press, San Diego, **1999**.

[13]   J. B. Condon, *Surface Area and Porosity Determinations by Physisorption: Measurements and Theory*, Elsevier, Amsterdam, **2006**.

[14]   K. S. W. Sing, D. H. Everett, R. A. W. Haul, L. Moscou, R. A. Pierotti, J. Rouquerol and T. Siemieniewska, *Pure Appl. Chem.* , 1985, **57**, 603-619.

[15]   A. W. Adamson and A. P. Gast, *Physical Chemistry of Surfaces*, John Wiley & Sons, New York, **1997**.

[16]   J. L. C. Rowsell and O. M. Yaghi, *J. Am. Chem. Soc.*, 2006, **128**, 1304-1315.

[17]   K. S. Walton and R. Q. Snurr, *J. Am. Chem. Soc.*, 2007, **129**, 8552-8556.

[18]   C. Scherb, *Controlling the Surface Growth of Metal-Organic Frameworks*, Ludwig-Maximilians Universität, München, **2009**.

[19]   G. Sauerbrey, *Zeitschriften für Physik*, 1959, **155**, 206-222.

3 Extending the Structure-directing Concept to Functionalized Metal-organic frameworks

This chapter is based on the publication indicated below:

Camilla Scherb,[a] Jennifer J. Williams,[b] Florian M. Hinterholzinger,[a] Sebastian Bauer,[c] Norbert Stock[c] and Thomas Bein*[a], *Journal of Materials Chemistry* 2011, **21**, 14849 − 14856.

Abstract

The generation of thin films of oriented functionalized metal–organic frameworks (MOFs) on self-assembled monolayers was achieved via direct growth from solution. Specifically, the direct growth from solvothermally pretreated synthesis solutions of two different MOF structures with amino functionality was investigated: the flexible framework structure NH_2–Fe–MIL-88B and the mesoporous MOF NH_2–Fe–MIL-101 with its remarkably large unit cell. Both MOF structures can be grown in a highly oriented fashion on self-assembled monolayers of 16-mercaptohexadecanoic acid on gold. With the help of a quartz crystal microbalance we demonstrate that the introduction of amino groups into the framework strongly affects the host–guest interactions towards ethanol molecules: thin films of NH_2-Fe–MIL-88B show a

significantly higher uptake of ethanol than unfunctionalized Fe−MIL-88B films. In situ XRD experiments during sorption of ethanol showed that the amino group does have an impact on the cell parameters of the structure, but the flexibility ("breathing") during ad- and desorption of ethanol is similar for the functionalized and the unfunctionalized structures. It is anticipated that the implementation of chemical functionalities into oriented MOF films will lead to selective host−guest interactions that are of key importance for chemical sensing and other applications.

3.1   Introduction

Extending the concept of directing the structure and orientation of MOFs using self-assembled monolayers for surface functionalization, we now ask if we can implement chemical functionalities into films of oriented MOF structures. For example, uncoordinated functional groups on the organic ligands could offer tunable interactions with encapsulated species. This could result in more selective materials with a higher capacity in fields such as chemical sensing, gas separation or storage.[1]
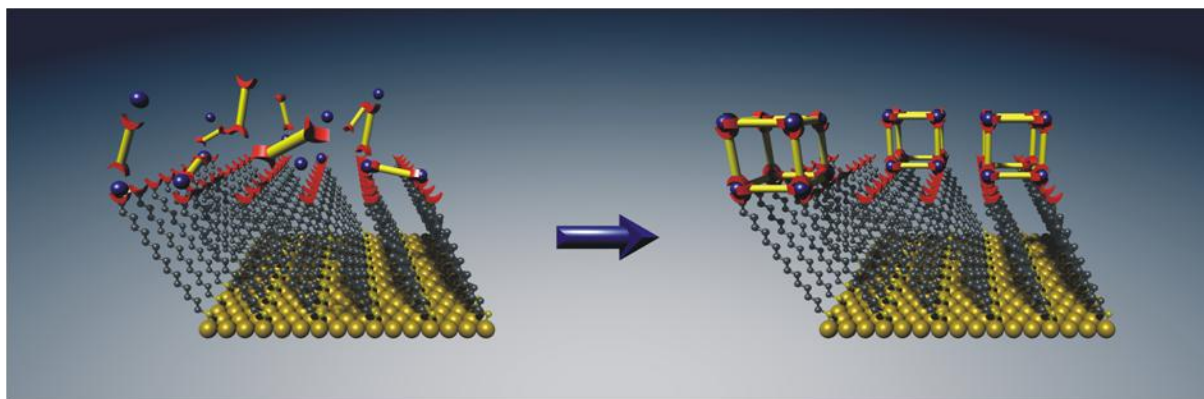
Scheme 3-1   Concept of direct growth of MOFs on SAM-functionalized gold substrates.

There are two different approaches to implementing functionalities in MOFs. The first employs organic ligands with additional functional groups that are not involved in coordination of the metal centers but rather change the functionality of the pore walls. Kitagawa *et al.* have focused their research efforts on this challenge. They modified the organic linkers in such a way that the host–guest interactions desired for a particular application were obtained by inserting unsaturated metal-centres.[2] In a different study, the same group reports the implementation of hydrogen-bonding groups for specific host–guest interactions within dynamic porous coordination polymers.[3] The second approach refers to the post-synthetic modification of the organic linkers, which in most cases requires the presence of at least one modifiable functional group.[4, 5] For example, Kim and co-workers showed that the pendant pyridyl groups in a chiral zinc network could be methylated.[6] Burrows *et al.* reported a post-synthetic modification starting from an aldehyde-functionalized dicarboxylate to a hydrazone ligand.[7] In other studies it has been demonstrated that the amino groups in 2-amino-1,4-benzenedicarboxylate MOFs can be converted into amides, urethanes,[8-10] or salicylidenes.[11]

Following the first approach, Bauer *et al.* were able to obtain powders of the amino-functionalized isoreticular compounds of the previously reported structures MIL-53, MIL-88B and MIL-101 (MIL = Matériaux Institute Lavoisier) by employing highthroughput synthetic methods.[12] Their study revealed that the insertion of functional groups in the organic linker can strongly change the synthesis conditions required for a desired structure. It was found that the nature of the reaction medium has the most profound impact on structure formation. Furthermore, the concentration of the starting mixture (*i.e.,* the solvent content) and the temperature were also identified as key parameters for the formation of the different competing hybrid phases. Building on our previous results on the structure-directed and oriented growth of the unfunctionalized MIL-88B crystals on carboxylate terminated SAMs,[13] we report here the direct growth of amino-functionalized oriented MILs on SAMs. The sorption behavior of these films was investigated using a quartz crystal microbalance (QCM).

3.2   Experimental

Preparation of self-assembled monolayers on gold

The gold-coated slides (glass slides (10×13 mm^2) coated with 10 nm Ti/100 nm Au by electron-beam evaporation, *Olympus AG*) were cleaned in ethanol and methanol. The cleaned gold slides were immersed in a 1 mM ethanolic solution (6 pieces in 30 mL) of 16-mercaptohexadecanoic acid (MHDA; 90%, *Aldrich*) and left at RT for

48 h. The SAM-functionalized gold slides were repeatedly washed with ethanol, and stored in fresh absolute ethanol until needed.

Synthesis of NH$_2$–Fe–MIL-88B

In a glass reactor, 1.00 g (5.52 mmol) of 2-amino-1,4-benzenedicarboxylic acid (99%, *Aldrich*) were dissolved in 15 mL dimethylformamide (DMF) (p.a., *Acros Organics*). The amount of 2.784 g (11.04 mmol) of FeCl$_3 \cdot$ 6H$_2$O (p.a., *Merck*) was added to the solution. The sealed-glass reactor was left for 24 h in a preheated oven at 150 °C. After cooling the synthesis mixture to room temperature, the crystalline product was filtered and stored for further characterization.

Preparation of the crystallization solution for film growth of NH$_2$–Fe–MIL-88B on –COOH terminated SAMs

In a 25 mL glass reactor, 0.25 g (1.4 mmol) of 2-amino-1,4-benzenedicarboxylic acid (99%, *Aldrich*) were dissolved in 15 mL dimethylformamide (DMF) (p.a., *Organics*). The amount of 0.746 g (2.8 mmol) FeCl$_3 \cdot$ 6H$_2$O (p.a., *Merck*) and 1.38 mL of 1 M HCl was added to the clear solution. The sealed-glass reactor was left for 24 h in a preheated oven at 150 °C. After cooling the synthesis mixture to room temperature, the amorphous product was removed by filtration and the filtered solution was used for the growth of thin films.

Film-synthesis of NH$_2$–Fe–MIL-88B

The SAM-functionalized gold-slides were placed upside-down on Teflon®-supports into the filtered synthesis solution of NH$_2$–Fe–MIL-88B (3 pieces in 15 mL). The growth step took place at room temperature in a closed glass reactor. Immersion times were varied between 4 d and 11 d.

Synthesis of bulk NH$_2$–Fe–MIL-101 and preparation of the crystallization solution for film growth of NH$_2$–Fe–MIL-101

In a 25 mL glass reactor, 0.225 g (1.24 mmol) of 2-amino-1,4-benzenedicarboxylic acid (99%, *Aldrich*) were dissolved in 15 mL dimethylformamide (DMF) (p.a., *Acros Organics*). The amount of 0.675 g (2.5 mmol) FeCl$_3$ · 6H$_2$O (p.a., *Merck*) was added to the clear solution. The sealed glass reactor was left for 24 h in a preheated oven at 110 °C. After cooling the synthesis mixture to room temperature, the crystalline product was filtered off and stored for further characterization. The filtered solution was used for the growth of thin films.

Film growth of NH$_2$–Fe–MIL-101

The SAM-functionalized gold-slides were placed upside-down on Teflon®-supports into the filtered synthesis solution of NH$_2$–Fe–MIL-101 (3 pieces in 15 mL). The growth step took place at room temperature in a closed glass reactor. Immersion times were varied between 3 d and 10 d.

3.3   Characterization

X-Ray diffraction (XRD) measurements of powders were performed on a STOE powder diffractometer in transmission geometry (Cu-Kα_1, $\lambda = 1.5406$ Å), those of films using a Bruker D8 in θ–θ geometry (Cu-Kα_1, $\lambda = 1.5406$ Å; Cu-Kα_2, $\lambda = 1.5444$ Å). A specially designed sample cell, the details of which are given in our previous publication[14] was used for the measurement of X-ray diffraction patterns under controlled partial pressures of a sorptive. The gas input in the lower part of the cell is connected to the flow-controlling system described in the ESI†. The cell was positioned onto the sample holder of a Scintag XDS 2000 X-ray diffractometer (Cu-Kα radiation, $\lambda = 1.54$ Å) measuring in θ–θ geometry. The powder patterns were recorded at angles between 5° and 35° 2θ with an interval of 0.01° 2θ and at a scan rate of 5° to 10° 2θ per minute. Characterization of the self-assembled monolayers was performed by reflection absorption infrared (RAIR) spectroscopy, using a Bruker IFS 66v FTIR spectrometer. The sample chamber with a high performance variable angle reflection accessory (A-513) was maintained at 2 mbar during the entire measurement by means of an Edwards rotary-pump. In a typical measurement on gold surfaces, an angle of incidence of 83° to the surface normal was used. A cleaned gold slide was measured as background prior to the measurements. The morphology of the crystals was studied using a JEOL JSM-6500F scanning electron microscope.

3.4   Results and discussion

For the direct growth of the amino-functionalized MOF crystals, the gold substrates were modified with monolayers of $HS(CH_2)_{16}COOH$ following known procedures[15, 16] (see Experimental section). The formation of the self-assembled monolayers was confirmed by RAIR, as shown in Figure 3-1.
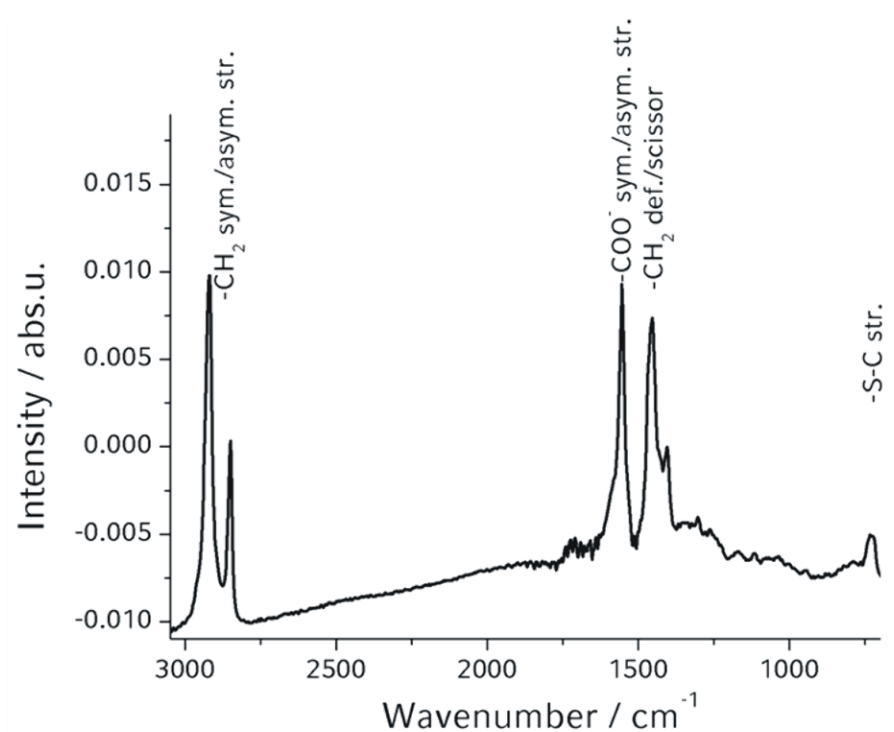

Figure 3-1   RAIR-spectrum of the MHDA self-assembled monolayer on a gold substrate.

The absorption band at 1554 cm^{-1}, characteristic for the presence of a carboxylate group, is indicated in the spectrum. The methylene groups of the aliphatic chains present high-frequency modes at 2920 and 2850 cm^{-1} associated with the

asymmetric and symmetric C−H stretching vibrations, respectively; we also observe the band at 721 cm^{-1}assigned to the stretching vibration of the S−C bond.

**Direct growth of NH$_2$–Fe–MIL-88B**

Here we demonstrate the direct growth of an oriented aminofunctionalized MOF, NH$_2$–Fe−MIL-88B on functionalized Au (111) substrates. The hexagonal 3D structure of NH$_2$–Fe−MIL-88B is built up from trimers of FeO$_6$ octahedra linked to benzenedicarboxylate anions. Thus the 3D pore system of MIL-88B consists of tunnels along the *c* axis connected by bipyramidal cages.[17] The structure of MIL-88B as well as the isoreticular amino-functionalized form is well known for their structural flexibility, which is reflected by large changes in their lattice parameters depending on the contents of the pores.[12, 13, 17-19] In a previous study, we reported the oriented growth of Fe−MIL-88B crystals on self-assembled monolayers. The X-ray diffractograms of the crystals grown on the functionalized surface clearly exhibit [001] orientation, as only the 002 and the 004 reflections of Fe−MIL-88B are observed (Figure 3-2, right).[13] As shown in the XRD patterns of the synthesized film samples (depicted in Figure 3-2 (left)), it was possible to obtain highly oriented films of NH$_2$−Fe−MIL-88B crystals on carboxylate-terminated self-assembled monolayers. As with the unfunctionalized Fe−MIL-88B structures, we obtained oriented growth in [001] direction. This can be seen by comparing the powder pattern of bulk NH$_2$−Fe−MIL-88B crystals with the diffraction patterns of the thin films of Fe−MIL-88B (Figure 3-2).
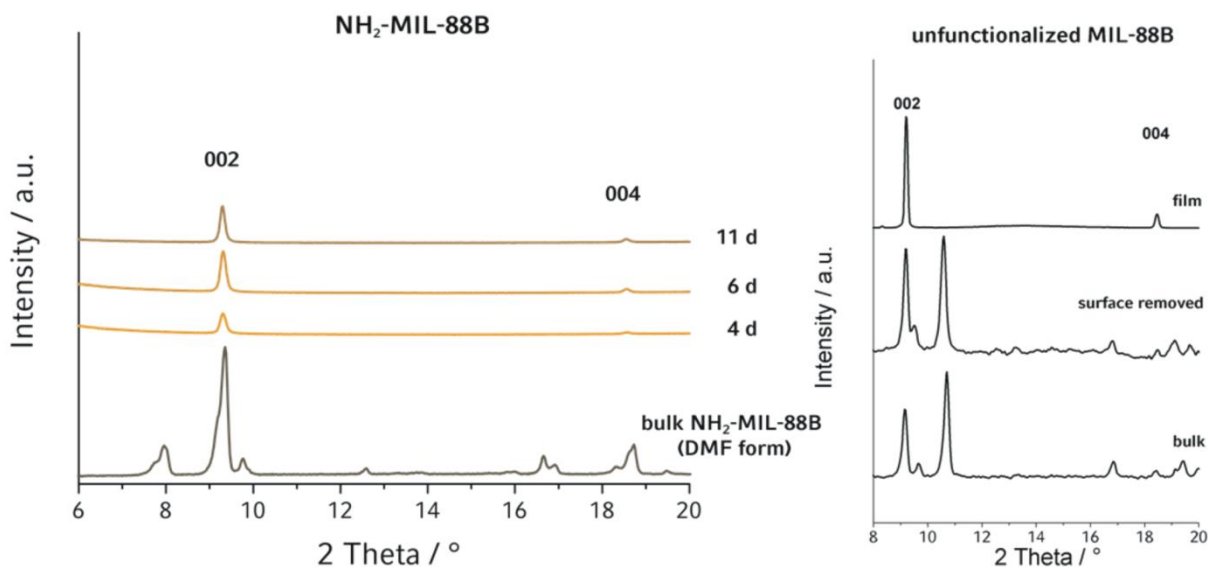
Figure 3-2   Left: X-ray diffraction measurements of crystals grown on functionalized gold substrates compared to the XRD pattern of bulk NH₂–Fe–MIL-88B crystals. The immersion time of the substrates in the crystallization solution varied between 4 d and 11 d; right: XRD pattern of film on gold substrate (top), powder pattern of the removed crystals (center), and powder pattern of bulk Fe–MIL-88B (bottom).

The synthesis conditions for the first successful growth of NH₂–Fe–MIL-88B were determined starting from the synthesis of Fe–MIL-88B thin films and substituting the benzenedicarboxylic acid by 2-amino-benzenedicarboxylic acid. A second step of solvothermal treatment was found not to be necessary because, contrary to the unfunctionalized system, precipitation of NH₂–Fe–MIL-88B at room temperature was already observed after one solvothermal step. However, the growth of NH₂–Fe–MIL-88B crystals was observed to be much slower than that of Fe–MIL-88B. This led us to investigate the effect of pH-variations of the crystallization solution on crystal growth. Different volumes of 1 M HCl were added to the initial reaction mixture, resulting in the formation of amorphous precipitation products during the

post-solvothermal crystallization step at room temperature. The product of these reactions on the SAM-functionalized gold substrates is $NH_2-Fe-MIL$-88B. The X-ray diffraction patterns of directly grown $NH_2-Fe-MIL$-88B crystals on carboxylate terminated SAMs are presented in Figure 3-3.
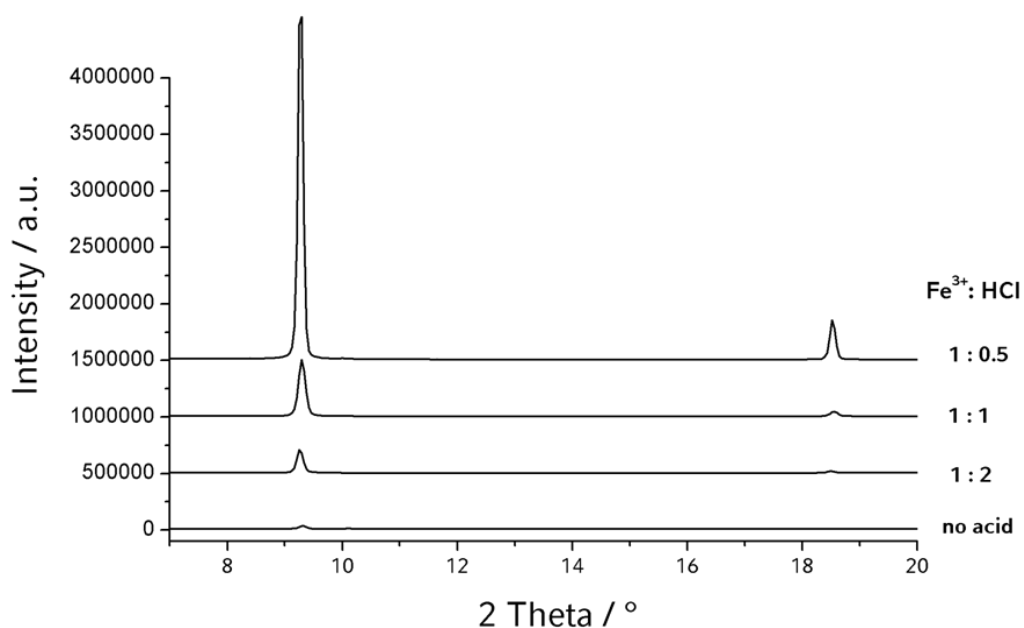
Figure 3-3   **X-Ray diffraction patterns of $NH_2-Fe-MIL$-88B thin films grown from crystallization solutions with different HCl content. The immersion time of the substrates in the crystallization solution was 11 d for all samples. Graphs are offset.**

Compared to the direct growth without addition of HCl, peak intensities of all samples from acidified batches are much more intense. We observe a maximum intensity for the 002 and the 004 reflections for a molar ratio of Fe^{3+} : HCl = 1 : 0.5. Despite this improved crystal growth on the surface, the bulk products of both precipitation steps, i.e. at 150 °C and at room temperature, are amorphous.

Bauer *et al.* observed that addition of HCl led to the formation of mixtures of powders of NH_2–Fe–MIL-53 and NH_2–Fe–MIL-88B when water was used as the reaction medium. For DMF as the reaction medium, as in our case, the addition of NaOH favored the formation of NH_2–Fe–MIL-88B over the precipitation of NH_2–MIL-101. The addition of HCl to the synthesis in DMF is not mentioned in the study of Bauer *et al.* We can thus state that as the bulk product of the crystallization at room temperature is amorphous while NH_2–Fe–MIL-88B crystallizes on the functionalized substrates, we observe the catalysis of nucleation of NH_2–Fe–MIL-88B on the surface of the –COOH SAM. These terminal carboxyl groups of the SAM are presumed to mimic the functional groups of the NH_2–BDC ligand. Consequently, it is assumed that the terminal carboxylate groups of the SAM lead to a surface enrichment of metal ions and metal coordination allowing the subsequent attachment of the organic ligands. This interface-catalysed enrichment of the MOF building blocks is thought to enhance the nucleation rate of the MOF structure on the surface. To further compare these results to our previous study on Fe–MIL-88B, SEM images were taken of the samples synthesized with and without addition of HCl (Figure 3-4).
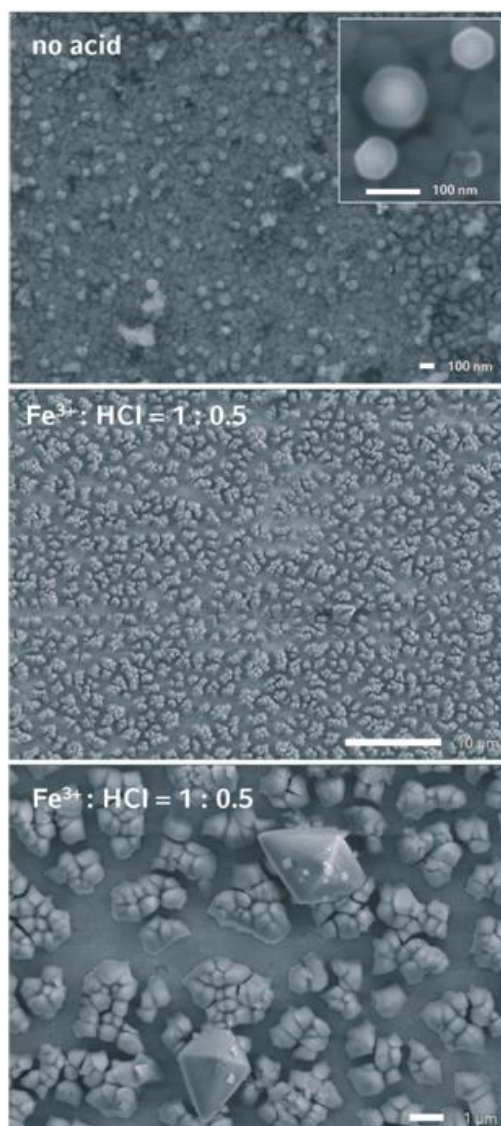
Figure 3-4   Scanning electron micrographs of NH$_2$–Fe–MIL-88B crystals grown for 11 d on carboxylate terminated substrates.

It is obvious that direct growth of NH$_2$–Fe–MIL-88B takes place, even without addition of HCl. This can be seen from the magnified image in Figure 3-4 (top). The XRD data shown in Figure 3-2 also indicate that direct growth is occurring. However, even after longer immersion times of 11 d, only a few crystals have formed on the surface indicating that crystal growth had stopped at some point. In

contrast, the samples grown with addition of HCl show intergrowth of crystals and

almost the complete sample surface is covered. The cracks between the islands of

crystals can be attributed to both the contraction of the flexible crystals during

drying after synthesis in DMF as well as to shrinkage resulting from the ultra-high

vacuum (UHV) in the SEM chamber. The homogeneity of the dense coatings is

proven by optical light microscopy in addition to atomic force microscopy. The

images clearly show that the cracks between the crystals are due to the UHV

applied during scanning electron microscopy (see Figure 3-5 and Figure 3-6).
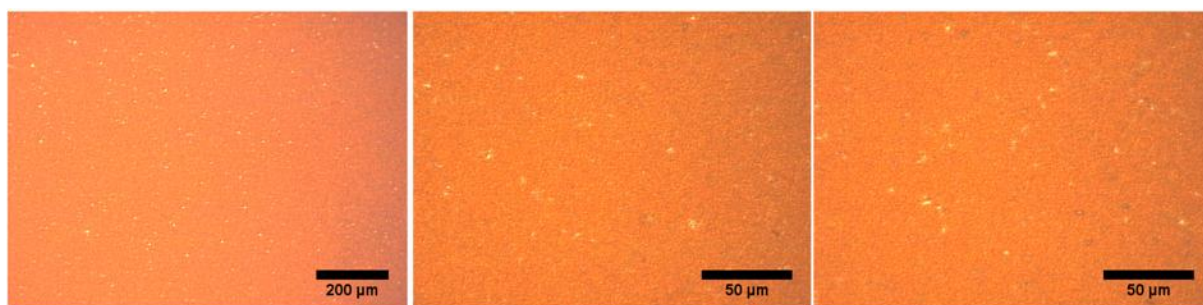
Figure 3-5   **Optical light microscope images of NH$_2$-MIL-88B thin films with different magnifications (left: x10 objective, middle: x50, right: x50) illustrating the formation of homogeneous and densely packed thin films. No obvious cracks are visible prior to an exposure to vacuum.**
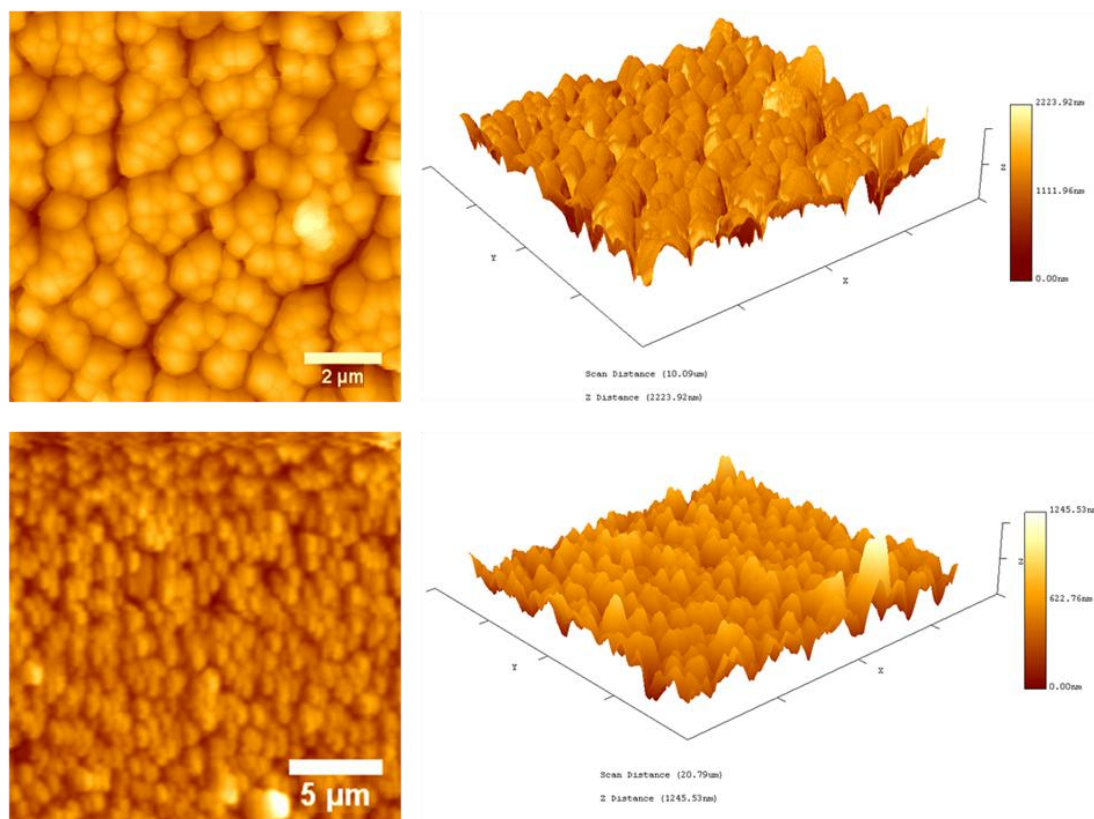
Figure 3-6   Atomic force micrographs of NH_2-MIL-88B thin films prepared from the batch containing a HCl content of Fe^{3+} : HCl = 1 : 0.5. The AFM images show a rather dense layer of intergrown NH_2-MIL-88B crystals completely covering the gold surface (left column: top view image; right column: hight field image). AFM pictures are displayed for two differently scaled sections (top: 10 μm, bottom: 20 μm).

In addition, further data on the MOF film thickness for differently prepared NH_2–Fe–MIL-88B batches are provided by scanning electron microscopy (Figure 3-7).
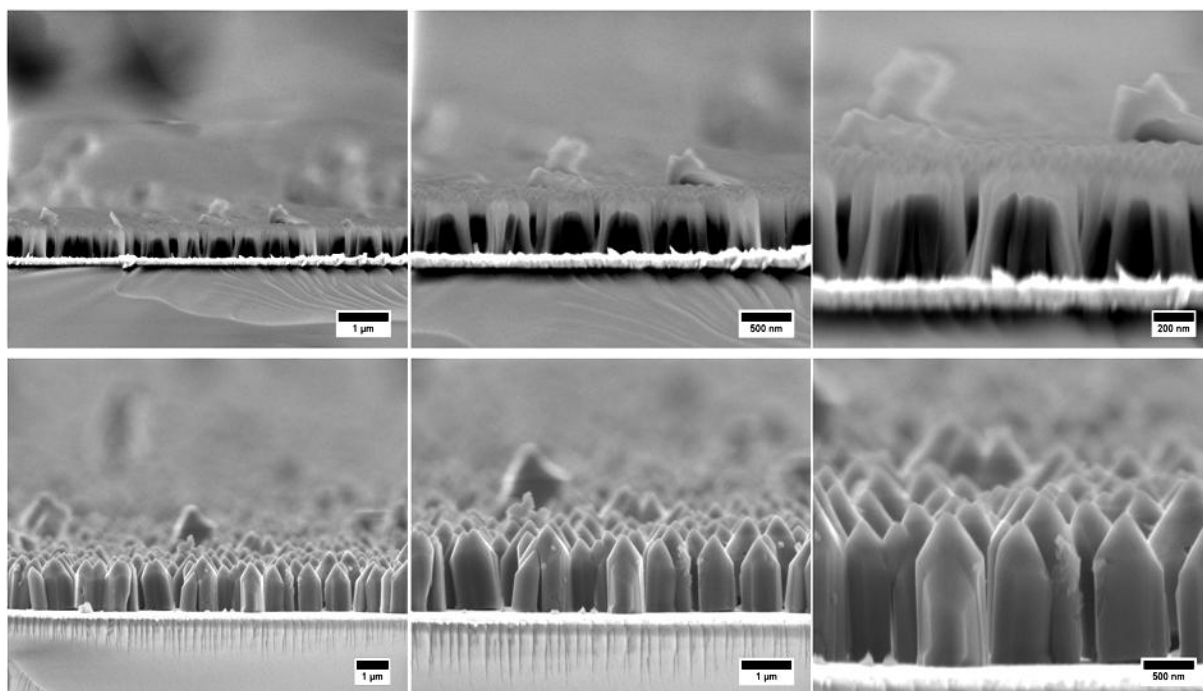
Figure 3-7   Scanning electron micrographs of NH_2-MIL-88B thin films grown from crystallization solutions with different HCl content (top: Fe^{3+} : HCl = 1 : 1; bottom: Fe^{3+} : HCl = 1 : 0.5). The immersion time of the substrates in the crystallization solution was 11 days for both samples. The film thickness obviously depends on the different experimental conditions. As revealed by the cross-sections, an almost three-fold thicker layer of NH_2-MIL-88B crystals is obtained for the batch prepared with Fe^{3+} : HCl = 1 : 0.5.

To study the differences between the functionalized and unfunctionalized Fe−MIL-88B films, sorption measurements with ethanol on a quartz crystal microbalance (QCM) were performed at room temperature. Figure 3-8 represents the ethanol sorption isotherms of thin films of Fe−MIL-88B and NH_2−Fe−MIL-88B. Both isotherms show similar characteristic features.
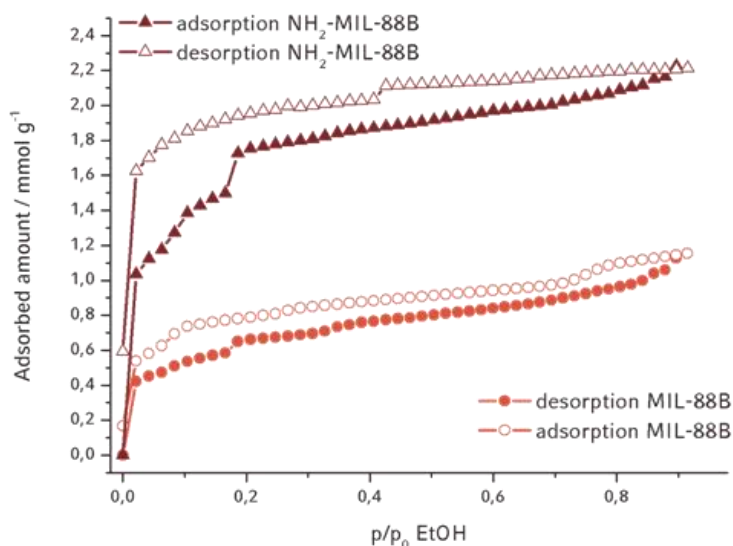
Figure 3-8   Ethanol sorption isotherms of Fe–MIL-88B and NH$_2$–Fe–MIL-88B thin
films, recorded with a quartz crystal microbalance at room temperature.
The fact that the isotherms are not closing completely is attributed to
very long equilibration times for the last desorption step.

The first dosing step of ethanol leads to a steep increase in the amount adsorbed. At
a relative pressure of ethanol of 0.16 there is another step in both isotherms. Both
isotherms show hysteresis, however, this effect seems to be more pronounced for
the amino-functionalized MOF films. The most remarkable difference between both
isotherms is the total adsorbed amount. The adsorbed amount of ethanol recorded
for the NH$_2$–Fe–MIL-88B crystals on the film at a relative pressure of ethanol of 0.16
is almost three times as high as that for the unfunctionalized films. At a relative
pressure of 0.91 the amino-functionalized crystals adsorbed a total amount of
2.21 mmol g^{-1}, while the total adsorbed amount of the MIL-88B crystals is only
1.15 mmol g^{-1}. The observed step in the isotherms and the differences in the

adsorbed amount of ethanol raise the question as to whether these effects can be correlated to structural changes in the flexible MIL-88B structure. To answer this question, the X-ray diffractograms of the film and powder samples of Fe−MIL-88B and of its isoreticular amino-functionalized analogue were recorded during the ad- and desorption of ethanol (sorption@XRD measurements). During the sorption@XRD measurements, which were performed at room temperature, the sorptive concentration in the flow was progressively increased, and then decreased. The results of the sorption@XRD measurements on thin films of Fe−MIL-88B with [001] orientation are depicted in Figure 3-9 (a).
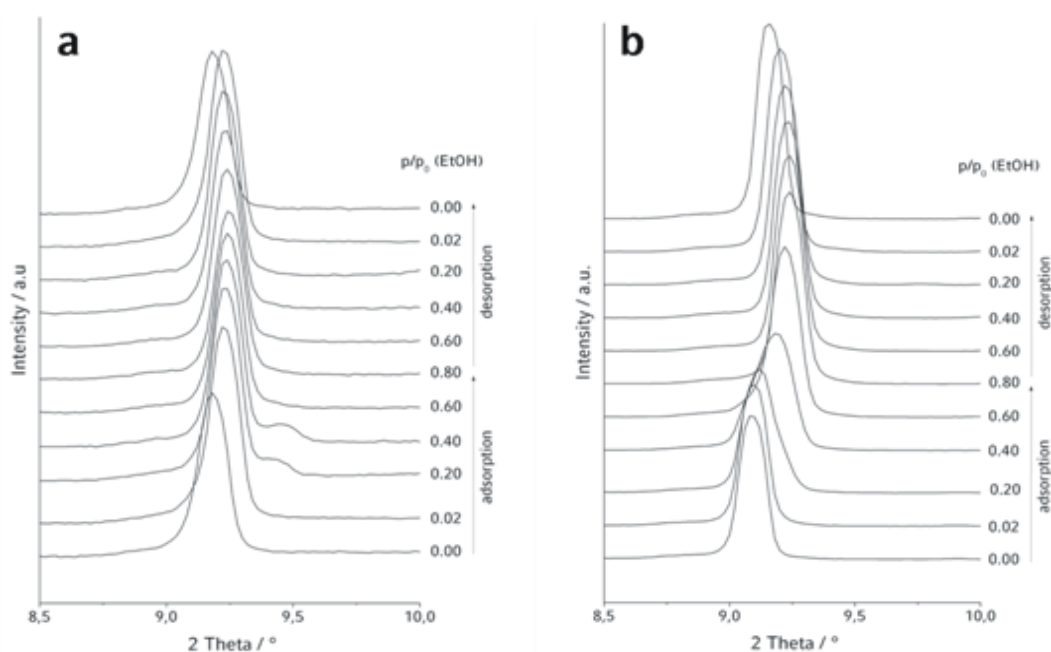

Figure 3-9   **(a) Shift in the 002 reflection of oriented Fe−MIL-88B and (b) NH$_2$−Fe− MIL-88B crystals on MHDA functionalized substrates upon ethanol adsorption and desorption.**

The increase in the relative pressure of ethanol during adsorption evokes a shift in the 002 reflection to higher 2θ values, while during desorption the reflection shifts back towards low 2θ values. The related shifts for ethanol in the functionalized NH_2-Fe$-$MIL-88B are displayed in Figure 3-9 (b). The 002 reflection of oriented Fe$-$MIL-88B crystals shifts by about 0.08° 2θ during the adsorption in the sorption@XRD measurement, whereas the analogous shift for NH_2-Fe$-$MIL-88B is 0.15° 2θ upon adsorption. Upon desorption from the unfunctionalized MOF, the 002 reflection shifts back to its original position, while the shift is not fully reversible with the amino-functionalized crystals. Importantly, these stepwise structural changes do not occur at the same partial pressures for the two MOF systems (see Chapter 9.2, Table S 9-1 and Table S 9-2). As the XRD data from the oriented films only reveal structural changes in one crystallographic direction, the same sorption@XRD measurements were also performed on the corresponding powder samples, prepared as thin layers with random crystal orientation (Figure 3-10 and
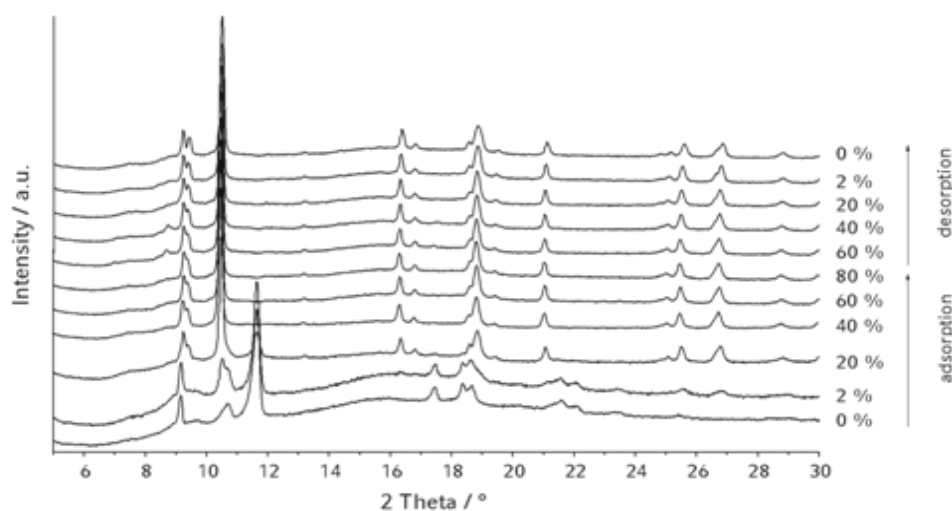
Figure 3-11).
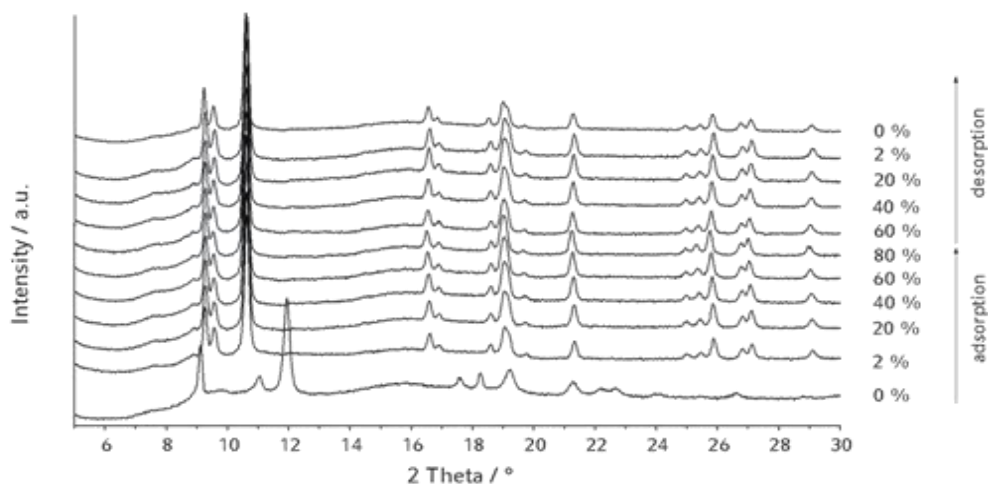
**Figure 3-10   X-Ray diffraction patterns of bulk Fe–MIL-88B prepared as a thin layer of
randomly oriented crystals during the sorption@XRD measurement.**

In agreement with the experiments on the grown films, sorption@XRD measurements of the powder samples show a similar shift in the 002 reflection to smaller 2θ values for the functionalized and unfunctionalized crystals. As shown in Figure 3-10, the complete diffraction pattern changes under a relative ethanol pressure of 0.02, compared to the pattern of the dried powder sample (p/p_0 0.00). During the following adsorption steps no further significant changes in the diffraction pattern are detected. This result is in good agreement with the QCM measurements (Figure 3-8), where a steep increase in the amount adsorbed is shown for the first adsorption step, *i.e.* at p/p_0 0.02; and no large increase in the slope of the isotherm is observed for higher relative pressures. During desorption, the X-ray diffraction patterns show only small shifts in the reflections in the direction of their original position. Thus, under these conditions the small

remaining amount of guest molecules is able to lock the structure of Fe−MIL-88B in its ethanolic form. Extended drying (N$_2$-flow: 100%) at room temperature removes all ethanol guest molecules from the pores (see Chapter 9.2, Figure 9-1).

Figure 3-11 shows the XRD data of the amino-functionalized NH$_2$−Fe−MIL-88B for various relative pressures of ethanol.

Figure 3-11   X-Ray diffraction patterns of bulk NH$_2$−Fe−MIL-88B showing the shift in the reflection positions of a thin layer of randomly oriented crystals during the sorption@XRD measurement.

In contrast to the unfunctionalized structure the diffraction patterns change remarkably during the first two dosing steps to *p/p$_0$* 0.02 and 0.2, respectively. Similar to the unfunctionalized system, beyond this pressure and upon desorption only small changes are observed. The structural changes at *p/p$_0$* 0.02 and 0.2

observed in the sorption@XRD measurements can be directly correlated to the steps in the sorption isotherm of NH_2–Fe–MIL-88B, which occur in the same partial pressure ranges. Quantitative analysis of the structural changes in Fe–MIL-88B, based on the shift in 002, 100 and 101 reflection positions (

Table 3-1), shows a significant increase in the unit cell volume by more than 500 $Å^3$ after the first dosing step, resulting from a decrease in c by about 0.4 Å and an increase in a by 1.4 Å. Similarly, for NH_2–Fe–MIL-88B the cell volume increases by about 500 $Å^3$ (decrease in c by 0.2 Å and increase in a by 1.4 Å). Both structures exhibit approximately the same increase in the cell volume during adsorption of ethanol. However, the total cell volume of NH_2–Fe–MIL-88B is slightly larger, which implies that the presence of the amino group causes a slight increase in the cell volume but does not influence the flexibility of the structure (Table 3–2).

Table 3-1   **Lattice parameters *a* and *c* of Fe–MIL-88B after indexing using the Werner algorithm for different relative pressures of ethanol**

p/p_0	Lattice parameter a / Å	Lattice parameter c / Å	Cell volume /A^3
0.00	9.3	19.4	1662
0.02	10.7	19.1	2167
0.40	10.7	19.0	2175
0.80	10.7	19.0	2184

Table 3-2   Lattice parameters *a* and *c* of NH$_2$–Fe–MIL-88B after indexingusing the Werner algorithm for different relative pressures of ethanol

p/p_0	Lattice parameter a / Å	Lattice parameter c / Å	Cell volume /A^3
0.00	9.5	19.3	1756
0.02	10.6	19.3	2180
0.40	10.9	19.1	2250
0.80	10.9	19.1	2260

Summarizing, the structural changes in these flexible frameworks observed upon adsorption are fairly similar and cannot explain the much higher uptake of ethanol of the amino-functionalized host, as revealed by the QCM experiments. We therefore attribute the strong difference in sorption behavior to the incorporated amino functionality within the pores of NH$_2$–Fe–MIL-88B. It is proposed that significant host–guest interactions such as hydrogen bonding cause the larger

adsorbed amount of ethanol at a defined relative pressure. Similar observations supporting this interpretation have been recently made in computational studies.[20] The authors were able to demonstrate the significant impact of ligand functionalization on CO$_2$ and CH$_4$ adsorption loading. The calculated isotherms show a considerable enhancement in the CO$_2$ uptake with respect to the original form of the MOF. The increased adsorption is asserted to result from additional interactions such as hydrogen bonding.

**Direct growth of oriented NH$_2$–Fe–MIL-101 on a self-assembled Monolayer**

The direct growth methodology was also extended to the synthesis of thin films of NH$_2$–Fe–MIL-101 on carboxylate terminated self-assembled monolayers. The intriguing properties of bulk NH$_2$–Fe–MIL-101 are demonstrated by thermogravimetric analysis (TGA) and nitrogen sorption data; the results are depicted in Figure 9-2 and Figure 9-3. The crystallization solution used in this synthesis was prepared in the same way as the synthesis solution for bulk NH$_2$–Fe–MIL-101.[21] NH$_2$–Fe–MIL-101 is isoreticular to MIL-101, which has a cubic unit cell with a cell parameter of 89 Å. After an immersion time of 3 d, the 222 reflection at 3.4° 2θ and the 333 reflection at 5.1° 2θ of NH$_2$–Fe–MIL-101 can be clearly detected (Figure 3-12).
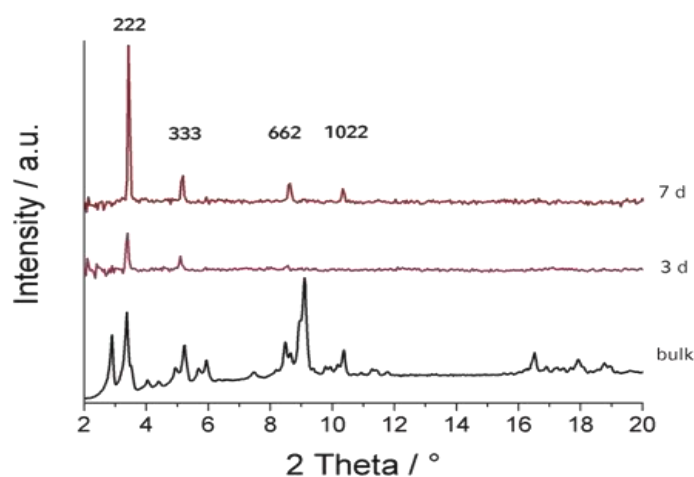
Figure 3-12 X-Ray diffraction data of NH$_2$–Fe–MIL-101 crystals grown on functionalized gold substrates (immersion times of the substrates in the crystallization solution of 3 d and 7 d) compared to the powder pattern of bulk NH$_2$–Fe–MIL-101 crystals. The background of the XRD patterns of the film samples was subtracted.

The increase in the immersion time to 7 d leads to a strong increase in the intensities of the 222 and 333 reflections. Small additional reflections at 8.6° and 10.3° 2θ (662 and 1022 reflections of NH_2–Fe–MIL-101), indicate the appearance of a few additional less oriented crystals. We conclude that the crystal populations on the SAM have a strongly preferred orientation in the [111]-direction.

Scanning electron microscopy (SEM) of the films shows crystals with a distinct sphere-like morphology with sizes between 100 and 500 nm (Figure 3-13).
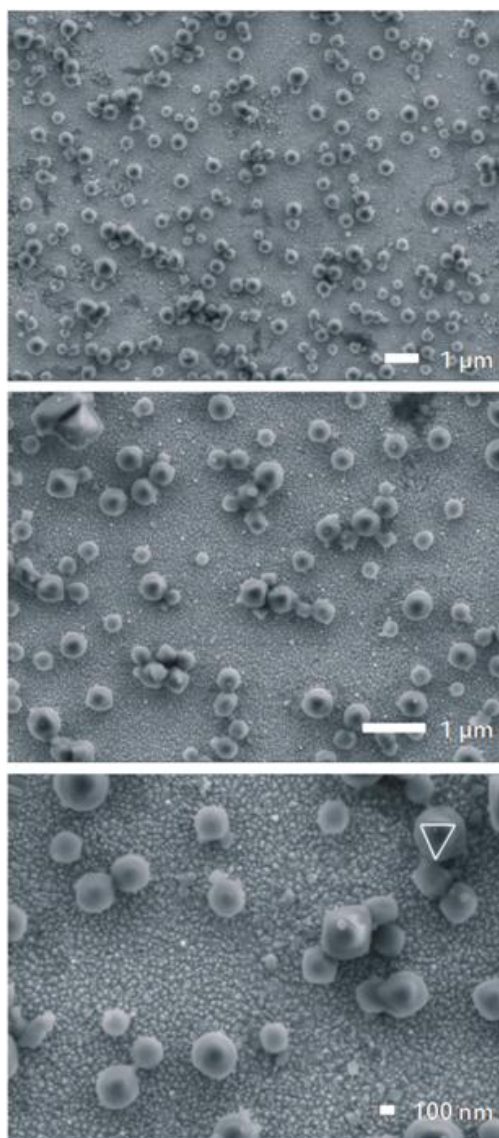
Figure 3-13   Scanning electron micrographs of NH_2–Fe–MIL-101 samples after immersion time of 10 d, at different magnifications.

Higher magnification reveals that most of the crystals have a triangular top-face (Figure 3-13, bottom), in good agreement with the preferred [111]-orientation of the crystals deduced from the XRD results. NH_2–Fe–MIL-101 crystallizes in a cubic symmetry and the bulk crystals show an octahedral morphology, which would appear with triangular habit viewed in the [111] direction.

3.5   Conclusions

In this study, we have shown that functionalized metal–organic frameworks can be grown on self-assembled monolayers and that a preferred orientation of the crystals can be achieved. This was demonstrated for the flexible structure of NH_2–Fe–MIL-88B as well as the large cage structure of NH_2–Fe–MIL-101. The influence of the implemented functionality on the sorption properties of MIL-88B compared to its modified analogue was investigated by QCM experiments. A considerably enhanced uptake of ethanol was demonstrated for the amino-functionalized MOF. We attribute this impact of ligand modification to secondary interactions such as hydrogen bonding with the guest molecules. Moreover, a correlation of the adsorbed amount of ethanol with structural changes in the flexible Fe–MIL-88B systems was observed *in situ* by sorption@XRD measurements. Our study shows that the concept of oriented crystal growth on SAM-modified gold substrates can be extended to functionalized porous structures. The growth method apparently can be generalized to an increasing number of MOF structures, such that comparative sorption experiments in thin films become possible. We anticipate that the ability to direct the growth of functionalized MOFs in the form of thin oriented films will be of particular interest in applications such as selective chemical sensors, where both the control of crystal growth orientation and functionalization of the organic linker are expected to have a strong impact on sensitivity, kinetics and selectivity through specific host–guest interactions.

3.6   References

[1]   O. M. Yaghi, M. O'Keeffe, N. W. Ockwig, H. K. Chae, M. Eddaoudi and J. Kim, *Nature*, 2003, **423**, 705-714.

[2]   S. Kitagawa, S.-i. Noro and T. Nakamura, *Chem. Commun.*, 2006, 701-707.

[3]   S. Kitagawa and K. Uemura, *Chem. Soc. Rev.*, 2005, **34**, 109-119.

[4]   Z. Wang and S. M. Cohen, *Chem. Soc. Rev.*, 2009, **38**, 1315.

[5]   Y.-F. Song and L. Cronin, *Angew. Chem., Int. Ed.*, 2008, **47**, 4635-4637.

[6]   J. S. Seo, D. Whang, H. Lee, S. I. Jun, J. Oh, Y. J. Jeon and K. Kim, *Nature*, 2000, **404**, 982-986.

[7]   A. D. Burrows, C. G. Frost, M. F. Mahon and C. Richardson, *Angew. Chem., Int. Ed.*, 2008, **47**, 8482-8486.

[8]   K. K. Tanabe, Z. Wang and S. M. Cohen, *J. Am. Chem. Soc.*, 2008, **130**, 8508-8517.

[9]   Z. Wang and S. M. Cohen, *J. Am. Chem. Soc.*, 2007, **129**, 12368-12369.

[10]   Z. Wang and S. M. Cohen, *Angew. Chem., Int. Ed.*, 2008, **47**, 4699-4702.

[11]   M. J. Ingleson, J. Perez Barrio, J.-B. Guilbaud, Y. Z. Khimyak and M. J. Rosseinsky, *Chem. Commun.*, 2008, 2680-2682.

[12]   S. Bauer, C. Serre, T. Devic, P. Horcajada, J. Marrot, G. Ferey and N. Stock, *Inorg. Chem.*, 2008, **47**, 7568-7576.

[13]   C. Scherb, A. Schoedel and T. Bein, *Angew. Chem., Int. Ed.*, 2008, **47**, 5777.

[14]   C. Scherb, R. Koehn and T. Bein, *J. Mater. Chem.*, 2010, **20**, 3046-3051.

[15]   A. Ulman, *Chem. Rev.*, 1996, **96**, 1533-1554.

[16]   H. Wang, S. Chen, L. Li and S. Jiang, *Langmuir*, 2005, **21**, 2633-2636.

[17]   S. Surble, C. Serre, C. Mellot-Draznieks, F. Millange and G. Ferey, *Chem. Commun.*, 2006, 284-286.

[18]   C. Serre, C. Mellot-Draznieks, S. Surblé, N. Audebrand, Y. Filinchuk and G. Férey, *Science*, 2007, **315**, 1828-1831.

[19]   C. Mellot-Draznieks, C. Serre, S. Surblé, N. Audebrand and G. Férey, *J. Am. Chem. Soc.*, 2005, **127**, 16273-16278.

[20]   A. Torrisi, R. G. Bell and C. Mellot-Draznieks, *Cryst. Growth & Des.* , 2010, **10**, 2839-2841.

[21]   S. Bauer, C. Serre, T. Devic, P. Horcajada, J. Marrot, G. Ferey and N. Stock, *Inorg. Chem.* , 2008, **47**, 7568-7576.

4   One-dimensional Metal-organic Framework Photonic Crystals Used as Platforms for Vapor Sorption

This chapter is based on the publication indicated below:

Florian M. Hinterholzinger,[a‡] Annekathrin Ranft,[b‡] Johann M. Feckl,[a] Bastian Rühle,[a] Thomas Bein*[a] and Bettina V. Lotsch*[b], *Journal of Materials Chemistry* 2012, **22**, 10356 − 10362.

Abstract

We present the fabrication of one-dimensional photonic crystals (Bragg stacks) based on a microporous metal–organic framework material and mesoporous titanium dioxide. The Bragg stack heterostructures were obtained using two complementary synthesis approaches utilizing the bottom-up assembly of heterogeneous, *i.e.* two-component photonic crystal multilayer structures. Zeolitic imidazolate framework ZIF-8 and mesoporous titanium dioxide were chosen as functional components with different refractive indices. While ZIF-8 is intended to impart molecular selectivity, mesoporous TiO_2 is used to ensure high refractive index contrast and to guarantee molecular diffusion within the Bragg stack. The combination of micro- and mesoporosity within one scaffold endows the 1D-MOF

PC with characteristic adsorption properties upon exposure to various organic vapors. In this context, the sorption behavior of the photonic material was studied as a function of partial pressure of organic vapors. The results show that the multilayered photonic heterostructures are sensitive and selective towards a series of chemically similar solvent vapors. It is thus anticipated that the concept of multilayer heterogeneous photonic structures will provide a versatile platform for future selective, label-free optical sensors.

4.1   Introduction

Metal–organic frameworks represent a class of hybrid materials with promising properties for various applications.[1, 2 3-5] In particular, the modular tailorability, the rich host–guest interactions, and the widely tunable sorption behavior make MOFs attractive candidates for chemical sensing.[6, 7] However, only a few reports are dealing with MOF-based sensors,[8, 9] in which the intrinsic framework luminescence[10-14] or the refractive index modulation of Fabry–Pérot interference peaks have been explored for signal transduction.[15] The tunability of the effective refractive index (RI) of MOFs *via* adsorption of guests inspired us to correlate these properties with the underlying optics of photonic crystals (PCs), which are composed of alternating dielectric layers featuring periodic changes in their effective refractive indices.[16-18]

One-dimensional assemblies, which represent the structurally simplest form of photonic crystals, are also known as Bragg stacks (BS) or Bragg mirrors. 1D-PC

multilayer structures interacting with visible light require layer thicknesses corresponding to optical wavelengths.[19] As a consequence of the periodicity in the dielectric function, specific wavelengths are efficiently reflected due to diffraction and interference of incident light at each interface of the periodically stacked composite.[20] Enhanced reflectivity is achieved by increasing the number of bilayers or by choosing dielectric materials featuring a high refractive index contrast (Scheme 4-1).[21]
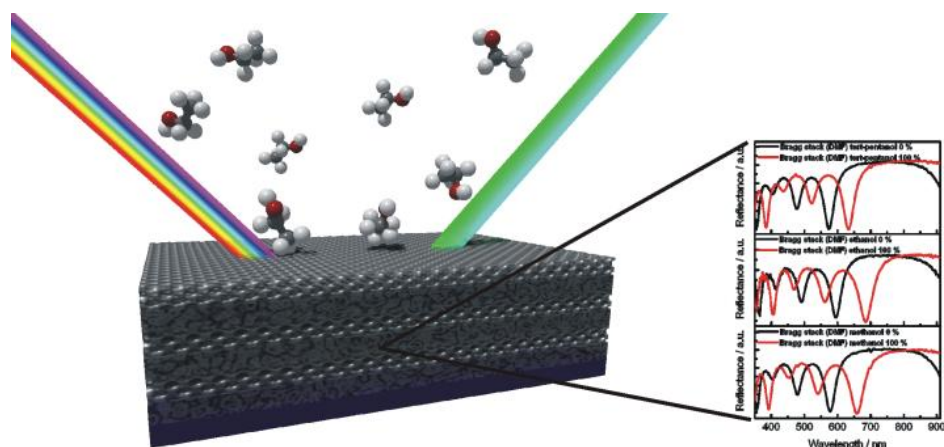
Scheme 4-1   Schematic representation of a multilayered photonic crystal architecture illustrating the structure- and angle-dependent reflection of incident light as well as the optical response upon exposure to external stimuli.

Currently, intensive research efforts are focused on the development of tunable optical sensors with a label-free operation and compact set-up. There are several approaches ranging from plasmonic noble metal nanotubes[22] or field effect transistors based on reduced graphene[23] to Bragg stacks built up from an alternating polymer architecture,[24] which deal with the implementation of these

materials as tunable and label-free sensors. In particular, detection platforms based on Bragg stacks can be realized by translating stimuli-induced optical thickness changes of the constituent materials into a color change of the multilayer photonic structure. So far, several studies are dealing with tailor-made inorganic or hybrid materials to implement functionality within one-dimensional photonic crystals.[25] While there are several examples of versatile SiO_2–TiO_2 systems,[26-28] including both dense and porous morphologies as well as nanoparticle-based Bragg stacks,[29, 30] smart hybrid photonic materials with intrinsic functionality are still rare.

In principle, a Bragg stack offers a versatile platform for the detection of molecular interactions and the development of chemical sensors, whereas the realization of chemical selectivity in sensors remains a great challenge. Very recently, several groups reported a new transduction scheme based on the fabrication of MOF-containing ordered 3D photonic structures.[31, 32] The selectivity issue is addressed by integrating metal–organic frameworks into three-dimensional inverse opal structures. While Wu *et al.*[32] employed a colloidal crystal templating approach using a polystyrene opaline ''mold'', the group of J. Hupp[31] deposited MOF crystals onto a silica template to obtain hybrid MOF–silica colloidal crystal (MOF–SCC) films. The authors have shown that the introduction of an ordered porous structure imparts useful optical features to HKUST-1 and ZIF-8. For MOF–SCC an optical signal displayed by distinct stop band shifts upon analyte sorption is readily observed.

Contrary to 3D photonic materials, we introduce herein a one-dimensional photonic architecture based on a microporous metal–organic framework and titanium dioxide. Thus, an optical transducer system is built, which is used to efficiently

convert molecular adsorption into an optical response. As a microporous material, the intensively studied zeolitic imidazolate framework ZIF-8[33] was chosen; this is expected to impart size- and chemoselectivity and, thus, functionality to the 1D-MOF PC. Complementary material properties in one single platform, such as hydrophobicity/hydrophilicity, dual pore-size regimes, and high refractive index contrast, can be additionally integrated by our combined assembly approach.

Ultimately, the presented results are expected to extend the toolbox for designing nanoporous and at the same time highly selective photonic crystals, to promote our understanding of molecular interactions in porous materials, and to provide novel concepts for label-free chemo-optical sensors.

4.2   Experimental section

All chemicals (zinc nitrate hexahydrate, 2-methylimidazole; nitric acid (0.1 M), titanium(IV) ethoxide, titanium tetrachloride) as well as solvents are commercially available and were used as received. *Tert*-butyl alcohol was dried over a 4 Å molecular sieve at 28 °C and filtered prior to use.

Route A

Preparation of dense ZIF-8 films

ZIF-8 thin films were prepared on silicon wafers, similar to the approach reported in ref. 14 and 15. The substrates were pre-cleaned in piranha solution (H_2SO_4/H_2O_2,

70:30 (v/v)) at 70 °C for 30 minutes, rinsed with distilled water and dried under nitrogen flow.

For ZIF-8 thin film preparation, 500 mL methanolic stock solutions of $Zn(NO_3)_2 \cdot 6H_2O$ (25 mM, 99%, *Aldrich*) as well as of 2-methylimidazole (*mIm*) (50 mM, 99%, *Aldrich*) were prepared. A ZIF-8 thin film was obtained by immersing the cleaned substrates in a fresh mixture of 10 mL $Zn(NO_3)_2$ stock solution and 10 mL *mIm* stock solution for 30 minutes at room temperature. For optimization of homogeneity and to enhance surface smoothness, two different strategies were employed. The beakers were either put in an ultrasonic bath or fixed on a shaker during film growth. The as-prepared ZIF-8 thin film was washed with methanol and dried under nitrogen flow. Thicker films could be obtained by simply repeating the process with fresh solutions.

Synthesis of ultrasmall titanium dioxide nanoparticles and film preparation

Titanium dioxide nanoparticles were synthesized as described earlier.[34] In brief, a nonaqueous sol-gel route in *tert*-butyl alcohol under microwave irradiation was used to yield ultrasmall (3 nm), crystalline (anatase), non-agglomerated and highly dispersible nanoparticles.

For all syntheses, titanium tetrachloride (0.7 mL, 6.4 mmol, 99.995 %, *Aldrich*) was dissolved in toluene (5 mL) and added to *tert*-butyl alcohol (15 mL, 160 mmol, *Aldrich*) under continuous stirring. Microwave heating was performed in microwave autoclaves with an initial heating power of 1200 W (Synthos 3000, Anton Paar). The

solution was heated to 80 °C within 1 min and then kept at 50 °C for 20 min resulting in a slightly yellow, transparent solution of nanoparticles. To obtain the fully crystalline nanoparticles, this heating procedure was repeated one more time after a cooling period to room temperature. The solution was then colorless and titanium dioxide could be flocculated by the addition of *n*-heptane (*n*-heptane:*tert*-butanol/toluene 2:1 volume ratio; Sigma) and separated by centrifugation at 50000 rcf for 15 min.

For the preparation of the mesoporous (mp) titania films the nanoparticle pellet (0.4 g) was redispersed in ethanol (8.3 mL) and Pluronic F127 (0.1 g, *BASF*) was added as structure directing agent (SDA).

Fabrication of Bragg stack 1 (BS-1)

For the fabrication of Bragg stack 1 **(BS-1)** thoroughly washed and dense ZIF-8 thin films were coated with a fresh colloidal suspension of redispersed ultrasmall titanium dioxide nanoparticles. The films were deposited by spin-coating using a Laurell WS-400B-6NPP-Lite-AS spin-coater at a speed of 5000 rpm to give a film thickness of ~50 nm. To remove the SDA, the films were first heated to 100 °C (3 h ramp, 1 h dwell time) to increase the film stability followed by an extraction of the SDA with ethanol under reflux for 1 h.

The complete removal was confirmed by reflection absorption infrared (RAIR) spectroscopy in addition to scanning electron microscopy (SEM) (Figure 4-1 and

Figure 4-2). The whole procedure was repeated 3 times to obtain multiple alternating ZIF-8/mp-TiO$_2$ architectures.

Route B

Synthesis of ZIF-8 nanoparticles

ZIF-8 nanoparticles were prepared by a modified literature synthesis.[35] In a typical experiment, Zn(NO$_3$)$_2$ · 6 H$_2$O (1.03 g, 3.45 mmol, 99%, *Grüssing*) was dissolved in methanol (70 mL, puriss, *Sigma*) and rapidly added to a pre-cooled (0 °C) solution of 2-methylimidazole (2.27 g, 27.7 mmol, 99%, *Aldrich*) in methanol (70.0 mL). The mixture was stirred and cooled constantly throughout the reaction until the solution slowly turned turbid. After 30 min, the nanocrystals were separated from the solvent by centrifugation. Colloidal suspensions of ZIF-8 were obtained by redispersing the particles after centrifugation in DMF (or methanol) (670 mg ZIF-8 / 1 mL DMF).

Synthesis of titania nanoparticles

Titania nanoparticles were synthesized according to the literature.[36] In a typical procedure, Ti(OEt)$_4$ (6.25 mL, *Aldrich*) was slowly added to HNO$_3$ (0.1 M, 37.5 mL, puriss, *Acros*) under stirring and heated to 80 °C for 8 h. After cooling to room temperature, the opalescent mixture was sonicated for at least 3 h in order to break up agglomerates. Colloidal suspensions of titania in a solvent sufficiently volatile for spin-coating were obtained by repeated collection of the particles by centrifugation and redispersion in DMF (or methanol) (130 mg TiO$_2$ / 1 mL DMF).

Fabrication of Bragg stack 2 (BS-2)

Silicon wafers were used as substrates for the film deposition by spin-coating. The substrates were precleaned with soap and water and subsequently treated with Piranha solution (H_2SO_4/H_2O_2, 2:1). After thoroughly rinsing with deionized water, the wafers were dried under nitrogen flow and stored in ethanol. Before film deposition, the substrates were plasma-cleaned and rinsed with ethanol under spinning for 5 s. The preparation of the Bragg reflector was performed by spin-coating alternatingly colloidal suspensions of ZIF-8 and titania onto the substrate at a speed of 4000 rpm (1500 acceleration) for 60 s, starting with ZIF-8. The film thickness was adjusted by the particle concentration in the suspensions and by multiple coating steps. After each deposition, the film was annealed at 200 °C for 30 min.

4.3   Characterization

X-ray diffraction (XRD) measurements of powders and thin films were performed using a Bruker D8 (Cu-Kα1 = 1.5406 Å; Cu-Kα2 = 1.5444 Å) in *theta-theta* geometry. The films were measured between 5° and 20° *two theta*, with a step-size of 0.05° *two theta* and a scan-speed of 0.3° min[-1]. The data of the powder samples were collected between 5° and 45° *two theta* with a step-size of 0.05° *two theta* and a scan-speed of 3° min[-1].

SEM micrographs of **BS-1** were recorded with a JEOL JSM-6500F scanning electron microscope (SEM) equipped with an Oxford EDX analysis system; those of **BS-2** with a Merlin (Zeiss) FE-SEM. Ellipsometry measurements were performed with a Woollam M2000D at an angle of 75° in the spectral range of 190 - 1000 nm. The data were fitted between 350 and 1000 nm using a Cauchy-type material as model layer. Reflectance measurements were recorded with the same ellipsometer using s-polarized light at an incident angle of 75°.

The recording of isotherms was performed at ambient temperature using a home-made Labview-controlled gas mixer. Digital mass flow controllers (W-101A-110-P, F-201C, Bronkhorst High-Tech) ensured the accurate dosing of the carrier gas nitrogen and the liquid analyte, which was vaporized in a controlled evaporation and mixing element (W-101A, Bronkhorst High-Tech). Partial pressures (p) were calculated using the van der Waals equation.[28, 37] The relative pressure pp_0^{-1} relates to the saturation pressure p_0.

4.4   Results and discussion

Bragg stack preparation and structural properties

Two different strategies were employed for the fabrication of 1D-MOF photonic crystals consisting of either dense or porous ZIF-8 layers, and differently sized mesoporous titanium dioxide nanoparticle derived films. Stability, pore accessibility as well as high optical quality multilayer films are key requirements for the

fabrication of analyte-responsive transducer systems. Those features were addressed by the choice of suitable deposition and post-treatment parameters. For the mp-TiO$_2$ deposition in **BS-1**, both a complete removal of the template (Figure 4-1 and Figure 4-2) as well as minimum etching of the ZIF-8 underlayer had to be achieved.
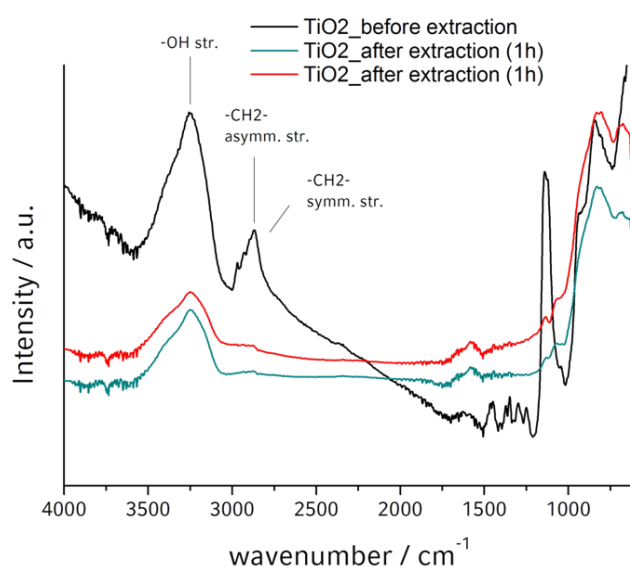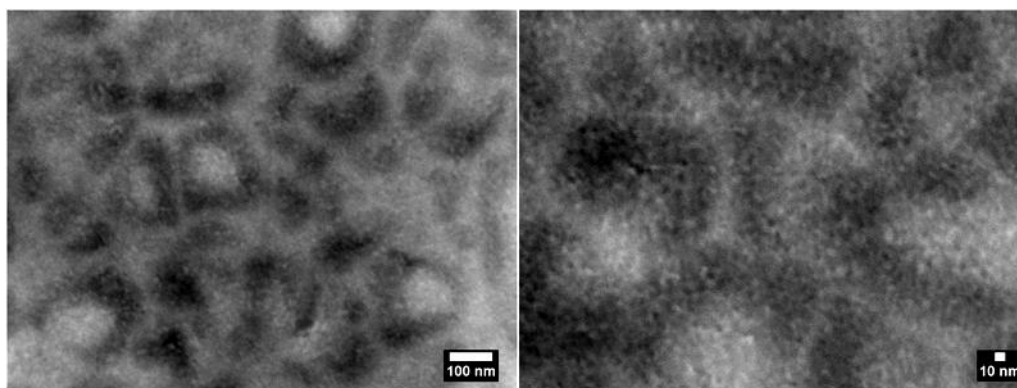

Figure 4-1   RAIR spectra of a TiO$_2$ thin film before and after the ethanol extraction procedure.

Figure 4-2   **SEM micrographs demonstrating the mesoporous structure of a thin TiO$_2$ film after ethanol extraction (magnification: x100.000 (left); x250.000 (right)).**

In Figure 4-3 the X-ray diffraction patterns of both 3-bilayer Bragg stacks (photographs shown in Figure 4-6) are depicted and compared to simulated data. The mild annealing temperatures employed in either case, in addition to the solvent extraction carried out under non-acidic conditions (**BS-1**), retain the crystallinity and stability of the ZIF-8 layers. The diffraction patterns of the multilayered ZIF-8–TiO$_2$ composites show excellent agreement with the simulated ZIF-8 data, apart from peak broadening, indicating a slightly smaller grain size of the ZIF-8 crystals within the BSs.
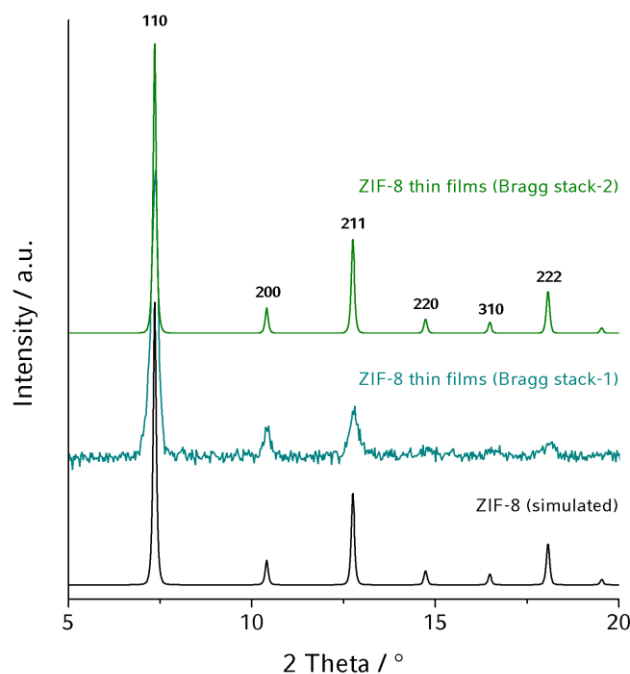
Figure 4-3   X-ray diffraction patterns (background corrected) of the 3-bilayer Bragg stack 1 (middle) as well as of Bragg stack 2 (top) after temperature treatment and complete removal of the structure-directing agent (F127), compared to simulated data (bottom line).

In contrast to **BS-1**, which features dense ZIF-8 layers, **BS-2** is composed of ZIF-8 nanocrystals (approx. 50 nm diameter, see Figure 4-4), forming uniform layers, and nanoparticle-based TiO_2 layers with TiO_2 particles around 10–15 nm in diameter. Therefore, we expect **BS-2** to exhibit a fairly high degree of textural mesoporosity in both layers, in addition to the intrinsic microporosity provided by the ZIF-8 crystals.
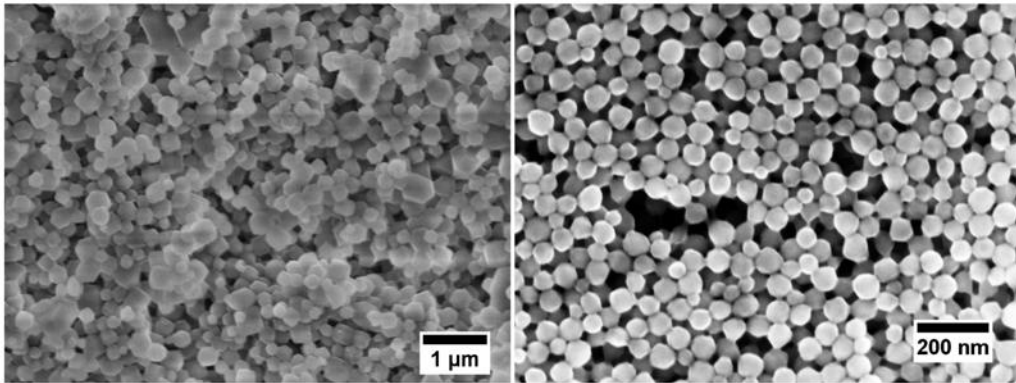
Figure 4-4   Scanning electron microscopy (SEM) images showing a bulk ZIF-8 powder sample obtained from the mixture solution used for the fabrication of BS-1 (left) as well as ZIF-8 nanoparticles used for the preparation of BS-2 (right).

The coexistence of both materials embedded in the 1D-MOF PC structure is confirmed by scanning electron microscopy (SEM). In Figure 4-5 representative 3-bilayer Bragg stacks composed of alternating microporous ZIF-8 layers and porous titania layers deposited on a silicon substrate are depicted.
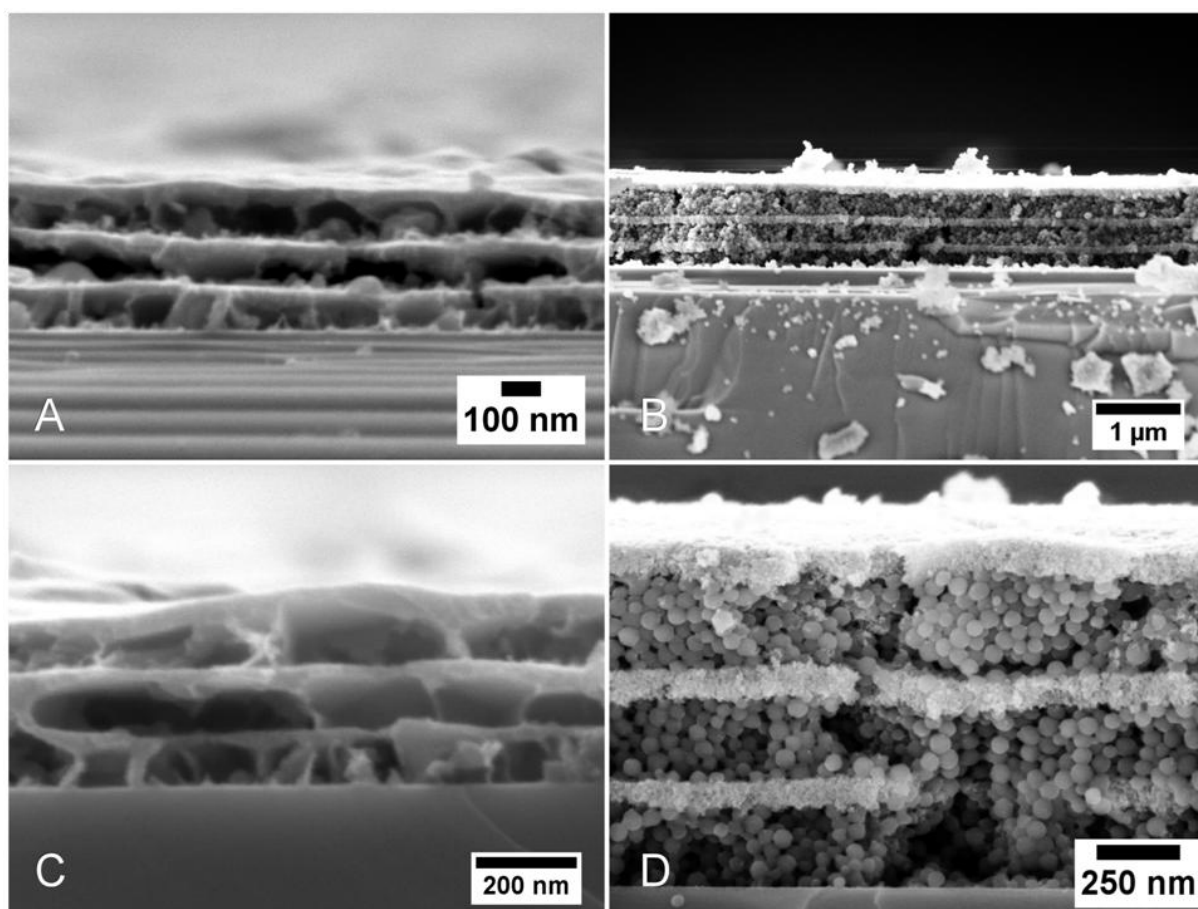
Figure 4-5   Scanning electron micrographs showing cross-sections of both 3-bilayer Bragg stacks with an average film thickness of ~ 50nmfor each titania layer and ~ 70 nm for each ZIF-8 layer for BS-1 (A and C) as well as for BS-2 (DMF, B and D) exhibiting a layer thickness of ~ 50 nm for each titania layer and ~ 200 nm for ZIF-8 layers, respectively. ZIF-8–TiO$_2$-BSs are depicted for different magnifications (A: ~ 80 000; B: ~ 15 000; C: ~ 100 000; D: ~ 60 000).

The differently prepared Bragg stacks exhibit a ZIF-8 layer thickness of approximately 70 nm in **BS-1** and about 200 nm in **BS-2**, respectively. TiO$_2$ layers deposited on each ZIF-8 film have a thickness of about 50 nm in both Bragg stacks. The crosssectional SEM micrographs reveal that both fabrication methods yield fairly uniform layer thicknesses throughout the entire architecture. Figure 4-5 also

demonstrates the alteration of both materials seen by the differences in material contrast. While the dark layers represent the ZIF-8 material exhibiting a lower electron density, the brighter thin films consist of TiO_2 nanoparticles. Not only the deposition of ZIF-8 layers on silicon, as already shown by several groups,[15, 38] but also adhesion between ZIF-8 and mesoporous/nanoparticle titania layers was achieved using our dual assembly approach. In contrast to the deposition of MOF material on inverse opal structures,[31, 32] no surface modification is necessary when preparing ZIF-8-based onedimensional photonic structures. Regarding the stability and crystallinity of the multilayered Bragg stacks, no delamination or amorphization upon heating, extraction or adsorption of volatile species is observed, which is consistent with the corresponding XRD results (see Figure 4-3). In conclusion, robust, uniform and high-optical quality multilayered photonic crystals composed of two different materials with varying morphologies can reproducibly be fabricated and thus provide the basis for chemical sensing studies.

**Vapor adsorption and optical sensing**

The combination of a microporous MOF material with mesoporous metal oxide layers is supposed to endow the material with a unique combination of size-selectivity and analyte sensitivity. The integration of both morphologies within one photonic structure is expected to act as a molecular sieving platform, readily adsorbing analyte molecules with small kinetic diameters in both layers, whereas the access of larger guests is exclusively possible into the mesoporous titania layers. Essentials such as high specific surface areas, pore accessibility, efficient diffusion

and molecular sieving abilities are all addressed by our highly porous 1D-MOF photonic crystals.
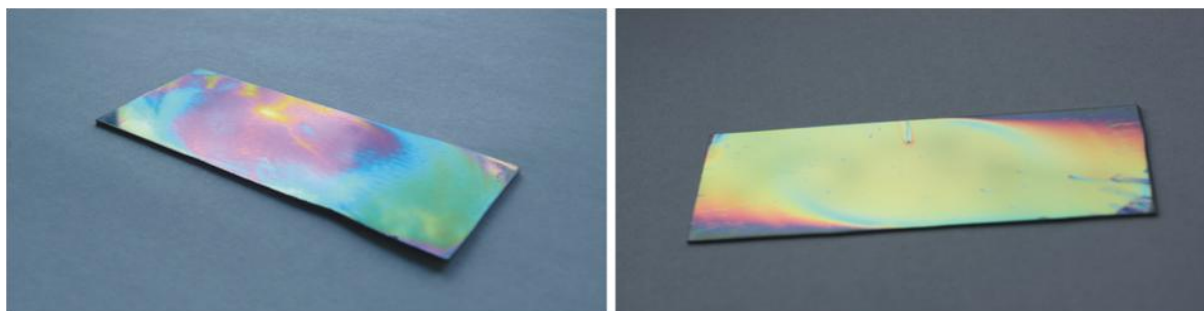
Figure 4-6   **Photographs of 3-bilayer Bragg stack 1 (left) and Bragg stack 2 (right) on a 5 x 2.5 cm^2 Si substrate in air.**

The optical response of the 1D-MOF PCs to guest adsorption was investigated by performing sorption experiments of volatile analyte molecules. According to the optical Bragg equation, sorption of volatile species into the porous layers influences the effective refractive index of a bilayer by which analyte-induced color changes can be efficiently monitored. Figure 4-7 the reflectance spectra of both Bragg stacks are demonstrated.
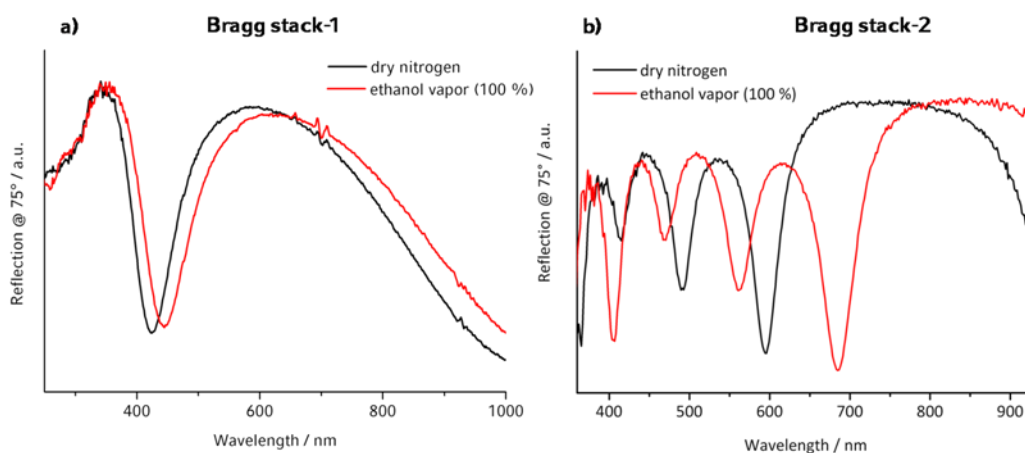
Figure 4-7   **Reflectance spectra of Bragg stack 1 (a) and Bragg stack 2 (DMF) (b) illustrating the optical shift upon ethanol exposure recorded at the highest partial pressure ($p/p_0 \approx 1.0$).**

Here, the optical response is triggered by the adsorption of ethanol vapor at the highest partial pressure ($p/p_0 \approx 1.0$), which entails pronounced red-shifts of the Fabry–Pérot fringe of **BS-1** from $\lambda \approx 585$ to $\lambda \approx 630$ nm as well as of the stop band of **BS-2**, derived from nanoparticles redispersed in DMF, from $\lambda \approx 740$ to $\lambda \approx 840$ nm, respectively. We attribute the significantly larger optical shift of **BS-2** to the thicker ZIF-8 layers and amplified external surface area (and hence accessibility), which underlines the enhanced contribution of the "active" component to the observed overall optical shift of the BS.[39] Compared to the 3D-MOF (HKUST-1) hybrid photonic crystals recently reported by the groups of J. Hupp and G. Li,[31, 32] which show optical shifts of 9 nm and 16 nm upon ethanol sorption, respectively, a significant increase with respect to the optical response can be monitored in our system. However, when infiltrating 30 mm thick polystyrene template films with ZIF-8, Wu *et al.* observed a distinct shift of about 75 nm upon methanol

adsorption.[32] Compared to the inherently smaller absolute shifts observed with **BS-1,** which are presumed to result from the significantly smaller thickness of the ZIF-8 films, an even higher sensitivity upon sorption of organic vapors can be deduced from the reflectance spectrum of **BS-2** (Figure 4-7 and Figure 9-20). Note that only a short heating period of 15 minutes at 200 °C was applied to Bragg stack 2 prior to the sorption experiments compared to the activation procedure reported by Wu *et al.*[32] The samples were additionally subjected to a high-rate flow of dry nitrogen (Varian Chrompack Gas-clean Moisture Filter CP 17971, outlet concentration <0.1 ppm), which highlights the facile analyte uptake and release during a series of sorption measurements.

Analyte-induced variations of the optical thickness give rise to distinct optical shifts not only for ethanol and methanol but also for other larger analytes such as isobutanol and *tert*-pentanol. Adsorption isotherms monitoring the optical shift as a function of relative vapor pressure were recorded for **BS-2** (Figure 4-8c) as well as for the dense and porous ZIF-8 films as reference (Figure 4-8a and b). The latter show that the smaller alcohols are readily adsorbed by this MOF, including analyte molecules with larger kinetic diameters compared to the aperture size of ZIF-8 (3.4 Å).[33] These results are consistent with literature data, as it was previously shown that molecules such as ethanol or isobutanol exhibiting kinetic diameters of 4.5 Å (ref. 40) and 5 Å (ref. 41) are readily adsorbed owing to the flexibility of the pore apertures in ZIF-8.[40-42] Hence, *tert*-pentanol (2-methyl-1-propanol) was chosen as a sterically demanding analyte molecule with a kinetic diameter larger than 5 Å.[43] The dense ZIF-8 reference film only shows a minute optical shift of 4 nm, which is

consistent with the almost complete exclusion of *tert*-pentanol from the ZIF-8 pore system (Figure 4-8a). The nanoparticle-based ZIF-8 film shows a larger optical shift of about 30 nm at the highest partial pressure (p/p_0 = 1.0, Figure 4-8b), which is in agreement with the presence of a significant degree of textural mesoporosity.

In order to probe the host–guest interactions within the comparatively more complex Bragg stack environment, optical adsorption isotherms were recorded exemplarily for **BS-2**, as depicted in Figure 4-8c. Specifically, the initial stages during adsorption of alcohol vapors and the expected pore size-specific adsorption isotherms achieved through the incorporation of different porosities are of key interest.
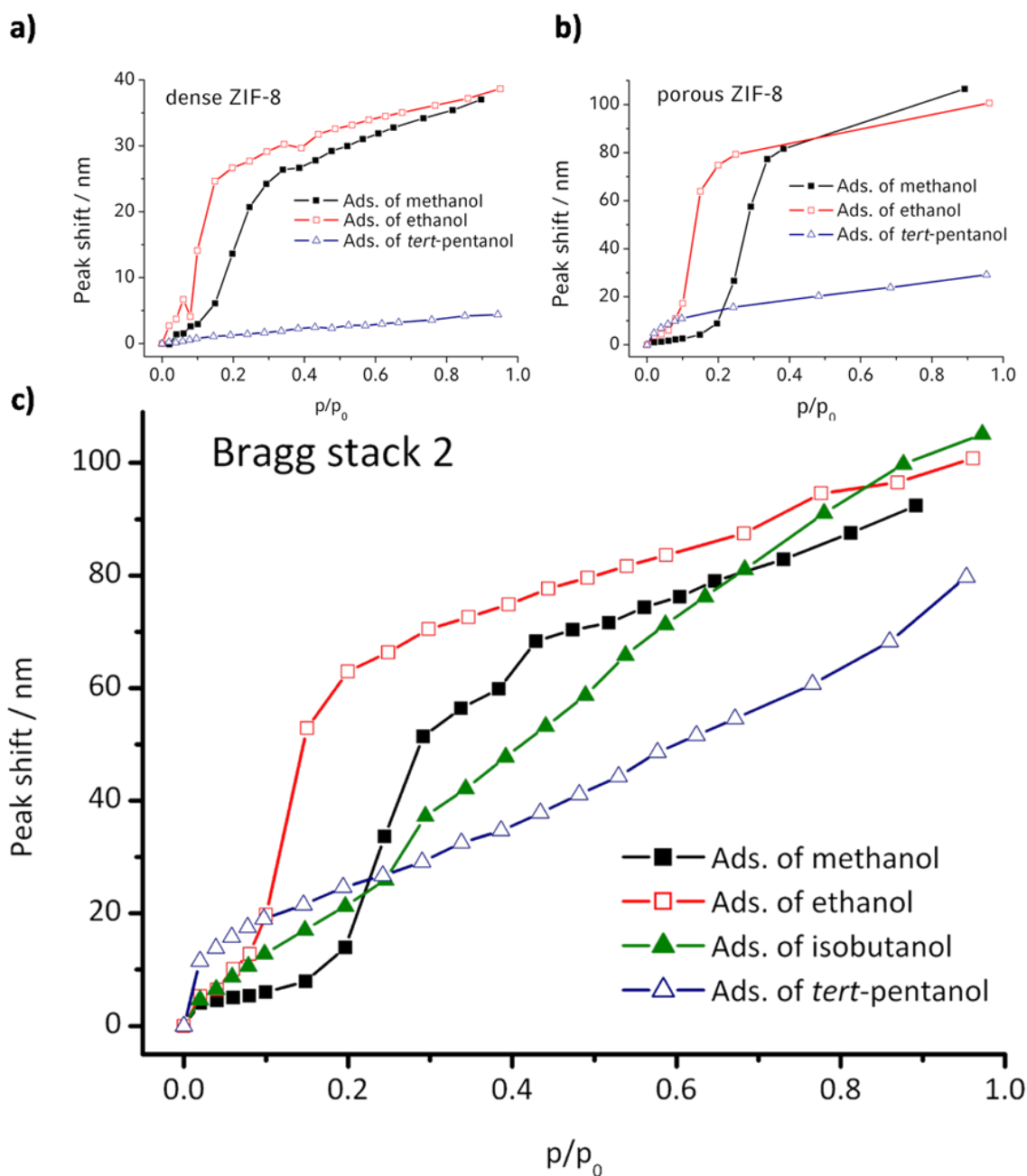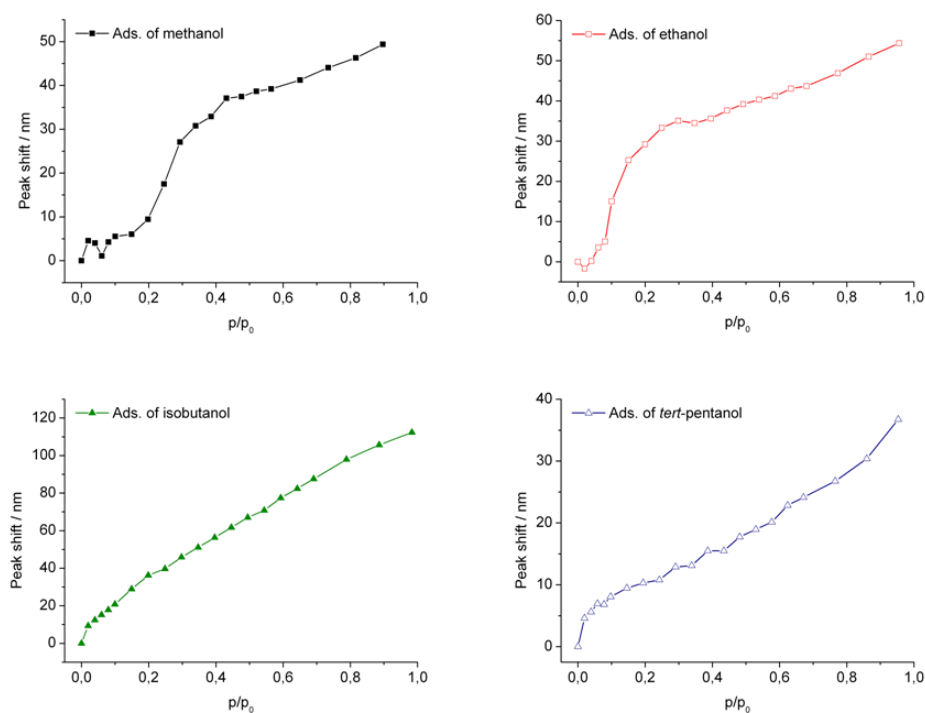
Figure 4-8   Optical vapor sorption isotherms demonstrating the adsorption performance of (a) dense and (b) nanoparticulate ZIF-8 reference samples as well as of (c) BS-2 (DMF) during exposure to a series of alcohol vapors.

During the first two dosing steps the 1D-MOF Bragg stack rapidly responds to all analyte molecules, indicated by varying red-shifts ranging from 5 to 15 nm (Figure

4-8c). At a partial pressure of p/p_0 = 0.1 and p/p_0 = 0.2, respectively, a steep increase in the methanol and ethanol isotherms is observed. However, a larger optical shift is recorded for ethanol, which is attributed to more beneficial interactions between ethanol and ZIF-8 owing to the larger hydrophobicity of ethanol compared to that of methanol. At the respective threshold pressures, pronounced optical shifts of about 50–60 nm are recorded, which gradually increase up to saturation pressure. The S-shaped isotherms upon methanol and ethanol adsorption recorded for both the single ZIF-8 films and for **BS-2** are in good agreement with the results obtained by Remi *et al.*[44] The authors attribute the S-shaped isotherms to changes in the framework triggered by interactions with guest-molecules, which was additionally confirmed and described elsewhere.[42] In contrast to the distinct S-shaped isotherms, isobutanol sorption experiments yield an almost linearly increasing adsorption behavior with an absolute shift of about 100 nm at the highest partial pressure. In contrast, the adsorption isotherm of *tert*-pentanol exhibits a convex shape featuring the highest uptake during the first dosing steps, which we attribute to the textural porosity of both ZIF-8 and titania layers arising from the nanoparticle architecture, as seen also for the porous ZIF-8 film (Figure 4-8b). However, this analyte exhibits the smallest overall uptake, which is consistent with the exclusion of *tert*-pentanol from the ZIF-8 pores, as demonstrated also for the individual ZIF-8 films. In contrast, the smaller analytes (methanol, ethanol, isobutanol) are more readily adsorbed owing to their smaller kinetic diameters.

As discussed above, an important finding is the fact that distinctly shaped isotherms are obtained for each of the four analytes over the entire relative pressure range, as

additionally demonstrated by reproduced sorption experiments using Bragg stacks derived from two different synthesis batches (Figure 4-9).

Figure 4-9   Reproduced optical vapor sorption isotherms demonstrating the adsorption of methanol, ethanol and *tert*-pentanol performed with Bragg stack 2 which was fabricated by redispersing the ZIF-8 nanoparticles in methanol (BS-2 (MeOH), see Experimental section) as well as the adsorption of isobutanol into BS-2 prepared with nanoparticles redispersed in DMF (BS-2 (DMF)).

Owing to the different fabrication methods and the resulting differences in the ZIF-8 layer thicknesses, less pronounced absolute shifts of about 50 nm are recorded using the **BS-2** (MeOH) as compared to **BS-2** (DMF) used in Figure 4-8c and for isobutanol adsorption (Figure 4-9). Therefore, the optical shift for isobutanol agrees well with the results obtained with **BS-2** (DMF) shown in Figure 4-8c, whereas the

absolute shifts for the other solvent vapors are smaller. Nevertheless, note that the shapes of all four optical isotherms are in good agreement with the isotherms shown in Figure 4-8, indicating the same host-guest interactions as in **BS-2** and thus, the same analyte selectivity to operate.

The characteristic sorption behavior indicates a high degree of chemical selectivity inherent to the MOF-BS, which is especially noticeable at low relative pressures. Comparison of the shapes of the isotherms for the BS and the individual ZIF-8 thin films (Figure 4-8) confirms that the optical response is dominated by ZIF-8.

4.5   Conclusions

In summary, a one-dimensional MOF-based photonic crystal heterostructure with embedded micro- and mesoporosity is presented. The fabrication of the 1D-MOF PC was achieved *via* two different inexpensive bottom-up synthesis approaches. The strategy of combining a microporous MOF material with mesoporous titanium dioxide layers provides the basis for a highly sensitive signal transduction scheme with an amplified overall optical response, while maintaining high chemical specificity. Hence, molecular recognition is translated into a readable optical signal without the use of any reporter systems.

The concept of MOF-based one-dimensional photonic crystal structures extends the scope of chemoselective optical signal transducer systems. We anticipate a generalization of the assembly of 1D photonic materials in terms of the large variety

and tunability of MOFs or related materials. Thus, we believe that the above proof-of-concept experiments provide a basis for the design of highly sensitive and chemically selective optical sensors.

4.6   References

[1]   O. M. Yaghi, M. O'Keeffe, N. W. Ockwig, H. K. Chae, M. Eddaoudi and J. Kim, *Nature*, 2003, **423**, 705-714.

[2]   G. Ferey, *Chem. Soc. Rev.*, 2008, **37**, 191-214.

[3]   U. Mueller, M. Schubert, F. Teich, H. Puetter, K. Schierle-Arndt and J. Pastre, *J. Mater. Chem.*, 2006, **16**, 626-636.

[4]   J. R. Li, R. J. Kuppler and H. C. Zhou, *Chem. Soc. Rev.*, 2009, **38**, 1477.

[5]   S. T. Meek, J. A. Greathouse and M. D. Allendorf, *Adv. Mater.*, 2011, **23**, 249-267.

[6]   C. Scherb, J. J. Williams, F. Hinterholzinger, S. Bauer, N. Stock and T. Bein, *J. Mater. Chem.*, 2011, **21**, 14849-14856.

[7]   O. Shekhah, J. Liu, R. A. Fischer and C. Woll, *Chem. Soc. Rev.*, 2011, **40**, 1081–1106.

[8]   M. D. Allendorf, C. A. Bauer, R. K. Bhakta and R. J. T. Houk, *Chem. Soc. Rev.*, 2009, **38**, 1330-1352.

[9]   L. E. Kreno, K. Leong, O. K. Farha, M. Allendorf, R. P. Van Duyne and J. T. Hupp, *Chem. Rev.*, 2011, **112**, 1105-1125.

[10]   H. Xu, F. Liu, Y. Cui, B. Chen and G. Qian, *Chem. Commun.*, 2011, **47**, 3153-3155.

[11]   B. Chen, L. Wang, Y. Xiao, F. R. Fronczek, M. Xue, Y. Cui and G. Qian, *Angew. Chem., Int. Ed.*, 2009, **121**, 508-511.

[12]   B. Gole, A. K. Bar and P. S. Mukherjee, *Chem. Commun.*, 2011, **47**, 12137-12139.

[13]   K. C. Stylianou, R. Heck, S. Y. Chong, J. Bacsa, J. T. A. Jones, Y. Z. Khimyak, D. Bradshaw and M. J. Rosseinsky, *J. Am. Chem. Soc.*, 2010, **132**, 4119-4130.

[14]   Y. Takashima, V. M. Martínez, S. Furukawa, M. Kondo, S. Shimomura, H. Uehara, M. Nakahama, K. Sugimoto and S. Kitagawa, *Nat. Commun.*, 2011, **2**, 168.

[15]   G. Lu and J. T. Hupp, *J. Am. Chem. Soc.*, 2010, **132**, 7832-7833.

[16]   L. D. Bonifacio, B. V. Lotsch, D. P. Puzzo, F. Scotognella and G. A. Ozin, *Adv. Mater.*, 2009, **21**, 1641-1646.

[17]   S. John, *Phys. Rev. Lett.*, 1987, **58**, 2486-2489.

[18]   A. Arsenault, S. Fournier-Bidoz, B. Hatton, H. Miguez, N. Tetreault, E. Vekris, S. Wong, S. Ming Yang, V. Kitaev and G. A. Ozin, *J. Mater. Chem.*, 2004, **14**, 781-794.

[19]   J. D. Joannopoulos, P. R. Villeneuve and S. Fan, *Nature*, 1997, **386**, 143-149.

[20]   H. Lee, *J. Appl. Phys.*, 2003, **93**, 819.

[21]   M. Bardosova, *Appl. Phys. Lett.*, 2006, **89**, 093116.

[22]   J. McPhillips, A. Murphy, M. P. Jonsson, W. R. Hendren, R. Atkinson, F. Höök, A. V. Zayats and R. J. Pollard, *ACS Nano*, 2010, **4**, 2210-2216.

[23]   R. Stine, J. T. Robinson, P. E. Sheehan and C. R. Tamanaha, *Adv. Mater.*, 2010, **22**, 5297-5300.

[24]   Z. Wang, J. Zhang, J. Xie, Z. Wang, Y. Yin, J. Li, Y. Li, S. Liang, L. Zhang, L. Cui, H. Zhang and B. Yang, *J. Mater. Chem.*, 2012, **22**, 7887-7893.

[25]   S. I. Khartsev, *Appl. Phys. Lett.*, 2005, **87**, 122504.

[26]   M. C. Fuertes, F. J. López-Alcaraz, M. C. Marchi, H. E. Troiani, V. Luca, H. Míguez and G. J. A. A. Soler-Illia, *Adv. Funct. Mater.*, 2007, **17**, 1247-1254.

[27]   S. Y. Choi, M. Mamak, G. von Freymann, N. Chopra and G. A. Ozin, *Nano Letters*, 2006, **6**, 2456-2461.

[28]   J. Kobler, B. V. Lotsch, G. A. Ozin and T. Bein, *ACS Nano*, 2009, **3**, 1669-1676.

[29]   D. Lee, M. F. Rubner and R. E. Cohen, *Nano Letters*, 2006, **6**, 2305-2312.

[30]   S. Colodrero, M. Ocaña, A. R. González-Elipe and H . Míguez, *Langmuir*, 2008, **24**, 9135-9139.

[31]   G. Lu, O. K. Farha, L. E. Kreno, P. M. Schoenecker, K. S. Walton, R. P. Van Duyne and J. T. Hupp, *Adv. Mater.*, 2011, **23**, 4449-4452.

[32]   Y.-n. Wu, F. Li, W. Zhu, J. Cui, C.-a. Tao, C. Lin, P. M. Hannam and G. Li, *Angew. Chem., Int. Ed.*, 2011, **50**, 12518-12522.

[33]   K. S. Park, Z. Ni, A. P. Côté, J. Y. Choi, R. Huang, F. J. Uribe-Romo, H. K. Chae, M. O'Keeffe and O. M. Yaghi, *Proc. Natl. Acad. Sci.*, 2006, **103**, 10186-10191.

[34]   J. M. Szeifert, J. M. Feckl, D. Fattakhova-Rohlfing, Y. Liu, V. Kalousek, J. Rathousky and T. Bein, *J. Am. Chem. Soc.*, 2010, **132**, 12605-12611.

[35]   J. Cravillon, S. Münzer, S.-J. Lohmeier, A. Feldhoff, K. Huber and M. Wiebcke, *Chem. Mater.*, 2009, **21**, 1410-1412.

[36]   B. V. Lotsch, F. Scotognella, K. Moeller, T. Bein and G. A. Ozin, *Proc. SPIE*, 2010, **7713**, 7713V.

[37]   C. Scherb, R. Koehn and T. Bein, *J. Mater. Chem.*, 2010, **20**, 3046-3051.

[38]   A. Demessence, C. Boissiere, D. Grosso, P. Horcajada, C. Serre, G. Ferey, G. J. A. A. Soler-Illia and C. Sanchez, *J. Mater. Chem.*, 2010, **20**, 7676-7681.

[39]   M. D. Allendorf, R. J. T. Houk, L. Andruszkiewicz, A. A. Talin, J. Pikarsky, A. Choudhury, K. A. Gall and P. J. Hesketh, *J. Am. Chem. Soc. *, 2008, **130**, 14404-14405.

[40]   G. Zhu, Y. Li, H. Zhou, J. Liu and W. Yang, *Mater. Lett.*, 2008, **62**, 4357-4359.

[41]   X.-L. Liu, Y.-S. Li, G.-Q. Zhu, Y.-J. Ban, L.-Y. Xu and W.-S. Yang, *Angew. Chem., Int. Ed.*, 2011, **50**, 10636-10639.

[42]   D. Fairen-Jimenez, S. A. Moggach, M. T. Wharmby, P. A. Wright, S. Parsons and T. Düren, *J. Am. Chem. Soc.*, 2011, **133**, 8900-8902.

[43]   M. Kodaka, *J. Phys. Chem. B*, 2003, **108**, 1160-1164.

[44]   J. Cousin Saint Remi, T. Rémy, V. Van Hunskerken, S. van de Perre, T. Duerinck, M. Maes, D. De Vos, E. Gobechiya, C. E. A. Kirschhock, G. V. Baron and J. F. M. Denayer, *ChemSusChem*, 2011, **4**, 1074-1077.

5   Highly Oriented Growth and Post-synthetic Dye Labeling of Mesoporous and Functionalized Metal-organic Framework Thin Films

This chapter is based on the publication indicated below:

Florian M. Hinterholzinger,[a] Stefan Wuttke,[a] Pascal Roy,[b] Thomas Preuße,[b] Andreas Schaate,[c] Peter Behrens,[c] Adelheid Godt[b] and Thomas Bein[*a] *Dalton Transaction* 2012, **41**, 3899 − 3901.

Abstract

Mesoporous amino-functionalized metal–organic framework thin films with the UiO-68 topology were grown in a highly oriented fashion on two different self-assembled monolayers on gold. The oriented MOF films were covalently modified with the fluorescent dye Rhodamine B inside the pore system, as demonstrated with size-selective fluorescence quenching studies. Our study suggests that mesoporous metal–organic frameworks are promising hosts for the covalent attachment of numerous functional moieties in a molecularly designed crystalline environment.

5.1   Introduction

Metal‑organic frameworks (MOFs) are a class of porous materials synthesized in a building-block fashion from metal ion or metal cluster nodes interconnected by organic molecules. These porous solids can be used for several applications such as gas storage, separation, catalysis, drug delivery or as chemical sensors due to their exceptional porosity and structural diversity.[1-4] The diffusional access of guest molecules to the interior of the MOF structures can be facilitated by presenting them as thin films. The key principle for the fabrication of MOF chemosensors is the incorporation of a recognition-transduction mode.[5, 6] This can be achieved by implementing organic functional groups, e.g. −NH$_2$ or −OH groups, in order to functionalize the internal pore surface of the MOF. These groups are intended to act as anchoring points for the covalent attachment of a receptor and/or transducer by using post-synthetic modification (PSM).[7, 8] One significant challenge in this area is the development of large-pore MOFs with adequate chemical and thermal stability, whose internal surface can be appropriately functionalized.[9]
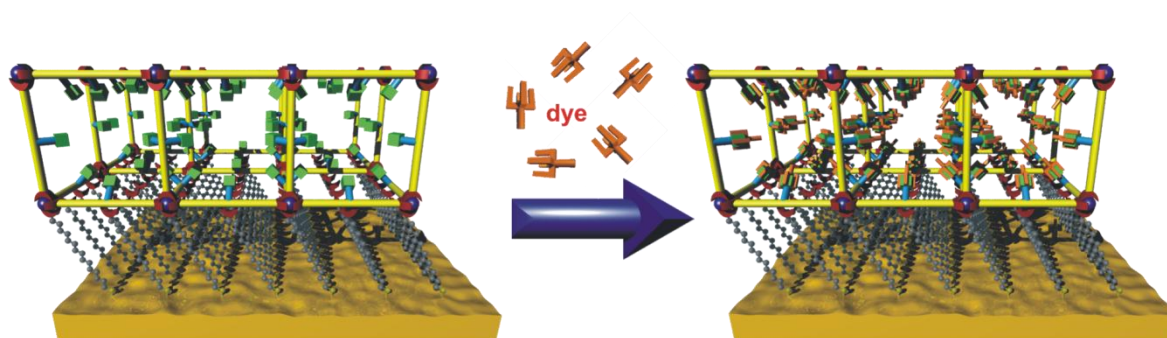
Scheme 5-1   Schematic representation of oriented and functionalized MOF crystals grown on SAM-modified gold substrates (left) followed by the post-synthetic modification of the MOF thin film with dye molecules (right).

Based on our previous results on the substrate-directed oriented growth of various MOF films,[10-12] we report here the highly oriented growth of the mesoporous and functionalized MOF UiO-68-NH$_2$ on SAM-modified gold substrates. UiO-68-NH$_2$ is a zirconium-based MOF with 2'-amino-4,4''-dicarboxy-1,1':4',1''-terphenyl as the linker.[13] UiO-68-NH$_2$ exhibits the desired stability as well as mesopores of 2.7 nm with accessible large windows of 1.0 nm for the incorporation of sterically demanding molecules. This is demonstrated by the post-synthetic covalent modification of UiO-68-NH$_2$ films with a dye molecule, that is, Rhodamine B isothiocyanate (Scheme 5-1). Finally, selective quenching experiments provide evidence for the successful attachment of the dye to the internal surface of the oriented functionalized MOF thin film and the accessibility of the interior for guest molecules.

5   Highly Oriented Growth and Post-synthetic Dye Labeling of
     Mesoporous and Functionalized Metal-organic Framework
     Thin Films

5.2   Experimental section

Chemicals

Zirconium(IV) chloride (99.9 %, *Aldrich*) and benzoic acid (*Aldrich*), 16-mercaptohexadecanoic acid (95 %, *Aldrich*), 11-mercapto-1-undecanol (97 %, *Aldrich*), phosphorus oxide chloride (*Aldrich*) and 2,4,6-trimethylpyridine (*Aldrich*), Rhodamine B isothiocyanate (*Aldrich*), diquat dibromide monohydrate (*Aldrich*), colloidal gold (~ 5 nm, *Aldrich*) as well as solvents are commercially available and were used as received. 2'-Amino-4,4''-dicarboxy-1,1':4',1''-terphenyl (*H$_2$-tpdc-NH$_2$*) was synthesized according to the literature.[13]

Self-assembled monolayers on gold substrates

Microscope glass slides (*Menzel*, 76x26 mm) were cleaned in an ultrasonic bath according to a solvent protocol (acetone, 2-propanol, Hellmanex/H$_2$O (1:100), H$_2$O, 2-propanol (Chromasolv)) followed by oxygen plasma cleaning for 30 min. The pre-cleaned microscope glass slides were mounted in a Univex 350 vacuum sputter-coating unit (Oerlikon Leybold Vacuum), and the slides were coated with Ti/Au by electron-beam evaporation under room temperature and ultra high vacuum. The gold substrates were cut in 1 x 1.3 cm pieces and cleaned for 10 min with EtOH and then for 10 min with MeOH in an ultrasonic bath. For the preparation of 11-mercapto-1-undecanephosphonate (MUP) SAMs the cleaned gold slides were immersed in a 1 mM ethanolic solution (6 pieces in 20 mL) of 11-mercapto-1-

undecanol at room temperature for 48 h. The phosphorylation of the as-prepared self-assembled organic monolayer was achieved by immersing the gold slides in a mixture (6 pieces in 40 mL) of phosphorus oxide chloride (0.1 M) and 2,4,6-trimethylpyridine (0.1 M) in acetonitrile. For the preparation of carboxyl-terminated SAMs the cleaned gold slides were immersed in a 1 mM ethanolic solution (6 pieces in 20 mL) of 16-mercaptohexadecanoic acid (16-MHDA) at room temperature for 48 h. Afterwards the SAM-functionalized gold slides were washed repeatedly with ethanol and stored in absolute ethanol until needed.

Preparation of the crystallization solution for the oriented film growth of UiO-68-NH$_2$

In a 50 mL glass reactor, zirconium(IV) chloride (0.120 g, 0.514 mmol, 1.0 eq.) and benzoic acid (1.88 g, 15.42 mmol, 30 eq.) were dissolved in dimethylformamide (DMF, 20 mL) in an ultrasonic bath. *H$_2$-tpdc-NH$_2$* (0.17 g, 0.514 mmol, 1.0 eq.) and water (0.028 mL, 1.54 mmol, 3.0 eq.) were subsequently added to the clear solution. The sealed glass reactor was kept for 24 h in a preheated oven at 120 °C. After cooling the synthesis mixture to room temperature, the bulk material was removed by filtration and the filtrate was used for the growth of thin films.

Oriented film growth of UiO-68-NH$_2$

The SAM-functionalized gold-slides were placed upside-down in Teflon$^\text{®}$ supports into the filtered synthesis solution of UiO-68-NH$_2$ (6 pieces in 20 mL). The growth

took place at room temperature in a closed glass reactor. Immersion times were varied between 5-30 d.

Fluorescence dye labeling of UiO-68-NH₂ thin films

For dye labeling experiments, Rhodamine B isothiocyanate (2 mg, 0.003 mmol) was dissolved in absolute ethanol (50 mL). UiO-68-NH$_2$ thin films were immersed in the ethanolic dye solution for 5 h under stirring. The films were repeatedly washed with ethanol and dried under nitrogen. Note that higher concentrations of the dye solution can result in a loss of crystallinity.
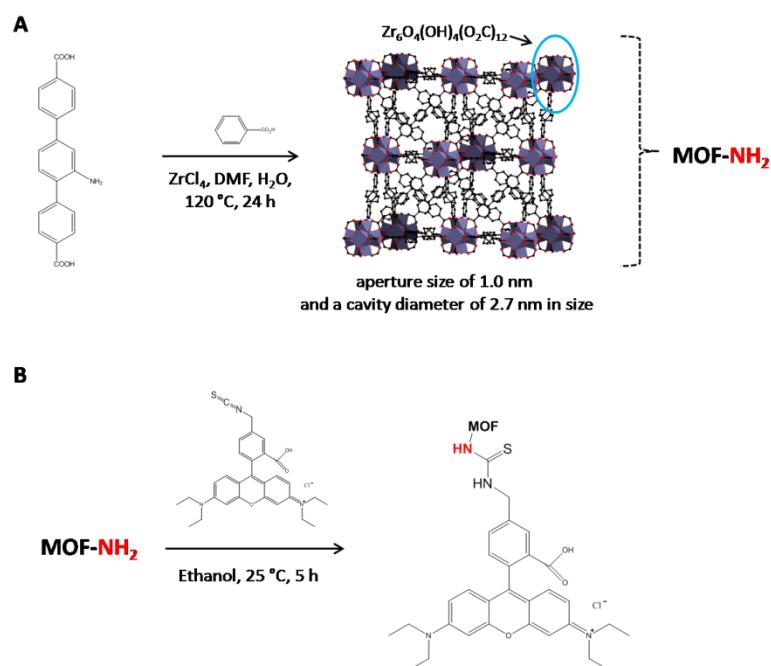
Scheme 5-2   **Synthesis route for the preparation of UiO-68-NH$_2$ crystals (A) as well as the post-synthetic dye labeling reaction with fluorescein isothiocyanate (B).**

Quenching experiments of dye labelled UiO-68-NH$_2$ thin films

Quenching experiments of as-prepared Rhodamine B labeled thin films were carried out either using a monodisperse colloidal gold solution (~ 5 nm; 50 µL/mL) or diquat dibromide monohydrate (0.018 g, 5 mM) which were dissolved in a 1:1 mixture of EtOH/H$_2$O (10 mL). The dye-labeled films were placed in a beaker which was mounted on a shaker and left in the quencher solution for 24 h.

5.3   Characterization

X-ray diffraction (XRD) measurements were performed using a Bruker D8 diffractometer (Cu-Kα1 = 1.5406 Å; Cu-Kα2 = 1.5444 Å) in *theta-theta* geometry. The films were measured between 5° and 20° two theta, with a stepsize of 0.05° *two theta* and a scan-speed of 5° min^{-1}.

Scanning electron microscopy (SEM) images were recorded with a JEOL JSM-6500F microscope equipped with an Oxford energy-dispersive X-ray (EDX) analysis system.

Fluorescence microscopy was performed using a Nikon Eclipse Ti-inverted fluorescence microscope.

Characterization of the self-assembled monolayers (SAMs) was performed by reflection absorption infrared (RAIR) spectroscopy, using a Bruker IFS 66v FTIR

spectrometer. The sample chamber with a high performance variable angle reflection accessory (A-513) was maintained at 2 mbar during the entire measurement by means of an Edwards rotary-pump. In a typical measurement on gold surfaces, an angle of incidence of 83° to the surface normal was used. A cleaned gold slide was measured as background prior to the measurements.

5.4   Results and discussion

In order to achieve the preferred crystallographic orientation of UiO-68-NH$_2$ crystals, Au (111) substrates were modified with both 11-mercapto-1-undecanephosphonate (MUP) SAMs (denoted as MOF film (a), Figure 5-1, top/middle) and 16-mercaptohexadecanoic acid (MHDA) SAMs (denoted as MOF film (b), Figure 5-1, bottom) that either exhibit terminal phosphonate groups or carboxyl groups, respectively. The idea to include SAMs with terminal phosphonate groups was inspired by results obtained with zincophosphate frameworks.[14] The modified gold substrates were subsequently immersed in a saturated UiO-68-NH$_2$ crystallization solution. After several days at room temperature, crystal layers with perfect crystallographic orientation grew on the monolayers. In Figure 5-1 the XRD patterns of both the as-prepared and the post-synthetically dye-labeled UiO-68-NH$_2$ thin films are presented.
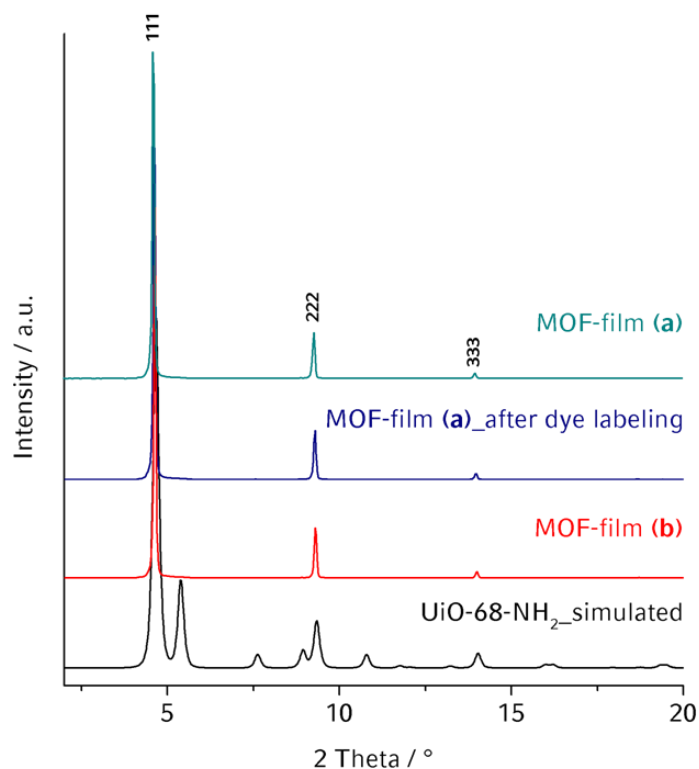
Figure 5-1   X-ray diffraction patterns (background corrected) of highly oriented UiO-68-NH$_2$ thin films grown on self-assembled monolayers of 11-mercapto-1-undecanephosphonate (MUP, MOF film (a), top/middle) and 16-mercaptohexadecanoic acid (MHDA, MOF film (b), bottom) on gold substrates. The as-prepared and dye-labeled films are compared to simulated data.

By comparing the simulated powder pattern of bulk UiO-68-NH$_2$ with the diffraction patterns of the thin films (Figure 5-1), the structure-directed orientation of the UiO-68-NH$_2$ crystals layers along the [111] direction is clearly apparent. The crystal orientation is additionally confirmed by reflections of higher order lattice planes. Note that the highly oriented crystal morphology was even observed for the films

that were post-synthetically modified with a dye solution, proving the chemical stability of the MOF structure. Moreover, the diffraction patterns of UiO-68-NH$_2$ thin films prepared on both phosphonate-terminated SAMs (MOF film (a), Figure 5-1, top) and on carboxyl-terminated SAMs (MOF film (b), Figure 5-1, bottom) exclusively show the reflections corresponding to (111) as well as to higher order lattice planes of the MOF.

The immersion times for UiO-68-NH$_2$ film growth were varied between 5-30 days. It was found that an immersion time of 7 days was sufficient to result in the surface growth of UiO-68-NH$_2$ crystals in a highly oriented fashion (Figure 5-2 and Figure 5-3).
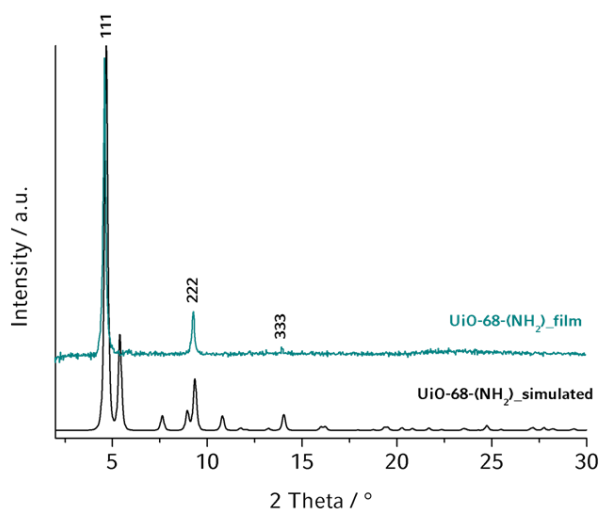
Figure 5-2   **X-ray diffraction pattern (background corrected) of a highly oriented UiO-68-NH$_2$ thin film grown for 7 d on 11-mercapto-1-undecanephosphonate (MUP) SAM functionalized gold substrates compared to simulated data.**
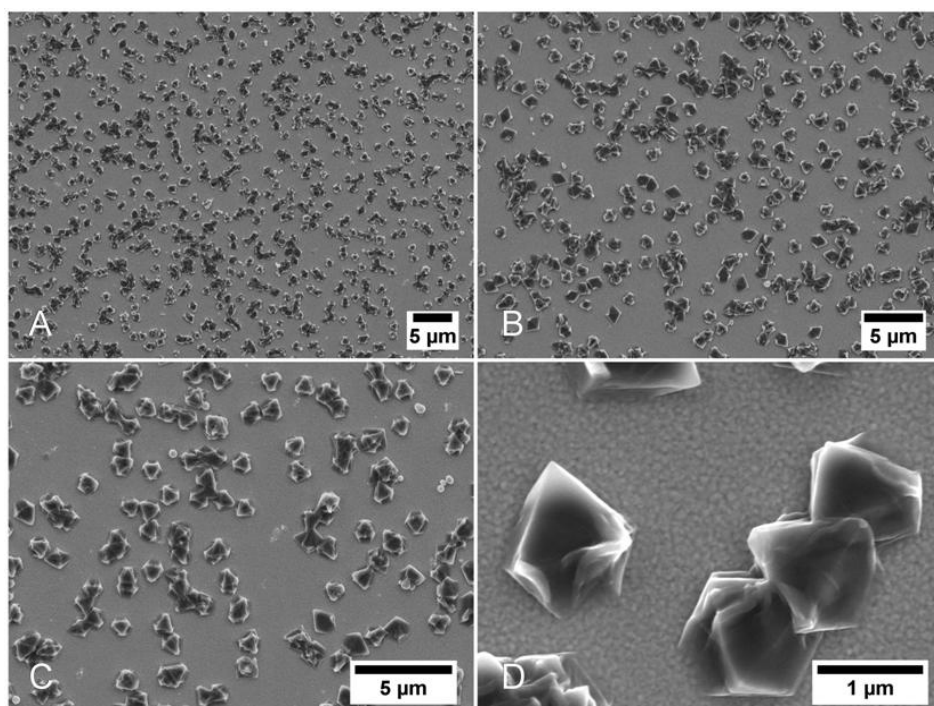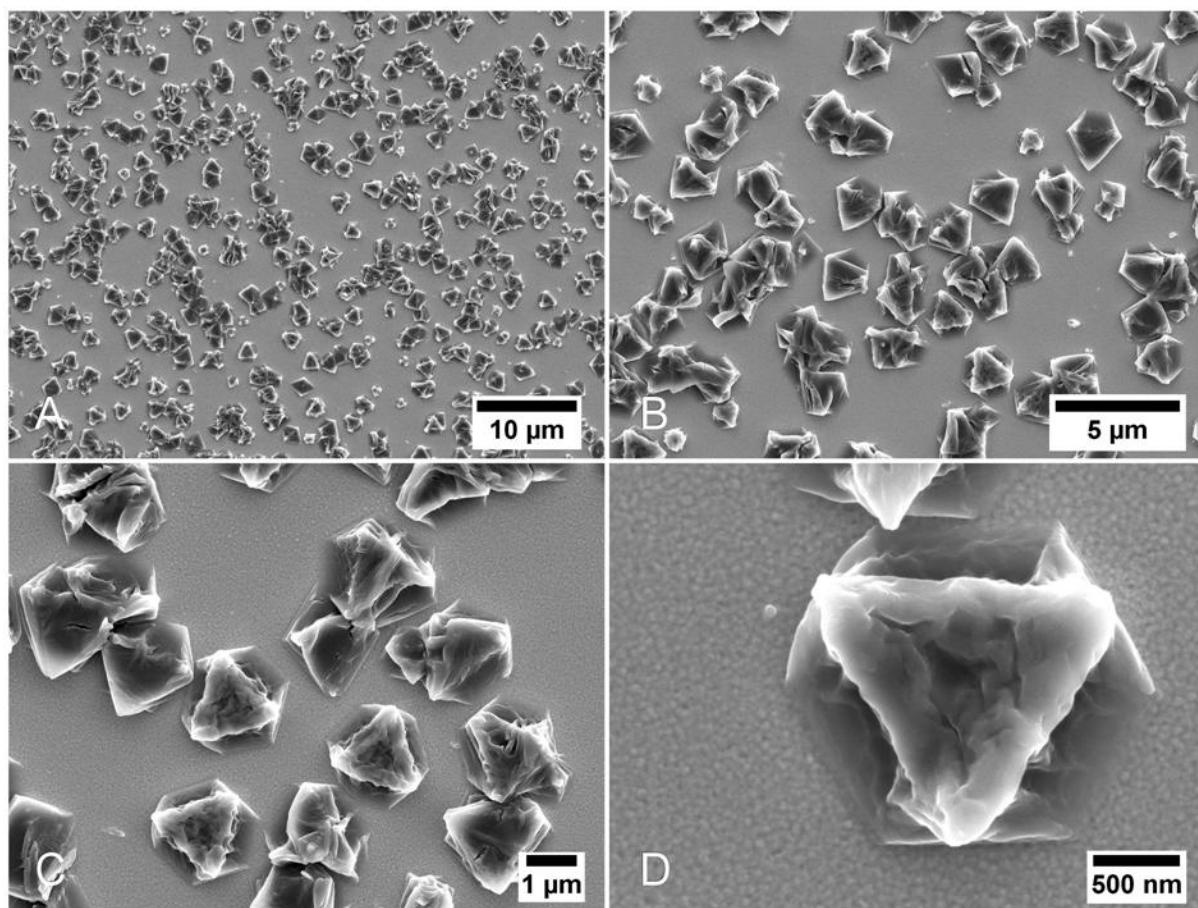
Figure 5-3   Scanning electron micrographs showing highly oriented growth of UiO-68-NH$_2$ crystals along the preferred [111] direction on a 16-mercaptohexadecanoic acid SAM modified gold substrate. The functionalized substrate was immersed in the crystallization solution for 7 days.

With the intention to achieve a dense coverage of the gold surface, immersion times were extended to 30 days (as in the case for the dye-labeled MOF thin film (a), Figure 5-1, top). Furthermore, a secondary crystal growth was carried out by additionally immersing the MOF film in a freshly prepared crystallization solution (MOF film (b), Figure 5-1, bottom). It was observed that both approaches, the extended immersion time as well as the secondary growth in a fresh crystallization solution, result in a somewhat higher surface coverage with UiO-68-NH$_2$ crystals (Figure 5-3).

The oriented surface growth of the UiO-68-NH$_2$ crystals is also reflected in the SEM pictures shown in Figure 5-4.

Figure 5-4   **Scanning electron micrographs showing the highly oriented growth of UiO-68-NH$_2$ crystals along the preferred [111] orientation. MOF film (b) was synthesized by immersing the 16-mercaptohexadecanoic acid SAM-modified substrates in the crystallization solution for 20 days at room temperature followed by a second growth step of 10 days in a freshly prepared crystallization solution. The SEM images are depicted at different magnifications (see scale bars).**

The SEM images show a UiO-68-NH$_2$ crystal population that is attached to MHDA-SAM functionalized gold substrates. The presented surface coverage was obtained

by performing the secondary growth step as mentioned above. Micrometer-sized octahedral are displayed in Figure 5-4. The preferred orientation along the [111] direction is clearly shown by the presence of the triangular (111) faces of the UiO-68-NH$_2$ octahedra, which is in excellent agreement with the 111 reflection intensity deduced from the XRD results (Figure 5-1).

The ability to grow mesoporous amino-functionalized MOF thin films provides the basis for post-synthetic modification (PSM) reactions and thus for the incorporation of functionality into the scaffold. PSM reactions on bulk samples are being intensively studied,[7, 15, 16] whereas post-synthetic modifications of MOF thin films are still very rare.[17] This is due to the limited number of addressable MOF candidates meeting the requirements (functional group, chemical stability and accessible large pores) for post-synthetic modifications. We emphasize that the highly oriented UiO-68-NH$_2$ thin films described here feature all the desired properties, a chemically addressable amino group and large pores of 2.7 nm diameter that are accessible through the large windows of 1.0 nm diameter. Thus, the UiO-68-NH$_2$ thin films were modified using the fluorescent dye Rhodamine B isothiocyanate. The films were immersed in an ethanolic Rhodamine B isothiocyanate solution for 5 h at room temperature to achieve covalent coupling (see Chapter 5.2).
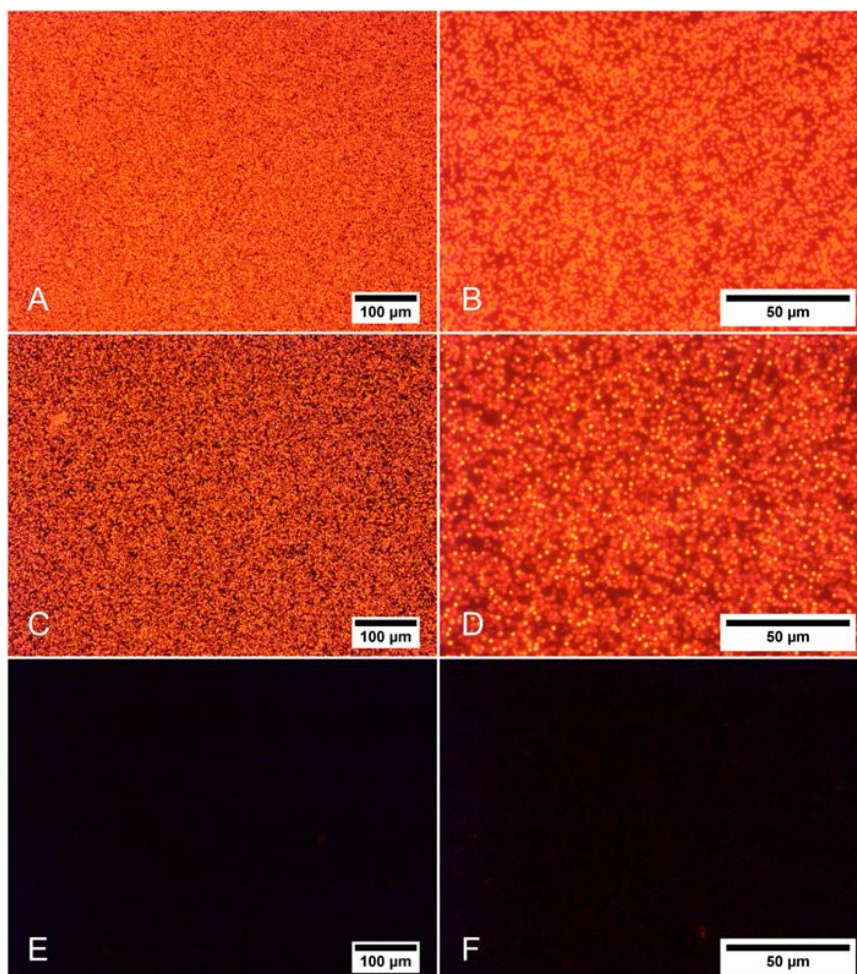
Figure 5-5   Fluorescence microscopy images demonstrating the post-synthetic labeling of oriented UiO-68-NH$_2$ thin films (A + B, MOF film (a)) with Rhodamine B as well as the results of fluorescence quenching experiments using a colloidal AuNP solution (C + D, MOF film (b)) and diquat dibromide monohydrate (E + F, MOF film (a)). The fluorescence images are shown at different magnifications (see scale bars).

In Figure 5-5 (A+B, MOF film (a)) the fluorescence images of UiO-68-NH$_2$ thin films after dye labeling are depicted. Bright red fluorescence due to the covalently bound Rhodamine B is observed. In order to provide evidence for the successful dye labeling of the interior of the MOF crystals, two different quenching experiments

were carried out. Gold nanoparticles (AuNPs) with an average diameter of 5 nm were used as a colloidal suspension for quenching experiments of dye molecules bound to the external surface of UiO-68-NH$_2$ crystal layers.[18] Clearly, the red fluorescence is mostly retained after exposure to the AuNPs (Figure 5-5, C+D, MOF film (b)) indicating that dye labeling mainly occurred within the mesopores of UiO-68-NH$_2$. To support this interpretation as well as to prove the accessibility of the dye modified pores, diquat dibromide monohydrate with a kinetic diameter of about 0.7 nm was chosen for quenching the fluorescence of Rhodamine B.[19] Near complete fluorescence quenching of the dye-labeled UiO-68-NH$_2$ thin films was achieved as indicated in Figure 5-5 (E+F, MOF film (a)). This observation demonstrates complete molecular access into the mesopore system of the crystal layer.

5.5   Conclusion

In summary, highly oriented UiO-68-NH$_2$ thin films were obtained by room temperature growth on two different types of self-assembled monolayers. It was shown for the first time that MOF thin films could be grown in a highly oriented fashion on phosphonate termini of an organic monolayer. Moreover, the post-synthetic pore modification of UiO-68-NH$_2$ thin films with a fluorescent dye was achieved and confirmed by quenching experiments with differently sized quenching agents. The concept of oriented crystal growth on SAM-modified gold substrates

could successfully be extended to functionalized and mesoporous MOF structures. We anticipate that mesoporous UiO-68‑NH$_2$ thin films will offer a versatile platform for precisely designing various host‑guest interactions within a stable pore system featuring a well-defined molecular framework.

5.6   References

[1]   G. Ferey, *Chem. Soc. Rev.*, 2008, **37**, 191-214.

[2]   O. M. Yaghi, M. O'Keeffe, N. W. Ockwig, H. K. Chae, M. Eddaoudi and J. Kim, *Nature*, 2003, **423**, 705-714.

[3]   D. J. Tranchemontagne, J. L. Mendoza-Cortes, M. O'Keeffe and O. M. Yaghi, *Chem. Soc. Rev.*, 2009, **38**, 1257-1283.

[4]   J. R. Long and O. M. Yaghi, *Chem. Soc. Rev.* , 2009, **38**, 1213-1214.

[5]   M. D. Allendorf, C. A. Bauer, R. K. Bhakta and R. J. T. Houk, *Chem. Soc. Rev.*, 2009, **38**, 1330-1352.

[6]   L. E. Kreno, K. Leong, O. K. Farha, M. Allendorf, R. P. Van Duyne and J. T. Hupp, *Chem. Rev.*, 2011, **112**, 1105-1125.

[7]   Z. Wang and S. M. Cohen, *Chem. Soc. Rev.*, 2009, **38**, 1315.

[8]   S. M. Cohen, *Chem. Sci.*, 2010, **1**, 32-36.

[9]   B. Liu, M. Ma, D. Zacher, A. Bétard, K. Yusenko, N. Metzler-Nolte, C. Wöll and R. A. Fischer, *J. Am. Chem. Soc.*, 2011, **133**, 1734-1737.

[10]   E. Biemmi, C. Scherb and T. Bein, *J. Am. Chem. Soc.*, 2007, **129**, 8054.

[11]   A. Schoedel, C. Scherb and T. Bein, *Angew. Chem., Int. Ed.*, 2010, **49**, 7225.

[12]   C. Scherb, J. J. Williams, F. Hinterholzinger, S. Bauer, N. Stock and T. Bein, *J. Mater. Chem.*, 2011, **21**, 14849-14856.

[13]   A. Schaate, P. Roy, A. Godt, J. Lippke, F. Waltz, M. Wiebcke and P. Behrens, *Chem.– Eur. J.*, 2011, **17**, 6643-6651.

[14]   S. Feng and T. Bein, *Nature*, 1994, **368**, 834-836.

[15]   Z. Wang, K. K. Tanabe and S. M. Cohen, *Inorg. Chem.*, 2009, **48**, 296-306.

[16]   K. K. Tanabe and S. M. Cohen, *Chem. Soc. Rev.*, 2011, **40**, 498-519.

[17]   O. Shekhah, H. K. Arslan, K. Chen, M. Schmittel, R. Maul, W. Wenzel and C. Woll, *Chem. Commun.*, 2011, **47**, 11210-11212.

[18]   V. Cauda, A. Schlossbauer, J. Kecht, A. Zürner and T. Bein, *J. Am. Chem. Soc.*, 2009, **131**, 11361-11370.

[19]   A. B. Fischer and I. Bronstein-Bonte, *J. Photochem.*, 1985, **30**, 475-485.

6   A chemoluminescent metal-organic framework

This chapter is based on the publication indicated below:

Stefan Wuttke,[a‡] Bastian Rühle,[a‡] Florian M. Hinterholzinger,[a] Pascal Roy,[b] Adelheid Godt*[b] and Thomas Bein*[a], *manuscript in preparation.*

6.1   Introduction

The great interest in metal-organic frameworks (MOFs) is a consequence of the simultaneous occurrence of important characteristics in a single material. MOFs are crystalline solids that are connected by strong metal-ligand interactions, which can confer permanent porosity to the material, *i.e.,* it is possible to remove the solvent and impurity molecules completely without structural collapse. The pore size, shape, and dimensionality of the MOF pore system as well as its local chemical environment can be easily controlled by the judicious selection of the building blocks (metal and organic linkers) and their connection.[1, 2] This ability of tailoring the pore functionality and with it the scaffold has been used to integrate different functionalities for different purposes such as incorporation of catalysts for various catalytic reactions,[3, 4] tuning the pore radii and surface area for gas storage or separation,[5, 6] synthesis of MOFs with contrast agents for magnetic resonance

imaging diagnostics,[7] or the synthesis of luminescent MOFs for applications as fluorescent sensors.[8, 9]

Luminescence as a transduction mechanism has many advantages that can be summarized in the following way: measurements are usually very sensitive, easily performed, and they can offer high spatial resolution with even single molecule visualization as well as high temporal resolution. Therefore, luminescence is frequently used as a reporter mode for the design of a chemo-sensor. In this context, fluorescence is by far the most widely investigated type of luminescence. However, to the best of the author's knowledge, no MOF featuring chemoluminescence has been reported so far. Chemiluminescence is defined as the emission of electromagnetic radiation when an electron in an excited state of an atom or molecule returns to its ground state energy level. However, in chemoluminescence the excitation of the electron is induced by a chemical reaction rather than by absorption of photons, as it is the case for fluorescence. A distinct advantage in comparison to fluorescence spectroscopy is the absence of external light sources, which means that the analytically relevant emission can be measured against a completely dark background − resulting in a potentially higher sensitivity with this transducer concept.

To implement chemiluminescence into a MOF structure, we chose 9,10-diphenylanthracene for the incorporation into a MOF scaffold because it exhibits intense chemiluminescence elicited by the reaction between oxalic acid esters and hydrogen peroxide in the presence of a base.[10] It is important that the MOF remains stable under the conditions of chemiluminescence, in this case stable against a

mixture of hydrogen peroxide and sodium salicylate as well as the compounds formed *in situ* to bring about chemiluminescence. Several studies have demonstrated that Zr-based MOF structures are chemically quite robust.[11-14] In order to design a MOF with diphenylanthracene moieties being part of the linker, we chose the UiO-66 topology. The framework of UiO-66 consists of $Zr_6O_4(OH)_4(CO_2)_{12}$ clusters, where each one is connected with twelve other clusters by a dicarboxylate linker.[11, 12]

6.2   Experimental section

Chemicals

Zirconiumtetrachloride (99.9%, *Aldrich*), *N,N*-dimethylformamide (DMF; 99.8%, *Aldrich*), bis(2,4,6-trichlorophenyl)oxalate (TCPO; 98%, TCI), dimethyl phthalate (99%, *Aldrich*), dibutyl phthalate (99%, *Aldrich*), hydrogen peroxide (30%; *Merck*), *tert*-butanol (99.7%, *Aldrich*), and sodium salicylate (99.5%, *Aldrich*) were used as received.

Synthesis of 4,4'-(anthracene-9,10-diyl)dibenzoic acid

The synthesis of 4,4'-(anthracene-9,10-diyl)dibenzoic acid was carried out in the group of Prof. Adelheid Godt at the University of Bielefeld.

Synthesis of UiO-68(anthracene)

The synthesis was performed in a high throughput (HT) parallel reactor with 24 wells each containing the same reaction mixture. 4,4'-(Anthracene-9,10-diyl)dibenzoic acid (16.9 mg, 40 µmol), zirconium tetrachloride (9.3 mg, 40 µmol), water (1.1 µL, 61.1 µmol) and DMF (1 mL) were added to each well. The HT parallel reactor containing the reaction mixture was heated to 200 °C for 21 h. After cooling to room temperature the precipitate was isolated. It was washed three times with DMF and then three times with dichloromethane and was finally dried at reduced pressure.

Chemiluminescence experiments

For carrying out the chemiluminescence experiments, we followed a published procedure with slight modifications.[15] UiO-68(anthracene) (1 mg) was suspended in a solution of bis(2,4,6-trichlorophenyl)oxalate (TCPO) (30 mg, 66.8 µmol) in dibutyl phthalate (1 mL) using vortex shaking and brief sonification. In another vessel, a polypropylene beaker, a solution of tert-butanol (3.55 mL, 37.8 mmol), aqueous H_2O_2 (30 %; 3.00 mL, 38.1 mmol), and sodium salicylate (1.80 mg, 11.25 µmol) in dimethyl phthalate (13.45 mL) was prepared and stirred at room temperature for 5 min at 500 rpm. Then, more sodium salicylate (1.80 mg, 11.25 µmol) was added and the solution was stirred at room temperature for another 5 min at 500 rpm. To start the chemiluminescence reaction, equal volumes (1 mL each) of both solutions were combined.

For testing the stability of UiO-68(anthracene) during the chemilumenscence experiment the two solutions were prepared as described above, however 5 mg of UiO-68(anthracene) were used. The two solutions were combined and the resulting mixture was stirred for 10 min at room temperature. The solid was isolated by centrifugation (5 min at 14000 rpm (16873 rcf)), washed three times with dichloromethane (15 mL), dried with a stream of nitrogen, and finally subjected to X-ray diffraction analysis.

For the chemiluminescence experiment monitored with optical microscopy, the two solutions were prepared as described above, however without adding the UiO-68(anthracene). Both solutions were centrifuged at 14000 rpm (16873 rcf) for 4 min in an Eppendorf tabletop centrifuge (Model No. 5418) to remove any particulate matter from the solutions. MOF crystallites were spread out at the bottom of one microwell of an 8-well Lab-Tek II Chambered #1.5 German Coverglass System (NUNC, 155409 - 8 Chamber). The two solutions were mixed at a volume ratio of 1:1, and this mixture (400 µL) was added to the MOF crystallites in the microwell.

6.3   Characterization

Methods

Powder X-ray diffraction (PXRD) measurements were performed using a Bruker D8 diffractometer (Cu-Kα1 = 1.5406 Å; Cu-Kα2 = 1.5444 Å) in *theta-theta* geometry equipped with a Lynx-Eye detector. The powder samples were measured between 2° and 45° two theta, with a step size of 0.05° two theta.

Chemiluminescence was monitored using a PTI fluorescence spectrometer featuring a PTI 814 photomultiplier detector, a PTI MD5020 motor driver, and a Quantum Northwest TC 125 sample holder. No excitation light was used since the samples emit light. The bandpass of the detector was set to 2 nm, and each 30 s an emission spectrum was recorded from 350 nm to 550 nm at a step width of 1 nm and an integration time of 0.1 s per step.

Microscopy images were recorded using a Nikon Eclipse Ti-U inverted microscope equipped with a Nikon Plan Fluor 10x/0.30 objective and an Andor iXon+ DU897-BV back-illuminated electron multiplying charge-coupled device (EM-CCD) camera in kinetic mode with an exposure time of 2 seconds and a kinetic cycle time of 5 seconds. 1 pixel on the detector corresponds to 1.57 μm. The detector was cooled to -80 °C during measurements. No excitation light was used.

FTIR measurements were performed in transmission mode on a Bruker Equinox 55s between 4000 and 400 cm^{-1} at a resolution of 4 cm^{-1}.

Nitrogen sorption measurements were performed on a Quantachrome Instruments Autosorb at 77 K. The sample was heated to 393 K for 12 hours prior to sorption studies. Pore sizes and pore volumes were calculated using a NLDFT equilibrium model of N_2 on silica, based on the adsorption isotherm. The BET surface area was calculated over the range of $0.05 - 0.20$ p/p_0. The pore volume was calculated based on the uptake (cm^3/g) at a relative pressure of 0.30 p/p_0.

Thermogravimetric analyses of the bulk samples were performed on a Netzsch STA 440 C TG/DSC with a heating rate of 1 K min^{-1} in a stream of synthetic air at about 25 mL min^{-1}.

6.4   Results and discussion

The UiO-68(anthracene) was synthesized under solvothermal synthesis conditions from 4,4'-(anthracene-9,10-diyl)dibenzoic acid and $ZrCl_4$ in DMF and H_2O at 120 °C for 24 h. The reaction conditions were found *via* high-throughput screening of the effects of various molar ratios of starting materials, various concentrations, different solvent ratios, and of the addition of benzoic acid. It turned out in this case that the addition of benzoic acid, the modulator used for the syntheses of UiO-66, UiO-67, UiO-68(NH_2) and the structurally closely related PIZOFs[12] was not needed, which simplifies the purification of the MOF.

X-ray diffraction analysis confirmed that the solid is isostructural (isoreticular) to UiO-68 and that UiO-68(anthracene) was obtained in a purely crystalline form (Figure 6-1).
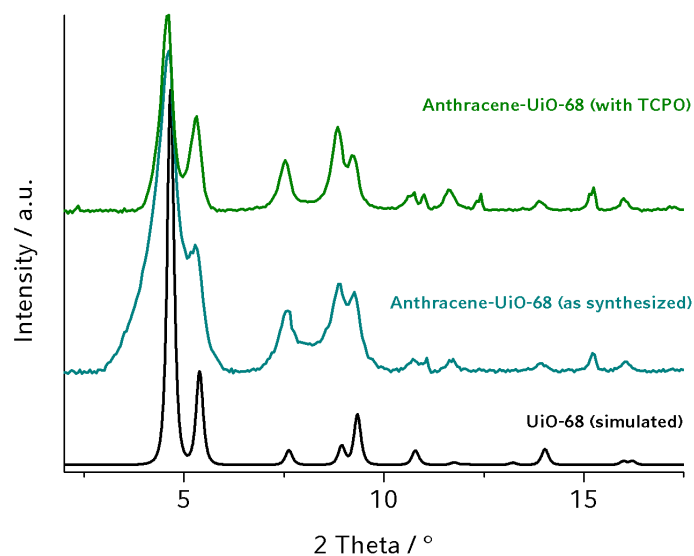
Figure 6-1   PXRD patterns of the UiO-68(anthracene) before (blue) and after (green) exposure to the conditions of the chemiluminescence reaction, and the simulated PXRD pattern of UiO-68 (black).

Thermogravimetric analysis (TGA) showed two significant weight loss steps (Figure 6-2 (a)). The first endothermic step with a mass loss of 6 % in the range between 25 °C and 420 °C is attributed to the evaporation of solvent. The second weight loss of 67 % between 420 °C and 530 °C is due to the decomposition of the organic linkers. Thus, this MOF exhibits an exceptional thermal stability in comparison to other MOFs, especially when considering the mesoporous nature of this MOF (the UiO-68 structure features mesopores of 2.7 nm with large windows of 1.0 nm as described in reference 12). Often a mesoporous MOF structure leads to poor thermal stability. Moreover, the measured BET surface area of about 1349 m^2g^{-1} is so far the highest reported surface area of a UiO-68 structure (Figure 6-2 (b)).
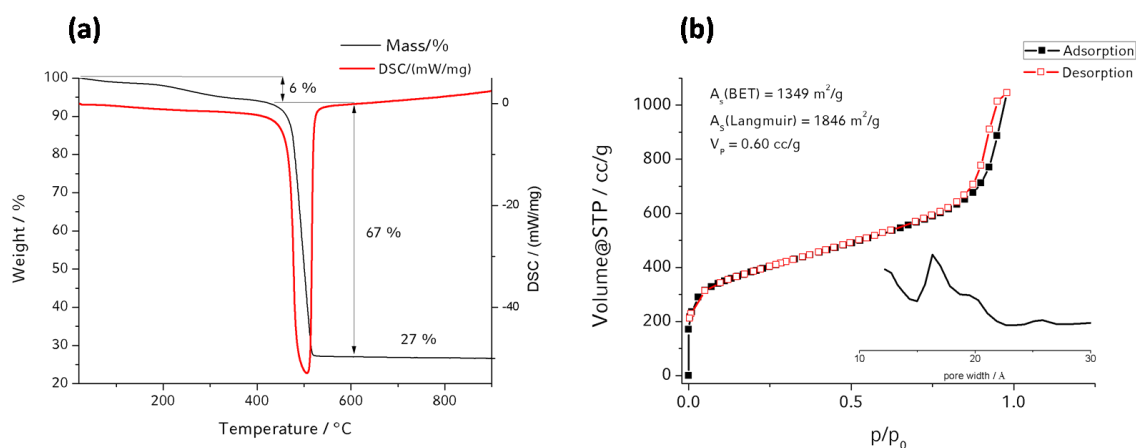
Figure 6-2   **(a) Thermogravimetric analysis of UiO-68(anthracene) in flowing air with a heating rate of 1 K min^{-1} and a flow rate of 25 mL min^{-1}. (b) Results of the Physisorption measurement performed with nitrogen at 77 K on bulk UiO-68(anthracene) showing the characteristic shape of the isotherm, the specific surface area (BET/Langmuir), the pore volume and the calculated pore-size distribution (NLDFT).**

One of the most common and efficient ways to excite chemiluminescence of diphenylanthracene is an energy transfer resulting from the reaction of oxalic acid esters, such as bis(2,4,6-trichlorophenyl)oxalate (TCPO), with hydrogen peroxide to the diphenylanthracene moiety,[16-19] as depicted in a simplified manner in Scheme 6-1. In fact, the detailed mechanism of the energy transfer might be more involved, including the formation of an encounter complex between an intermediate (*e.g.*, dioxetandione) and the diphenylanthracene moiety, followed by radical formation *via* single electron transfers, thus rendering the whole process a chemically initiated electron exchange luminescence.[16, 17, 19]
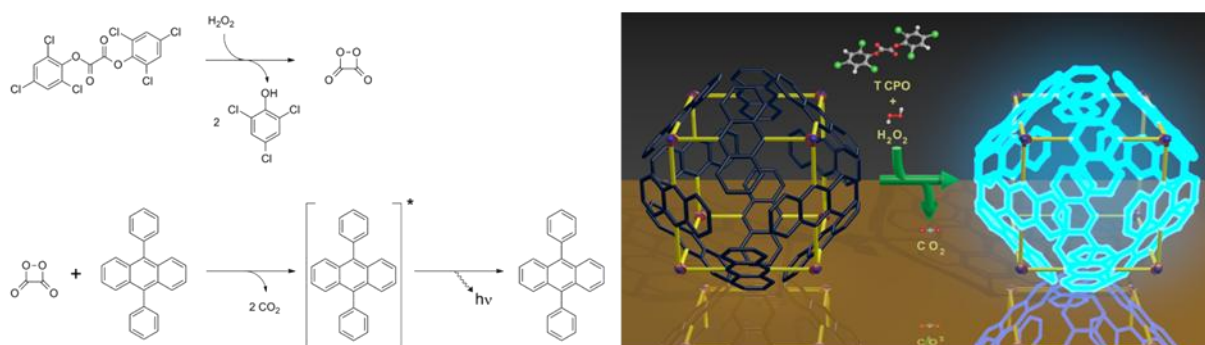
Scheme 6-1 **Simplified representation of the assumed mechanism leading to the electronic excitation and subsequent chemiluminescence of 9,10-diphenylanthracene through reaction with 1,2-dioxetan-3,4-dione formed** *in-situ.*[19] **The asterisk indicates an electronically excited state.**

When performing the chemiluminescence reaction we followed a published procedure[15] with slight modifications (see Experimental section). In general, these reactions are carried out in a rather apolar organic solvent in order to dissolve the TCPO in the presence of a small amount of a weak base such as sodium salicylate. Presumably, the base assists in the formation of the proposed 1,2-dioxetan-3,4-dione through deprotonation of the intermediate oxalic peroxyacid.[18] Figure 6-3a shows the strong chemiluminescence observed when mixing the MOF with the components mentioned above. The chemiluminescence was monitored with a photoluminescence setup. It reached its emission maximum after approximately 10 min (Figure 6-3a,b).
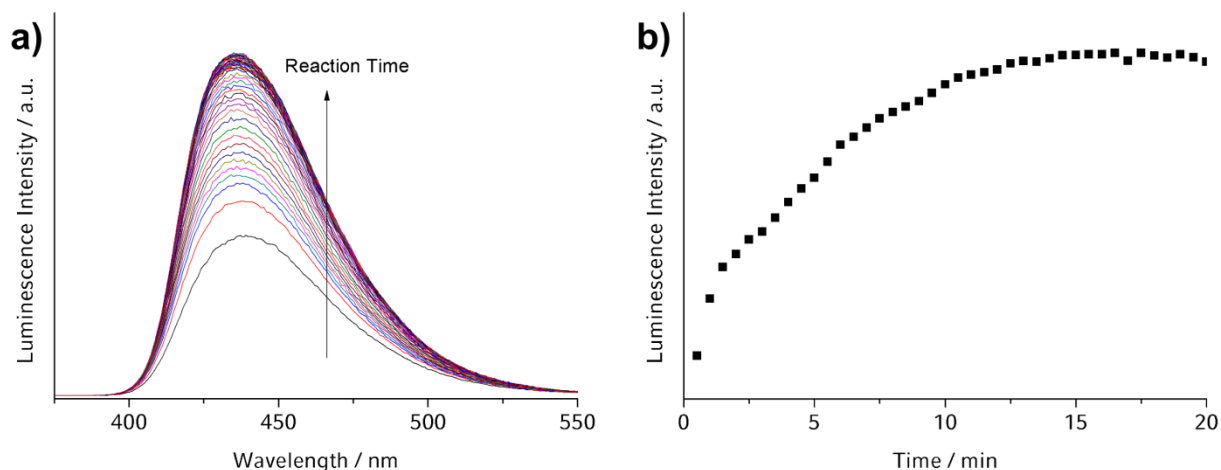
Figure 6-3   **(a) Chemiluminescence spectra of the UiO-68(anthracene) in a mixture of dimethyl and dibutylphthalate at different points in time. (b) Development of the fluorescence intensity at λ_{max}= 436 nm over time.**

To ensure that the observed luminescence is indeed emitted from the metal-organic framework and does not result from linker molecules in the solution as a result of framework decomposition, we carried out the following experiments. We subjected the UiO-68(anthracene) to the reagents and conditions of the chemiluminescence reaction, isolated the solid material from the dispersion, and characterized the material by X-ray diffraction. The PXRD pattern (Figure 6-1) clearly indicates that the crystalline structure of the framework was maintained. Furthermore, we used optical microscopy in order to identify the source of luminescence. When observing MOF particles sitting at the bottom of a container with a fluorescence microscope (without using excitation light) upon addition of a solution of bis(2,4,6-trichlorophenyl)oxalat (TCPO) and a solution of hydrogen peroxide and sodium salicylate, strong luminescence originating from the MOF crystallites was seen, whereas the background luminescence did not show a significant increase. This is shown by the development of the mean integrated intensities within two equally

sized rectangular regions of interest (ROIs) over time, one containing a MOF crystallite (ROI 1) and one containing only background (ROI 2) (Figure 6-4). If the framework had decomposed, free linker molecules should have diffused into the surrounding solution and would have caused an increase in background luminescence.
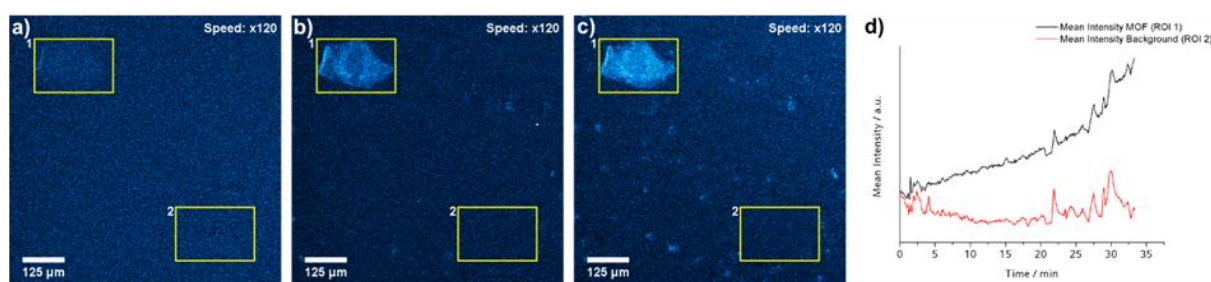
Figure 6-4   **(a-c) Images taken from a movie showing the luminescence after 0 min (a), 14 min (b) and 28 min (c) following addition of a solution of bis(2,4,6-trichlorophenyl)oxalate (TCPO) in dibutylphthalate and a solution of hydrogen peroxide and sodium salicylate in dimethylphthalate and *tert*-butanol to particles of UiO-68(anthracene) sitting at the bottom of a vessel. (d) Graph showing the mean integrated intensities of the two regions of interest (ROIs) highlighted in (a-c). ROI 1 contains the MOF crystallite, ROI 2 contains only background.**

6.5   Conclusions

In conclusion, the synthesis of the novel MOF UiO-68(anthracene) was developed *via* a high-throughput approach. In contrast to the structurally related UiO-68(NH_2) and PIZOFs, no modulation agent is necessary to obtain a highly crystalline material. Nitrogen sorption analysis demonstrates the high porosity of this MOF, and thermogravimetry points to exceptional thermal stability.

Strikingly, UiO-68(anthracene), a Zr-based MOF with 4,4'-(anthracene-9,10-diyl)dibenzoate as the linker and the topology of UiO-66, shows strong chemiluminescence once exposed to a solution of bis(2,4,6-trichlorophenyl)oxalate, hydrogen peroxide and sodium salicylate. During the chemiluminescence reaction the structure of UiO-68(anthracene) persists. To the best of our knowledge, this is the first ever MOF structure showing the phenomenon of chemiluminescence.

6.6   References

[1]   G. Ferey, *Chem. Soc. Rev.*, 2008, **37**, 191-214.

[2]   S. Kitagawa, R. Kitaura and S.-i. Noro, *Angew. Chem., Int. Ed.*, 2004, **43**, 2334-2375.

[3]   L. Ma, C. Abney and W. Lin, *Chem. Soc. Rev.*, 2009, **38**, 1248-1256.

[4]   A. Corma, H. García and F . X. Llabrés i Xamena, *Chem. Rev.*, 2010, **110**, 4606-4655.

[5]   L. J. Murray, M. Dinca and J. R. Long, *Chem. Soc. Rev.*, 2009, **38**, 1294-1314.

[6]   J.-R. Li, J. Sculley and H.-C. Zhou, *Chem. Rev.*, 2012, **112**, 869-932.

[7]   P. Horcajada, R. Gref, T. Baati, P. K. Allan, G. Maurin, P. Couvreur, G. Férey, R. E. Morris and C. Serre, *Chem. Rev.*, 2012, **112**, 1232-1268.

[8]   Y. Cui, Y. Yue, G. Qian and B. Chen, *Chem. Rev.*, 2012, **112**, 1126-1162.

[9]   L. E. Kreno, K. Leong, O. K. Farha, M. Allendorf, R. P. Van Duyne and J. T. Hupp, *Chem. Rev.*, 2012, **112**, 1105-1125.

[10]   L. Faulkner and A. Bard, *J. Am. Chem. Soc.*, 1968, **90**, 6284-6290.

[11]   J. Cavka, H., S. Jakobsen, U. Olsbye, N. Guillou, C. Lamberti, S. Bordiga and K. Lillerud, P., *J. Am. Chem. Soc. *, 2008, **130**, 13850-13851.

[12]   A. Schaate, P. Roy, A. Godt, J. Lippke, F. Waltz, M. Wiebcke and P. Behrens, *Chem.– Eur. J.*, 2011, **17**, 6643-6651.

[13]   H.-L. Jiang, D. Feng, T.-F. Liu, J.-R. Li and H.-C. Zhou, *J. Am. Chem. Soc.*, 2012, **134**, 14690-14693.

[14]   F. M. Hinterholzinger, S. Wuttke, P. Roy, Preu, A. Schaate, P. Behrens, A. Godt and T. Bein, *Dalton Trans.*, 2012, **41**, 3899-3901.

[15]   J. R. Schleck, G. J. Keiko and V. M. Chopdekar, *US Patent 5, 281, 367*, **1994**.

[16]   E. A. Chandross, *Tetrahedron Letters*, 1963, **4**, 761-765.

[17]   G. B. Schuster, *Acc. Chem. Res.*, 1979, **12**, 366-373.

[18]   C. V. Stevani, I. P. de Arruda Campos and W. J. Baader, *J. Chem. Soc., Perkin Trans.*, 1996, **2**, 1645-1648.

[19]   C. V. Stevani, S. M. Silva and W. J. Baader, *Eur. J. Org. Chem.*, 2000, **24**, 4037-4046.

7   Highly sensitive and selective fluoride detection in water through fluorophore release from a metal-organic framework

This chapter is based on the publication indicated below:

Florian M. Hinterholzinger,[a‡] Bastian Rühle,[a‡], Stefan Wuttke[a], Konstantin Karaghiosoff[b] and Thomas Bein*[a], *submitted.*

Abstract

The detection, differentiation and visualization of compounds such as gases, liquids or ions are key challenges for the design of selective optical chemosensors. Optical chemical sensors employ a transduction mechanism that converts a specific analyte recognition event into an optical signal. Here we report a novel concept for fluoride ion sensing where a porous crystalline framework serves as a host for a fluorescent reporter molecule. The detection is based on the decomposition of the host scaffold which induces the release of the fluorescent dye molecule. Specifically, the hybrid composite of the metal-organic framework NH_2-MIL-101(Al) and fluorescein acting as reporter shows an exceptional turn-on fluorescence in aqueous fluoride-containing solutions. Using this novel strategy, the optical detection of fluoride is extremely sensitive and highly selective in the presence of many other anions.

7.1   Introduction

Over the past decades a great deal of attention has been devoted to the discovery of new analytical methods for the reliable detection of target species.[1-4] The real-time monitoring of fluoride ion concentration in aqueous and physiological media as well as its quantitative determination across a large concentration range is of vital importance for various environmental and health-care issues as well as in industrial and scientific applications.[5-8] Several strategies have been reported on fluoride detection using recognition-transduction schemes based on the optical read-out of a luminescent or colorimetric signal. Examples include molecular recognition protocols using boron-based anion receptors[5, 6, 9-11] or mesoporous silica host materials[12] that are equipped with a reporter molecule to monitor either luminescence quenching or turn-on processes, whereas recently a sensitive colorimetric fluoride sensor based on supramolecular interactions such as charge or electron transfer, respectively, was described.[13] However, most of the molecule-based analytical methods suffer from interference with other anions or are incompatible with aqueous media, which greatly limits the scope of their use.[14, 15] Here we demonstrate how the analyte-induced degradation of a hybrid host material with embedded reporter molecules can be efficiently used as an extremely sensitive signal transduction mode (Figure 7-1). It is thus anticipated that our new recognition-transduction mechanism contributes to the development of optically encoded chemosensors and hence for the sensitive visualization of specific host-guest interactions.
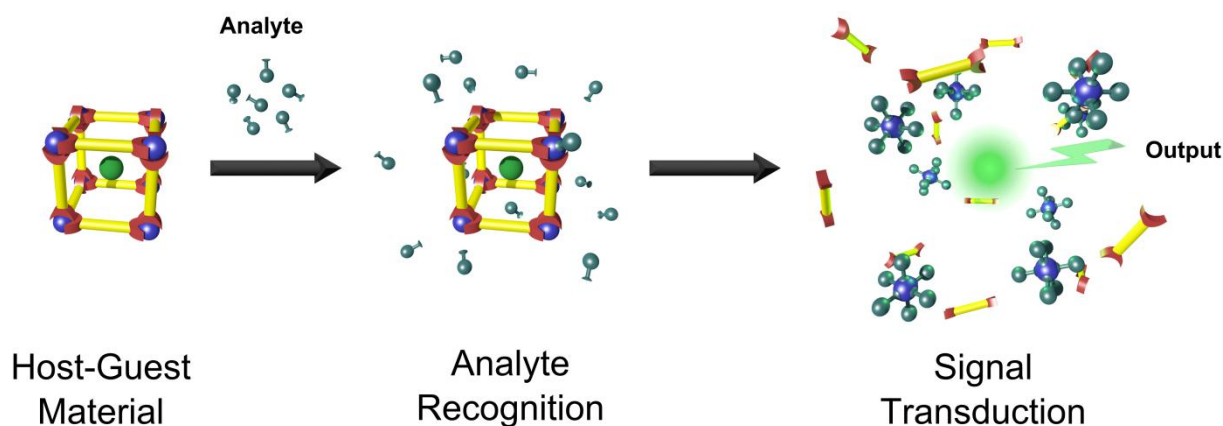
Figure 7-1   **Schematic illustration of the recognition-transduction scheme by metal-anion complexation-induced decomposition of a MOF framework. The MOF scaffold with covalently entrapped reporter molecules serves as a non-emissive host-guest material for the detection of analyte species. The recognition is realized as a competitive metal-anion complexation in an aqueous analyte-containing environment. The degradation process leads directly to the turn-on of the fluorescence of the reporter molecules, which is correlated with the fluoride ion concentration.**

Metal-organic frameworks (MOFs), also known as porous coordination polymers (PCPs),[16-18] have attracted great interest in the last decade as a new class of highly porous materials ideally suited for applications in gas adsorption, separation processes[19-21] and chemical sensing.[22-24] The underlying modular concept of combining inorganic metal-clusters and organic linker molecules allows for the targeted design of three-dimensional crystalline molecular skeletons with defined pore dimensions, uniform pore shapes and versatile functionalities.

Our strategy for visualizing the recognition of a target ion requires the implementation of a fluorescent reporter molecule into the confined crystalline

environment of a hybrid host material. As a consequence of the confinement of the reporter molecules within the three-dimensional host, almost complete fluorescence quenching is observed. However, the selective trapping of fluoride ions from aqueous analytes directly correlates with an intense turn-on fluorescence signal that can easily be monitored by fluorescence spectroscopy. More specifically, the turn-on of fluorescence that is triggered by the controlled decomposition of the host material exhibits great advantages over luminescence quenching methods reported for luminescent MOFs.[22, 25] The turn-on fluorescence is an extremely sensitive technique, having the capability to detect even single molecules in solution and has great potential for the highly sensitive monitoring of the fluoride ion concentration in different media. Although there are several reports dealing with the intrinsic luminescence of MOFs and its use in chemical sensing,[22, 26, 27] none of these optical detection schemes tolerates aqueous environments and simultaneously shows turn-on fluorescence response triggered by the highly selective capture of fluoride ions.

Here we report on highly selective and extremely sensitive fluoride sensors based on an amino-functionalized metal-organic framework designated NH_2-MIL-101(Al)[28] that covalently binds fluorescein 5(6)-isothiocyanate (FITC) as fluorescent reporter molecule. We demonstrate an unprecedented methodology for the detection of fluoride ions in aqueous solutions that is based on the decomposition of the MOF and provides an intense turn-on switching response induced by the release of the quenched reporter molecules. The intact crystalline MOF material with embedded fluorescein dyes itself is non-fluorescent and selectively binds fluoride ions from water. The capture of fluoride ions results in the formation of different aluminum

7   Highly sensitive and selective fluoride detection in water
     through fluorophore release from a metal-organic
     framework

complexes, which induces the structural decomposition of the MOF host. The detection mechanism after infiltrating the MOF with an aqueous fluoride-containing analyte solution is revealed by ^{19}F and ^{27}Al-NMR titration experiments. To the best of our knowledge, the fluorescein-labeled MOF composite material is the first example of a MOF-based fluoride sensor system which tolerates aqueous environments, exhibits high selectivity versus other anions and covers a broad range of anion concentrations. We anticipate that the general concept of creating a fluorescence output by the controlled release of quenched fluorescence dye molecules from a porous host can be extended to other analyte detection schemes, thus adding to the toolbox for the development of advanced optical chemosensors and the understanding of signal transduction schemes.

7.2   Experimental section

Chemicals

Aluminum(III) chloride hexahydrate (99.9%, *Aldrich*), 2-amino terephthalic acid (99%, *Aldrich*), *N,N*-dimethylformamide (99.8%, *Aldrich*), fluorescein 5(6)-isothiocyanate (90%, *Aldrich*, FITC), sodium fluoride (99%, *Grüssing*), sodium chloride (99.8%, *Aldrich*), sodium bromide (99%, *Fluka*), sodium iodide (99%, *VWR*), sodium bicarbonate (99.5%, *Fluka*), disodium sulphate (99%, *Grüssing*), sodium acetate trihydrate (99.5%, *Merck*), sodium nitrate (98%, *Applichem*) as well as all solvents are commercially available and were used as received without further

purification. Millipore water (ρ> 18 MΩcm) was used for ^{19}F and ^{27}Al NMR, for fluorescence titrations and for the preparation of stock solutions.

Synthesis of NH$_2$-MIL-101(Al)

The solvothermal synthesis of NH$_2$-MIL-101(Al) was carried out according to a slightly modified literature synthesis.[28] In a 50 mL glass reactor, aluminum(III) chloride hexahydrate (0.51 g, 2.11 mmol, 1.0 eq.) and 2-amino terephthalic acid (0.56 g, 3.09 mmol, 1.5 eq.) were dissolved in 30 mL *N,N*-dimethylformamide (DMF) in an ultrasonic bath. The sealed glass reactor was kept for 72 h in a preheated oven at 403 K. The resulting yellow powder was filtered under vacuum and washed with acetone. To remove organic species trapped within the pores, the samples were extracted in boiling methanol for 8 h and stored at 373 K.

Synthesis of NH$_2$-MIL-101(Al)-FITC

For dye labeling experiments, fluorescein 5(6)-isothiocyanate (FITC; 15.0 mg, 0.0385 mmol) was dissolved in absolute ethanol (50 mL). NH$_2$-MIL-101(Al) (100 mg, 0.157 mmol) was added to the ethanolic dye solution and left for 48 h on an orbital shaker. NH$_2$-MIL-101(Al)-FITC was filtered and repeatedly washed with ethanol and deionized water.

Fluorescence titrations of NH$_2$-MIL-101(Al)-FITC

For fluorescence titration measurements, a stock solution of NH$_2$-MIL-101(Al)-FITC in water with a mass concentration of 1 mg/mL was freshly prepared and sonicated very briefly (a few seconds) in an ultrasonic bath to obtain a homogeneous suspension of the MOF in water with a hydrodynamic particle size of approximately 300 nm as determined by dynamic light scattering (Figure 9-37). Then, 100 µL of this stock solution was diluted in 2900 µL of water (resulting in a total volume of 3 mL and a final mass concentration of 33 µg/mL) in a quartz glass cuvette and stirred magnetically at room temperature. While stirring, the fluorescence emission was monitored continuously at 520 nm every second, using an excitation wavelength of 485 nm and an integration time of 1 second. The bandpass for excitation and emission was 4 nm. When the solution was equilibrated and the fluorescence signal did not change any more over time (typically after 20-40 minutes), a sodium fluoride solution (freshly prepared by dissolving an appropriate amount of NaF in water) was dispensed stepwise in portions of 2.5 µL from a 50 µL syringe into the fluorescence cuvette. After each step, the fluorescence was monitored for 4 minutes using the same parameters as above.

Titrations with other salt solutions and with the unlabeled MOF were performed accordingly, using 4.8 mM stock solutions of the corresponding salts and a MOF mass concentration of 33 µg/mL.

For data analysis, the mean fluorescence signal was calculated for each salt addition step from the last 60 seconds of the 4 minutes measurement interval (typically, the change in fluorescence signal was negligible 10 to 180 seconds after salt addition), the background fluorescence (*i.e.*, the fluorescence signal before fluoride addition) was subtracted, the values were normalized to the resulting starting intensity, and then plotted against the anion concentration in the cuvette. Dilution of the solution due to volume changes caused by the addition of the salt solutions was neglected (the total volume change was 2 % max.). Errors were calculated from the deviation of two individual measurements made with different MOF and salt stock solutions. Lines through the origin were fitted using a linear regression model.

NMR titrations of NH_2-MIL-101(Al)-FITC

For ^{19}F and ^{27}Al NMR titrations, a stock solution of NH_2-MIL-101(Al)-FITC in H_2O with a mass concentration of 1.2 mg/mL was prepared. Then, 0, 40, 80, 120, 160, 200, 240, 280, 320, 360 and 400 µL of freshly prepared aqueous NaF stock solutions (7.43 mM) was added to 400 µL of the MOF stock solution in an 1.5 mL Eppendorf cup, and the total volume was adjusted to 800 µL with H_2O. The resulting solutions were mixed by shaking on a vortexer and by sonication in an ultrasonic bath and subsequently transferred to an NMR tube.

^{19}F and ^{27}Al NMR spectra were recorded at room temperature at 376.17 MHz and 104.17 MHz and with 2048 and 4096 scans, respectively. The FIDs were processed using zero filling, phase correction and Gauss- and exponential window functions

prior to FFT. In the case of ^{27}Al NMR spectra, the background was subtracted for each spectrum individually by using the Whittaker smoother algorithm as implemented in MestReNova v5.2.5. For uncorrected spectra, see Figure 9-36.

7.3 Characterization

Powder X-ray diffraction (PXRD) measurements were performed using a Bruker D8 diffractometer (Cu-Kα1 = 1.5406 Å; Cu-Kα2 = 1.5444 Å) in *theta-theta* geometry equipped with a Lynx-Eye detector. The powder samples were measured between 2° and 45° two theta, with a step-size of 0.05° two theta.

Scanning electron microscopy (SEM) images were recorded with a JEOL JSM-6500F microscope equipped with a field emission gun, operated at an acceleration voltage of 5 kV and a working distance of 10 mm. Prior to measurements a thin gold layer (purity: 99.95%) was deposited on the samples using an Oerlikon Leybold Vacuum UNIVEX 350 sputter coater system operated at a base pressure of $1x10^{-6}$ mbar, an Argon pressure of $1x10^{-2}$ mbar, a power of 25 W and a sputtering time of 5 min.

Fluorescence titrations were carried out using a Hamilton Microlab 500 semiautomatic precision liquid processor with a Hamilton 1705TLLX 50 μL syringe connected to a PTI fluorescence spectrometer featuring a PTI 814 photomultiplier detector, a PTI MD5020 motor driver, a Quantum Northwest TC 125 sample holder, and an Ushio UXL-75XE Xenon short arc lamp in a PTI A-1010B arc lamp housing driven by a PTI LPS-220B lamp power supply.

FTIR measurements were performed in transmission mode on a Bruker Equinox 55s between 4000 and 400 cm^{-1} and a resolution of 4 cm^{-1}.

Raman spectra were recorded using a Bruker FRA106/S FT Raman module attached to a Bruker Equinox 55s FTIR spectrometer and a Coherent Compass 1064-500N Nd:YAG laser. Measurements were performed with a laser power of 100mW at a wavelength of 1064 nm.

Nitrogen sorption measurements were performed on a Quantachrome Instruments Autosorb at 77 K. Sample outgassing was performed for 12 hours at 393 K. Pore size and pore volume were calculated by a NLDFT equilibrium model of N_2 on silica, based on the adsorption branch of the isotherms. BET surface area was calculated over the range of partial pressure between $0.05 - 0.20$ p/p_0. The pore volume was calculated based on the uptake (cm^3/g) at a relative pressure of 0.30 p/p_0.

Thermogravimetric analyses of the bulk samples were performed on a Netzsch STA 440 C TG/DSC with a heating rate of 1 K min^{-1} in a stream of synthetic air at about 25 mL min^{-1}.

Dynamic light scattering (DLS) was performed on a Malvern Zetasizer-Nano instrumentequipped with a 4 mW He-Ne laser (633 nm) and an avalanche photodiode detector.

NMR spectra were recorded on a Jeol EX 400 or a Jeol Eclipse 400 instrument at room temperature and at a frequency of 376.17 MHz with 2048 scans for ^{19}F NMR and 104.17MHz with 4096 scans for ^{27}Al NMR.

7.4   Results and discussion

Recently, the group of F. Kapteijn reported on the amino-functionalized analogue of a large-pore metal-organic framework, designated NH$_2$-MIL-101(Al)[28]. The aluminum-based MOF scaffold with implemented amino-functionality represents an ideal candidate for the post-synthetic dye-labeling that was performed by exposing the porous host to FITC at room temperature. Powder X-ray diffraction (PXRD) measurements of the as-synthesized MOF material, as well as the post-synthetically fluorescein-labeled host are in good agreement with simulated data indicating that the crystalline structure remains intact upon dye-labeling (Figure 7-2).
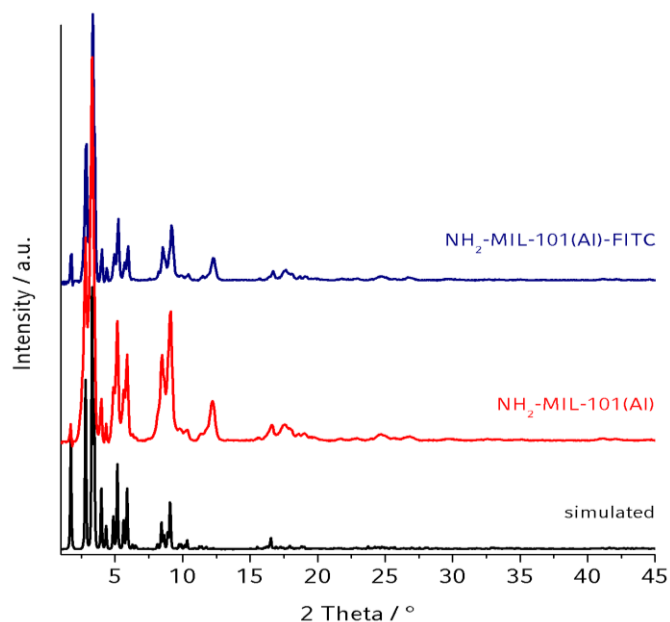
Figure 7-2   X-ray diffraction patterns (background corrected) of as synthesized NH$_2$-MIL-101(Al) (middle) as well as of post-synthetically fluorescein labeled NH$_2$-MIL-101(Al) bulk material (top) compared to simulated data (bottom).

Scanning electron microscope measurements (SEM) additionally confirm that the crystal morphology of the host MOF does not change significantly after being post-synthetically modified with fluorescein dye molecules (Figure 7-3).
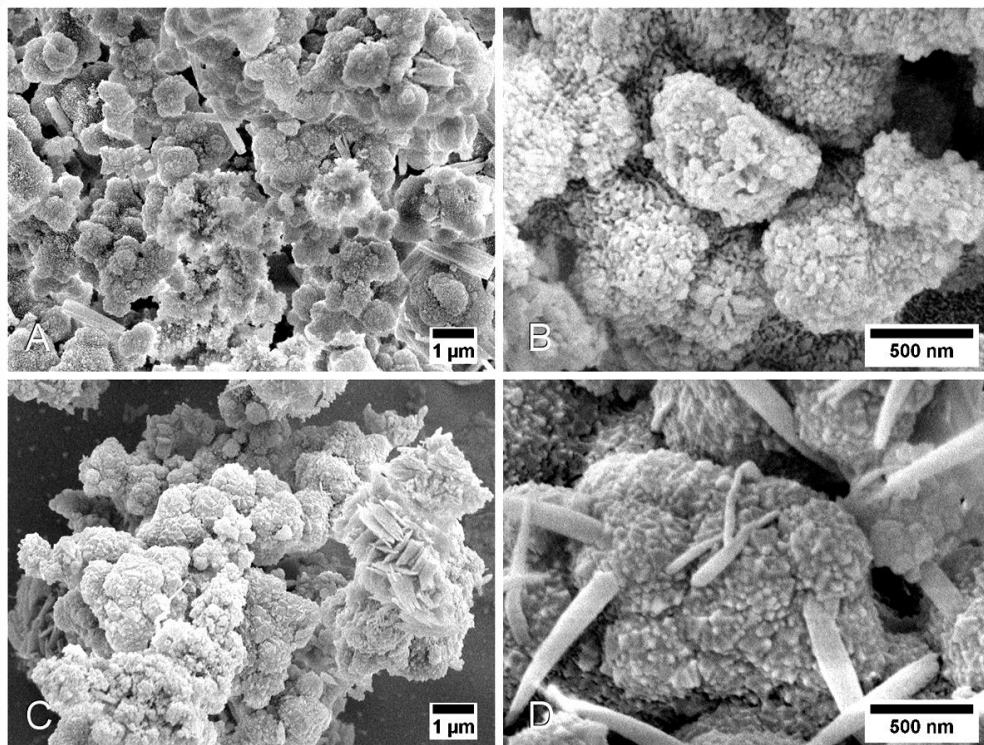
Figure 7-3   **Scanning electron microscopy (SEM) images of a polycrystalline bulk NH$_2$-MIL-101(Al) powder sample. A, B, after FITC labeling. C,D, before FITC labeling.**

After dye loading, a significant decrease of the specific surface area from 2315 m^2/g to 698 m^2/g as well as a reduction of the pore volume of the host material is revealed by physisorption experiments. This indicates a successful introduction of FITC into the porous structure of the host (Figure 7-4).
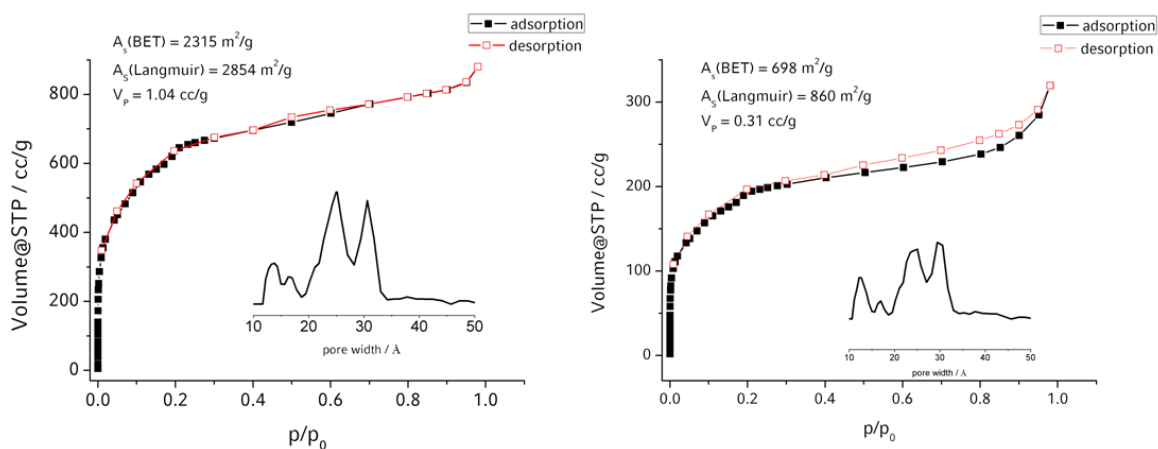
Figure 7-4   Physisorption measurement performed with nitrogen at 77 K for bulk
NH$_2$-MIL-101(Al) (left) and for NH$_2$-MIL-101(Al)-FITC (right) showing the
characteristic shape of the isotherm, the specific surface area
(BET/Langmuir), the pore volume and the calculated pore-size
distribution (NLDFT).

Infrared and Raman spectroscopy show the presence of a strong characteristic
absorption band corresponding to the isothiocyanate group of free FITC, whereas
no such absorption band is observed after fluorescein is incorporated into the host
framework (Figure 7-5).
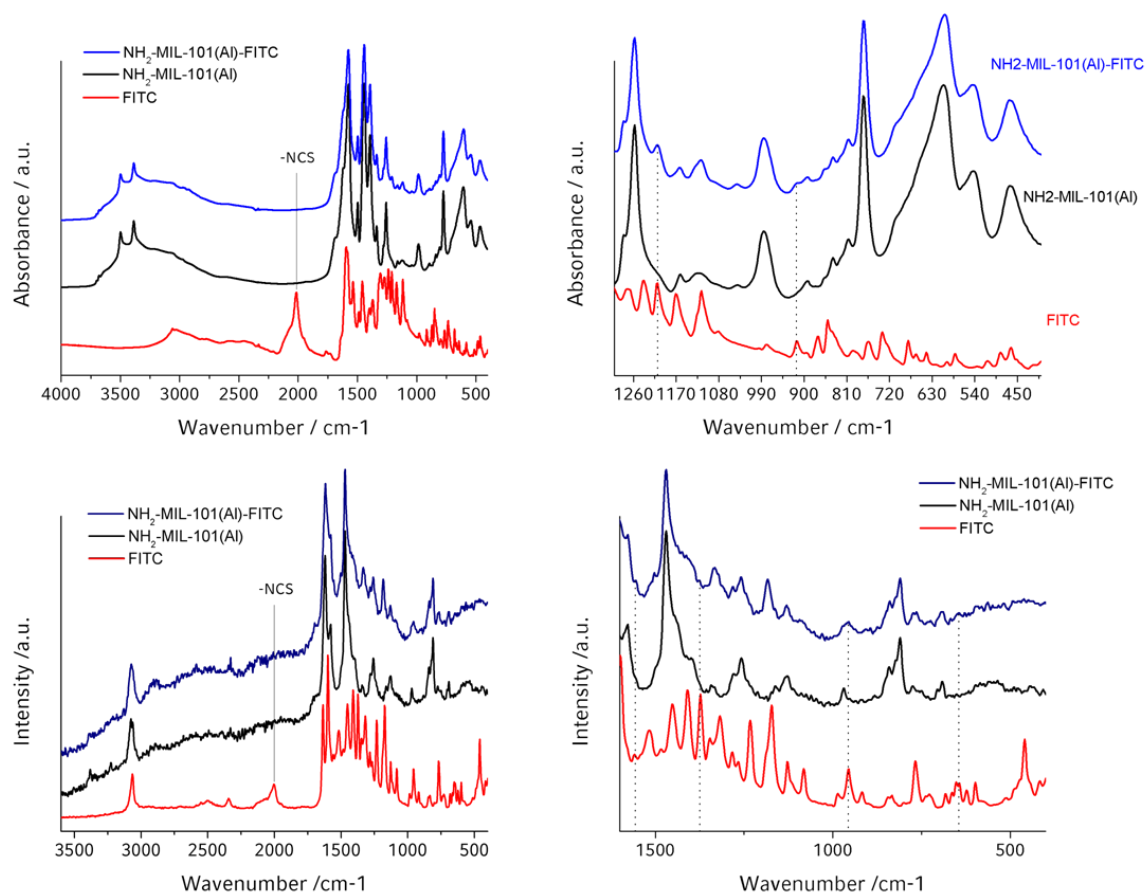
Figure 7-5   IR (top) and Raman (bottom) spectra of bulk fluorescein-5(6) isothiocyanate (red), NH$_2$-MIL-101(Al) (black) as well as of NH$_2$-MIL-101(Al)-FITC (blue) illustrating the absence of the isothiocyanate absorption band after the post-synthetic dye modification of the MOF structure. Zoom-in (right column) showing additional absorption bands that indicate the inclusion of the dye reporter molecule into the MOF structure.

Fluorescence spectroscopy shows that the fluorescence intensity of the fluorescein guests drops significantly (almost to the background level, Figure 7-6) once they are incorporated into the framework. We believe that this is caused by the well-known concentration- or self-quenching-effect of fluorescent dyes like fluorescein,[29, 30] or

by interactions of fluorescein either with aromatic groups of the linker molecules, the metal centers, or the amino groups inside the MOF. Inspired by this observation, we developed the novel MOF-based fluoride sensing concept using the selective release of the fluorescent dye: Since the framework is not connected by strong covalent bonds, it can be broken up under mild conditions by other, more strongly coordinating ligands for the respective metal. While this "instability" can certainly be a disadvantage in certain applications, it is of key importance for the working principle of the fluoride sensor and the new sensing pathway presented in this work: upon replacing the MOF-linker molecules by other ligands, the fluorescent guest is released into the solution where its fluorescence is dequenched and a strong increase in the fluorescence signal can be detected. Due to the fact that the degradation of the framework is based on different affinities of the metal ions constituting the MOF towards linker and analyte molecules, this pathway has the potential of being highly selective and tailorable by choosing suitable MOFs (*i.e.*, metal/linker combinations) for the respective target analytes. The fact that the release of the fluorescent dye results in a fluorescence increase rather than a quenching or loss of color contributes to the high sensitivity of this approach. Both the high selectivity based on strong interactions of aluminum with fluoride ions[31] and the high sensitivity based on the fluorescence dequenching are demonstrated in the following for NH_2-MIL-101(Al)-FITC.
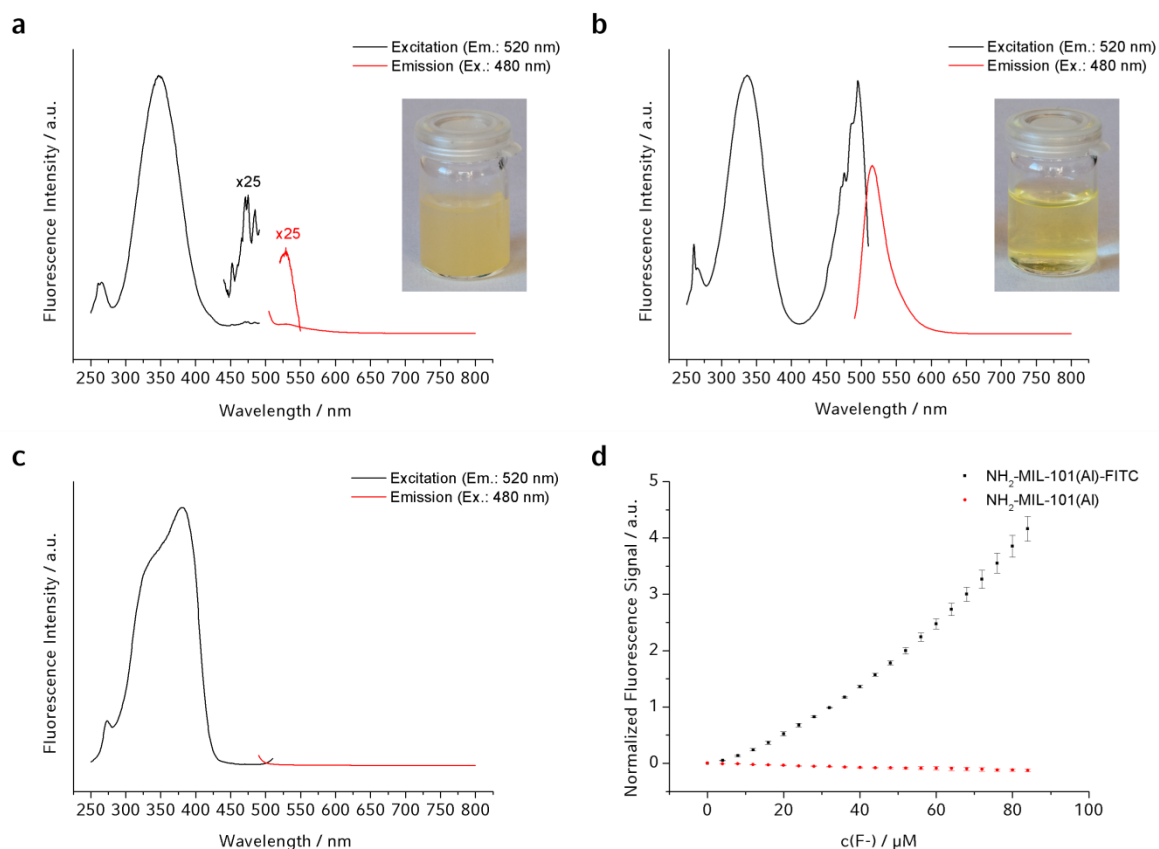
Figure 7-6   Fluorescence spectroscopy data. a, Excitation and emission spectra of NH$_2$-MIL-101(Al)-FITC before fluoride addition. b, Excitation and emission spectra of NH$_2$-MIL-101(Al)-FITC after fluoride addition. c, Excitation and emission spectra of 2-amino terephthalic acid, representing the linker molecule in NH$_2$-MIL-101(Al). d, Comparison of fluorescence titrations of NH$_2$-MIL-101(Al)-FITC and unlabeled NH$_2$-MIL-101(Al) (error bars indicate the deviation of two individual measurements with different MOF and titration stock solutions; for a more detailed description of experimental details, data analysis, and raw spectral data see Experimental section). Insets in (a) and (b), Photographs of the MOF stock solution before (a) and after (b) fluoride addition.

The remarkable selectivity of the sensor is demonstrated by fluorescence titrations of NH_2-MIL-101(Al)-FITC with sodium salt solutions of different anions, which show that there is virtually no interference by other halides (Figure 7-7).

Anion	Ratio
F^-	1.00000
Cl^-	0.00475
Br^-	0.00221
I^-	0.00456
NO_3^-	0.00254
CH_3COO^-	0.03404
SO_4^{2-}	0.05236
HCO_3^-	0.28300
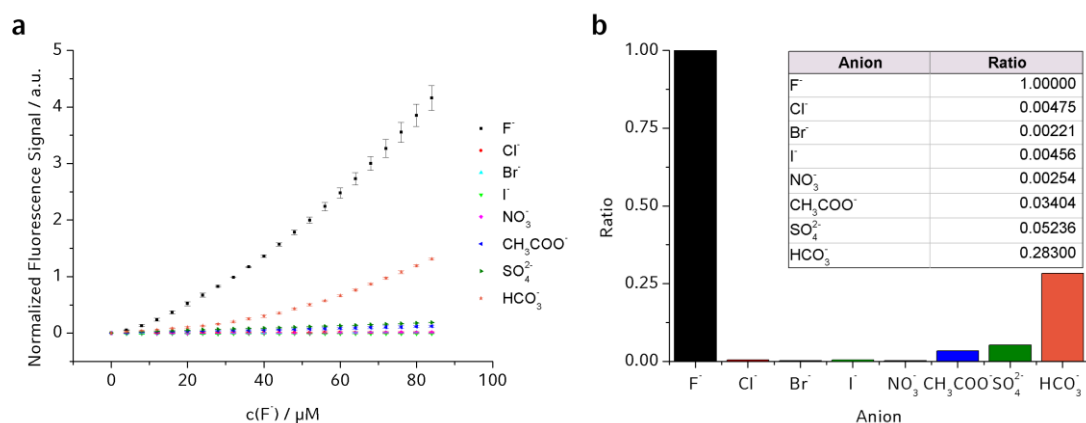
Figure 7-7   **Sensor selectivity data obtained from fluorescence titrations with different salt solutions. a, Data obtained from fluorescence titrations of NH_2-MIL-101(Al)-FITC with sodium salts of different anions. Error bars indicate the deviation of two individual measurements with different MOF and titration stock solutions. b, Ratio of slopes obtained by fitting a line through the origin to the data in a. For a more detailed description of experimental details, data analysis, and raw spectral data see Experimental section.**

The strongest interference among the anions tested in this work is caused by sodium bicarbonate, which can be expected to mimic the coordination chemistry of the linker molecules, *i.e.*, coordination of aluminum *via* carboxylate groups. Interestingly, sodium acetate shows only very weak interference, although it also exhibits a carboxylate group. The absence of strong acetate interference also proves that the recorded fluorescence increase does not simply depend on an increase of

the pH, since the basicity of acetate is higher than that of fluoride (pK_A(CH_3COOH) $\approx$ 4.75 *vs.* pK_A(HF) $\approx$ 3.45).[32] However, the fluorescence signal is much stronger after fluoride addition than after acetate addition, indicating that the fluorescence increase is triggered by coordination of fluoride to aluminum metal centers rather than by a rise of the pH.

Additionally, more detailed information about the different fluoride species in solution as well as mechanistic insights into the dissolution process were gained by performing NMR titration experiments, which prove that the framework is indeed dissolved by coordination of fluoride to aluminum ions from the framework.

Chemical Shift [ppm]	Fluoride Species	Chemical Shift [ppm]	Aluminum Species
-119.2	"Free" F^-	4	$[AlF_x(H_2O)_{6-x}]^{(3-x)+}$
-153.6	$[AlF_4(H_2O)_2]^-$		
-154.4	$[AlF_3(H_2O)_3]$		
-155.6	$[AlF_2(H_2O)_4]^+$		
-156.0	$[AlF(H_2O)_5]^{2+}$		
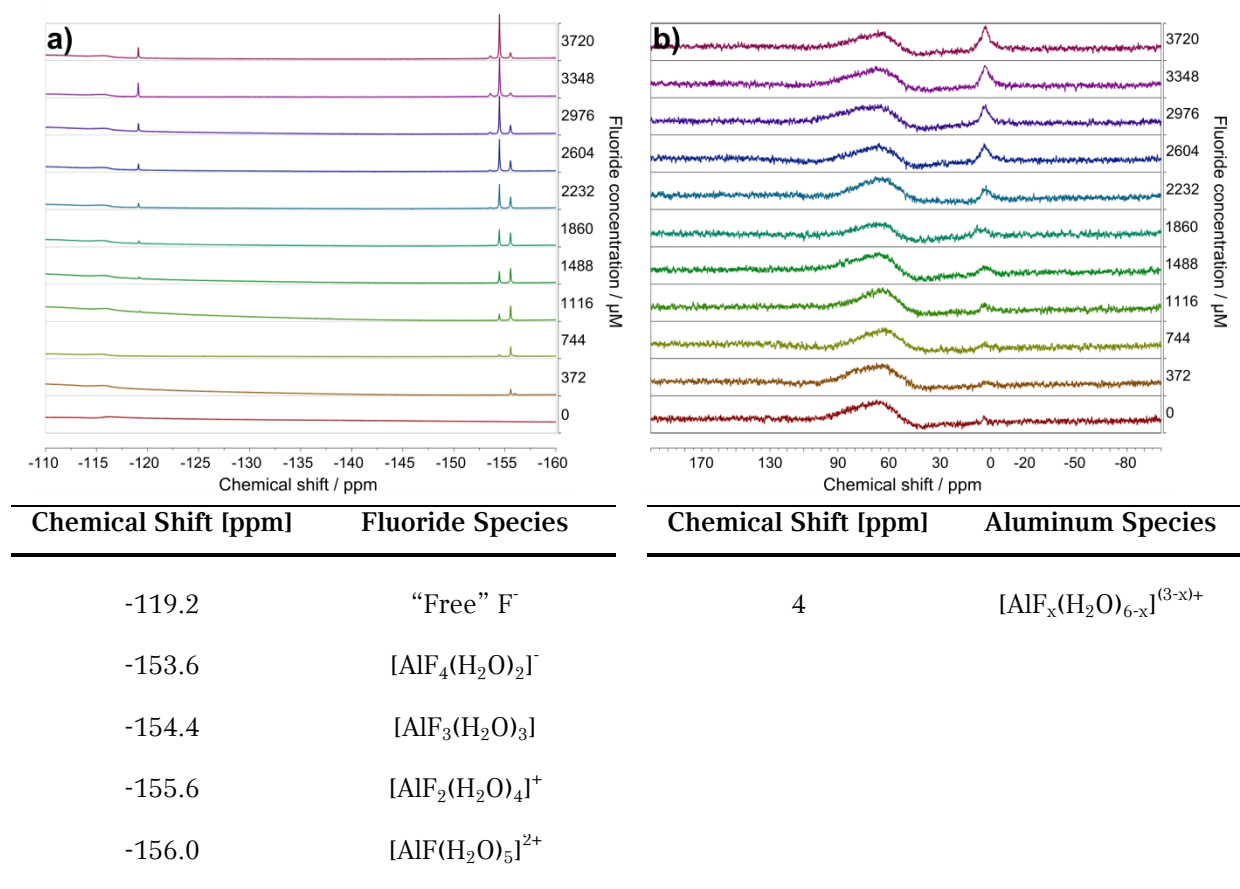
Figure 7-8 ^{19}F and ^{27}Al NMR titration of NH_2-MIL-101(Al)-FITC. a, ^{19}F NMR. b, ^{27}Al NMR. The broad signal in the ^{27}Al NMR between $\delta \approx 50$ ppm and $\delta \approx 110$ ppm arises from aluminum atoms from the NMR probe head or the NMR glass tube (see Experimental section). The concentration of fluoride was adjusted to the values given in the figure. The peak assignments are based on references.[33, 34] For a detailed description of experimental parameters, FID processing and raw spectral data see Experimental section.

Figure 7-8**a** shows the ^{19}F NMR spectra after sequential additions of NaF to NH_2-MIL-101(Al)-FITC in water. The data demonstrate how the number of fluoride ions

binding to aluminum increases with increasing fluoride concentration. The peaks of the aluminum complexes with high fluoride content (*i.e.,* more than four fluoride atoms) cannot be observed here, most probably because they are too broad. Similar observations were made by Sur *et al.*[33] and by Bodor *et al.*[34]. Sur *et al.* attribute the line broadening mainly to a two-site exchange between free fluoride ions and fluoroaluminum complexes, although scalar relaxation mechanisms are also discussed. Bodor *et al.* also attribute the broadening to fluoride exchange; however, the authors also briefly mention precipitation and the formation of mixed aluminum hydroxo species as possible causes.

Going deeper into the exact nature of the aluminum fluoride species that are formed is beyond the scope of this work, but our NMR titration experiments clearly show that differently coordinated molecular aluminum fluoride species are formed upon fluoride addition to a dispersion of the MOF in water. In agreement with the literature, we found complexes with one and two fluoride atoms bound to aluminum at low fluoride concentrations. With increasing fluoride concentration, aluminum species that are coordinated by more and more fluoride ions are formed, while the amount of aluminum species with lower fluoride amounts decreases. Interestingly, the amount of "free" fluoride (*i.e.,* fluoride ions that are not coordinating a metal ion) observed at $\delta \approx$ -119.2 ppm is very low at the beginning, and after the corresponding peak starts to develop at about 1000 μM, it stays at a low level. We propose the following detection mechanism: aluminum fluoride complexes and linker molecules (together with the fluorescent dye) are liberated from the framework into the solution *via* a displacement of linker molecules by fluoride ions.

This is also backed up by the ^{27}Al NMR spectra (Figure 7-8b), which feature a broad peak at $\delta \approx 4$ ppm that can be assigned to $[AlF_x(H_2O)_{6-x}]^{(3-x)+}$.[33, 34] Before fluoride addition, no signals can be observed in the ^{27}Al NMR, indicating that there is no appreciable amount of aluminum present in the solution at the beginning. Only after addition of fluoride, aluminum fluoride complexes can be found in solution. This indicates that the aluminum source is really the MOF and that the fluoride complexes that can be observed by NMR are indeed formed by a degradation of the metal-organic framework.

In addition to the remarkable selectivity of NH_2-MIL-101(Al)-FITC towards fluoride, we could also demonstrate a very high sensitivity covering a broad range of fluoride ion concentrations from approximately 15 µg up to at least 1600 µg of fluoride per 1 L of water, or 15 to 1600 ppb. (Figure 7-9).
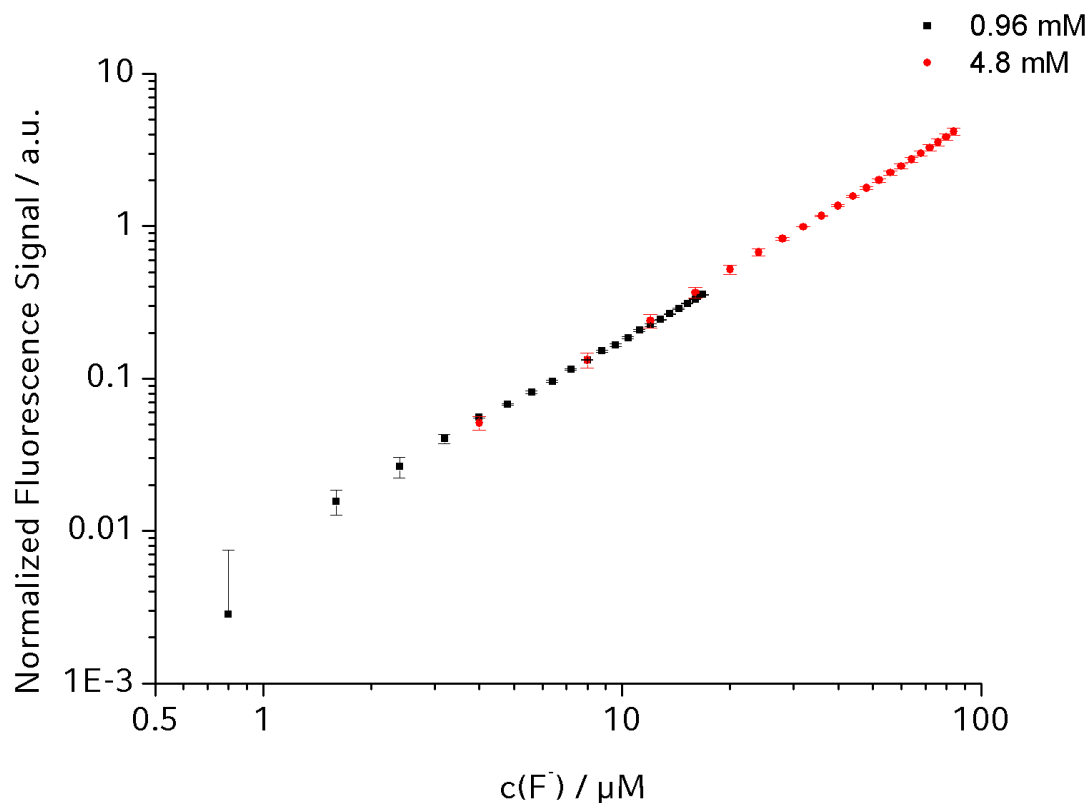
Figure 7-9   **Fluorescence titration curves. The data show fluorescence titrations of NH$_2$-MIL-101(Al)-FITC with two titration solutions of different concentration. Error bars indicate the deviation of two individual measurements with different MOF and titration stock solutions. For a more detailed description of experimental details, data analysis, and raw spectral data see Experimental section.**

We believe that the main reason for the high sensitivity is the efficient quenching and dequenching of fluorescein fluorescence upon incorporation into and liberation from the host framework, respectively. The slight deviation from linear behavior at low fluoride concentration (which can be better seen in a non-double-logarithmic plot, as for example in Figure 7-6d) is attributed to the initial coordination of

fluoride ions to trace amounts of free aluminum precursor still present in the porous framework or from coordination to unsaturated metal centers inside the MOF. Both effects do not lead to a replacement of linker molecules by fluoride and hence the amount of fluorescein that is released into the solution is lower than expected. Once all these metal ions are coordinated by fluoride, further addition of fluoride results in linker displacement and liberation of fluorescein into the solution and the concomitant fluorescence dequenching discussed above. Assuming a homogeneous distribution of fluorescein throughout the framework, the fluorescence signal should hence increase linearly with fluoride concentration, until the framework is more or less completely dissolved, at which point the fluorescence signal should level off. However, that point was not reached in the titrations shown here.

7.5   Conclusion

In this study we have introduced a new signal transduction scheme in the field of MOFs, which is based on the efficient quenching of fluorescent guests upon incorporation into the porous framework and the subsequent dequenching upon analyte-specific degradation of the host material. This new sensing concept was illustrated with the dye-loaded MOF NH_2-MIL-101(Al), thus introducing a highly sensitive and selective fluoride sensor that is compatible with aqueous analyte solutions. Deeper insights into the transduction mechanism were gained by ^{19}F and ^{27}Al NMR titration studies, revealing that the porous host framework is indeed dissolved upon fluoride ion addition due to competing coordination of fluoride to

metal centers inside the metal organic framework. We believe that the high sensitivity of the system is controlled by the coordination chemistry and the different affinities of the metal ions inside the framework towards linker molecules, fluoride ions, and other interfering ions. Fluorescence titration experiments were used to quantitatively show the remarkable selectivity and sensitivity of our fluoride sensor. We attribute the high sensitivity to the fact that a turn-on fluorescence signal rather than a color- or fluorescence-quenching based signal transduction scheme is used. All in all, the sensitivity of the sensor presented in this work is far better than that of the commonly used optical fluoride detection methods in aqueous solution according to data presented by the World Health Organization (WHO) and the American Public Health Association,[35, 36] namely the sodium-2-(parasulfophenylazo)-dihydroxy-3,6-napthalene disulfonate (SPADNS) method and the complexone method. These references give a fluoride detection range of 0.1 to 1.4 mg/L for the SPADNS method and a range of 0.05 to 2.0 mg/L for the complexone method, at comparable anion selectivity. In our work, we have demonstrated a detection range from 0.015 mg/L up to at least 1.6 mg/L.

We believe that the general concept of releasing fluorescent guest molecules from MOFs can be extended to other combinations of analytes and metal coordination environments, thus adding to the growing toolbox of optical chemosensors.

7.6   References

[1]   C. McDonagh, C. S. Burke and B. D. MacCraith, *Chem. Rev.*, 2008, **108**, 400-422.

[2]   M. I. J. Stich, L. H. Fischer and O. S. Wolfbeis, *Chem. Soc. Rev.*, 2010, **39**, 3102-3114.

[3]   O. S. Wolfbeis, *Anal. Chem.*, 2004, **76**, 3269-3284.

[4]   M. Schäferling, *Angew. Chem. Int. Ed.*, 2012, **51**, 3532-3554.

[5]   C. R. Wade, A. E. J. Broomsgrove, S. Aldridge and F. o. P. Gabbaï, *Chem. Rev.*, 2010, **110**, 3958-3984.

[6]   E. Galbraith and T. D. James, *Chem. Soc. Rev.*, 2010, **39**, 3831-3842.

[7]   S. Kubik, *Chem. Soc. Rev.*, 2010, **39**, 3648-3663.

[8]   S. Jagtap, M. K. Yenkie, N. Labhsetwar and S. Rayalu, *Chem. Rev.*, 2012, **112**, 2454-2466.

[9]   C. Dusemund, K. R. A. S. Sandanayake and S. Shinkai, *J. Chem. Soc., Chem. Comm.*, 1995, 333-334.

[10]   C. R. Wade and F. P. Gabbai, *Dalton Trans.*, 2009, 9169-9175.

[11]   Y. Kim and F. o. P. Gabbaï, *J. Am. Chem. Soc.*, 2009, **131**, 3363-3369.

[12]   A. B. Descalzo, D. Jimenez, J. E. Haskouri, D. Beltran, P. Amoros, M. D. Marcos, R. Martinez-Manez and J. Soto, *Chem. Comm.*, 2002, 562-563.

[13]   S. Guha and S. Saha, *J. Am. Chem. Soc.*, 2010, **132**, 17674-17677.

[14]   M. Boiocchi, L. Del Boca, D. E. Gómez, L. Fabbrizzi, M. Licchelli and E. Monzani, *J. Am. Chem. Soc.*, 2004, **126**, 16507-16514.

[15]   H. Zhao and F. P. Gabbaï, *Nat Chem*, 2010, **2**, 984-990.

[16]   O. M. Yaghi, M. O'Keeffe, N. W. Ockwig, H. K. Chae, M. Eddaoudi and J. Kim, *Nature*, 2003, **423**, 705-714.

[17]   S. Kitagawa, R. Kitaura and S.-i. Noro, *Angew. Chem. Int. Ed.*, 2004, **43**, 2334-2375.

[18]   G. Ferey, *Chem. Soc. Rev.*, 2008, **37**, 191-214.

[19]   J.-R. Li, R. J. Kuppler and H.-C. Zhou, *Chem. Soc. Rev.*, 2009, **38**, 1477-1504.

[20]   K. Sumida, D. L. Rogow, J. A. Mason, T. M. McDonald, E. D. Bloch, Z. R. Herm, T.-H. Bae and J. R. Long, *Chem. Rev.*, 2011, **112**, 724-781.

[21]   G. Ferey, C. Serre, T. Devic, G. Maurin, H. Jobic, P. L. Llewellyn, G. De Weireld, A. Vimont, M. Daturi and J.-S. Chang, *Chem. Soc. Rev.*, 2011, **40**, 550-562.

[22]   M. D. Allendorf, C. A. Bauer, R. K. Bhakta and R. J. T. Houk, *Chem. Soc. Rev.*, 2009, **38**, 1330-1352.

[23]   L. E. Kreno, K. Leong, O. K. Farha, M. Allendorf, R. P. Van Duyne and J. T. Hupp, *Chem. Rev.*, 2012, **112**, 1105-1125.

[24]   N. Yanai, K. Kitayama, Y. Hijikata, H. Sato, R. Matsuda, Y. Kubota, M. Takata, M. Mizuno, T. Uemura and S. Kitagawa, *Nat Mater*, 2011, **10**, 787-793.

[25]   G. Lu, O. K. Farha, L. E. Kreno, P. M. Schoenecker, K. S. Walton, R. P. Van Duyne and J. T. Hupp, *Adv. Mater.*, 2011, **23**, 4449-4452.

[26]   K. C. Stylianou, R. Heck, S. Y. Chong, J. Bacsa, J. T. A. Jones, Y. Z. Khimyak, D. Bradshaw and M. J. Rosseinsky, *J. Am. Chem. Soc.*, 2010, **132**, 4119-4130.

[27]   Y. Takashima, V. M. Martínez, S. Furukawa, M. Kondo, S. Shimomura, H. Uehara, M. Nakahama, K. Sugimoto and S. Kitagawa, *Nat. Commun.*, 2011, **2**, 168.

[28]   P. Serra-Crespo, E. V. Ramos-Fernandez, J. Gascon and F. Kapteijn, *Chem. Mater.*, 2011, **23**, 2565-2572.

[29]   A. Imhof, M. Megens, J. J. Engelberts, D. T. N. de Lang, R. Sprik and W. L. Vos, *J. Phys. Chem. B*, 1999, **103**, 1408-1415.

[30]   C. Bojarski, J. Grabowska, L. Kulak and J. Kusba, *Journal of Fluorescence*, 1991, **1**, 183-191.

[31]   R. P. Agarwal and E. C. Moreno, *Talanta*, 1971, **18**, 873-880.

[32]   P. W. Atkins, A. Höpfner and C. A. Trapp, *Physikalische Chemie*, VCH, Weinheim [u.a.], 1996.

[33]   S. K. Sur and R. G. Bryant, *Zeolites*, 1996, **16**, 118-124.

[34]   A. Bodor, I. Toth, I. Banyai, Z. Szabo and G. T. Hefter, *Inorg. Chem.*, 2000, **39**, 2530-2537.

[35]   World Health Organization (WHO), *Fluoride in Drinking-water by J. Fawell, K. Bailey, J. Chilton, E. Dahi, L. Fewtrell and Y. Magara* ISBN: 1900222965, Published by IWA Publishing, London, UK., 2006.

[36]   American Public Health Association, American Water Works Association and Water Environment Federation, *Standard methods for the examination of water and wastewater*, American Public Health Association, 1998.

8   General Conclusion

Within the course of this thesis different synthetic pathways were developed to implement functionalized MOFs as selective and sensitive chemical sensor materials. Along these lines, tailored MOFs and MOF thin films were synthesized and used as model systems to incorporate a specific recognition-transduction mode that translates molecular recognition events into a readable optical output signal.

In the first study, it was demonstrated that the concept of direct crystal growth on functionalized substrates can be extended to functionalized metal–organic frameworks. Thin films of two different model systems such as the MOF NH_2–Fe–MIL-88B as well as the large cage structure of NH_2–Fe–MIL-101 were grown in a highly oriented fashion on self-assembled monolayers. The influence of the implemented functionality on the sorption properties of MIL-88B compared to its modified analogue was investigated by QCM experiments. A considerably enhanced uptake of ethanol was demonstrated for the amino-functionalized MOF. *In-situ* sorption@XRD measurements allowed us to correlate the adsorbed amount of ethanol with structural changes in the flexible Fe–MIL-88B systems. Our study suggests that the growth method apparently can be generalized to an increasing number of MOF structures, such that comparative sorption experiments in thin films become possible. We anticipate that the ability to direct the growth of functionalized MOFs in the form of thin oriented films will be of particular interest for chemical sensing applications, where both the control of crystal growth orientation and

functionalization of the organic linker are expected to have a strong impact on sensitivity, kinetics and selectivity through specific host–guest interactions.

The aforementioned results prompted us to create another crystalline and porous structure in the form of a thin film. The ability to control the growth of the most prominent representative of zeolitic imidazolate frameworks (ZIFs), that is ZIF-8, is fundamental for the assembly one-dimensional photonic crystal structures (Bragg stacks). It could be demonstrated that such an architecture could be endowed with sensing capabilities by simply combining two porous materials with different refractive indices. The selectivity towards different analytes was addressed by combining micro- and mesoporosity within the optical transducer system. The response upon exposure to a series of chemically similar organic vapors was monitored as a function of the partial pressure. These proof-of-concept studies are viewed as promising examples of tunable optical sensors offering label-free operation and compact set-up.

Functionalization of the inner pore surface of MOFs was achieved by employing elongated spacer molecules. The modular synthesis pathways resulted in the large-pore and crystalline MOF structure UiO-68-NH$_2$ allowing for the incorporation of space-demanding reporter features. It could be demonstrated that the concept of oriented crystal growth on SAM-modified gold substrates was successfully extended to such functionalized and mesoporous MOF structures. The post-synthetic pore modification of UiO-68-NH$_2$ thin films with a fluorescent dye was achieved and confirmed by quenching experiments with differently sized quenching agents.

Further studies comprised a chemically triggered luminescence reaction within an intrinsically luminescent MOF. For the first time, chemiluminescence integrated into a zirconium-based MOF with anthracene linker moieties could be demonstrated as optical read-out of a particular recognition event. Strong chemiluminescence originating from the UiO-68(anthracene) structure was observed upon subjecting the MOF to an analyte solution. This transducer concept relies on a chemical reaction that could be used to efficiently detect a specific analyte. In terms of sensor design, the presented signal transduction is expected to contribute to the development of novel chemo-sensitive materials based on the emission of light.

In the latest study we introduce a novel concept in which a porous crystalline framework serves as a host material for a fluorescent reporter molecule. Here the pathway towards sensing is based on the efficient quenching of fluorescent guests upon incorporation into a porous MOF framework and their subsequent dequenching upon analyte-specific degradation of the host material. This new sensing concept was illustrated with the dye-loaded MOF NH_2-MIL-101(Al), thus introducing a highly sensitive and selective fluoride sensor that is compatible with aqueous analyte solutions. Exceptional turn-on fluorescence in aqueous fluoride-containing solutions as well as unprecedented selectivity for fluoride in competition with other halogenide ions and other anions was observed. A mechanistic understanding of the processes that result in the degradation of the crystalline framework was revealed by NMR titration experiments. We believe that our innovative concept of implementing tailored MOF structures as host species for analyte-induced decomposition combined with a triggered reporter release can be widely extended in the field of MOF-based chemosensors.

To conclude, different synthetic pathways towards the implementation of tailored MOFs as chemical sensors were explored and exciting new results that significantly contribute to the development of novel sensing platforms were obtained. The findings have shown that MOFs are promising candidates for prospective future studies including the development of efficient sensing capabilities by accommodating tailored receptor-transducer units within the stable environment of a MOF structure, thus contributing to our understanding of molecular recognition events and adding to the growing toolbox for future chemical sensor design.

9   Appendix

9.1   List of abbrevations

1D	One-dimensional
2D	Two-dimensional
3D	Three-dimensional
AASBU	Automated assembly of secondary building units
AFM	Atomic Force Microscopy
BDC	1,4-Benzenedicarboxylic acid
BET	Brunauer, Emmett, Teller
BTC	1,3,5-Benzenetricarboxylic acid
CEM	Controlled evaporation mixer
COF	Covalent organic framework
CRT	Cathode ray tube
DFT	Density functional theory
DMF	*N,N*-Dimethylformamide

DSC	Differential scanning calorimetry
FC	Flow controller
FT	Fourier transformation
HKUST-1	Hong-Kong University of Science and Technology structure 1
ID	Identification number
IR	Infrared
IRMOF	Isoreticular metal-organic framework
IUPAC	International Union of Pure and Applied Chemistry
µCP	Micro-Contact printing
MFC	Mass flow controller
MFM	Magnetic Force Microscopy
MHD	16-Mercaptohexadecanol
MHDA	16-Mercaptohexadecanoic acid
MIL	Matériaux de l'Institut Lavoisier
MOF	Metal-organic framework
MS	Microsoft
MUD	11-Mercaptoundecanol

MUP	11-Mercaptoundecanephosphonate
QCM	Quartz-crystal microbalance
RAIRS	Reflection-Adsorption IR spectroscopy
RT	Room temperature
SAM	Self-assembled monolayer
SBU	Secondary building unit
SEM	Scanning electron microscopy
SPM	Scanning probe microscopy
STM	Scanning tunnelling microscopy
TEM	Transmission electron microscopy
TGA	Thermogravimetric analysis
TiO_2	Titanium dioxide
UiO	University of Qslo
UMCM	University of Michigan Crystalline Material
XRD	X-ray diffraction
ZIF-8	Zeolitic imidazolate framework No. 8

9.2   Supplementary Information for Chapter 3

Table S 9-1   Lattice parameter *c* of Fe-MIL-88B after indexing using Werner algorithm for different relative pressures of ethanol.

p/p_0	2 Theta	lattice parameter c / $Å^3$
0,00	9,18	19,3
0,02	9,22	19,2
0,20	9,23	19,2
0,40	9,24	19,1
0,60	9,24	19,1
0,80	9,25	19,1
0,60	9,24	19,1
0,40	9,23	19,1
0,20	9,22	19,2
0,02	9,22	19,2
0,00	9,18	19,3

Table S 9-2   Lattice parameter *c* of NH_2-Fe-MIL-88B after indexing using Werner algorithm for different relative pressures of ethanol.

p/p_0	2 Theta	lattice parameter c / $Å^3$
0,00	9,09	19,4
0,02	9,10	19,4
0,20	9,12	19,4
0,40	9,19	19,2
0,60	9,22	19,2
0,80	9,24	19,1
0,60	9,24	19,1
0,40	9,23	19,2
0,20	9,22	19,2
0,02	9,20	19,2
0,00	9,16	19,3
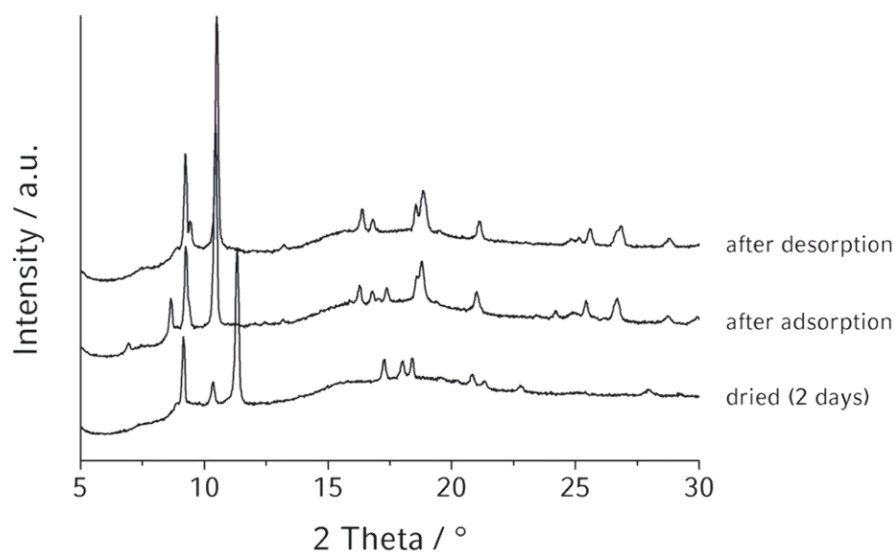
Figure 9-1   XRD pattern of the ethanolic form of bulk NH$_2$-Fe-MIL-88B crystals showing the effect of extended drying.
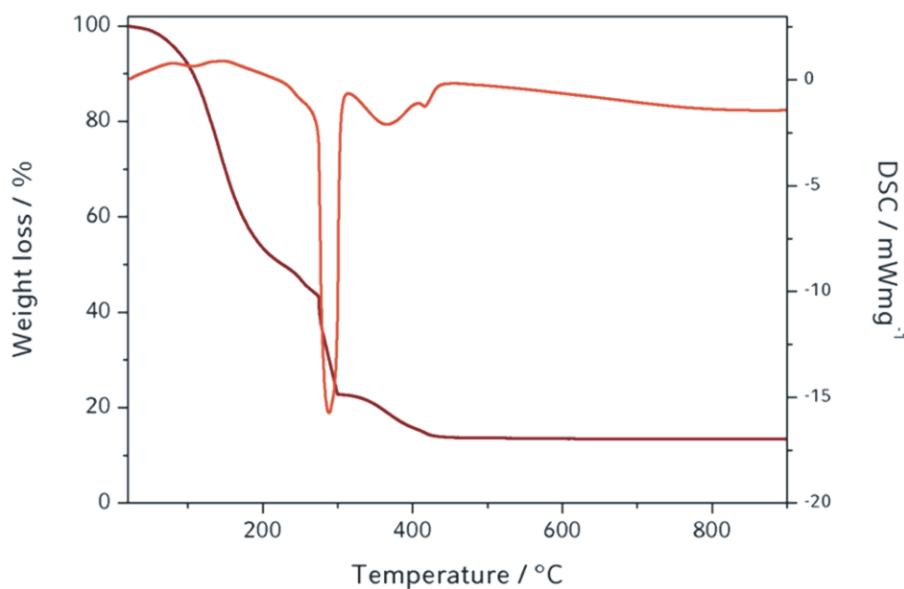
Figure 9-2   TGA and DSC data of NH$_2$-Fe-MIL-101. The first step of 56 wt. % in the TGA is assigned to the loss of solvent and water molecules from inside the pores. The decomposition of the organic parts of NH$_2$-MIL-101 subsequently takes place above 250 °C within two steps, which can also

be seen in the differential scanning calorimetry (DSC) in red. These two steps show a weight loss of 30 % and of 70 % corresponding to the crystals with filled pores and those with empty pores, respectively. This 70 % weight loss is in good agreement with the weight fraction of the organic parts of NH_2-Fe-MIL-101 ($Fe_3O(NH_2BDC)_3$), which can be calculated as 75 wt. %.
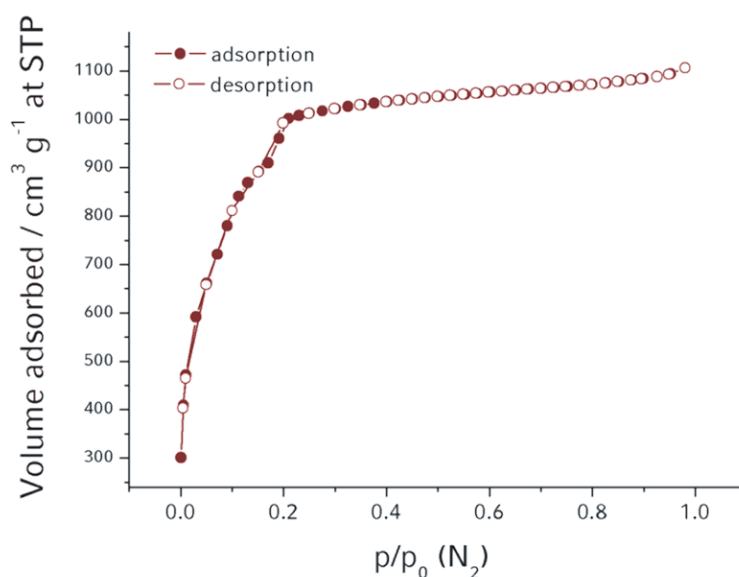
Figure 9-3   Nitrogen sorption isotherm at 77 K for bulk NH_2-Fe-MIL-101. The Type I isotherm of the amino-functionalized NH_2-Fe-MIL-101 is very similar to the isotherm of the unfunctionalized compound reported in the literature. The shapes of the isotherms are nearly identical, both providing a small step in the adsorption curve at 0.2 *p/p₀*. The overall adsorbed volume of nitrogen is slightly smaller for NH_2-Fe-MIL-101 than for MIL-101, which can be attributed to the amino groups present in the framework. The fact that the adsorption capacity of the material is only slightly reduced by the amino functionalization is of interest for thin film growth and for possible applications of these functionalized MOF thin films.

9.3   Supplementary Information for Chapter 4
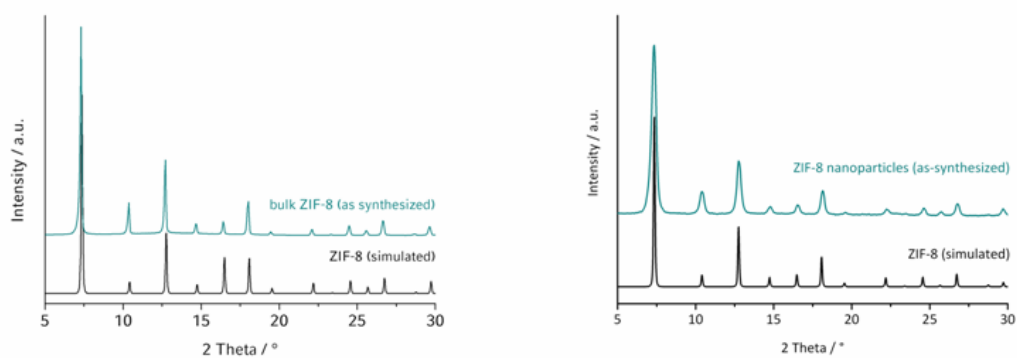
Figure 9-4   X-ray diffraction patterns (background corrected) of as-synthesized bulk ZIF-8 material (left) as well as of ZIF-8 nanoparticles (right) compared to simulated data.
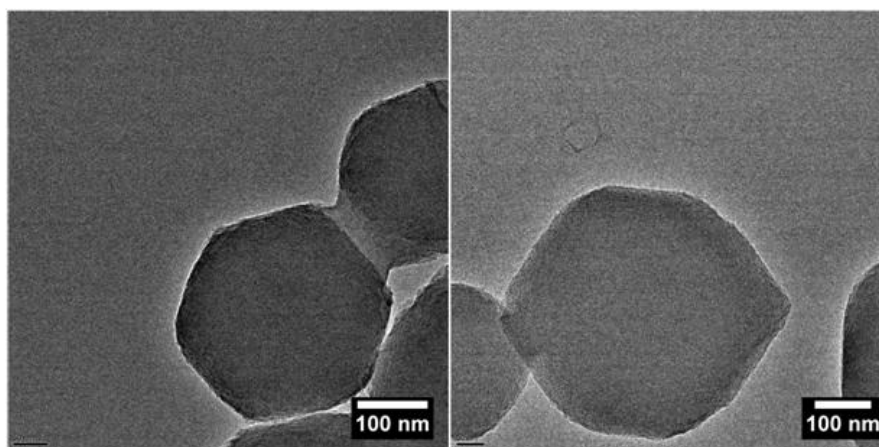
Figure 9-5   Transmission electron microscopy (TEM) micrographs showing as-synthesized ZIF-8 nanocrystals isolated from a powder sample obtained from the reaction solution used for dense ZIF-8 film growth.
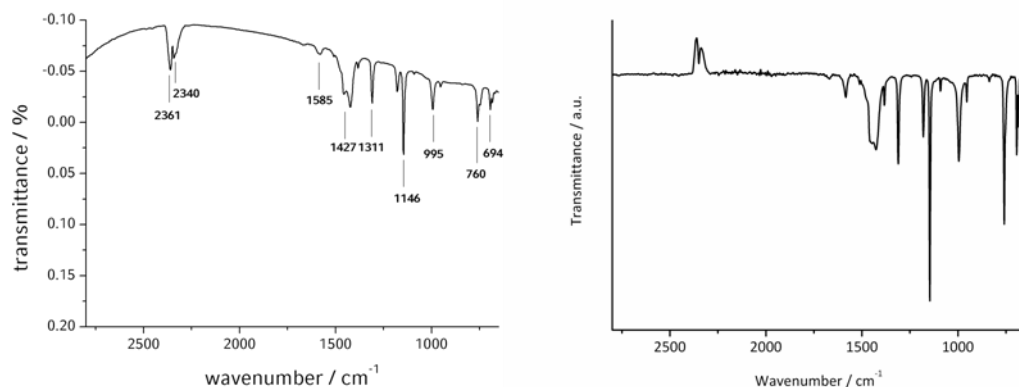
Figure 9-6   IR spectra of bulk ZIF-8 (left) as well as of ZIF-8 nanoparticles (right).
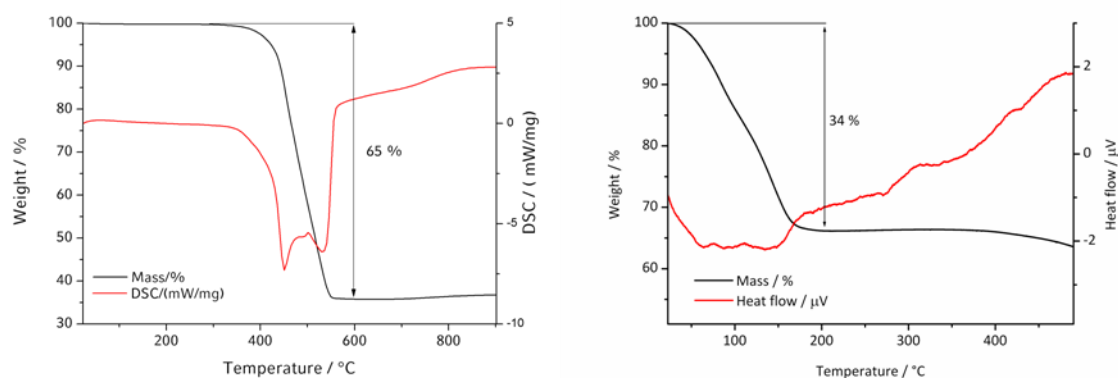
Figure 9-7   Thermogravimetric analysis (TGA), differential scanning calorimetry (DSC) and differential thermal analysis (DTA) of bulk ZIF-8 (left) and ZIF-8 nanoparticles (right), respectively, illustrating a one-step weight loss as well as the decomposition of bulk ZIF-8.
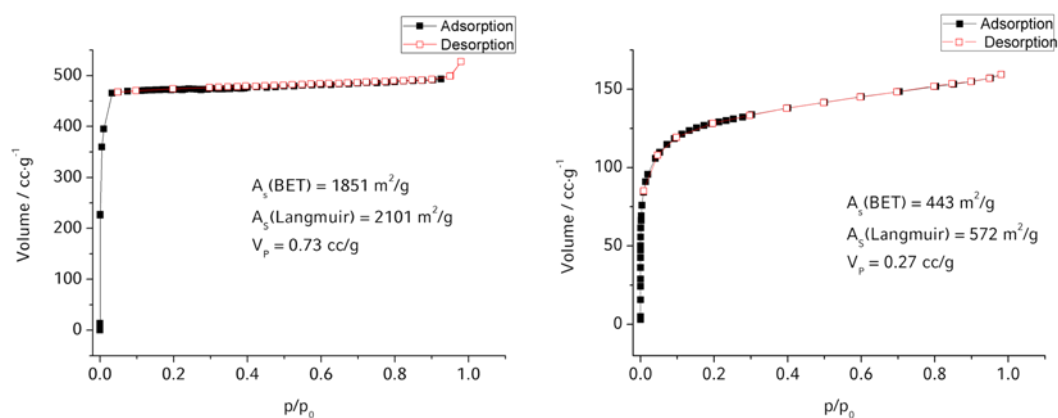
Figure 9-8   Physisorption measurement performed with nitrogen at 77 K for bulk ZIF-8 (left) and on a titania nanoparticle sample (right) synthesized without structure-directing agent (F127) showing a type I isotherm, the specific surface area (BET/Langmuir) and the pore volume.
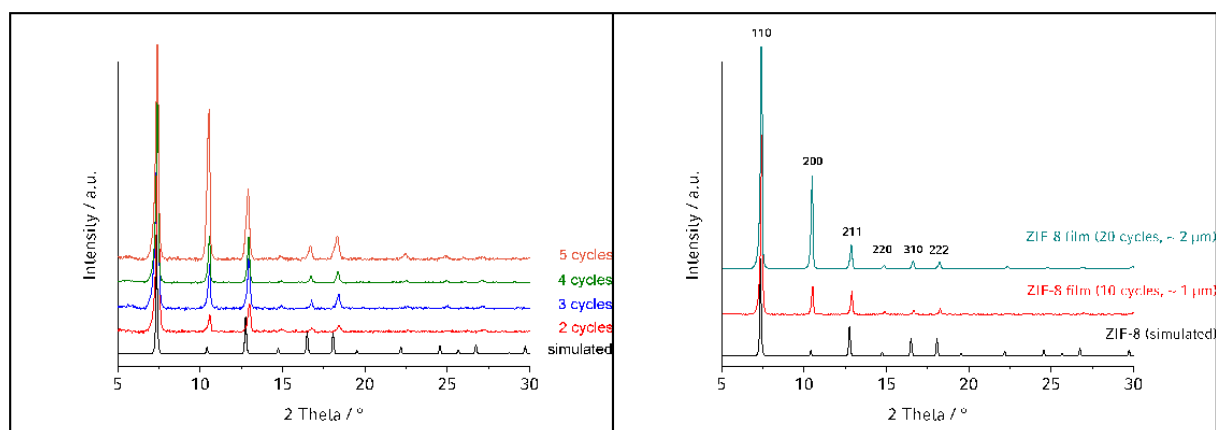
Figure 9-9   X-ray diffraction patterns (background corrected) of ZIF-8 thin films after different growing cycles compared to simulated data.
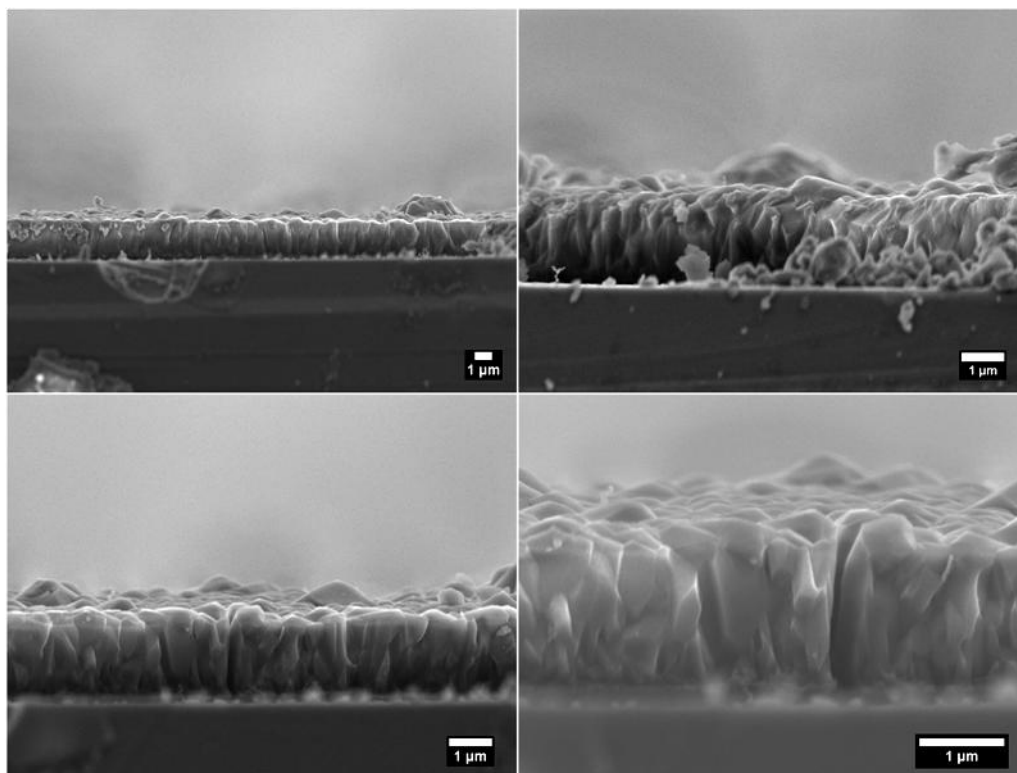
Figure 9-10   SEM micrographs showing a ZIF-8 thin film after 10 immersion cycles.
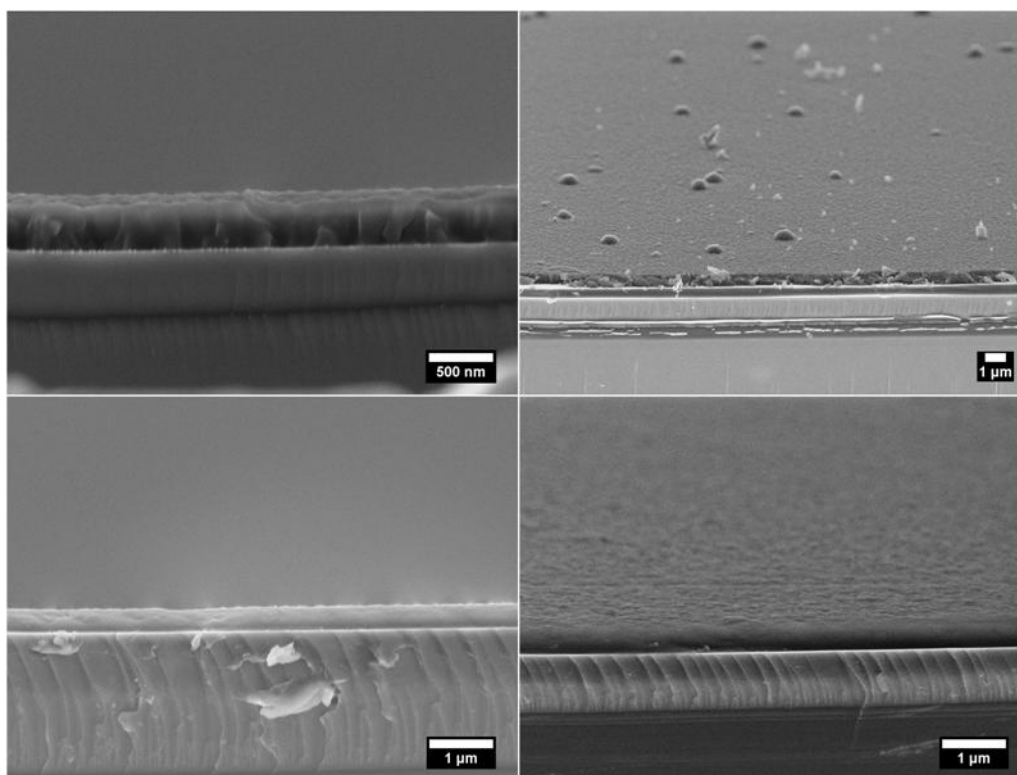
Figure 9-11   SEM micrographs showing ZIF-8 thin films grown in a crystallization solution while shaking (top) as well as under ultrasonic irradiation (bottom)
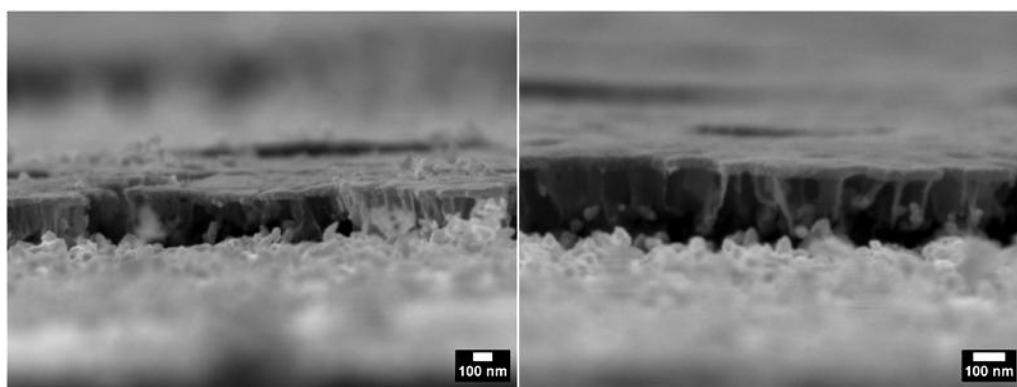
Figure 9-12   SEM micrographs showing bilayered Bragg stack-1 with an average film thickness of ~ 50 nm for each titania layer and ~ 200 nm for each ZIF-8 layer, respectively.
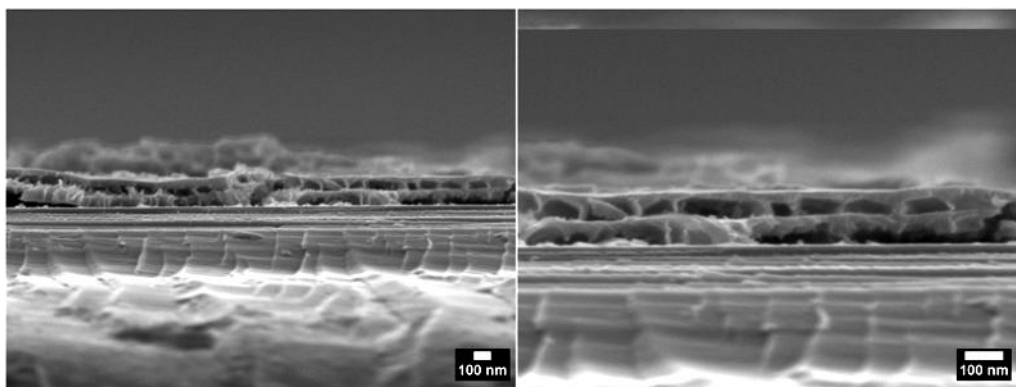
Figure 9-13   SEM micrographs showing the two bilayered Bragg stack-1 with an average film thickness of ~ 50 nm for each titania layer and ~ 70 nm for each ZIF-8 layer, respectively.
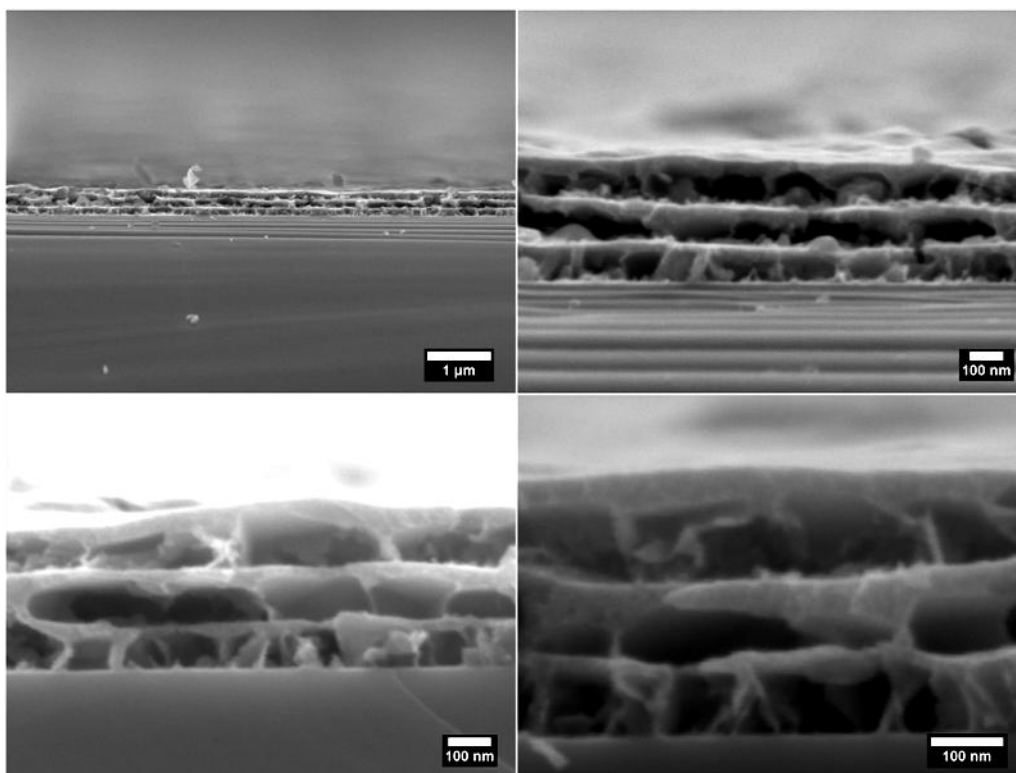
Figure 9-14   Scanning electron micrographs showing the 3 bilayered Bragg stack-1 with an average film thickness of ~ 50 nm for each titania layer and ~ 70 nm for each ZIF-8 layer, respectively.
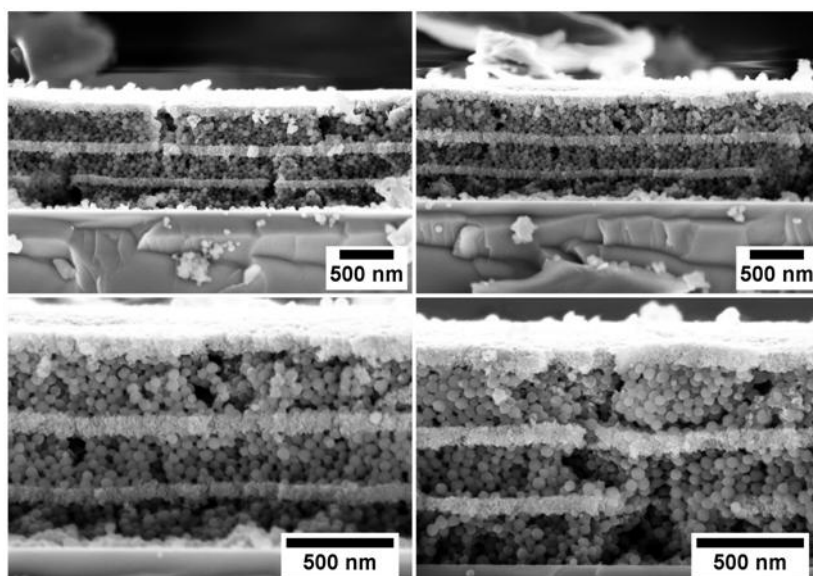
Figure 9-15   Scanning electron micrographs showing the 3 bilayered Bragg stack-2 with an average film thickness of ~ 50 nm for each titania layer and ~ 200 nm for each ZIF-8 layer, respectively.
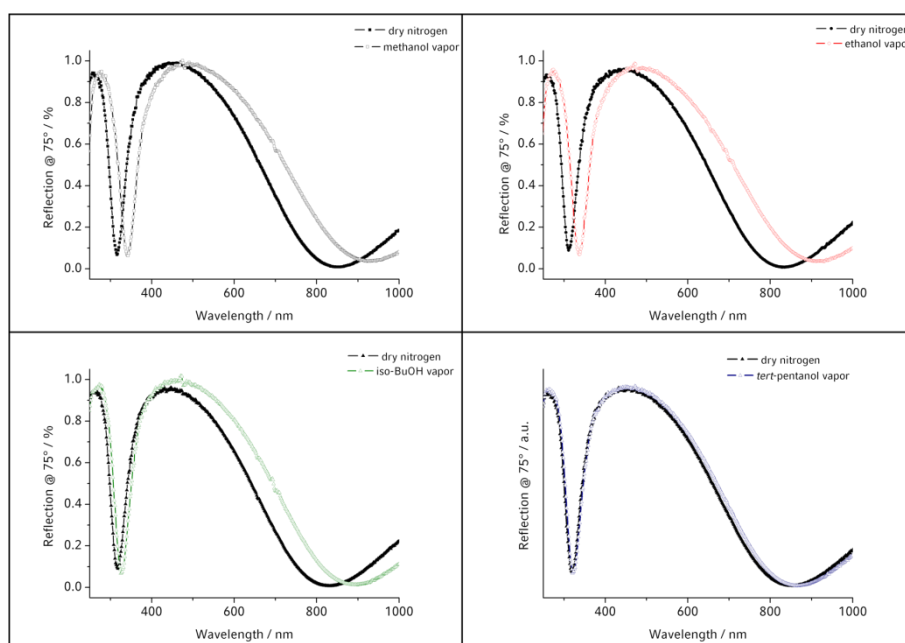
Figure 9-16   Reflectance spectra of a dense 200 nm single-layered ZIF-8 reference sample showing the pronounced optical shift monitored at saturation pressure upon exposure to methanol (top, left), ethanol (top, right) and

iso-butanol (bottom, left), respectively, as well as no optical response upon *tert*-pentanol sorption (bottom, right).
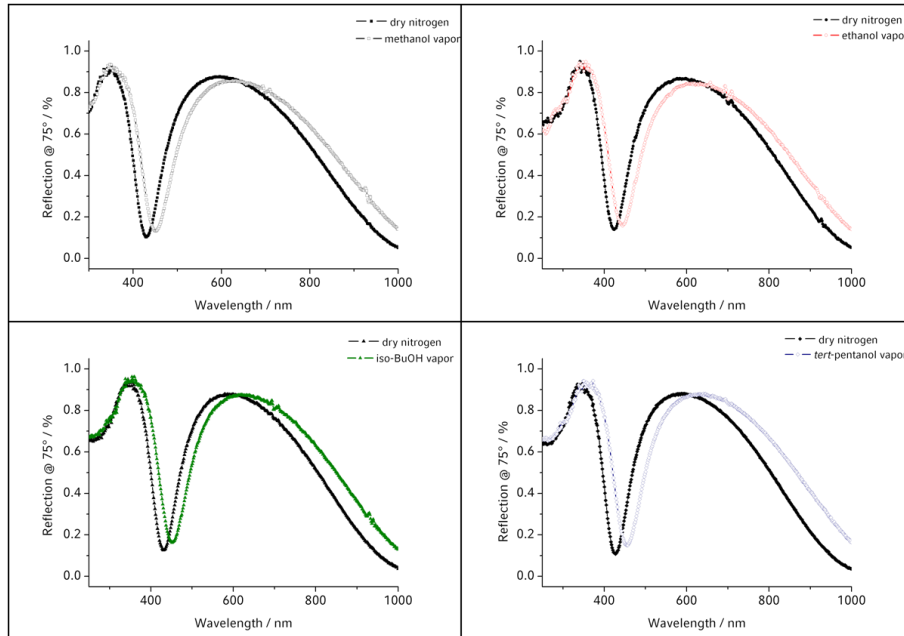
Figure 9-17   Reflectance spectra of the three-bilayer Bragg stack 1 showing the pronounced optical shift monitored at saturation pressure upon exposure to methanol (top, left), ethanol (top, right) and *iso*-butanol (bottom, left) as well as upon *tert*-pentanol (bottom, right) sorption.
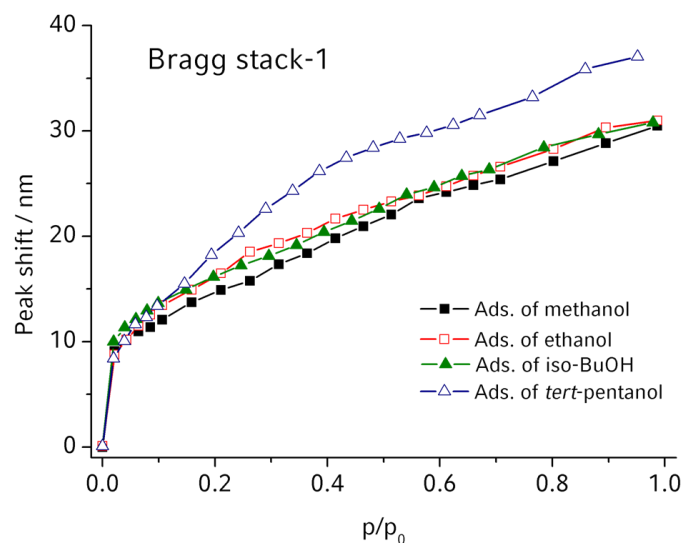
Figure 9-18   Optical vapor sorption isotherms demonstrating the adsorption performance of BS-1 during exposure to a series of alcohol vapors.
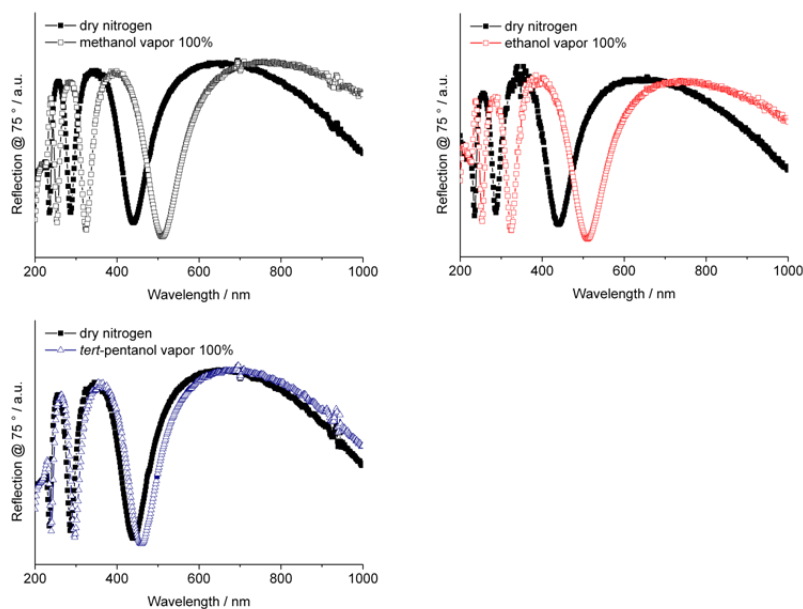
Figure 9-19   Reflectance spectra of a porous 400 nm single-layered ZIF-8 reference sample showing the pronounced optical shift monitored at saturation pressure upon exposure to methanol (top, left), ethanol (top, right) and *tert*-pentanol (bottom, left).
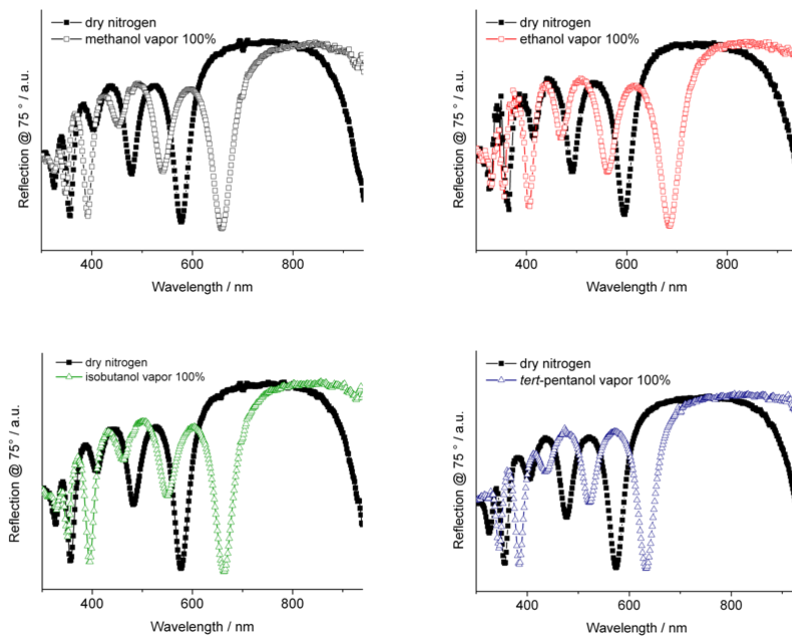
Figure 9-20   Reflectance spectra of the three-bilayer Bragg stack 2 (DMF) showing the pronounced optical shift monitored at saturation pressure upon exposure to methanol (top, left), ethanol (top, right), isobutanol (bottom, left) and *tert*-pentanol (bottom, right).

9.4   Supplementary Information for Chapter 5
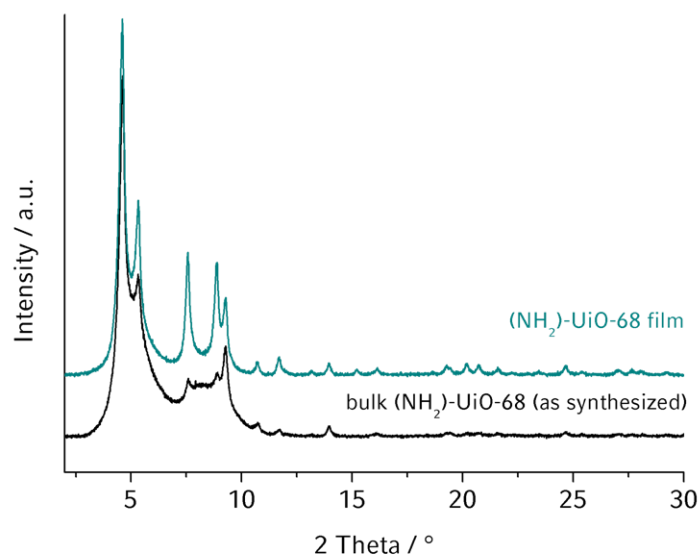
Figure 9-21   X-ray diffraction pattern (background corrected) of a randomly oriented UiO-68-NH$_2$ thin film grown on a glass substrate compared to the XRD pattern of as-synthesized bulk UiO-68-NH$_2$ crystals. The glass substrates were immersed in the crystallization solution for 5 days.
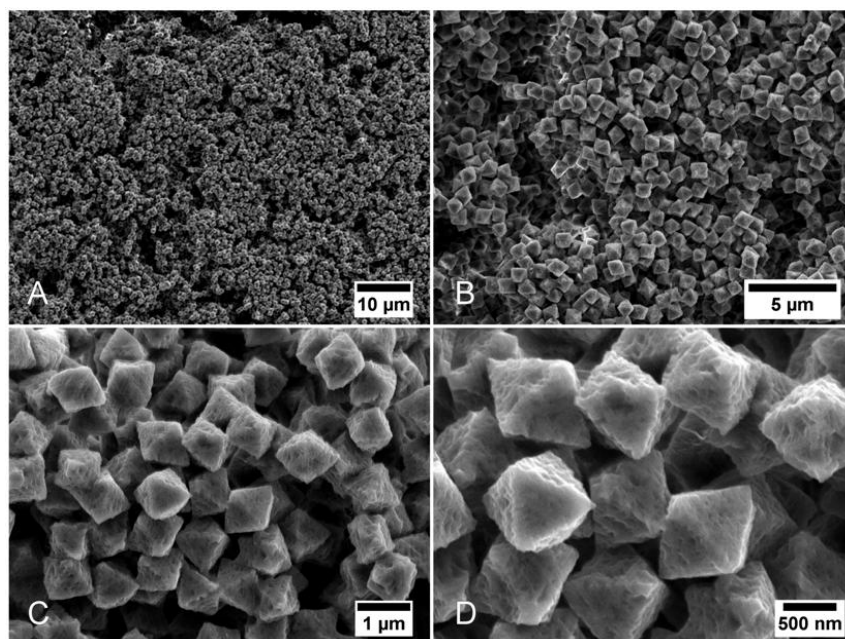
Figure 9-22   Scanning electron microscopy (SEM) images showing randomly oriented UiO-68-NH$_2$ crystals attached to the surface of a microscope slide. The microscope slides were immersed in the crystallization solution for 5 days.
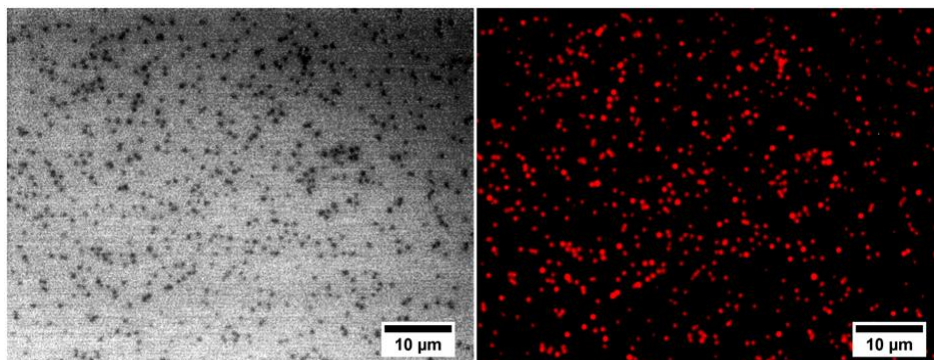
Figure 9-23   Bright-field image (left) and fluorescence image (right) of a Rhodamine B labeled UiO-68-NH$_2$ thin film that was immersed in the crystallization solution for 6 days.
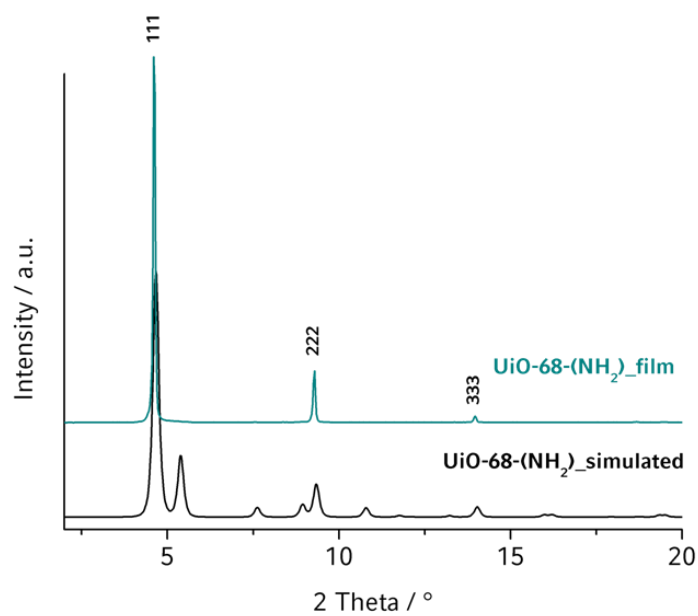
Figure 9-24   X-ray diffraction pattern (background corrected) of a highly oriented UiO-68-NH$_2$ thin film grown on 11-mercaptoundecanephosphonate (MUP) functionalized gold substrates compared to simulated data. The substrate was immersed in the crystallization solution for 30 d.
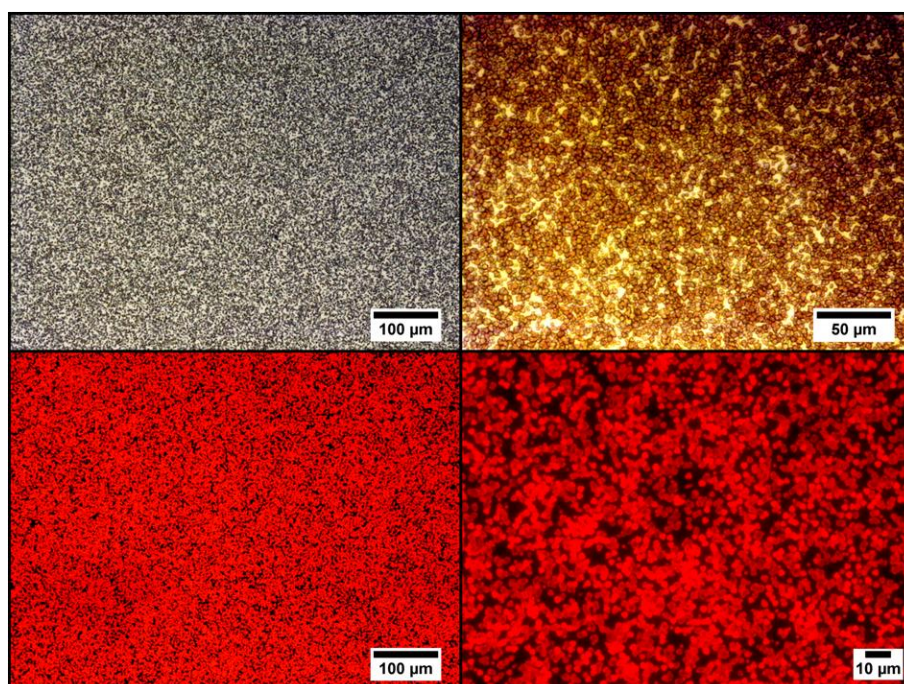
Figure 9-25   Bright-field (top) and fluorescence images (bottom) of a Rhodamine B labeled UiO-68-NH$_2$ thin film grown on a 16-mercaptohexadecanoic acid (MHDA) functionalized gold substrate. The films were immersed for 20 days in the filtered mother liquor followed by immersion for 10 days in a freshly prepared crystallization solution.
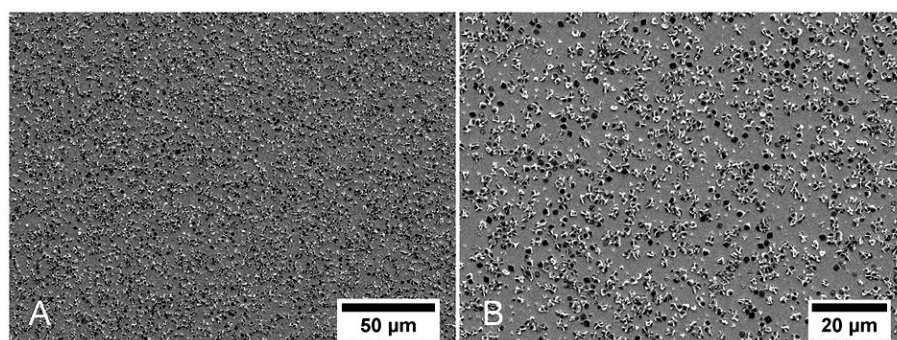
Figure 9-26   Scanning electron micrographs showing highly oriented growth of MOF-films after AuNPs quenching experiments. MOF thin films were obtained by immersing the gold substrates for 21 days in the filtered crystallization solution followed by an additional growth step in a freshly prepared mother liquor for 19 days.
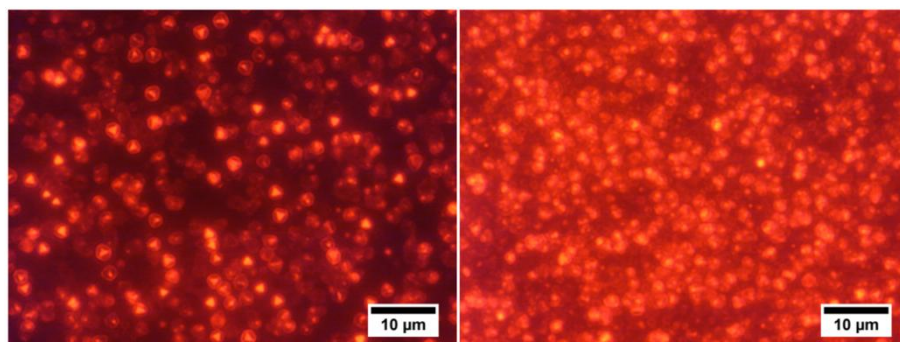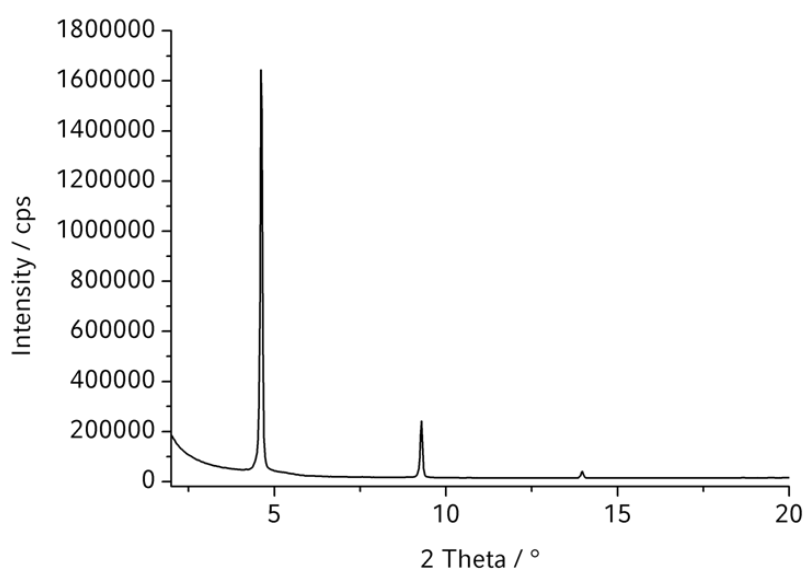
Figure 9-27   Fluorescence images of MOF-films after AuNP quenching experiments. MOF thin films were obtained by immersing the gold substrates for 21 days in the filtered crystallization solution followed by an additional growth step in a freshly prepared mother liquor for 19 days.
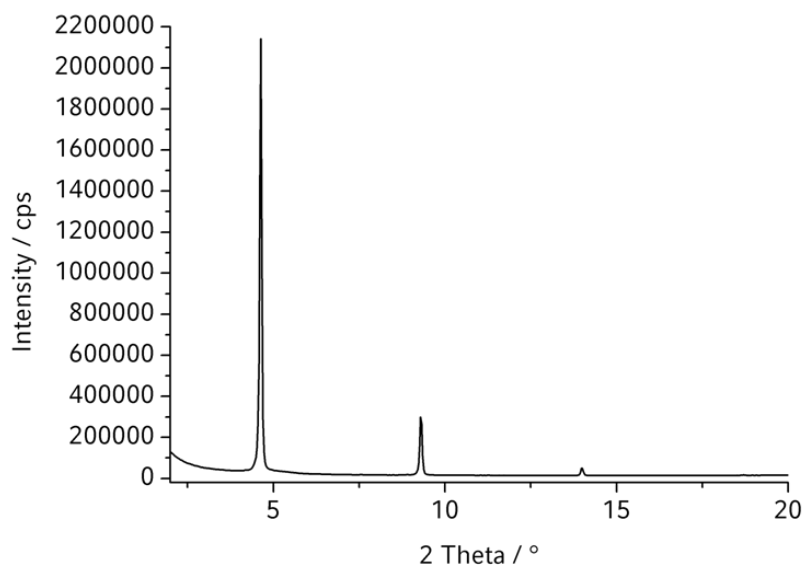

Figure 9-28   Original X-ray diffraction data of a highly oriented UiO-68-NH$_2$ thin film grown on a 11-mercaptoundecanephosphonate (MUP) SAM functionalized gold substrate for 30 days.

Figure 9-29   Original X-ray diffraction data of a highly oriented UiO-68-NH$_2$ thin film grown on a 16-mercapthexadecanoic acid (MHDA) SAM functionalized gold substrate for 21 days followed by an additional growth step in a freshly prepared crystallization solution for 19 days.
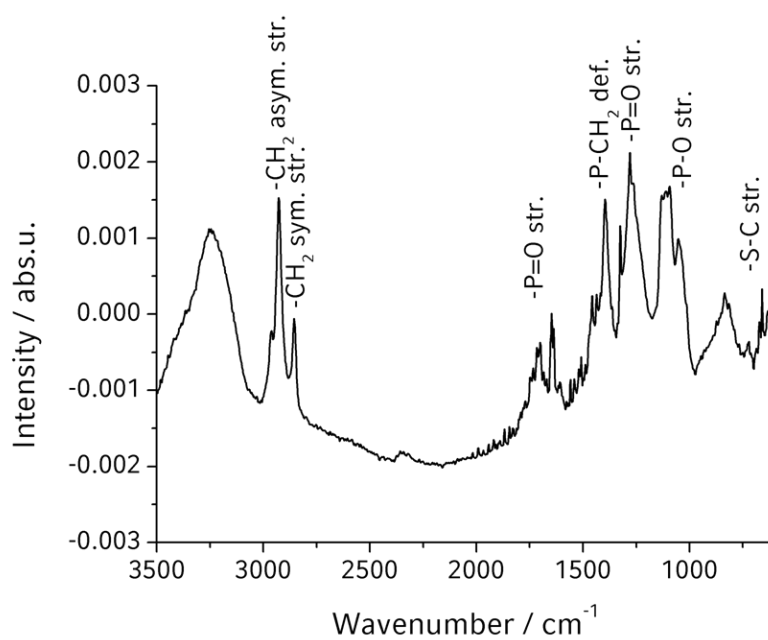
Figure 9-30   RAIR-spectrum   of   the   11-mercapto-1-undecanephosphonate   self-
assembled monolayer on a gold substrate that was immersed in a 1 mM
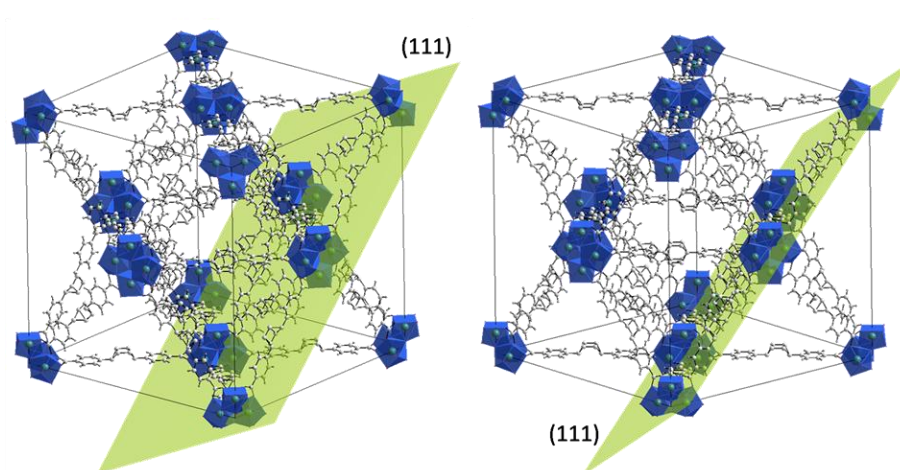ethanolic solution for 48 h.

Figure 9-31   Schematic representation of the unit cell of UiO-68-NH$_2$ as well as the 111
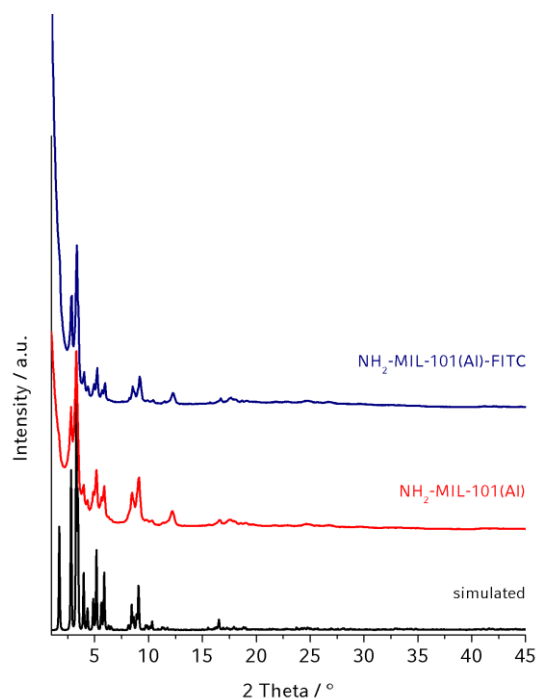lattice plane.

9.5   Supplementary Information for Chapter 7

Figure 9-32   Original X-ray diffraction patterns of as-synthesized NH_2-MIL-101(Al) (middle) as well as post-synthetically fluorescein labeled NH_2-MIL-101(Al) bulk material (top) compared to simulated data (bottom).

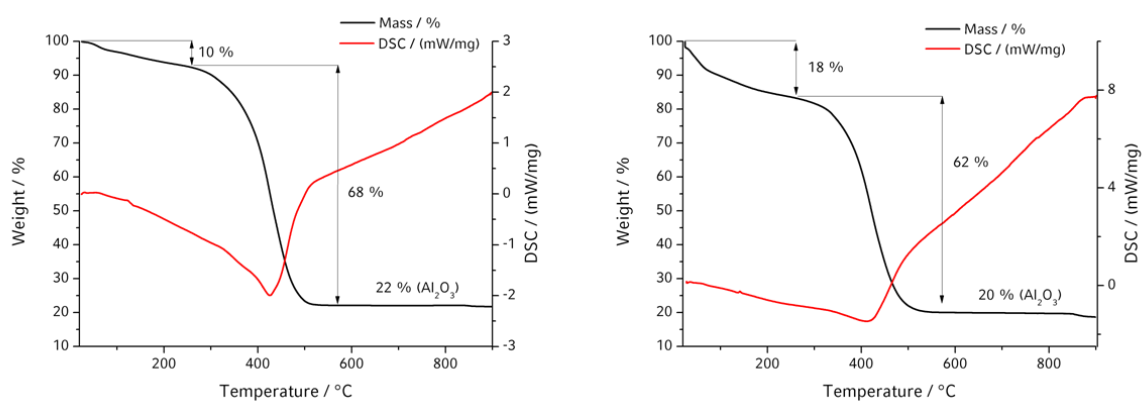**Figure 9-33**   Thermogravimetric analysis (TGA) and differential scanning calorimetry (DSC) of bulk NH_2-MIL-101(Al) (top) and NH_2-MIL-101(Al)-FITC (bottom)

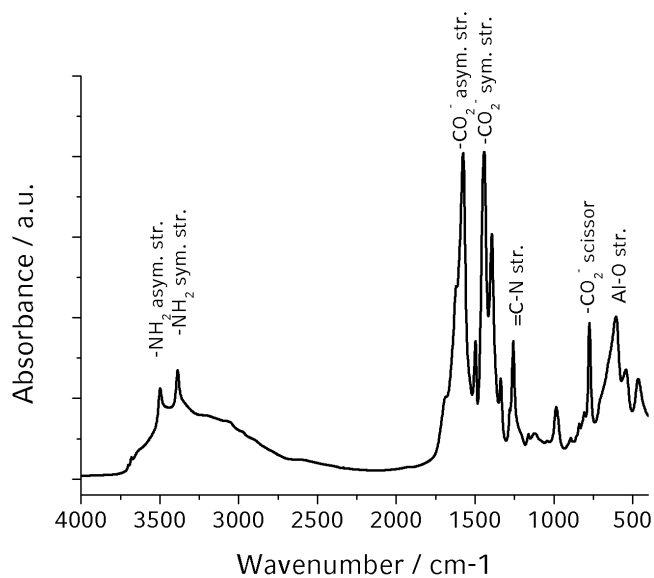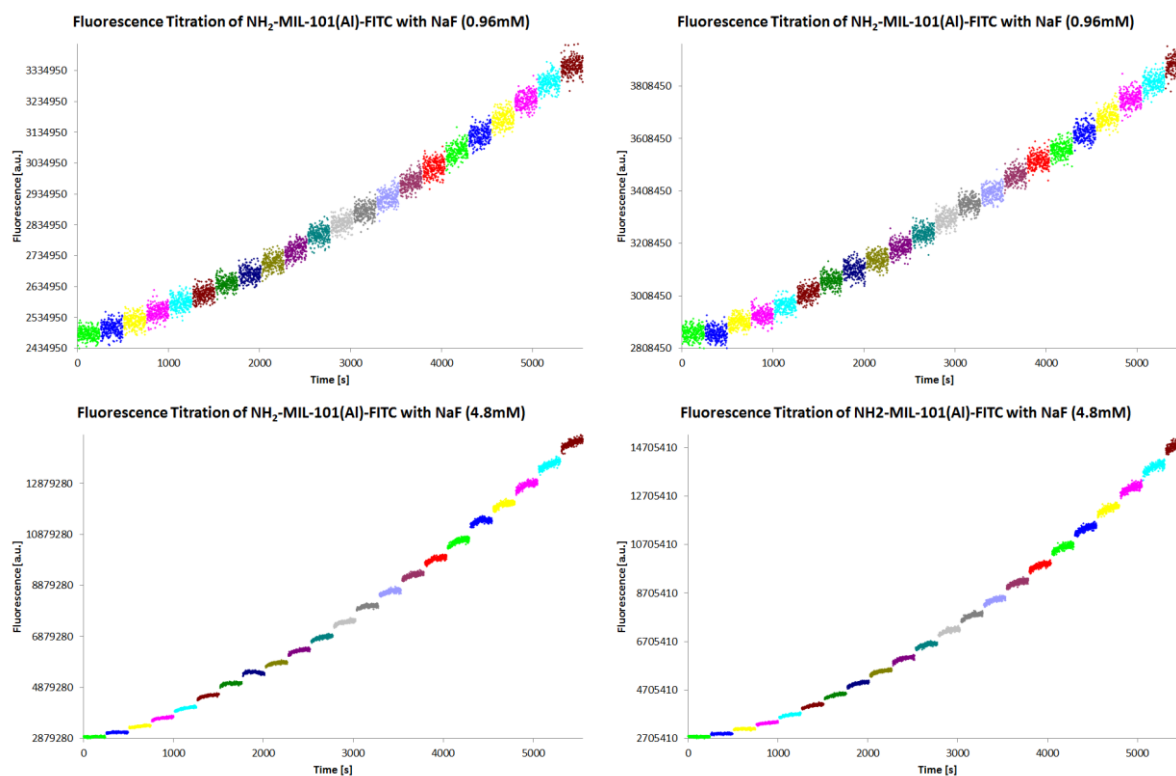illustrating the removal of residual molecules trapped within the pores as well as the decomposition of the framework.

Figure 9-34   IR spectrum of bulk NH$_2$-MIL-101(Al).

Fluorescence Titration of NH$_2$-MIL-101(Al)-FITC with NaCl (4.8mM)

Fluorescence Titration of NH$_2$-MIL-101(Al)-FITC with NaCl (4.8mM)

Fluorescence Titration of NH$_2$-MIL-101(Al)-FITC with NaBr (4.8mM)

Fluorescence Titration of NH$_2$-MIL-101(Al)-FITC with NaBr (4.8mM)

Fluorescence Titration of NH$_2$-MIL-101(Al)-FITC with NaI (4.8mM)

Fluorescence Titration of NH$_2$-MIL-101(Al)-FITC with NaI (4.8mM)

Fluorescence Titration of NH$_2$-MIL-101(Al)-FITC with NaNO$_3$ (4.8mM)

Fluorescence Titration of NH$_2$-MIL-101(Al)-FITC with NaNO$_3$ (4.8mM)
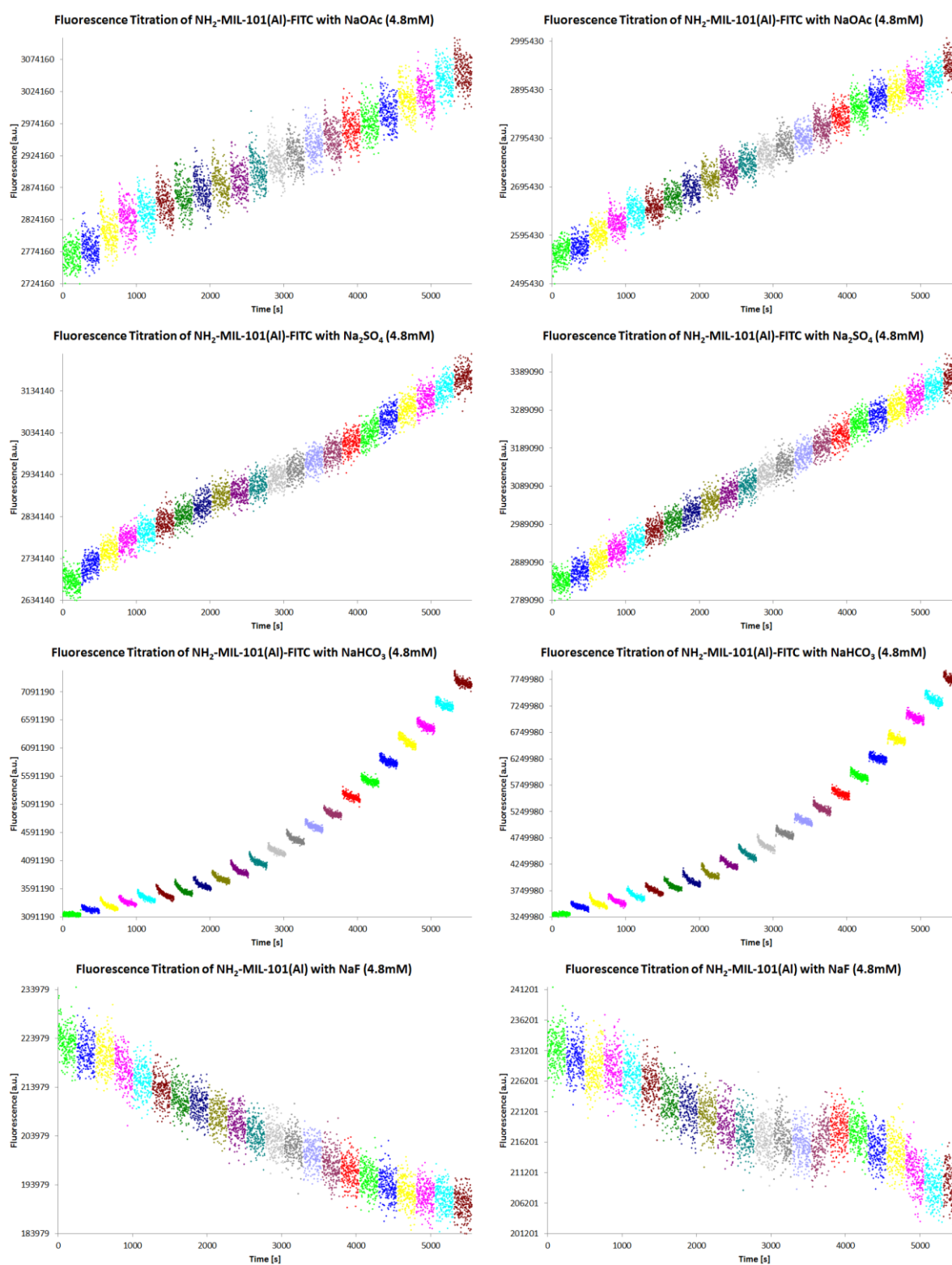
Figure 9-35 Raw fluorescence spectra. Shown are time-based fluorescence measurements (λ_{Ex}: 485 nm, λ_{Em}: 520 nm). For better visualization, a

different color was chosen for each 4 minute interval after a salt addition step of 2.5 µL, and the individual steps are separated by a time gap of 12 sec (corresponding to the approximate time for dispensing 2.5 µL of salt solution from the syringe). Fluorescence titration curves were constructed from these data sets by taking the average value of the last 60 points for each salt addition step and plotting this value against the salt concentration in the cuvette, as described above. The concentration value in brackets in the titles denotes the concentration of the respective titration solution. For each salt, two spectra (measurement and reproduction) are shown.
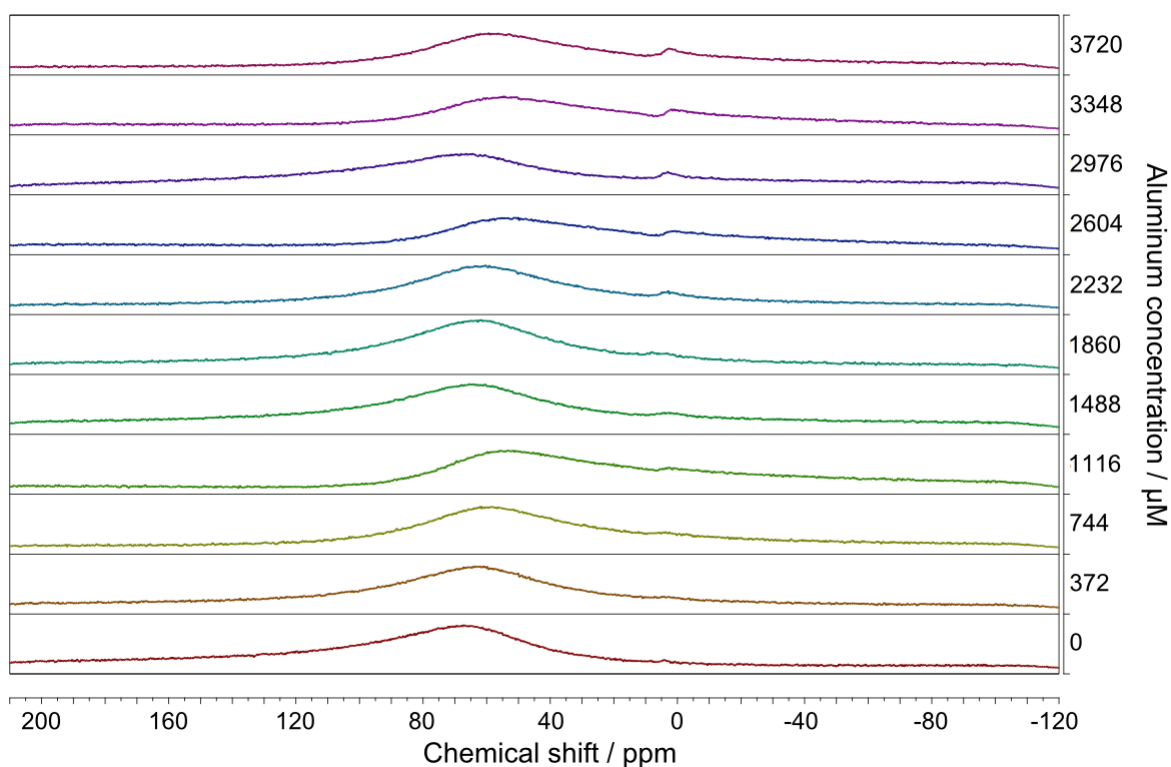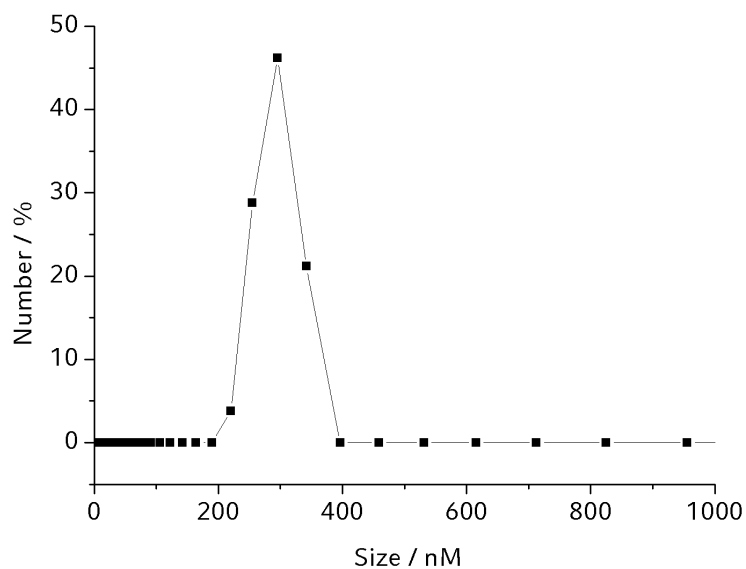

Figure 9-36 ^{27}Al NMR spectra before background correction.

Figure 9-37   Dynamic light scattering (DLS) measurement of a suspension of the labeled MOF in water (33 μg/mL), indicating a mean hydrodynamic size of the particles of approximately 300 nm.

10   Curriculum Vitae

PERSÖNLICHE DATEN

Geburtsdatum, Ort:	07. März 1983, München
Staatsangehörigkeit:	deutsch
Familienstand:	verheiratet

STUDIUM UND AUSBILDUNG

10/2009 – heute	**LUDWIG-MAXIMILIANS-UNIVERSITÄT, MÜNCHEN**
	Promotion in Physikalischer Chemie bei Prof. Dr. Thomas Bein, Thema: *Metal-organic Frameworks for Chemical Sensing Applications*
17. August 2009	**M. Sc.** Chemistry
10/2007 – 08/2009	**LUDWIG-MAXIMILIANS-UNIVERSITÄT, MÜNCHEN**
	Masterstudiengang Chemie
	Masterarbeit (Prof. Dr. Thomas Bein): *Oriented Growth of the Functionalized Metal-organic Framework CAU-1 on*

–OH and –COOH Terminated Self-assembled Monolayers

(1,0)

17. September 2007	**B. Sc.** Chemistry/Biochemistry
10/2003 – 09/2007	**LUDWIG-MAXIMILIANS-UNIVERSITÄT, MÜNCHEN** Bachelorstudiengang Chemie/Biochemie
17. Juli 2002	**Abitur**
09/1993 – 08/2002	**GYMNASIUM GRÖBENZELL, FÜRSTENFELDBRUCK**
09/1989 – 08/1993	**GRUNDSCHULE GOTZMANNSTRASSE, MÜNCHEN**

AUSLANDSAUFENTHALT

04/2008 – 08/2008	**STOCKHOLM UNIVERSITÄT, SCHWEDEN** Forschungspraktikum am Department für Organische Chemie bei Prof. Dr. Göran Widmalm

ZIVILDIENST

10/2002 – 08/2003 **STIFTUNG KATH. FAMILIEN- UND ALTENPFLEGEWERK, MÜNCHEN**

Betreuende, verpflegende und ambulante Tätigkeiten

BERUFLICHE ERFAHRUNG

09/2009 – heute **NANOSCAPE AG, MÜNCHEN**

Nebentätigkeit als freier Mitarbeiter

02/2009 – heute **ASSISTENTENTÄTIGKEIT AM LEHRSTUHL FÜR PHYSIKALISCHE CHEMIE, LUDWIG-MAXIMILIANS-UNIVERSITÄT, MÜNCHEN**

- Betreuung von Auszubildenden, Praktikanten und Diplomanden
- Organisation und Leitung von Praktika
- Lehr- und Prüftätigkeiten

10/2009 – heute **VERANTWORTL. WISSENSCHAFTLICHER ANGESTELLTER FÜR MESSGERÄTE, LUDWIG-MAXIMILIANS-UNIVERSITÄT, MÜNCHEN**

Wartung, Fehlerbehebung, Einweisung und

Firmenkontakt

ZUSATZQUALIFIKATIONEN

Sprachen   **Englisch**: verhandlungssicher

Französisch: gut

EDV Kenntnisse   MS Office, OriginLab, Corel Draw, POV-Ray, Material

Studio, MD Simulation

Methoden   Röntgendiffraktometrie, Rasterelektronenmikroskopie,

chem. und physikal. Beschichtungsverfahren (z.B. CVD,

SAMs, Sputter coating, E-beam evaporation), optische

Spektroskopie (IR, Raman, UV-Vis, Fluoreszenz, NMR),

Elementaranalytik, Ellipsometrie, Thermoanalytik,

Physisorption

11   Publications and Presentations

11.1   Publications

F. M. Hinterholzinger, B. Rühle, S. Wuttke, K. Karaghiosoff and T. Bein, "Highly sensitive and selective fluoride detection in water through fluorophore release from a metal-organic framework"; submitted.

S. Wuttke, B. Rühle, F. M. Hinterholzinger, A. Godt and T. Bein, "Chemoluminescence in an Anthracene Based Metal-organic Framework"; manuscript in preparation.

F. M. Hinterholzinger, A. Ranft, J. M. Feckl, B. Rühle, T. Bein and B. V. Lotsch, "One-dimensional Metal-organic Framework Photonic Crystals Used as Platforms for Vapor Sorption"; *J. Mater. Chem.*, 2012, **22**, 10356-10362.

F. M. Hinterholzinger, S. Wuttke, P. Roy, Preuße, A. Schaate, P. Behrens, A. Godt and T. Bein, "Highly Oriented Growth and Post-synthetic Dye Labeling of Mesoporous and Functionalized Metal-organic Framework Thin Films"; *Dalton Trans.*, 2012, **41**, 3899-3901.

E. Säwén, F. Hinterholzinger, C. Landersjö and G. Widmalm, "Conformational flexibility of the pentasaccharide LNF-2 deduced from NMR spectroscopy and molecular dynamics simulations"; *Org. Biomol. Chem.*, 2012, **10**, 4577-4585.

C. Scherb, J. J. Williams, F. Hinterholzinger, S. Bauer, N. Stock and T. Bein, "Extending the Structure-directing Concept to Functionalized Metal-organic frameworks"; *J. Mater. Chem.*, 2011, **21**, 14849-14856.

F. Hinterholzinger, C. Scherb, T. Ahnfeldt, N. Stock and T. Bein, "Oriented growth of the functionalized metal–organic framework CAU-1 on −OH- and −COOH- terminated self-assembled monolayers "; *Phys. Chem. Chem. Phys.*, 2010, **12**, 4515-4520.

11.2   Oral presentations

Stefan Wuttke, Christian Dietl, Florian M. Hinterholzinger, Henrik Hintz, Heinz Langhals and Thomas Bein, "Incorporation of fluorescent dye functionalities into MOF cavities via different strategies " Third International Conference on Multifunctional, Hybrid and Nanomaterials (Hybrid Materials 2013), March 03 – 07, **2013**, Sorrento, Italy.

Annekathrin Ranft, Florian Hinterholzinger, Felicitas Niekiel, Norbert Stock, Thomas Bein and Bettina V. Lotsch, "One-dimensional Metal-organic Framework

photonic crystals used as platforms for vapor sorption " *MOF Status Report Meeting 2012*, November 28 – 29, **2012**, Dresden, Germany.

Florian M. Hinterholzinger, Bastian Rühle, Stefan Wuttke, Konstantin Karaghiosoff and Thomas Bein, "Highly sensitive fluoride detection based on Metal-organic Frameworks" *3rd International Conference on Metal-Organic Frameworks and Open Framework Compounds*, September 16 – 19, **2012**, Edinburgh, UK.

Annekathrin Ranft, Florian Hinterholzinger, Johann Feckl, Bastian Rühle, Thomas Bein and Bettina V. Lotsch, "MOF-based Photonic Crystals for Optical Sensing Applications" *3rd International Conference on Metal-Organic Frameworks and Open Framework Compounds*, September 16 – 19, **2012**, Edinburgh, UK.

Thomas Preuße, Pascal Roy, Adelheid Godt, Andreas Schaate, Jann Lippke, Peter Behrens, Florian Hinterholzinger, Stefan Wuttke, Thomas Bein, "Postsynthetic Modification of Zr-based MOFs (UiOs and PIZOFs) through cycloaddition reactions" *3rd International Conference on Metal-Organic Frameworks and Open Framework Compounds*, September 16 – 19, **2012**, Edinburgh, UK.

Florian M. Hinterholzinger, Annekathrin Ranft, Johann M Feckl, Bettina V. Lotsch and Thomas Bein, "One-dimensional Metal-organic Framework Photonic Crystals Used as Platform for Selective Vapor Sensing" *2012 MRS Spring Meeting & Exhibit*, April 09 – 13, **2012**, San Francisco (CA), USA.

St. Wuttke, F. Hinterholzinger, P. Roy, J. Horstmann, A. Godt, T. Bein, "Oriented growth of functionalized mesoporous MOF crystal layers", *International Symposium on Metal-Organic Frameworks*, September 20 – 21, **2011**, Dresden, Germany.

11.3   Poster presentations

Florian M. Hinterholzinger, Stefan Wuttke, Pascal Roy, Thomas Preuße, Andreas Schaate, Peter Behrens, Adelheid Godt and Thomas Bein, "Highly Oriented Growth and Post-synthetic Dye Labeling of Mesoporous and Functionalized Metal-organic Framework Thin Films " *3rd International Conference on Metal-Organic Frameworks and Open Framework Compounds*, September 16 – 19, **2012**, Edinburgh, UK.

Florian Hinterholzinger, Camilla Scherb, Jennifer J. Williams, Sebastian Bauer, Norbert Stock and Thomas Bein, "Oriented Growth of Amino-Functionalized Metal-Organic Frameworks   Vapor Sorption Isotherms" 16th *International Zeolite Conference/7th International Mesostructured Materials Symposium*, July 04 – 09, **2010**, Sorrento, Italy.

Camilla Scherb, Florian Hinterholzinger, Alexander Schoedel, Jennifer Williams, Sebastian Bauer, Norbert Stock and Thomas Bein, "Oriented Growth of Amino-Functionalized Metal-Organic Frameworks   Vapor Sorption Isotherms" 2nd *International Conference on Metal-Organic Frameworks and Open Framework Compounds*, September 05 – 09, **2010**, Marseille, France.

<u>Florian Hinterholzinger</u>, Camilla Scherb, Jennifer J. Williams, Norbert Stock and Thomas Bein, "Oriented Growth of Amino-Functionalized Metal-Organic Frameworks on Carboxylate Terminated Organic Monolayers" 22 *Deutsche Zeolith-Tagung*, March 03 – 05, **2010**, Munich, Germany.